APPLIED COMPUTATIONAL ELECTROMAGNETICS SOCIETY JOURNAL

November 2021
Vol. 36 No. 11
ISSN 1054-4887

The ACES Journal is abstracted in INSPEC, in Engineering Index, DTIC, Science Citation Index Expanded, the Research Alert, and to Current Contents/Engineering, Computing & Technology.

The illustrations on the front cover have been obtained from the research groups at the Department of Electrical Engineering, The University of Mississippi

NOVEMBER 2021 REVIEWERS

Marco Arjona
Jiefu Chen
Isaac Barros da Silva
Mang He
Xinbo He
Kathir I.
Robert Ilgner
Srividhya K.
George Kyriacou
Damir Latypov
Daotong Li
Zhe Yu Li
Tao Liang
Jau-Jr Lin
Asmaa Majeed
Premkumar Manoharan
Zlatica Marinkovic
Adam Mock
Paolo Nepa
Antonio Orlandi
Camelia Petrescu
Jean Piou
R.Karpagam Raj
Rengasamy Rajkumar
Alain Reineix
Thomas Roth
Rashid Saleem
Junwu Tao
Yu Tian
Riccardo Torchio
Hossein Torkaman
Dattaprasad Torse
Ozgur Tuncer
Wei-Chung Weng
Mohammad Yazdani-Asrami
Fan Zhang
Bo Zhu

THE APPLIED COMPUTATIONAL ELECTROMAGNETICS SOCIETY JOURNAL

Vol. 36 No. 11 November 2021

TABLE OF CONTENTS

New Approximate Expressions for Evaluating the Fields of a Vertical Magnetic Dipole in a Dissipative Half Space

Hongyun Deng, Gaobiao Xiao, and Shifeng Huang

Key Laboratory of Ministry of Education of Design and Electromagnetic Compatibility of High Speed Electronic Systems, Shanghai Jiao Tong University, Shanghai 200240, China
hongyundeng@sjtu.edu.cn; gaobiaoxiao@sjtu.edu.cn; huangshifeng@sjtu.edu.cn

Abstract – In this paper, a set of new asymptotic approximate expressions for evaluating the electromagnetic (EM) fields generated by a vertical magnetic dipole placed in a dissipative half space is proposed. The lateral wave that guarantees the continuity of the EM fields at the interface is discussed in detail. Using the spectral method, the integral expressions of the field components are obtained. The dominant part is extracted from the lateral wave for large radial distance so that all field components in this situation can be approximately expressed with explicit expressions, which makes the method efficient. Besides, the proposed method has no restriction condition on the parameter choices of different half spaces, so it can be applied in more general situations. Some calculation results and comparisons are given to validate the effectiveness of this extraction method.

Index Terms – Asymptotic approximation, dissipative medium, lateral wave, spectral method, surface wave, magnetic dipole.

I. INTRODUCTION

The surface waves have been studied since the time of Sommerfeld [1]. In 1907, Zenneck discussed the waves crouching on the intersecting surface of the earth and the air that possesses the radial symmetry [2]. He wanted to explain the long-distance radio wave propagation on the earth by the surface wave over the ground. The discussion of the Zenneck wave is still going on, even if the long-distance propagation of the electromagnetic (EM) waves could be explained by the existence of the ionosphere nowadays. The study about such waves has its own meaning since it guarantees the continuity of the EM waves at the boundary of lossy media such as the earth, the sea water, and the sea crust [3–8]. This kind of surface waves only exist when the source is placed near the boundary, which means that sources like plane waves cannot excite such kind of waves [9]. Norton simplified the Sommerfeld's complicated integral solution of the surface waves by some approximations to give explicit expressions of the surface waves and make it more applicable [7]. On the other hand, Baños got further results following the work of Sommerfeld, but those were still too complicated [10]. They could not give the direct physical insight of the surface waves and were not convenient for engineering applications [3]. The surface waves excited by dipoles (electric and magnetic) placed near the boundary of dissipative medium are also called the lateral waves. It has many realistic application scenes such as communication with submerged submarines. King [3] gave an extensive discussion of the theory and application of the lateral waves generated by a vertical electric dipole in the sea. However, King's asymptotic approximation method has the restriction condition on the wave numbers of the two half spaces that $|k_1| \gg |k_0|$, and this condition is satisfied by the relevant parameters of the sea and the air. Researchers also tried to get numerical solutions of the lateral waves that travel along the interface of the sea and the air with the help of computers. However, the numerical methods are time-consuming when calculating the far fields because the integrands of the integral expressions of the fields oscillate severely, and it needs some special techniques [11–13]. Nowadays, there are different methods that could deal with the EM field problem in planar stratified media [14–17]. None of these methods could avoid the evaluation of Sommerfeld integrals and the evaluation of Sommerfeld integrals can be categorized into three types: the direct numerical method [18–20], the discrete complex image method [21–23], and the asymptotic method [3, 10]. The asymptotic method has the advantage of having high efficiency and being accurate when calculating the EM field in the far region.

In this paper, a novel asymptotic method to extract the dominant parts of the lateral waves is proposed. This method stems from the double saddle point method [10]. Nevertheless, no asymptotic series coefficients need to be specifically calculated like that in [10] due to the proposed extraction technique. All the field components generated by a vertical magnetic dipole (VMD; it can be regarded as a model of the closed electrical line carrying a time-varying electric current loop which supplies the

Submitted On: September 10, 2021
Accepted On: November 11, 2021

https://doi.org/10.13052/2021.ACES.J.361101

1054-4887 © ACES

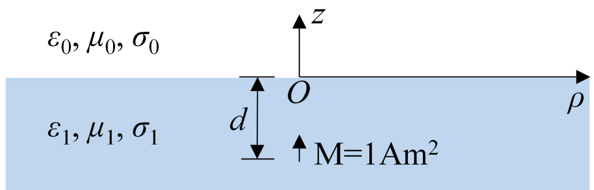

Fig. 1. A vertical magnetic dipole in the sea.

electricity to the electronic devices on a ship) in a dissipative half space have explicit expressions by neglecting the corresponding residual integrals. The fields of other types of dipoles can be dealt with in a similar way. The newly proposed method has no restriction condition on the wavenumbers of different half spaces; so it can be applied in more general problems than King's approximation method.

II. FORMULATION

A. Model

The basic model in this paper is depicted in Figure 1. Hereinafter, the cylindrical coordinate system is used, and the three coordinates are (ρ, ϕ, z). Due to the radial symmetry, ϕ is always assumed to be 0. The lower half space is sea, and the upper half space is air. The plane $z = 0$ is the interface of the two half spaces. A VMD is placed in the sea at the point $(\rho, z) = (0, -d)$ $(d > 0)$. M is the dipole moment. Assume that the permittivity and the permeability of the free space are ε_0 and μ_0, respectively. The sea has the permittivity of $\varepsilon_1 = 81_0$, the permeability of $\mu_1 = \mu_0$, and the conductivity of $\sigma_1 = 4$ S/m. The air has the permittivity of ε_0, the permeability of μ_0, and the conductivity of $\sigma_0 = 0$ S/m.

B. Integral expressions of the EM fields

Using the spectral method [24], the nonzero field components in the sea can be expressed as the following three integrals:

$$\begin{aligned} H_{1z} &= \int_{-\infty}^{\infty} dk_\rho \begin{bmatrix} e^{ik_{1z}(z+d)} + \\ Re^{-ik_{1z}(z+d)} \end{bmatrix} H_{\mathrm{VMD}} H_0^{(1)}\left(k_\rho \rho\right), \\ H_{1\rho} &= \int_{-\infty}^{\infty} dk_\rho \begin{bmatrix} e^{ik_{1z}(z+d)} - \\ Re^{-ik_{1z}(z+d)} \end{bmatrix} \frac{ik_{1z}}{k_\rho} H_{\mathrm{VMD}} H_0^{(1)\prime}\left(k_\rho \rho\right), \\ E_{1\phi} &= \int_{-\infty}^{\infty} dk_\rho \begin{bmatrix} e^{ik_{1z}(z+d)} + \\ Re^{-ik_{1z}(z+d)} \end{bmatrix} \frac{\omega\mu_1}{ik_\rho} H_{\mathrm{VMD}} H_0^{(1)\prime}\left(k_\rho \rho\right). \end{aligned} \tag{1}$$

The nonzero field components in the air can be expressed as the following three integrals:

$$\begin{aligned} H_{0z} &= \int_{-\infty}^{\infty} dk_\rho T e^{ik_{0z}z} H_{\mathrm{VMD}} H_0^{(1)}\left(k_\rho \rho\right), \\ H_{0\rho} &= \int_{-\infty}^{\infty} dk_\rho T e^{ik_{0z}z} \frac{ik_{0z}}{k_\rho} H_{\mathrm{VMD}} H_0^{(1)\prime}\left(k_\rho \rho\right), \\ E_{0\phi} &= \int_{-\infty}^{\infty} dk_\rho T e^{ik_{0z}z} \frac{\omega\mu_0}{ik_\rho} H_{\mathrm{VMD}} H_0^{(1)\prime}\left(k_\rho \rho\right). \end{aligned} \tag{2}$$

H_{1z} and $H_{1\rho}$(H_{0z} and $H_{0\rho}$) are the z component and the ρ component of the magnetic field in the sea (air), respectively. $E_{1\phi}$ ($E_{0\phi}$) is the ϕ component of the electrical field in the sea (air). R and T are, respectively, the reflection coefficient and the transmission coefficient. k_ρ is the radial wavenumber. $k_{0z} = \left(k_0^2 - k_\rho^2\right)^{1/2}$ and $k_{1z} = \left(k_1^2 - k_\rho^2\right)^{1/2}$. k_0 is the wavenumber in the air and k_1 is the wavenumber in the sea. ω is the angular frequency. H_{VMD} is the spectral expression of the VMD which equals $-iMk_\rho^3/8\pi k_{1z}$.$H_0^{(1)}$ $(\bullet)$is the zeroth-order Hankel function of the first kind. The prime means taking the derivative with respect to ρ.

The tangential components of the EM field should be continuous at the interface. Let z approaches zero in equations (1) and (2), and the linear equations of R and T can be written as eqn (3). Then, R and T can be obtained by solving eqn (3):

$$\begin{cases} \int_{-\infty}^{\infty} dk_\rho \frac{ik_{1z}}{k_\rho} H_{\mathrm{VMD}} \left[e^{ik_{1z}d} - Re^{-ik_{1z}d}\right] H_0^{(1)\prime}\left(k_\rho \rho\right) \\ \quad = \int_{-\infty}^{\infty} dk_\rho \frac{ik_{0z}}{k_\rho} H_{\mathrm{VMD}} T H_0^{(1)\prime}\left(k_\rho \rho\right), \\ \int_{-\infty}^{\infty} dk_\rho \frac{-i\omega\mu_1}{k_\rho} H_{\mathrm{VMD}} \left[e^{ik_{1z}d} + Re^{-ik_{1z}d}\right] H_0^{(1)\prime}\left(k_\rho \rho\right) \\ \quad = \int_{-\infty}^{\infty} dk_\rho \frac{-i\omega\mu_0}{k_\rho} H_{\mathrm{VMD}} T H_0^{(1)\prime}\left(k_\rho \rho\right). \end{cases} \tag{3}$$

$$\begin{cases} R = \dfrac{\mu_0 k_{1z} - \mu_1 k_{0z}}{\mu_0 k_{1z} + \mu_1 k_{0z}} e^{2ik_{1z}d}, \\ T = \dfrac{2k_{1z}\mu_1}{\mu_0 k_{1z} + \mu_1 k_{0z}} e^{ik_{1z}d}. \end{cases} \tag{4}$$

All components of the EM fields can then be expressed by Sommerfeld integrals. Unfortunately, they have no explicit expressions except for some special occasions, and their integrands oscillate severely when the radial distance is large. We will focus on these integrals in the following subsections.

C. EM fields in the sea

The nonzero EM field components in the sea $(-d < z < 0)$ are available by substituting eqn (4) into eqn (1). After some simple rearrangements, each field component can be decomposed into three parts as follows:

$$\begin{aligned} H_{1z} &= H_{1z}^{\mathrm{in}} + H_{1z}^{\mathrm{im}} + H_{1z}^{\mathrm{lat}}, \\ H_{1\rho} &= H_{1\rho}^{\mathrm{in}} + H_{1\rho}^{\mathrm{im}} + H_{1\rho}^{\mathrm{lat}}, \\ E_{1\phi} &= E_{1\phi}^{\mathrm{in}} + E_{1\phi}^{\mathrm{im}} + E_{1\phi}^{\mathrm{lat}}. \end{aligned} \tag{5}$$

The superscript "in" means the direct wave, "im" means the image wave, and "lat" means the lateral wave. They are defined by the following equations:

$$\begin{cases} H_{1z}^{\mathrm{in}} = -i\frac{M}{4\pi} \int_0^{\infty} dk_\rho \frac{k_\rho^3}{k_{1z}} e^{ik_{1z}(z+d)} J_0\left(k_\rho \rho\right), \\ H_{1z}^{\mathrm{im}} = i\frac{M}{4\pi} \int_0^{\infty} dk_\rho \frac{k_\rho^3}{k_{1z}} e^{ik_{1z}(d-z)} J_0\left(k_\rho \rho\right), \\ H_{1z}^{\mathrm{lat}} = -i\frac{M}{2\pi} \int_0^{\infty} dk_\rho \frac{k_\rho^3}{k_{1z}+k_{0z}} e^{ik_{1z}(d-z)} J_0\left(k_\rho \rho\right). \end{cases} \tag{6}$$

$$\begin{cases} H_{1\rho}^{\text{in}} = -\frac{M}{4\pi}\int_0^\infty dk_\rho k_\rho^2 e^{ik_{1z}(z+d)} J_1\left(k_\rho\rho\right), \\ H_{1\rho}^{\text{im}} = -\frac{M}{4\pi}\int_0^\infty dk_\rho k_\rho^2 e^{ik_{1z}(d-z)} J_1\left(k_\rho\rho\right), \\ H_{1\rho}^{\text{lat}} = \frac{M}{2\pi}\int_0^\infty dk_\rho \frac{k_\rho^2 k_{1z}}{k_{1z}+k_{0z}} e^{ik_{1z}(d-z)} J_1\left(k_\rho\rho\right). \end{cases} \tag{7}$$

$$\begin{cases} E_{1\phi}^{\text{in}} = \frac{\omega\mu_1 M}{4\pi}\int_0^\infty dk_\rho \frac{k_\rho^2}{k_{1z}} e^{ik_{1z}(d+z)} J_1\left(k_\rho\rho\right), \\ E_{1\phi}^{\text{im}} = -\frac{\omega\mu_1 M}{4\pi}\int_0^\infty dk_\rho \frac{k_\rho^2}{k_{1z}} e^{ik_{1z}(d-z)} J_1\left(k_\rho\rho\right), \\ E_{1\phi}^{\text{lat}} = \frac{\omega\mu_1 M}{2\pi}\int_0^\infty dk_\rho \frac{k_\rho^2}{k_{1z}+k_{0z}} e^{ik_{1z}(d-z)} J_1\left(k_\rho\rho\right). \end{cases} \tag{8}$$

All components of the direct wave and the image wave have explicit expressions according to Appendix A of [3], so only the lateral wave needs to be dealt with.

For the sake of simplicity, some notations are introduced as follows:

$$\begin{aligned} F_{1z}(\rho,x) &= \int_0^\infty dk_\rho \frac{k_\rho^3}{k_{1z}+k_{0z}} e^{ik_{1z}x} J_0\left(k_\rho\rho\right), \\ F_{1\rho}(\rho,x) &= \int_0^\infty dk_\rho \frac{k_\rho^2 k_{1z}}{k_{1z}+k_{0z}} e^{ik_{1z}x} J_1\left(k_\rho\rho\right), \\ F_{1\phi}(\rho,x) &= \int_0^\infty dk_\rho \frac{k_\rho^2}{k_{1z}+k_{0z}} e^{ik_{1z}x} J_1\left(k_\rho\rho\right). \end{aligned} \tag{9}$$

Now, the lateral wave in the sea can be written as

$$\begin{aligned} H_{1z}^{\text{lat}} &= \frac{M}{2\pi i} F_{1z}(\rho, d-z), \\ H_{1\rho}^{\text{lat}} &= \frac{M}{2\pi} F_{1\rho}(\rho, d-z), \\ E_{1\phi}^{\text{lat}} &= \frac{\omega\mu_1 M}{2\pi} F_{1\phi}(\rho, d-z). \end{aligned} \tag{10}$$

Take $F_{1z}(\rho,x)$ as an example. It can be rearranged as

$$F_{1z}(\rho,x) = \frac{\int_0^\infty dk_\rho k_\rho^3 \left(k_{1z}-k_{0z}\right) e^{ik_{1z}x} J_0\left(k_\rho\rho\right)}{k_1^2-k_0^2}. \tag{11}$$

The integral at the right-hand side can be further transformed to

$$\begin{aligned} &\int_0^\infty dk_\rho k_\rho^3 \left(k_{1z}-k_{0z}\right) e^{ik_{1z}x} J_0\left(k_\rho\rho\right) \\ &= \left[I_1(\rho,x,k_1) - e^{ix\sqrt{k_1^2-k_0^2}} I_1(\rho,x,k_0)\right] \\ &- \int_0^\infty dk_\rho k_\rho^3 k_{0z}\left[e^{ik_{1z}x} - e^{i\left(k_{0z}+\sqrt{k_1^2-k_0^2}\right)x}\right] J_0\left(k_\rho\rho\right). \end{aligned} \tag{12}$$

$I_1(\rho,x,k)$ is an auxiliary integral. It is defined in the appendix together with all other auxiliary integrals that would appear in this paper. Denote that

$$\begin{aligned} F_{1z}^{e}(\rho,x) &= \frac{1}{k_1^2-k_0^2} \times \\ &\left[I_1(\rho,x,k_1) - e^{ix\sqrt{k_1^2-k_0^2}} I_1(\rho,x,k_0)\right], \\ F_{1z}^{r}(\rho,x) &= \frac{1}{k_1^2-k_0^2} \times \\ &\int_0^\infty dk_\rho k_\rho^3 k_{0z}\left[e^{i\left(k_{0z}+\sqrt{k_1^2-k_0^2}\right)x} - e^{ik_{1z}x}\right] J_0\left(k_\rho\rho\right). \end{aligned} \tag{13}$$

Hence, $F_{1z}(\rho,x)$ is written as the sum of two parts

$$F_{1z}(\rho,x) = F_{1z}^{e}(\rho,x) + F_{1z}^{r}(\rho,x). \tag{14}$$

$F_{1z}^{e}(\rho,x)$ is extracted from the original integral which has an explicit expression and $F_{1z}^{r}(\rho,x)$ is the corresponding residual integral. Hereinafter, all the functions with a superscript "e" mean that they have explicit expressions. Correspondingly, all the functions with a superscript "r" mean the residual integrals. It seems that $F_{1z}^{r}(\rho,x)$ is more difficult to handle than the original Sommerfeld integral at first glance. However, it can be verified that $F_{1z}^{r}(\rho,x)$ could be neglected in the lateral wave when the radial distance is large.

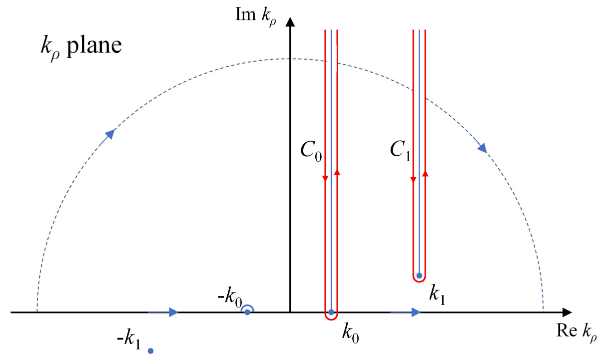

Fig. 2. The k_ρ plane.

Consider the integral in the complex plane shown in Figure 2. The horizontal axis is the real axis, while the vertical axis is the image axis.

Extending the integration path to the whole real axis and using the Cauchy theorem, the integration path is deformed to C_0 and C_1 as follows:

$$\begin{aligned} &\frac{1}{2}\left(k_1^2-k_0^2\right) F_{1z}^{r}(\rho,x) \\ &= \int_{-\infty}^{\infty} dk_\rho k_\rho^3 k_{0z}\left[e^{i\left(k_{0z}+\sqrt{k_1^2-k_0^2}\right)x} - e^{ik_{1z}x}\right] H_0^{(1)}\left(k_\rho\rho\right) \\ &= \int_{C_0+C_1} dk_\rho k_\rho^3 k_{0z}\left[e^{i\left(k_{0z}+\sqrt{k_1^2-k_0^2}\right)x} - e^{ik_{1z}x}\right] H_0^{(1)}\left(k_\rho\rho\right). \end{aligned} \tag{15}$$

Denote $f\left(k_\rho\right) = k_\rho^3 k_{0z}\left[e^{i\left(k_{0z}+\sqrt{k_1^2-k_0^2}\right)x} - e^{ik_{1z}x}\right] H_0^{(1)}\left(k_\rho\rho\right)$, and it has five branch points at $k_\rho = 0 \pm k_0 \pm k_1$. The branch points and the related branch cuts are also depicted in Figure 2. The branch cuts are parallel to the image axis. While passing the branch points, the integration path should have appropriate indentations as shown in Figure 2.

Using the double saddle point method [10], the integrals along the path C_0 and C_1 can be expanded with asymptotic series, respectively

$$\begin{aligned} \int_{C_0} f\left(k_\rho\right) dk_\rho &\sim e^{ik_0\rho}\left(\frac{A_3}{\rho^3} + \frac{A_4}{\rho^4} + \frac{A_5}{\rho^5} + \cdots\right), \\ \int_{C_1} f\left(k_\rho\right) dk_\rho &\sim e^{ik_1\rho}\left(\frac{B_2}{\rho^2} + \frac{B_3}{\rho^3} + \frac{B_4}{\rho^4} + \cdots\right). \end{aligned} \tag{16}$$

A_n and B_n are constants determined by the Taylor series of $f\left(k_\rho\right)$ at $k_\rho = k_0$ and $k_\rho = k_1$. For example, the A_3

term is

$$A_3=\frac{4k_0^2}{i\pi}\left[4e^{i\sqrt{k_1^2-k_0^2}x}-\frac{3k_0^2x^2}{2}-\frac{3ik_0^2x}{2\sqrt{k_1^2-k_0^2}}-4\right]. \tag{17}$$

The coefficients are lengthy but easy to be obtained by the commercial software Mathematica. What should be emphasized is that the exact forms of the coefficients A_n and B_n are not important in the realistic approximation because the residual integrals are to be neglected. The series is just used while proving the effectiveness of our method.

Since $Im(k_1)>0$, $e^{ik_1\rho}=o(1/r^n)$ $(n\in Z_+)$, it can be deduced from eqn (16) that only the integral on the path C_0 should be taken into consideration as $\rho\to\infty$. Therefore,

$$\int_{C_0+C_1} f(k_\rho)\,dk_\rho \sim e^{ik_0\rho}\left(\frac{A_3}{\rho^3}+\frac{A_4}{\rho^4}+\frac{A_5}{\rho^5}+\cdots\right). \tag{18}$$

Combining eqn (15) and (18), the asymptotic series of $F_{1z}^r(\rho,x)$ can be written as

$$F_{1z}^r(\rho,x)\sim\frac{e^{i\left(x\sqrt{k_1^2-k_0^2}+k_0\rho\right)}}{2\left(k_1^2-k_0^2\right)}\left(\frac{A_3}{\rho^3}+\frac{A_4}{\rho^4}+\frac{A_5}{\rho^5}+\cdots\right). \tag{19}$$

According to eqn (14)–(19), the relative error e_r between $F_{1z}(\rho,x)$ and $F_{1z}^e(\rho,x)$ is found to be

$$\begin{aligned} e_r=&\frac{F_{1z}(\rho,x)-F_{1z}^e(\rho,x)}{F_{1z}(\rho,x)}\\ =&\frac{o\left(1/\rho^2\right)}{o\left(1/\rho^2\right)+\mathrm{o}\left(1/\rho^2\right)+A/\rho^2}=o(1). \end{aligned} \tag{20}$$

The above equation means $e_r\to 0$ as $\rho\to\infty$, so $F_{1z}^e(\rho,x)$ is a good approximation of $F_{1z}(\rho,x)$. In other words, $F_{1z}^r(\rho,x)$ could be neglected in $F_{1z}(\rho,x)$ which confirms our previous observation.

It can be checked from (13) and (19) that the lowest negative order term $1/\rho^2$ is extracted and included in the explicit expression $F_{1z}^e(\rho,x)$, making it a more accurate approximate expression for the lateral wave at large radial distance. $F_\rho(\rho,z)$ and $F_\phi(\rho,x)$ can be dealt with in a similar way

$$\begin{aligned} F_\rho(\rho,x)&=F_{1\rho}^e(\rho,x)+F_{1\rho}^r(\rho,x),\\ F_\phi(\rho,x)&=F_{1\phi}^e(\rho,x)+F_{1\phi}^r(\rho,x). \end{aligned} \tag{21}$$

$F_{1\rho}^e(\rho,x)$, $F_{1\phi}^e(\rho,x)$, $F_{1\rho}^r(\rho,x)$, and $F_{1\phi}^r(\rho,x)$ are defined by eqn (22) and (23). Due to the term-wise differentiable property of the asymptotic series of the residual integrals [10], it can be proved that $F_{1\rho}^r(\rho,x)$ and $F_{1\phi}^r(\rho,x)$ could also be neglected when ρ is large enough.

$$\begin{cases} F_{1\rho}^e(\rho,x)=\frac{\rho}{2i\left(k_1^2-k_0^2\right)}\\ \qquad\times\frac{\partial}{\partial x}\left[I_2(\rho,x,k_1)-e^{i\sqrt{k_1^2-k_0^2}x}I_2(\rho,x,k_0)\right],\\ F_{1\phi}^e(\rho,x)=\frac{1}{k_1^2-k_0^2}\\ \qquad\times\left[I_2(\rho,x,k_1)-e^{i\sqrt{k_1^2-k_0^2}x}I_2(\rho,x,k_0)\right]. \end{cases} \tag{22}$$

$$\begin{cases} F_{1\rho}^r(\rho,x)=\frac{1}{i\left(k_1^2-k_0^2\right)}\times\frac{\partial^2}{\partial x\partial\rho}\int_0^\infty dk_\rho k_\rho k_{0z}\\ \qquad\left[e^{ik_{1z}x}-e^{i\left(k_{0z}+\sqrt{k_1^2-k_0^2}\right)x}\right]J_0(k_\rho\rho),\\ F_{1\phi}^r(\rho,x)=\frac{1}{k_1^2-k_0^2}\times\frac{\partial}{\partial\rho}\int_0^\infty dk_\rho k_\rho k_{0z}\\ \qquad\left[e^{ik_{1z}x}-e^{i\left(k_{0z}+\sqrt{k_1^2-k_0^2}\right)x}\right]J_0(k_\rho\rho). \end{cases} \tag{23}$$

Hence, the explicit expressions of the lateral waves in the sea are

$$\begin{aligned} H_{1z}^{\mathrm{lat}}&=\frac{M}{2\pi i}F_{1z}^e(\rho,d-z),\\ H_{1\rho}^{\mathrm{lat}}&=\frac{M}{2\pi}F_{1\rho}^e(\rho,d-z),\\ E_{1\phi}^{\mathrm{lat}}&=\frac{\omega\mu_1 M}{2\pi}F_{1\phi}^e(\rho,d-z). \end{aligned} \tag{24}$$

Thus, combining eqn (5) and (24), the EM field in the sea can be expressed with explicit expressions.

D. EM fields in the air

The nonzero EM field components in the air ($z>0$) can be expressed as

$$\begin{aligned} H_{0z}&=\frac{M}{2\pi i}\int_0^\infty dk_\rho\frac{k_\rho^3}{k_{1z}+k_{0z}}e^{ik_{1z}d}e^{ik_{0z}z}J_0(k_\rho\rho),\\ H_{0\rho}&=-\frac{M}{2\pi}\int_0^\infty dk_\rho\frac{k_{0z}k_\rho^2}{k_{1z}+k_{0z}}e^{ik_{1z}d}e^{ik_{0z}z}J_1(k_\rho\rho),\\ E_{0\phi}&=\frac{\omega\mu_0 M}{2\pi}\int_0^\infty dk_\rho\frac{k_\rho^2}{k_{1z}+k_{0z}}e^{ik_{1z}d}e^{ik_{0z}z}J_1(k_\rho\rho). \end{aligned} \tag{25}$$

Conventionally, there is no need to decompose the components of the EM fields in the air like in the sea. The components themselves constitute the lateral wave in the air. Under this circumstance, the problem is a little different from that in the sea because the exponential factors contain both k_{1z} and k_{0z}. Nevertheless, the core idea can be applied to extract the dominant term for the lateral wave from the integrals and abandon the residual integrals.

Denote that

$$\begin{aligned} F_{0z}(\rho,z,d)&=\int_0^\infty dk_\rho\frac{k_\rho^3}{k_{1z}+k_{0z}}e^{ik_{1z}d}e^{ik_{0z}z}J_0(k_\rho\rho),\\ F_{0\rho}(\rho,z,d)&=\int_0^\infty dk_\rho\frac{k_{0z}k_\rho^2}{k_{1z}+k_{0z}}e^{ik_{1z}d}e^{ik_{0z}z}J_1(k_\rho\rho),\\ F_{0\phi}(\rho,z,d)&=\int_0^\infty dk_\rho\frac{k_\rho^2}{k_{1z}+k_{0z}}e^{ik_{1z}d}e^{ik_{0z}z}J_1(k_\rho\rho). \end{aligned} \tag{26}$$

Now, the lateral wave in the air can be written as

$$H_{0z} = \frac{M}{2\pi i} F_{0z}(\rho, z, d),$$
$$H_{0\rho} = \frac{M}{2\pi} F_{0\rho}(\rho, z, d), \tag{27}$$
$$E_{0\phi} = \frac{M\omega\mu_0}{2\pi} F_{0\phi}(\rho, z, d).$$

Recalling eqn (18), the integral on C_1 plays an insignificant role in the lateral wave when ρ is large. To extract the dominant part from the integral expression of the lateral wave, we only need to make the lowest negative power term of the asymptotic series of the integrals on the integration path C_0 vanish like (16). To achieve this, the extraction is performed as follows:

$$F_{0z}(\rho, z, d) = F_{0z}^{e}(\rho, z, d) + F_{0z}^{r}(\rho, z, d),$$
$$F_{0\rho}(\rho, z, d) = F_{0\rho}^{e}(\rho, z, d) + F_{0\rho}^{r}(\rho, z, d), \tag{28}$$
$$F_{0\phi}(\rho, z, d) = F_{0\phi}^{e}(\rho, z, d) + F_{0\phi}^{r}(\rho, z, d).$$

Related functions in eqn (28) are defined in eqn (29) and (30). It can be verified that the lowest negative order terms vanish in the asymptotic series of the residual integrals. Hence, for large radial distance, all the residual integrals $F_{0z}^{r}(\rho, z, d)$, $F_{0\rho}^{r}(\rho, z, d)$, and $F_{0\phi}^{r}(\rho, z, d)$ can be neglected, and the EM fields in the air can be represented by the explicit expressions as shown in eqn (31).

$$\begin{cases} F_{0z}^{e}(\rho, z, d) = \frac{1}{i(k_1^2 - k_0^2)} \left(\frac{\partial}{\partial d} - \frac{\partial}{\partial z}\right) \\ \qquad \left[I_3(\rho, d, k_1) + e^{i\sqrt{k_1^2 - k_0^2}d} I_3(\rho, z, k_0)\right], \\ F_{0\rho}^{e}(\rho, z, d) = \frac{1}{k_1^2 - k_0^2} \frac{\partial}{\partial z} \left(\frac{\partial}{\partial d} - \frac{\partial}{\partial z}\right) \frac{\partial}{\partial \rho} \\ \qquad \left[I_4(\rho, d, k_1) + e^{i\sqrt{k_1^2 - k_0^2}d} I_4(\rho, z, k_0)\right], \\ F_{0\phi}^{e}(\rho, z, d) = \frac{i}{(k_1^2 - k_0^2)} \left(\frac{\partial}{\partial d} - \frac{\partial}{\partial z}\right) \frac{\partial}{\partial \rho} \\ \qquad \left[I_4(\rho, d, k_1) + e^{i\sqrt{k_1^2 - k_0^2}d} I_4(\rho, z, k_0)\right]. \end{cases} \tag{29}$$

$$\begin{cases} F_{0z}^{r}(\rho, z, d) = \frac{1}{i(k_1^2 - k_0^2)} \left(\frac{\partial}{\partial d} - \frac{\partial}{\partial z}\right) \int_0^\infty dk_\rho k_\rho^3 \\ \qquad \left(e^{ik_{1z}d} - e^{i\sqrt{k_1^2 - k_0^2}d}\right) \left(e^{ik_{0z}z} - 1\right) J_0(k_\rho \rho), \\ F_{0\rho}^{r}(\rho, z, d) = \frac{1}{k_1^2 - k_0^2} \frac{\partial}{\partial z} \left(\frac{\partial}{\partial d} - \frac{\partial}{\partial z}\right) \frac{\partial}{\partial \rho} \int_0^\infty dk_\rho k_\rho \\ \qquad \left(e^{ik_{1z}d} - e^{i\sqrt{k_1^2 - k_0^2}d}\right) \left(e^{ik_{0z}z} - 1\right) J_0(k_\rho \rho), \\ F_{0\phi}^{r}(\rho, z, d) = \frac{i}{(k_1^2 - k_0^2)} \left(\frac{\partial}{\partial d} - \frac{\partial}{\partial z}\right) \frac{\partial}{\partial \rho} \int_0^\infty dk_\rho k_\rho \\ \qquad \left(e^{ik_{1z}d} - e^{i\sqrt{k_1^2 - k_0^2}d}\right) \left(e^{ik_{0z}z} - 1\right) J_0(k_\rho \rho). \end{cases} \tag{30}$$

$$H_{0z} = \frac{M}{2\pi i} F_{0z}^{e}(\rho, z, d),$$
$$H_{0\rho} = \frac{M}{2\pi} F_{0\rho}^{e}(\rho, z, d), \tag{31}$$
$$E_{0\phi} = \frac{M\omega\mu_0}{2\pi} F_{0\phi}^{e}(\rho, z, d).$$

III. RESULTS

In this section, some numerical results and comparisons are given. First, the VMD is placed in the sea at $d = 10$m and the working frequency is $f = 50$ Hz. The lateral waves at $z = -0.5$ m and $z = 0.5$ m are considered. The results are compared with King's results and they are in good agreement. Then, the EM fields are calculated when the restriction condition $|k_1| \gg |k_0|$ is not satisfied. It can be seen from the numerical results that King's approximation method could not give accurate results in this situation. Nevertheless, our method could still give the accurate results.

Now consider the VMD placed in the sea at first.

Figure 3 shows the comparison of the integrands of H_{1z}^{lat} at different radial distances. It can be observed that

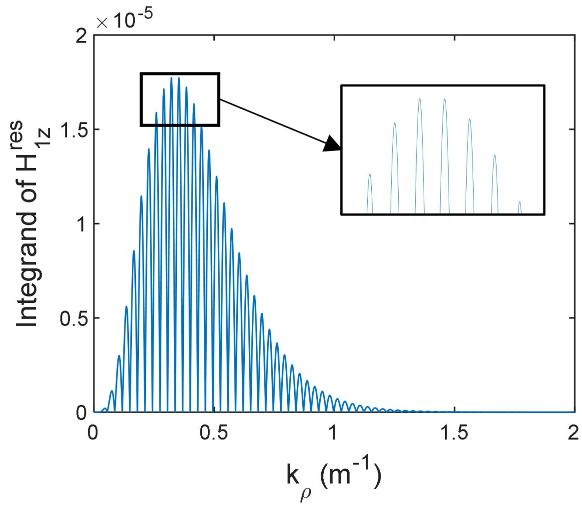

(a)

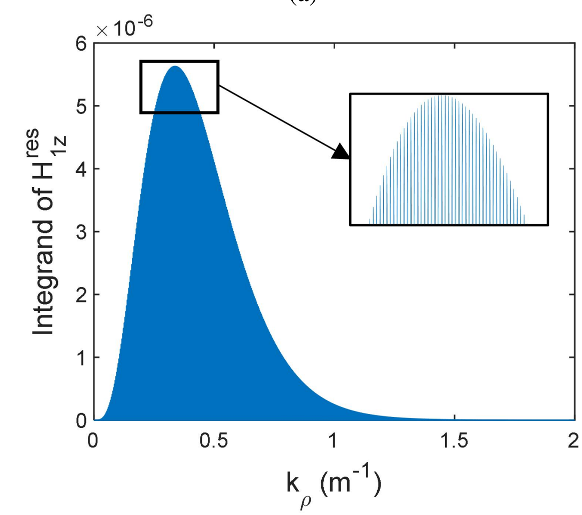

(b)

Fig. 3. The comparison of the integrands at (a) ρ = 100 m and (b) ρ = 1000 m.

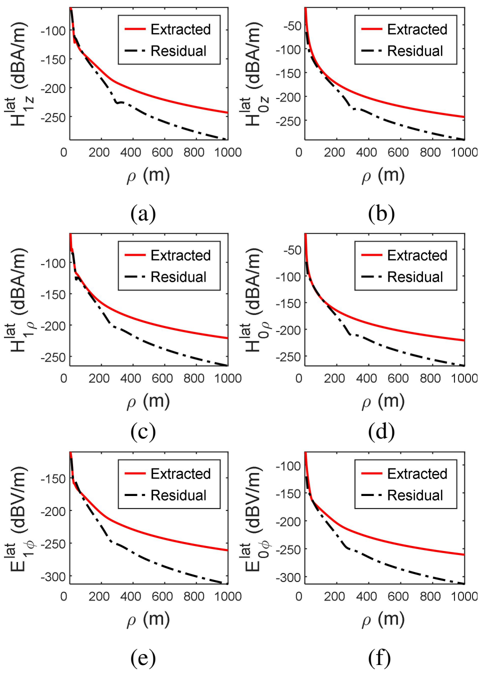

Fig. 4. The comparison of the extracted parts and the residual integrals: (a) H^{lat}_{1z}, (b) H^{lat}_{0z}, (c) $H^{\text{lat}}_{1\rho}$, (b) $H^{\text{lat}}_{0\rho}$, (e) $E^{\text{lat}}_{1\phi}$, and (f) $E^{\text{lat}}_{0\phi}$.

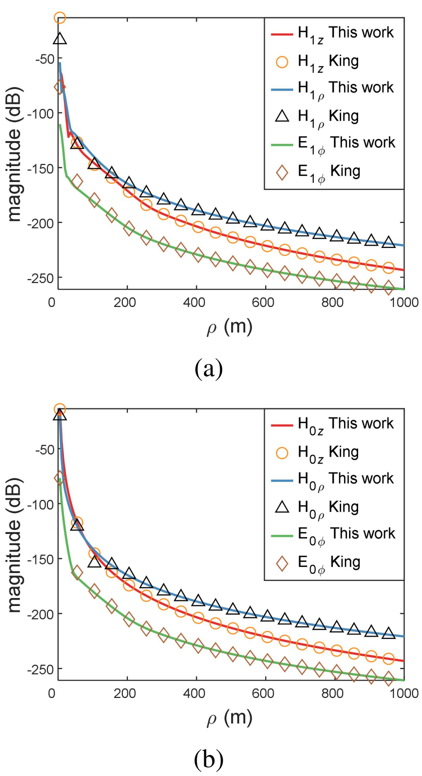

Fig. 5. The comparison of the results within $\rho < 1000$ m of our method and King's method. (a) Field in the sea. (b) Field in the air.

the integrands possess rapid oscillations, and the oscillation rate increases with ρ. Therefore, the direct numerical evaluation of the integral is inefficient when ρ is large.

In Figure 4, the solid curves represent the modulus of the extracted parts of the field components and the dashed lines represent the corresponding counterpart of residual parts. When ρ exceeds 200 m, the residual integrals become negligible compared with the extracted explicit parts.

The results of our method are also compared with the results obtained by the method of King (refer to Appendix D of [3]). Figure 5 shows the comparison in the range $\rho < 1000$ m. The solid lines are the results of our method, and the symbols are the results of King's method. While ρ is larger than about 200 m, the results of the two methods match very well because the requirement of $|k_1| \gg |k_0|$ for King's method is satisfied in this example.

Figure 6 shows the comparison within $\rho < 100$km. It is known that the traditional numerical methods

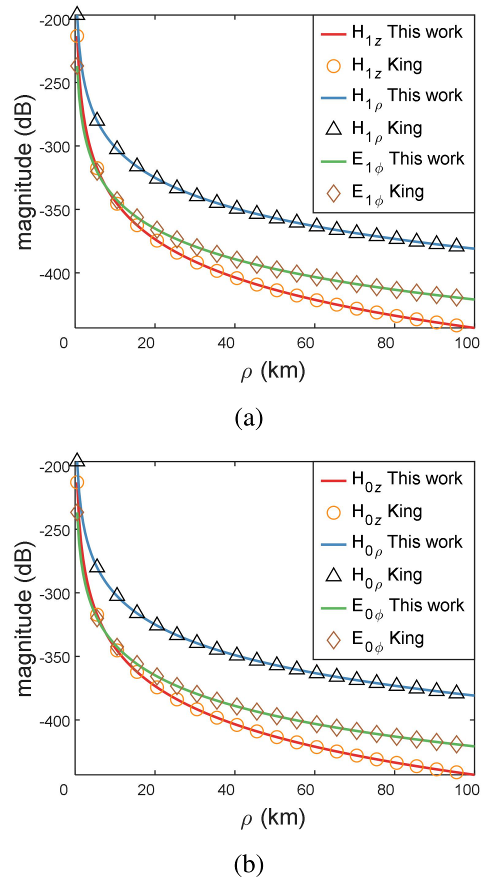

Fig. 6. The comparison of the results within $\rho < 100$ km of our method and King's method. (a) Field in the sea. (b) Field in the air.

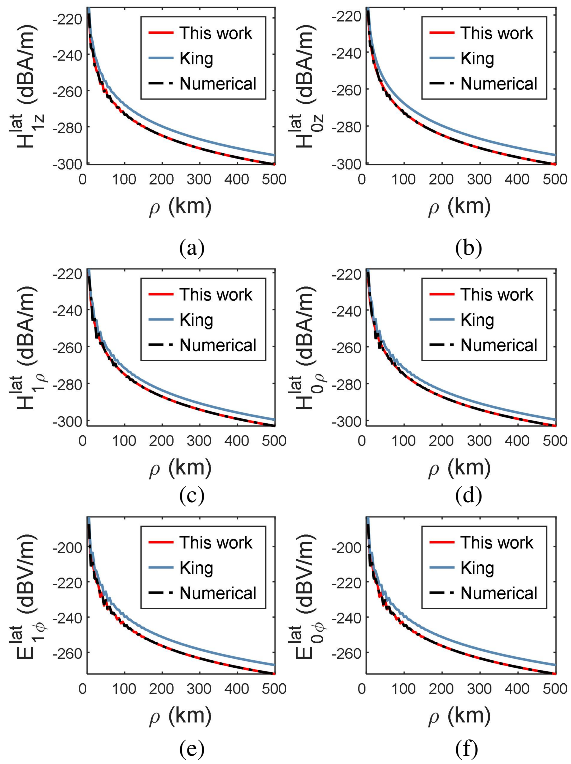

Fig. 7. The comparison of the results obtained by different methods: (a) H_{1z}^{lat}, (b) H_{0z}^{lat}, (c) $H_{1\rho}^{\mathrm{lat}}$, (b) $H_{0\rho}^{\mathrm{lat}}$, (e) $E_{1\phi}^{\mathrm{lat}}$, and (f) $E_{0\phi}^{\mathrm{lat}}$.

become very inefficient when ρ reaches such a large distance.

Next consider the problem when the restriction condition $|k_1| \gg |k_0|$ no longer holds. Specifically, the conductivity of the lower half space is 1×10^{-6} S/m and the permittivity of the upper half space is $200\varepsilon_0$ now. The working frequency f is 5.2 kHz and $d = 500$ m. The other parameters remain the same.

Figure 7 shows the comparison of the results of our method, King's method, and the direct numerical integration. It can be seen from the figure that the results of our method match very well with the direct numerical integration results, which are made converged with high accuracy but very time-consuming. However, the field components obtained by King's method could not give accurate results as shown in Figure 7.

IV. CONCLUSION

In this paper, a method for efficiently evaluating the fields of a VMD in a dissipative half space is proposed. Dominant explicit formulae for nonzero field components are extracted from their integral expressions. The residual integrals are negligible for large radial distance. Since no numerical integration is needed, this method is efficient for calculating the far fields. Besides, it has no restriction on the parameters of the media; so it has broader application scope than the King's method when dealing with different problems.

ACKNOWLEDGMENT

This work is supported by Shanghai Academy of Spaceflight Technology (SAST)—Shanghai Jiao Tong University advanced aerospace technology joint research center funded projects under Grant USCAST2019-21.

REFERENCES

[1] A. N. Sommerfeld, "Propagation of waves in wireless telegraphy," *Ann. Phys. (Leipzig)*, vol. 28, pp. 665-737, 1909.

[2] J. Zenneck, "Propagation of plane EM waves along a plane conducting surface," *Ann. Phys.(Leipzig)*, vol. 23, no. 1, pp. 907, 1907.

[3] R. W. King, M. Owens, and T. T. Wu, *Lateral Electromagnetic Waves: Theory and Applications to Communications, Geophysical Exploration, and Remote Sensing*, 1st ed. Springer-Verlag Inc., New York, USA, 1992.

[4] V. A. Houdzoumis, "Lateral waves over planar earth: a validity check of a proposed solution," *IEEE Transactions on Antennas and Propagation.*, vol. 57, no. 2, pp. 567-572, 2009.

[5] H. Wang, Y. Yang, K. Yang, and Y. Ma, "Verification and evaluation of lateral wave propagation in marine environment," *IEEE Antennas and Wireless Propagation Letters.*, vol. 19, no. 12, pp. 2413-2417, 2020.

[6] J. Zou, T. N. Jiang, J. B. Lee, and S. H. Chang, "Fast calculation of the electromagnetic field by a vertical electric dipole over a lossy ground and its application in evaluating the lightning radiation field in the frequency domain," *IEEE Transactions on Electromagnetic Compatibility.*, vol. 52, no. 1, pp. 147-154, 2010.

[7] K. A. Norton, "The propagation of radio waves over the surface of the earth and in the upper atmosphere," *Proceedings of the Institute of Radio Engineers.*, vol. 25, no. 9, pp. 1203-1236, 1937.

[8] R. W. P. King, "Lateral electromagnetic waves from a horizontal antenna for remote sensing in the ocean," *IEEE Transactions on Antennas and Propagation.*, vol. 37, no. 10, pp. 1250-1255, 1989.

[9] A. V. Osipov and S. A. Tretyakov, *Electromagnetic Scattering Theory with Applications*, 1st ed. John Wiley & Sons, Inc., Chichester, West Sussex, 2017.

[10] A. Baños, *Dipole Radiation in the Presence of a Conducting Half-Space*, 1st ed. Pergamon Press Inc., 1966.

[11] M. Siegel and R. King, "Radiation from linear antennas in a dissipative half-space," *IEEE Trans.*

Antennas Propagat., vol. 19, no. 4, pp. 477-485, Jul. 1971.
[12] M. Siegel and R. King, "Electromagnetic propagation between antennas submerged in the ocean," *IEEE Trans. Antennas Propagat.*, vol. 21, no. 4, pp. 507-513, Jul. 1973.
[13] L. Shen, R. W. King, and R. Sorbello, "Measured field of a directional antenna submerged in a lake," *IEEE Trans. Antennas Propagat.*, vol. 24, no. 6, pp. 891-894, Nov. 1976.
[14] W. C. Chew, *Waves and Fields in Inhomogeneous Media*, 1st ed. IEEE Press Inc., New York, USA, 1990.
[15] K. A. Michalski and D. Zheng, "Electromagnetic scattering and radiation by surfaces of arbitrary shape in layered media. I. theory," *IEEE Trans. Antennas Propagat.*, vol. 38, no. 3, pp. 335-344, Mar. 1990.
[16] P. YlaOijala, M. Taskinen, and J. Sarvas, "Multilayered media Green's functions for MPIE with general electric and magnetic sources by the hertz potential approach - abstract," *Progress In Electromagnetics Research*, vol. 33, no. 7, pp. 141-165, Apr. 2001.
[17] W. C. Chew, J. S. Xiong, and T. J. Cui, "The layered medium Green's function - a new look," *Microwave and Optical Technology Letters*, vol. 31, no. 4, pp. 252-255, Oct. 2001.
[18] K. A. Michalski, "Extrapolation methods for Sommerfeld integral tails," *IEEE Trans. Antennas Propagat.*, vol. 46, no. 10, pp. 1405-1418, Oct. 1998.
[19] J. Mosig, "The weighted averages algorithm revisited," *IEEE Trans. Antennas Propagat.*, vol. 60, no. 4, pp. 2011-2018, Jan. 2012.
[20] Y. Hua and T. K. Sarkar, "Generalized pencil-of-function method for extracting poles of an EM system from its transient response," *IEEE Trans. Antennas Propagat.*, vol. 37, no. 2, pp. 229-234, Feb. 1989.
[21] M. I. Aksun and G. Dural, "Clarification of issues on the closed-form Green's functions in stratified media," *IEEE Trans. Antennas Propagat.*, vol. 53, no. 11, pp. 3644-3653, Nov. 2005.
[22] M. Yuan, T. K. Sarkar, and M. Salazar-Palma, "A direct discrete complex image method from the closed-form Green's functions in multilayered media," *IEEE Antennas Wireless Propog. Lett*, vol. 54, no. 3, pp. 1025-1032, Mar. 2006.
[23] A. Alparslan, M. I. Aksun, and K. A. Michalski, "Closed-form Green's functions in planar layered media for all ranges and materials," *IEEE Antennas Wireless Propog. Lett*, vol. 58, no. 3, pp. 602-613, Mar. 2010.
[24] J. A. Kong, *Electromagnetic Wave Theory*, 1st ed. Jonn Wiley & Sons Inc., New Jersey, USA, pp. 220-325, 1986.

Hongyun Deng received the B.S. degree from Shanghai Jiao Tong University, Shanghai, China, in 2020. He is currently working toward the M.S. degree in electronic engineering with Shanghai Jiao Tong University. His research interests include computational electromagnetics and electromagnetic theory.

Gaobiao Xiao received the B.S. degree from Huazhong University of Science and Technology, Wuhan, China, in 1988, the M.S. degree from the National University of Defense Technology, Changsha, China, in 1991, and the Ph.D. degree from Chiba University, Chiba, Japan, in 2002. He has been a faculty member since 2004 with the Department of Electronic Engineering, Shanghai Jiao Tong University, Shanghai, China. His research interests are computational electromagnetics, coupled thermo-electromagnetic analysis, microwave filter designs, fiber-optic filter designs, phased array antennas, and inverse scattering problems.

Shifeng Huang received the B.S. and M.S. degrees from Wuhan University, Wuhan, China, in 2014 and 2017, respectively. He is currently working toward the Ph.D. degree in electronic engineering with Shanghai Jiao Tong University, Shanghai, China. His current research interests include computational electromagnetics and its application in electromagnetic compatibility and scattering problems.

The 3D Modeling of GATEM in Fractured Random Media Based on FDTD

Qiong Wu[1], Yuehan Zhang[1], Shanshan Guan[1], Dongsheng Li[1], and Yanju Ji[1,2*]

[1]College of Electrical Engineering and Instrumentation
Jilin University, Changchun 130026, China

[2]Key Laboratory of Earth Information Detection Instruments
Ministry of Education, Jilin University, Changchun 130026, China
wuqiong_515@sina.cn, yhzhang19@mails.jlu.edu.cn, guanshanshan@jlu.edu.cn,
lidongsheng86@sina.cn, jiyj@jlu.edu.cn

***Abstract* –** Grounded-source airborne time-domain electromagnetic (GATEM) method is an effective detection method of geological survey. The real geological media are rough, self-similar characteristics, and the diffusion process is anomalous diffusion. This paper primarily considers the GATEM responses of a grounded wire source in random media. Von Kármán function is used to establish three-dimensional (3D) random media model and the GATEM responses are realized based on 3D finite-difference time-domain (FDTD) method. The method is verified by homogeneous half-space model. The electromagnetic responses of random abnormal body model are analyzed, and the results show that the abnormal body can be clearly identified. The electromagnetic responses of a fractured model are analyzed, and the results show that the tilt angle of the fault can be reflected.

***Index Terms* –** FDTD, GATEM, Hurst exponent, random media.

I. INTRODUCTION

In recent years, there is a new kind of airborne electromagnetic method appearing on the international aviation, grounded-source airborne time-domain electromagnetic (GATEM) method, which is suitable for the large area where is difficult to access [1]. GATEM takes the form of a grounded wire transmitter and the receiver carried by aircraft [2]. It gathers large investigation depth of ground electromagnetic method and high efficiency of airborne electromagnetic method. It has been used in engineering, geological surveying, and mineral exploration [3–5].

The electromagnetic modeling of subsurface media is usually based on usually homogeneous media [5–8]. However, many geophysicists realize that electromagnetic induction of subsurface media is anomalous diffusion [9–11]. The mean-square displacement of subdiffusion process is slower (subdiffusion) or faster (superdiffusion) than that of Gauss diffusion process, and it is proportional to the fractional power of time [12]. This paper primarily focuses on the subdiffusion diffusion. For subdiffusion diffusion, the electromagnetic fractional diffusion model is defined and the fractional Maxwell equations are gradually being promoted [13–15]. The three-dimensional (3D) finite-difference (FD) of controlled-source electromagnetics (CSEM) is proposed in frequency domain for a multiscale random media model of fractured geologic formation which is based on a von Kármán autocorrelation function [16]. The one-dimensional (1D) GATEM modeling and interpretation method of fractional diffusion model for a rough medium is proposed [17].

In this paper, we mainly aim to obtain 3D time-domain response of a grounded wire source in fractured media. For the fractional diffusion model based on a von Kármán autocorrelation function, the electromagnetic field iterative equations are derived based on finite-difference time-domain (FDTD) method. The modeling method is validated by different models and compared with analytical solutions.

II. METHOD

A. 3D fractured random media model

The random media conductivity model of geologic formation can be expressed as [16, 18]:

$$\sigma = \sigma_0 + \sigma_\delta, \tag{1}$$

where σ_0 is the usual dimension of the conductor, σ_δ is the smaller scale random inhomogeneities.

The 3D computational model is divided by using Yee staggered grids. The autocorrelation function related to the grid step based on isotropic von Kármán function is:

$$C(r) = \frac{2^{1-\nu}}{\Gamma(\nu)}(r)^{\nu} K_\nu(r), \tag{2}$$

where ν represents roughness or Hurst exponent and $0<\nu<1$, a is the correlation length,

Submitted On: March 18, 2021
Accepted On: July 30, 2021
https://doi.org/10.13052/2021.ACES.J.361102

$r = \sqrt{(x^2+y^2+z^2)/a^2}$, $\Gamma(v)$ represents the gamma function, and K_v represents the Bessel function of the second kind of noninteger order.

The square root of the autocorrelation spectrum $f(C(r))$ and Fourier transform of a white noise field wn are calculated and multiplied in the wavenumber domain. The σ_δ is obtained by transforming results to the spatial domain. The smaller scale random inhomogeneities σ_δ is added to σ_0 to obtain the random media conductivity σ.

B. Modeling of GATEM in fractured random media model

The fractional Maxwell equations are:

$$\nabla \times E(t) = -\mu \frac{\partial H(t)}{\partial t}, \tag{3}$$

$$\nabla \times H(t) = \varepsilon \frac{\partial E(t)}{\partial t} + \sigma_r E(t), \tag{4}$$

where *E(t)* is the electric field, *H(t)* is the magnetic field, μ and ε are the magnetic permeability and permittivity, respectively.

It is necessary to subdivide the model, when calculating the GATEM response of a 3D anomalous body based on FDTD. In this paper, a non-uniform grid is used to calculate the GATEM response, as shown in Figure 1 (a). The mesh of a part area is relatively finely divided according to the needs, and the mesh of other areas is coarsely divided. The electric field is sampled at the edge of the Yee cell, and the magnetic field is sampled at the center of the Yee cell's face [19]. According to Figure 1 (b), the electric field is surrounded by four magnetic fields, and the magnetic field is surrounded by four electric fields.

The electric field iterative formulation based on FDTD is:

$$\begin{aligned}
&E_x^{n+1}(i+\frac{1}{2},j,k) = \frac{2\varepsilon-(\sigma_0+\sigma_\delta)\triangle t_n}{2\varepsilon+(\sigma_0+\sigma_\delta)\triangle t_n} {E_x}^n(i+\frac{1}{2},j,k) \\
&+\frac{2\triangle t}{(2\varepsilon+(\sigma_0+\sigma_\delta)\triangle t_n)\triangle y}[{H_z}^{n+1/2}(i+\frac{1}{2},j+\frac{1}{2},k) \\
&-{H_z}^{n+1/2}(i+\frac{1}{2},j-\frac{1}{2},k)] \qquad , \\
&-\frac{2\triangle t}{(2\varepsilon+(\sigma_0+\sigma_\delta)\triangle t_n)\triangle z}[{H_y}^{n+1/2}(i+\frac{1}{2},j,k+\frac{1}{2}) \\
&-{H_y}^{n+1/2}(i+\frac{1}{2},j,k-\frac{1}{2})]
\end{aligned} \tag{5}$$

where $E_x^{n+1}(i+\frac{1}{2},j,k)$ is the electric field of t^{n+1} at position $(i+\frac{1}{2},j,k)$, Δy and Δz are space step. Δt_n is the time step, and the initial moment is

$$t_0 = 1.13\mu\sigma_1\Delta_1^2, \tag{6}$$

where σ_1 is the electrical conductivity of top grid and Δ_1 is the top grid. In FDTD, to ensure the stability of calculation, it is necessary to follow Courant–Friedrichs–Lewy stability conditions. In practice, the maximum time step is [20]

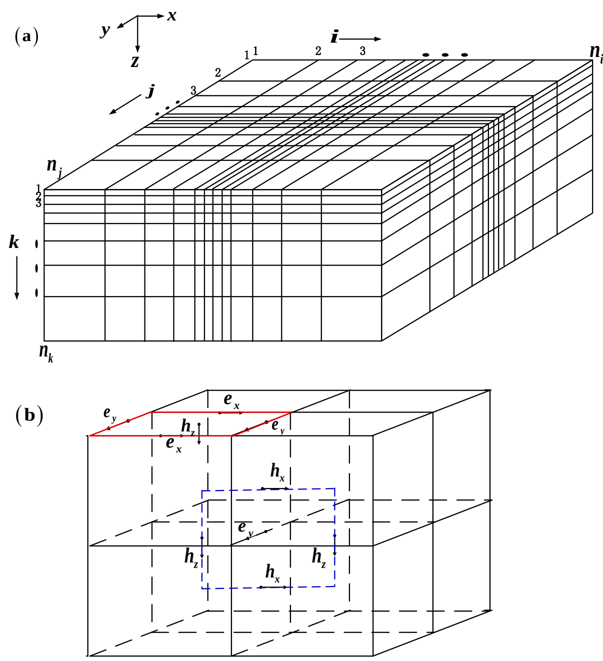

Fig. 1. (a) non-uniform grid, (b) Electric field and magnetic field at Yee's cell.

$$\Delta t_{\max} = \alpha(\frac{\mu\sigma_{\min}t}{6})^{\frac{1}{2}}\Delta_{min}, \tag{7}$$

where α ranges from 0.1 to 0.2, and σ_{min} is the minimum resistivity value in the model, Δ_{min} is the minimum grid spacing. For the magnetic fields, according to control equations, the iterative formulation is

$$\begin{aligned}
&{H_z}^{n+\frac{1}{2}}(i+\frac{1}{2},j+\frac{1}{2},k) = {H_z}^{n-\frac{1}{2}}(i+\frac{1}{2},j+\frac{1}{2},k) \\
&+\frac{\triangle t_{n-1}+\triangle t_n}{2\mu}[\frac{{E_x}^n(i+\frac{1}{2},j+1,k)-{E_x}^n(i+\frac{1}{2},j,k)}{\triangle y}, \\
&-\frac{{E_y}^n(i+1,j+\frac{1}{2},k)-{E_y}^n(i,j+\frac{1}{2},k)}{\triangle x}]
\end{aligned} \tag{8}$$

when t = nΔt_n,

$$\begin{aligned}
&\frac{\partial h_x^n(i,j+\frac{1}{2},k+\frac{1}{2})}{\partial t} \approx \frac{1}{(\triangle t_{n-1}+\triangle t_n)/2} \\
&[h_x^{n+\frac{1}{2}}(i,j+\frac{1}{2},k+\frac{1}{2}) - h_x^{n-\frac{1}{2}}(i,j+\frac{1}{2},k+\frac{1}{2})]
\end{aligned} . \tag{9}$$

For the GATEM system, the transmitter is a grounded electric source with several kilometres length wire, and the receiver and induction coil are towed by an aircraft in the air. For 3D modeling of GATEM based on FDTD, the initial condition of calculation is the electromagnetic response of a grounded wire source. When t = t_0, the electric fields of the grounded wire placed along the x-axis are

$$E_x = \{ \frac{I}{4\pi}\frac{x}{R_2}\int_0^\infty [(1-r_{TM})\frac{u_0}{\hat{y}_0}-(1+r_{TE})\frac{\hat{z}_0}{u_0}]J_1(\lambda R)d\lambda - \frac{I}{4\pi}\frac{x}{R_1}\int_0^\infty [(1-r_{TM})\frac{u_0}{\hat{y}_0}-(1+r_{TE})\frac{\hat{z}_0}{u_0}]J_1(\lambda R)d\lambda \}, - \frac{\hat{z}_0 I}{4\pi}\int_{-L}^{L}\int_0^\infty (1+r_{TE})e^{-u_0 z}\frac{\lambda}{u_0}J_0(\lambda R)d\lambda dx' \quad (10)$$

$$E_y = \frac{I}{4\pi}\frac{y}{R_2}\int_0^\infty [(1-r_{TM})\frac{u_0}{\hat{y}_0}-(1+r_{TE})\frac{\hat{z}_0}{u_0}]J_1(\lambda R)d\lambda - \frac{I}{4\pi}\frac{y}{R_1}\int_0^\infty [(1-r_{TM})\frac{u_0}{\hat{y}_0}-(1+r_{TE})\frac{\hat{z}_0}{u_0}]J_1(\lambda R)d\lambda, \quad (11)$$

where $\hat{y} = \sigma_0 + \sigma_\delta + i\varepsilon\omega$, $\hat{z} = i\mu\omega$, $R_1 = [(x+L)^2 + y^2]^{1/2}$, $R_2 = [(x-L)^2 + y^2]^{1/2}$, $R = [(x-x')^2 + y^2]^{1/2}$, L is the half length of the ground wire, I is the transmitter current, $u_0 = \lambda$ in quasistatic electromagnetic field, λ is the Hankel transform integral variable, r_{TE} is the reflection coefficient, and J_1 is the first-order Bessel function. The Bessel function integral is calculated via the Hankel transformation algorithm [21]. The time domain responses can be converted from frequency domain by digital filtering method [22].

III. RESULTS

A. The fractured random media conductivity model

Figure 2 is the conductivity distributions of fractured random media conductivity model. The correlation length a = 10 and the conductor σ_0 is 0.1 Sm^{-1}. The Hurst exponent v set as 0.2, 0.5, and 0.8. The conductivities are 0.1 Sm^{-1} to 0.145 Sm^{-1} for v = 0.2, 0.1 Sm^{-1} to 0.24 Sm^{-1} for v = 0.5, and 0.1 Sm^{-1} to 0.4 Sm^{-1} for v = 0.8; the maximum value of conductivities increased by more than four times. The Hurst exponent v is an important parameter that determines the change of conductivity.

B. Modeling results

To validate the 3D modeling method, the GATEM response of a specific random half-space model which $v \to 0$, the limit as $v \to 0$ corresponds to a homogeneous medium, is calculated and compared with analytical solution. The Hurst exponent $v = 10^{-6}$, and the conductor σ_0 is 0.01 Sm^{-1}. The conductivity distributions of random abnormal body are shown in Figure 3. The conductivities are almost 0.01 Sm^{-1}, and it can be approximated as a homogeneous medium model. The calculation parameters are as follows: all models have 221×221×75 grids. The grid is non-uniform and the smallest spacing is 10 m, the largest spacing is 120 m. The wire source is located at the center of the model with 1 m length, and the transmitter current is 20 A. The receiver coil is 500 m away from the wire source and the height is 0 m. The GATEM response is calculated as shown in Figure 4.

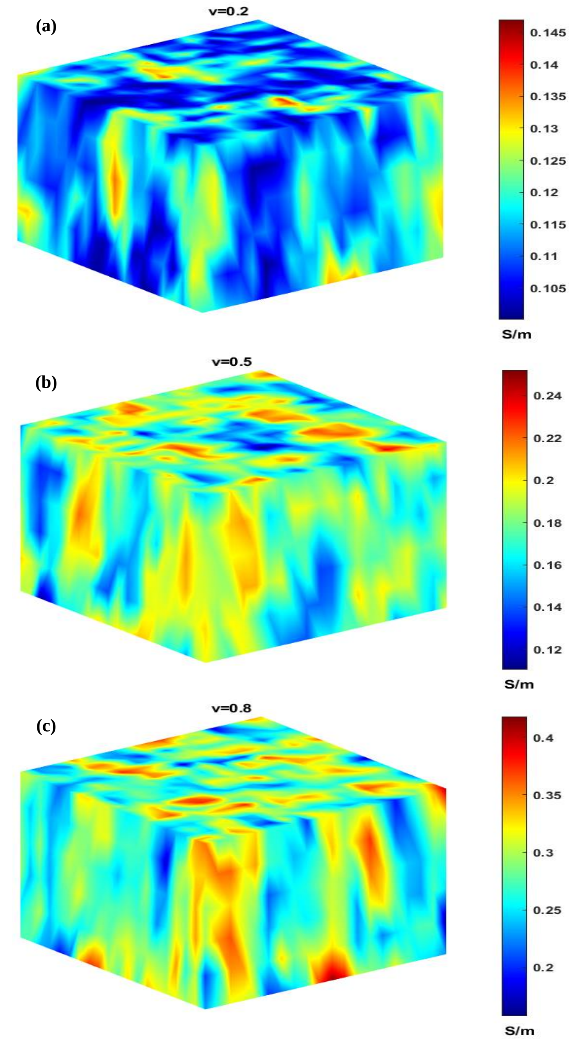

Fig. 2. Conductivity distribution of random media for Hurst exponent. (a) v = 0.2, (b) v = 0.5, (c) v = 0.8.

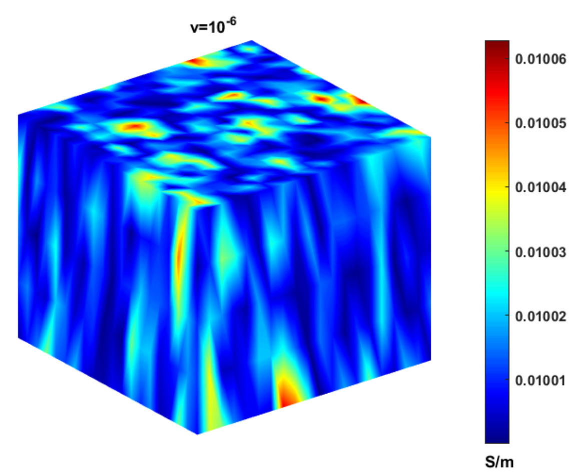

Fig. 3. Conductivity distribution of random media for roughness exponent $v = 10^{-6}$.

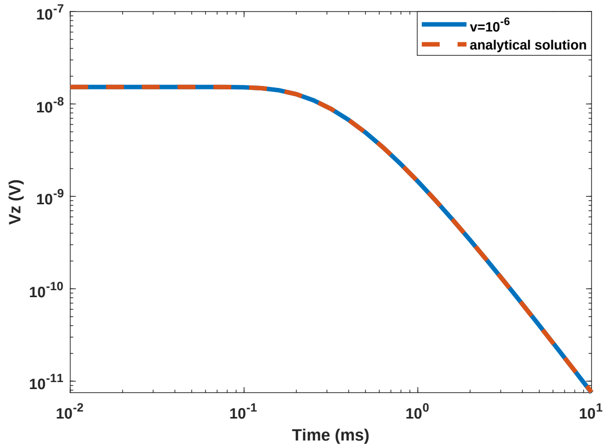

Fig. 4. Comparison of GATEM response in a random half-space model when $v = 10^{-6}$ and analytical solution.

The GATEM response is compared with the analytical solution obtained from equation (12) [23]. The induced voltage (Vz) can be obtained from $Vz = \mu S \frac{\partial hz}{\partial t}$, where S is the equivalent area of receiver coil. The modeling result coincides with the analytical solution. Figure 4 validates the correctness of the modeling method. The relative error is calculated and is less than 8%.

$$\frac{\partial hz}{\partial t} = \frac{Ids}{2\pi\mu\sigma_0}\frac{y}{r^5}\left[3erf(\alpha r) - \frac{2}{\pi^{1/2}}\alpha r(3+2\alpha^2 r^2)e^{-\alpha^2 r^2}\right], \tag{12}$$

where ds is the dipole length, r is the source–receiver distance, y is the horizontal transverse offset and $\alpha = (\mu\sigma_0)^{1/2} r$.

Figure 5 is a 3D theoretical random abnormal body model and the center of the long wire source is the origin.

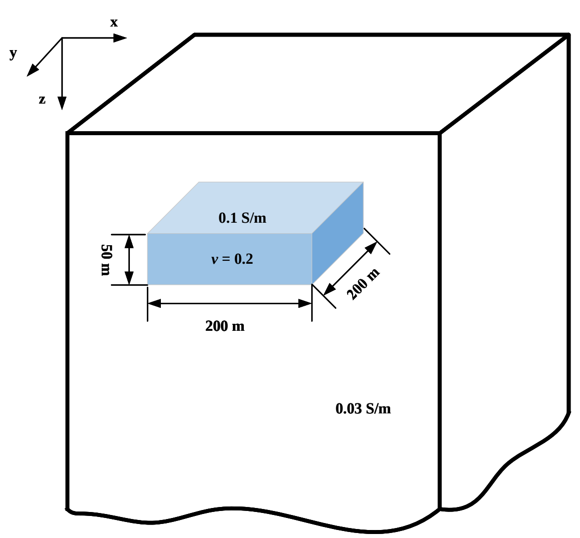

Fig. 5. A theoretical random abnormal body model.

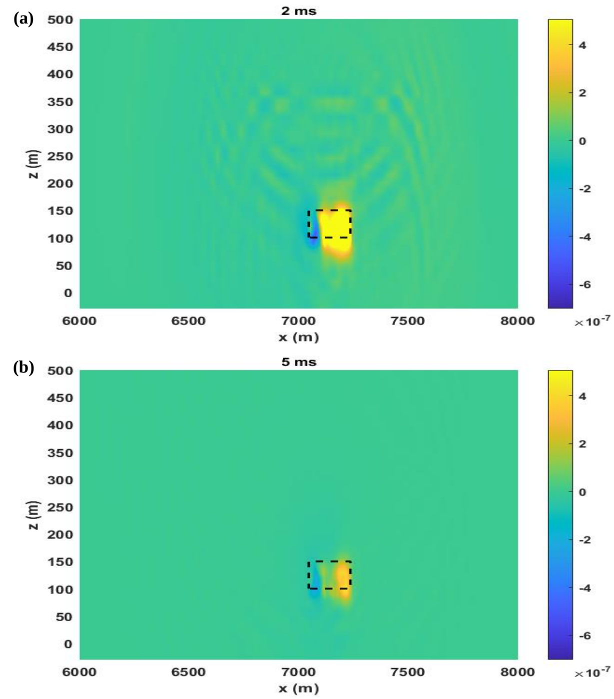

Fig. 6. The electromagnetic response slices of abnormal body model in x-z plane at 2 ms and 5 ms. The black dashed line is the position of the random abnormal body.

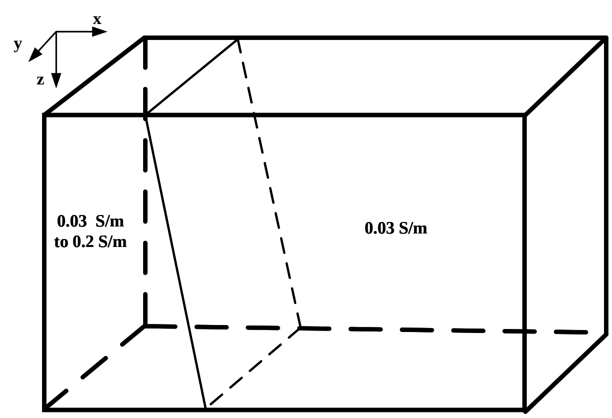

Fig. 7. The 3D fractured model.

The conductivity of bedrock is recorded as 0.03 Sm^{-1}, and the conductivity of random abnormal body is variable and the basic conductivity is 0.1 Sm^{-1}. The Hurst exponent is set as $v = 0.2$ and the conductivity distributions of random abnormal body is shown in Figure 1 (b). The depth of the abnormal body is 100 m and the size is 200 m $\times$ 200 m $\times$ 50 m. The electromagnetic response slices of abnormal body model with $v = 0.2$ in x-z plane at 2 ms and 5 ms are shown in Figure 6. From these slices

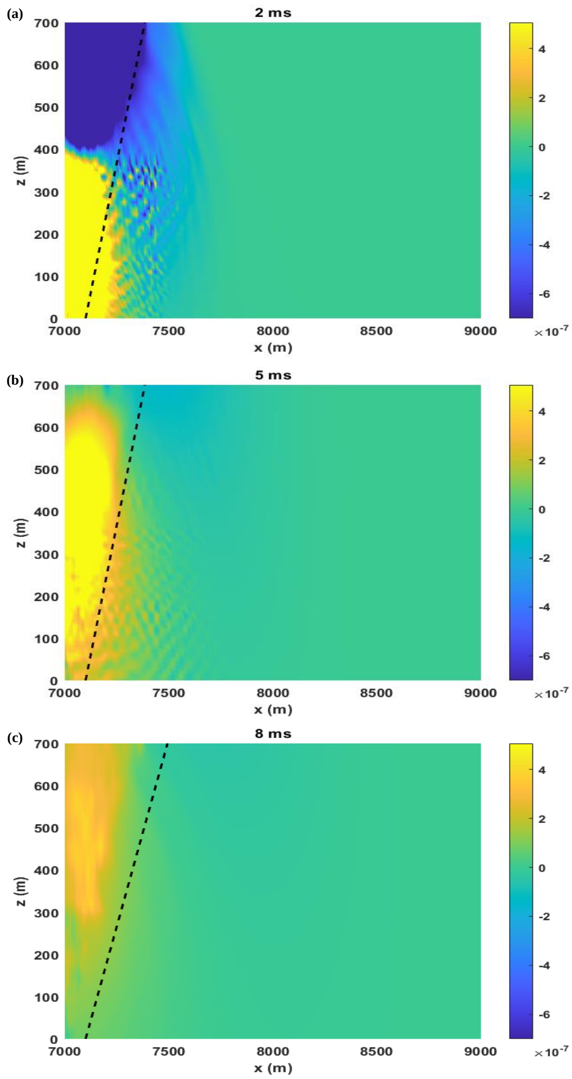

Fig. 8. The electromagnetic response slices in x-z plane at 2 ms, 5 ms, and 8 ms. The black dashed line is only the reference.

in Figure 6, the responses can well reflect the information of the random abnormal body.

A 3D fractured model is designed, as shown in Figure 7. The resistivity of the right area is 0.03 Sm^{-1} as the back ground. The basic conductivity of the left part changes linearly from 0.03 Sm^{-1} to 0.1 Sm^{-1}, and the Hurst exponent is $v = 0.5$, therefore, the conductivity is variable, ranging from 0.03 to 0.2 Sm^{-1}. The electromagnetic response slices in x-z plane at 2 ms, 5 ms, and 8 ms are shown in Figure 8. It can reflect the tilt angle of the fault.

IV. CONCLUSION

In this paper, 3D random media model is established by Von Kármán function. When establishing a random media model, Hurst exponent is an important parameter that determines the change in conductivity. The GATEM responses in random media are realized based on FDTD and the modeling results validated correctness. The results of the random abnormal body model show that the abnormal body can be identified. A fractured model is designed and the results show that the tilt angle of the fault can be reflected. Inversion of the 3D modeling for random media is the focus of our following research.

ACKNOWLEDGMENT

This study was performed under the project entitled "Research on Sub-diffusion Multi-parameter extraction method of Ground-source Airborne Electromagnetic data based on fully connected neural network (42004059)" and "Research on Key Technologies of Electromagnetic Detection of Induction-Polarization Symbiosis Effects of Dual Phase Conductive Medium Based on SQUID technique (42030104)" supported by the National Natural Science Foundation of China. We thank all members of the GATEM group of Jilin University (China) for their support of this study.

REFERENCES

[1] R. S. Smith, A. P. Annan, and P. D. McGowan, "A comparison of data from airborne, semi-airborne, and ground electromagnetic systems," *Geophysics*, vol. 66, no. 5, pp. 1379-1385, Oct. 2001.

[2] T. Mogi, Y. Tanaka, K. Kusunoki, T. Morikawa, and N. Jomori, "Development of grounded electrical source airborne transient EM (GREATEM)," *Exploration Geophysics (Melbourne)*, vol. 29, no. 2, pp. 61-64, Jun. 1998.

[3] T. Mogi, K. Kusunoki, H. Kaieda, H. Ito, A. Jomori, N. Jomori, and Y. Yuuki, "Grounded electrical-source airborne transient electromagnetic (GREATEM) survey of Mount Bandai, north-eastern Japan," *Exploration Geophysics*, vol. 40, no. 1, pp. 1-7, Feb. 2009.

[4] S. A. Allah, T. Mogi, H. Ito, A. Jymori, Y. Yuuki, E. Fomenko, K. Kiho, H. Kaieda, K. Suzuki, and K. Tsukuda, "Three-dimensional resistivity modelling of grounded electrical-source airborne transient electromagnetic (GREATEM) survey data from the Nojima fault, Awaji island, south-east Japan," *Exploration Geophysics*, vol. 45, no. 1, pp. 49-61, Dec. 2014.

[5] Y. Ji, Y. Zhu, M. Yu, D. Li, and S. Guan, "Calculation and application of full-wave airborne transient electromagnetic data in electromagnetic detection," *Journal of Central South University*, vol. 26, no. 4, pp. 1011-1020, Apr. 2019.

[6] Y. Shao and S. Wang, "Truncation error analysis of a pre-asymptotic higher-order finite difference scheme for maxwell's equations," *Applied Computational Electromagnetics Society Journal*, vol. 30, no. 2, pp. 167-170, Feb. 2015.

[7] M. Commer, P. V. Petrov, and G.A. Newman, "FDTD modelling of induced polarization phenomena in transient electromagnetics," *Geophysical Journal International*, vol. 209, no. 1, pp. 387-405, Apr. 2017.

[8] F. Naixing, Y. Zhang, Q. Sun, J. Zhu, W. T. Joines, and Q. H. Liu, "An accurate 3-D CFS-PML based Crank-Nicolson FDTD method and its applications in low-frequency subsurface sensing," *IEEE Transactions on Antennas and Propagation*, vol. 66, no. 6, pp. 2967-2975, Jun. 2018.

[9] B. Berkowitz and H. Scher, "Anomalous transport in random fracture networks," *Physical Review Letters*, vol. 79, no. 20, pp. 4038-4041, Nov. 1997.

[10] A. Guellab and W. Qun, "High-order staggered finite difference time domain method for dispersive debye medium (Artical)," *Applied Computational Electromagnetics Society Journal*, vol. 33, no. 4, pp. 430-437, Apr. 2018.

[11] C. J. Weiss, B. G. van Bloemen Waanders, and H. Antil , "Fractional operators applied to geophysical electromagnetics," *Geophysical Journal International*, vol. 220, no. 2, pp. 1242-1259, Feb. 2020.

[12] R. Metzler and J. Klafter, "The random walk's guide to anomalous diffusion: a fractional dynamics approach," *Physics Reports: A Review Section of Physics Letters (Section C)*, vol. 339, no. 1, pp. 1-77, Dec. 2000.

[13] M. E. Everett, "Transient electromagnetic response of a loop source over a rough geological medium," *Geophysical Journal International*, vol. 177, no. 2, pp. 421-429, May 2009.

[14] J. Ge, M. E. Everett, and C. J. Weiss, "Fractional diffusion analysis of the electromagnetic field in fractured media; Part I, 2D approach," *Geophysics*, vol. 77, no. 4, pp. WB213-WB218, Jul. 2012.

[15] X. Zhao, S. Wang, Q. Wu, and Y. Ji, "Time-domain electromagnetic fractional anomalous diffusion over a rough medium," *IEEE Transactions on Antennas and Propagation*, pp. 1-1, Dec. 2020.

[16] J. Ge, M. E. Everett, and C. J. Weiss, "Fractional diffusion analysis of the electromagnetic field in fractured media; Part 2, 3D approach," *Geophysics*, vol. 80, no. 3, pp. E175-E185, May 2015.

[17] Q. Wu, D. S. Li, C. D. Jiang, Y. J. Ji, Y. L. Wen, and H. Luan, "Ground-source Airborne Time-domain ElectroMagnetic (GATEM) modelling and interpretation method for a rough medium based on fractional diffusion," *Geophysical Journal International*, vol. 217, no. 3, pp. 1915-1928, Jun. 2019.

[18] L. Klimeš, "Correlation functions of random media," *Pure and Applied Geophysics*, vol. 159, no. 7, pp. 1811-1831, Jul. 2002.

[19] Kane Yee, "Numerical solution of initial boundary value problems involving Maxwell's equations in isotropic media," *IEEE Transactions on Antennas and Propagation*, vol. 14, no. 3, pp. 302-307, May 1966.

[20] T. Wang and G. W. Hohmanni, "A finite-difference, time-domain solution for three-dimensional electromagnetic modeling," *Geophysics*, vol. 58, no. 6, pp.797-809, Jun. 1993.

[21] F. N. Kong, "Hankel transform filters for dipole antenna radiation in a conductive medium," *Geophysical Prospecting*, vol. 55, no. 1, pp. 83-89, Jan. 2007.

[22] D. Guptasarma, "Computation of the time-domain response of a polarizable ground," *Geophysics*, vol. 47, no. 11, pp. 1574-1576, Nov. 1982.

[23] M. N. Nabighian, "Electromagnetic methods in applied geophysics, volume 1 theory," *Tulsa, Society of Exploration Geophysicists*, pp. 237, Jan. 1988.

Electromagnetic–AI-Based Design Optimization of SynRM Drives

A.A. Arkadan[1] and N. Al Aawar[2]

[1]Colorado School of Mines, Dept. of Electrical Engineering, Golden CO 80401, USA

[2]Marquette University, Dept. of Electrical and Computer Engineering, Milwaukee WI, 53233, USA
aaarkadan@mines.edu

Abstract – Characterization modules in electric machines and drives design optimization environments typically involve the use of electromagnetic finite element-state space models that require large number of iterations and computational time. It is shown in this work that the utilization of a Taguchi orthogonal arrays method in conjunction with a particle swarm optimization (PSO), search algorithm in a design optimization case study of a synchronous reluctance motor (SynRM) drive, resulted in about 80% reduction of computational time.

Index Terms – design optimization, particle swarm optimization, Taguchi algorithm, finite elements.

I. INTRODUCTION

Internal combustion engines (ICEs) running on fossil fuel and powering vehicles are major contributors to carbon emissions. In traction applications, hybrid (HEV) and electric (EV) vehicles utilizing electric motors are increasingly used as viable alternatives to ICE-driven ones. As such, electric motors design optimization is receiving more attention from researchers in this field. This is done to arrive at more efficient and reliable electric motor drive systems such as the axially laminated anisotropic (ALA) rotor synchronous reluctance motor (SynRM) drive. The SynRM has ideal characteristics for traction applications as it provides high developed torque per volume and has the ability to develop high torque at low speed for fast acceleration, and low torque at high speed for cruising purposes [1–3].

This paper presents a design optimization environment that employs three different computational modules. The first uses offline electromagnetic finite element (FE) and state space (SS) models of the motor drive system that account for anisotropy and predict the performance characteristics of the SynRM drive system. The FE-SS module is used to train, offline, a fuzzy logic (FL) module, which is used as a system identifier in the third module consisting of a particle swarm optimization (PSO) search algorithm. The input vector of the FL model is a design vector, *I*, and the output is a set of performance indicators. The PSO uses the FL module to evaluate a design objective function (OF) corresponding to the design vector in the search space. As can be appreciated, large number of PSO points are required to find an optimum design. A Taguchi orthogonal arrays method [4, 5] is employed to reduce computational time needed to reach an optimum design by determining the minimum number of input design parameter's combinations required to cover the whole search space of the optimization problem. The following sections include descriptions of the prototype motor drive system used, the FE-SS characterization module, and the implementation of a PSO design optimization environment and results.

II. MOTOR DRIVE SYSTEM DESCRIPTION AND CHARACTERIZATION MODULE

The block diagram of the prototype traction motor drive system modeled in this work is shown in Figure 1. The main components of the drive system include an ALA rotor SynRM motor rated at 100 kW and 6000 rpm, the drive power electronics, and associated controller and sensors. As can be appreciated, it is critical that the characterization module of such drive system accounts for effects of magnetic saturation and nonlinearities, material anisotropy, and effects of space and time harmonics when predicting the system performance characteristics.

This paper presents a multi-objective design optimization environment that includes a FE-SS characterization module. The objective of the design optimization environment implemented in this work is to maximize the developed torque while minimizing the torque ripple and total (Ohmic, core, and switching) losses of a prototype ALA SynRM drive system (Figure 1). The controller utilizes a decoupled d- and q-axis current control and a flux controller in the inner loop that are implemented with PI controllers [6, 7]. In addition, the power converter implemented in this case study is of the full wave, 3-phase, PWM inverter type, rated at 100 kW, with a 300 V DC bus voltage. The motor is designed for traction applications (Figure 2), and is rated at 100 kW and

Submitted On: March 1, 2021
Accepted On: September 29, 2021

https://doi.org/10.13052/2021.ACES.J.361103

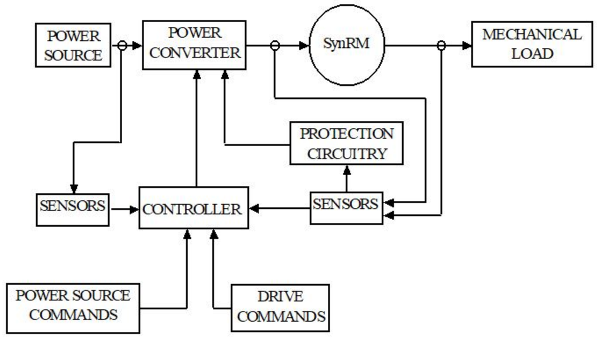

Fig. 1. SynRM drive system.

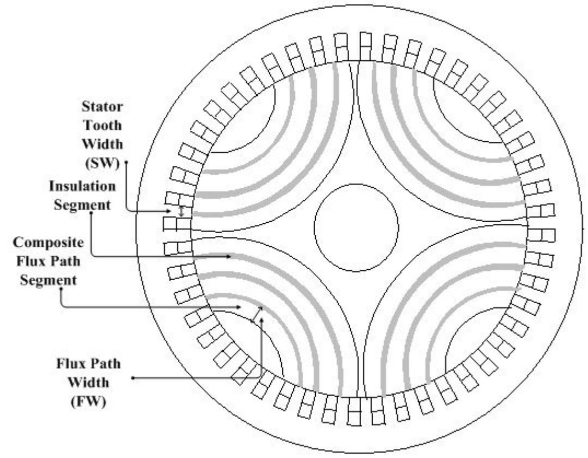

Fig. 2. ALA rotor SynRM cross-section.

6000 rpm. The motor stator is constructed from non-linear magnetic material that holds poly-phase windings like conventional AC machines. The rotor is made of ALA magnetic silicon steel laminations interleaved with thin insulation layers that form the rotor composite flux path segments.

The multi-objective design optimization environment implemented in this work includes a FE-SS characterization module that is used as a system identifier in the design optimization process. The SS model that governs the performance of the SynRM is expressed as:

$$\begin{bmatrix} \dot{I}_a \\ \dot{I}_b \\ \dot{I}_c \\ \dot{\omega}_m \\ \dot{\theta}_m \end{bmatrix} = \begin{bmatrix} & & & 0 & 0 \\ & A & & 0 & 0 \\ & & & 0 & 0 \\ 0 & 0 & 0 & 0 & 0 \\ 0 & 0 & 0 & 1 & 0 \end{bmatrix} \begin{bmatrix} I_a \\ I_b \\ I_c \\ \omega_m \\ \theta_m \end{bmatrix} + \begin{bmatrix} V_a \\ V_b \\ V_c \\ F \\ 0 \end{bmatrix}. \quad (1)$$

In equation (1), matrix A is given as:

$$\mathrm{A} = -\,inv\,(L) \cdot \left(R + \omega_m \cdot \frac{dL}{d\theta_m} \right), \quad (2)$$

where I and V represent the motor current and voltage quantities, L and R are the motor inductance and resistance matrices, θ and ω_m are the rotor angle and speed, respectively.

Furthermore, the voltages V_a, V_b, and V_c represent the system input voltage vector, which accounts for the drive power electronics and associated controllers [6–8]. Also, F, is given as

$$F = \frac{1}{J} \cdot \left(T_{dev} - \frac{\beta \cdot \omega_m}{2} - T_{mec} \right), \quad (3)$$

where J is the moment of inertia of the rotor, β is the friction coefficient, T_{mec} is the mechanical load, and T_{dev} is given as:

$$T_{dev} = \frac{1}{2} \cdot \left[I_a \;\; I_b \;\; I_c \right] \cdot \frac{dL}{d\theta_m} \cdot \begin{bmatrix} I_a \\ I_b \\ I_c \end{bmatrix}. \quad (4)$$

In addition, the FE formulations account for anisotropy by using a reluctivity tensor:

$$\overline{\overline{\nu}} = \begin{bmatrix} \nu_t \cos^2\alpha + \nu_n \sin^2\alpha & -(\nu_n - \nu_t)\cos\alpha\sin\alpha \\ -(\nu_n - \nu_t)\cos\alpha\sin\alpha & \nu_t \sin^2\alpha + \nu_n \cos^2\alpha \end{bmatrix}, \quad (5)$$

where ν_t and ν_n are the reluctivity normal and tangential components, and α is the angle of the easy magnetization axis with the x-axis [7]. As such, the FE-SS module accounts for space harmonics due to material nonlinearities and machine complex geometry, time harmonics due to switching electronics, and for rotor material anisotropy [6–8] when predicting the performance characteristics of the SynRM drive system.

III. THE TAGUCHI-FE-PSO DESIGN ENVIRNOMENT

The objective of this work is to maximize the developed torque while minimizing torque ripple as well as Ohmic, switching, and core losses of the SynRM drive system (Figure 1). To optimize the design of the motor drive system, the FE-PSO environment of Figure 3 was developed. It uses the FE-SS characterization module described above to predict the performance characteristics of the SynRM drive system, which include various SynRM currents and voltage waveforms as well as the torques profile, which are used to train offline a fuzzy logic (FL) module [9]. The FL module as shown in Figure 4, consists of a fuzzification and defuzzification inference units, a knowledge base formed from a database and a rule base unit. A Sugeno type FL is used in this work and the fuzzification is implemented using double-sided Gaussian membership functions [9]. The input vector of the FL model is the design vector, I_{Design}, and the output is a set of performance indicators. The FL module is incorporated within the PSO search algorithm, which is an evolutionary computation algorithm

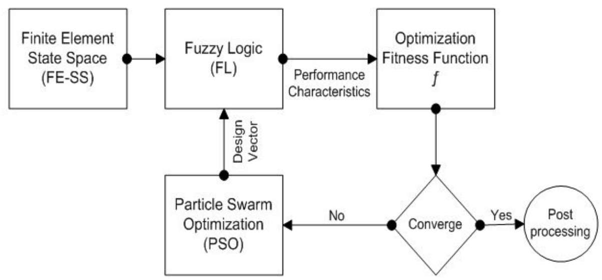

Fig. 3. FE-PSO design optimization environment.

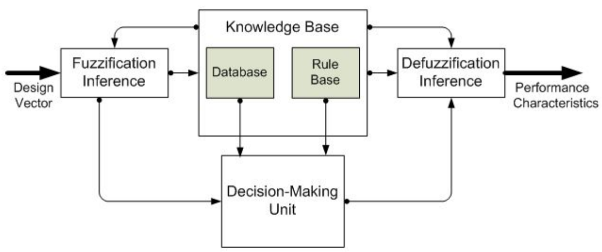

Fig. 4. Fuzzy logic module.

developed by Kennedy and Eberhart [10] and it mimics the social behavior of a flock of birds where information is shared among the individuals of a population. The PSO starts with an initial swarm of random particles in the search space where each particle is also assigned a randomized velocity. The velocity of each particle is dynamically updated based on the particle's best previous position reached and the best position reached among previous generations. The PSO uses the FL module to evaluate the OF corresponding to any values of the design vector in the search space. As can be appreciated from the above, large number of FE solutions and PSO iterations are required to find an optimum design. As such, a Taguchi-FE-PSO environment, as shown in Figure 5, is developed to reduce computational time needed to reach an optimum design. At the heart of this environment is the Taguchi orthogonal arrays method. The one used in this work is of the four-level, L16 orthogonal array type [4, 5], which is used to determine the minimum number of input design parameter's combinations required to cover the design optimization problem search space. The method assigns a range for each input design parameter. In addition, each range is divided into equal intervals.

IV. APPLICATION OF THE TAGUCHI-FE-PSO DESIGN ENVIRNOMENT AND RESULTS

As stated above, the objective of this work is to maximize the developed torque while minimizing torque ripple and losses of the SynRM drive system of Figures 1 and 2. The Taguchi-FE-PSO design optimization environment developed in this work utilizes the Taguchi four-level L16 orthogonal arrays method [4, 5] which is used to determine the minimum number of input design parameter's combinations required to cover the design optimization problem search space. The values of the design parameters are determined in the FE-SS module that predicts the performance characteristics of the SynRM drive system, which are used to train, offline, the FL module, that is used as a system identifier in the PSO search algorithm. It should be noted here that the SynRM drive system for traction applications was implemented with both EPA Urban and Highway Federal Driving Schedules [11] (Figures 6 and 7).

The Taguchi-FE-PSO design environment of Figure 5 was applied to find an optimum design for the prototype SynRM drive of Figure 1 operating at 90 Nm and 3000 rpm load conditions. In this optimization problem, the input design vector, I_{Design} consists of the number of flux paths (N), the stator tooth width (SW), and the rotor flux path width (FW), shown in Figure 2. The design optimization environment starts by defining an objective

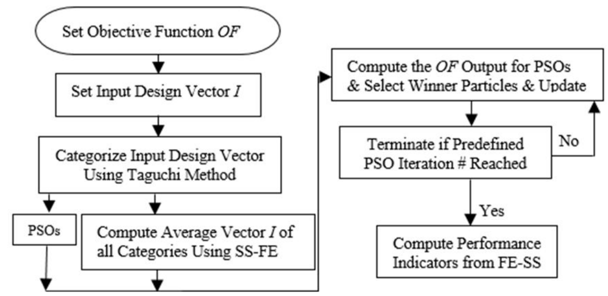

Fig. 5. Taguchi-FE-PSO design optimization environment.

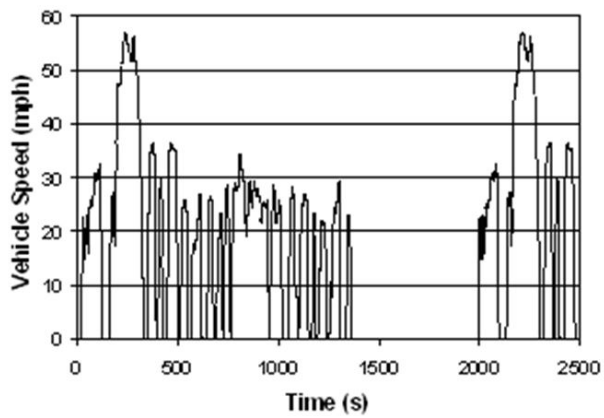

Fig. 6. Federal Urban Driving Schedule, "FUDS".

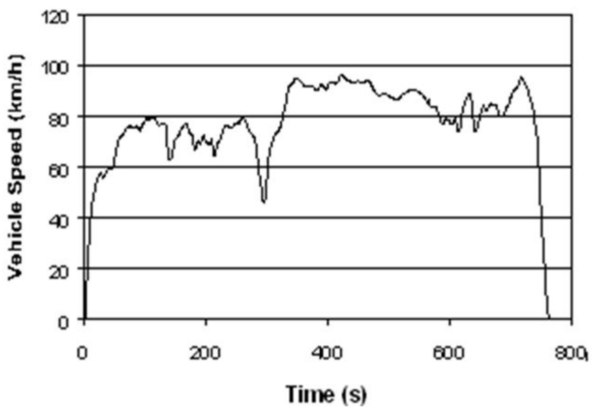

Fig. 7. Federal Highway Driving Schedule “FHDS”.

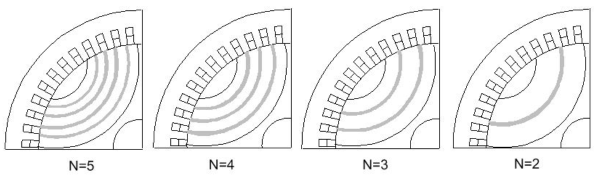

Fig. 8. Number of flux paths variation.

function (OF). It is defined as the weighted sum of the performance indicators that include torque ripple, T_r, the total losses in the machine, T_L, and the developed torque average, T_{avg}, constrained at a desired load, T_d:

$$OF = a \cdot T_r + \beta \cdot T_L + \lambda \cdot |T_{ave} - T_d|, \qquad (6)$$

where α and β are the weights of T_r and T_L, respectively, and λ is the Lagrangian multiplier.

Next, the input design parameters vector is defined as follows: P_1 = N, represents the possible number of rotor flux paths, and it is restricted to be in the range of 2–5, due to physical design constraints of the machine. That is, the rotor has four possible designs corresponding to N = 2, 3, 4, or 5, as shown in Figure 8; P_2 = SW, the stator tooth width; and P_3 = FW, the rotor flux path width, shown in Figure 2. The PSO search method would require many design trials. Furthermore, the search for the optimum design would require accurate evaluation of each design vector or trial, using the FE-SS module, at relatively high computational cost. As such, the Taguchi four-level, L16, orthogonal arrays method was used to determine the minimum number of input design parameter's combinations required to cover the design optimization problem search space. It assigns a range for each input design parameter and divides each range into equal intervals or levels designated as 1 for low, 2 for medium, 3 for high, and 4 for maximum, as given in Table 1. In addition, the search space ranges of SW and FW are given in Table 2 for each of the four possible rotor

Table 1: Taguchi array with three parameters

Category #	**P_1 = N**	**P_2 = SW**	**P_3 = FW**
1	1	1	1
2	1	1	1
3	1	2	2
4	1	2	2
5	2	1	2
6	2	1	2
7	2	2	1
8	2	2	1
9	3	2	1
10	3	2	1
11	3	1	2
12	3	1	2
13	4	2	2
14	4	2	2
15	4	1	1
16	4	1	1

Table 2: Range of design parameters

N	**SW (in.)**	**FW (in.)**
2	[0.09–0.16]	[0.08–0.34]
3	[0.09–0.16]	[0.08–0.32]
4	[0.09–0.16]	[0.08–0.23]
5	[0.09–0.16]	[0.10–0.18]

designs and were divided into equal intervals. The FE-SS module was used to compute the ALA rotor performance characteristics for the PSO trail particles of each of the 16 categories. Next, the results of the FE-SS module were used to train the corresponding adaptive neuro fuzzy inference system, ANFIS, for a category. In this work, the PSO starts by initiating 64 PSO trials or particles in each category. The output of each particle is computed by the category corresponding ANFIS. Next, the OF given in equation (5) is evaluated and compared with a preset threshold to select the winner particles. These winner particles are then cross-mutated with each other to define new trials.

The Taguchi-FM-PSO design environment of Figure 5 was applied to find an optimum design for the prototype SynRM drive of Figure 1 and Figure 2, operating at 90 Nm and 3000 rpm load conditions, and resulted in optimized design performance indicator's values. A summary of the main results is given in Table 3, which shows the performance characteristics of the system for the initial (N = 4) and optimal (N = 5) designs, as well as the initial and final values of the design parameters SW and FW. An inspection of these results reveals that the total losses were reduced by 61%, in addition to reducing the torque ripple by 42%. Furthermore, a sample performance profile, showing the percentage torque ripple and

Table 3: Initial and optimal design

Design/Parameters	Initial	Optimal	% Change
[**N**; **SW** (in); **FW** (in)]	[4;0.115;0.148]	[5;0.103;0.112]	N/A
Losses	6265 W	2401 W	–61%
Torque Ripple	52%	30%	–42%
Torque Average	90 Nm	90 Nm	N/A

Table 4: Computational time comparison

	FE-PSO	**Taguchi-FE-PSO**
% Computational Time	100%	20.4%

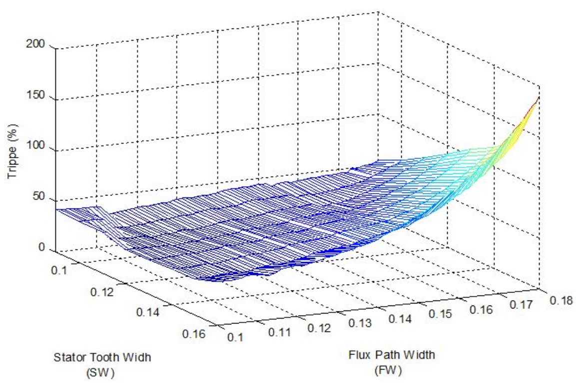

Fig. 9. Percentage torque ripple profile vs. search space.

corresponding search space, is shown in Figure 9. As expected, the complex geometry of this class of machines in addition to the electronic switching in the drive system showed an many local minima and many saddle points in the search space.

In addition to the above, this work includes a comparison of computational time needed to solve this design optimization problem by using both, the FE-PSO approach of Figure 3 and the Taguchi-FE-PSO approach of Figure 5. The results are presented in Table 4, which shows a comparison of the normalized computational time needed for both approaches. Based on these results, it can be stated that the implementation of the Taguchi orthogonal arrays method resulted in about 80% reduction of needed computational time.

V. CONCLUSIONS

This work utilized a Taguchi orthogonal arrays method in conjunction with a particle swarm optimization search algorithm to reduce the computational time needed to solve the design optimization problem of electric motor drives for traction applications. The results of a case study involving a prototype 100 kW ALA Rotor SynRM drive for traction applications showed an improved performance characteristics and demonstrated that the use of a Taguchi orthogonal arrays method resulted in about 80% reduction of computational time needed for implementing the FE-PSO design optimization environment.

REFERENCES

[1] K. Rajashekara, "Present status and future trends in electric vehicle propulsion technologies," *IEEE J. Emerg. and Sel. Topics Power Electron.*, vol. 1, no. 1, pp. 3-10, Mar. 2013.

[2] N. Al-Aawar and A. A. Arkadan, "Hybrid electric vehicle characterization using generalized notion of power," *Applied Computational Electromagnetics Society (ACES) Journal*, vol. 28, no. 11, pp. 1080-1087, Nov. 2013.

[3] J. M. German, *Hybrid Powered Vehicles*, SAE International, Warrendale, PA, 2003.

[4] R. N. Kacker, E. S. Lagergren, and J. J. Filliben, "Taguchi's orthogonal arrays are classical designs of experiments," *J. Res. Natl. Inst. Stand. Technol.*, vol. 96, no. 5, 577-591, Sep-Oct. 1991.

[5] A. A. Arkadan, N. Al-Aawar, and A. O. Hariri, "EM-Taguchi module for the characterization of WAD," *IEEE Trans. on Magnetics*, vol. 51, no. 3, Article 8202304, Mar. 2015.

[6] F. N. Isaac, A. A. Arkadan, A. A. Russell, and A. El-Antably, "Effects of anisotropy on the performance characteristics of an ALA synchronous reluctance motor drive system," *IEEE Trans. on Magnetics*, vol. 34, no. 5, pp. 3600-3603, Sep. 1998.

[7] F. N. Isaac, A. A. Arkadan, and A. El-Antably, "Magnetic field and core loss evaluation of ALA-rotor synchronous reluctance machines taking into account material anisotropy," *IEEE Trans. on Magnetics*, vol. 34, no. 5, pp. 3507-3510, Sep. 1998.

[8] A. A. Arkadan, F. N. Isaac, and O. A. Mohammed, "Parameters evaluation of axially laminated anisotropic synchronous reluctance motor drives," *IEEE Trans. on Mag.*, vol. 36, pp. 1950-55, Jul. 2000.

[9] T. Takagi and M. Sugeno, "Derivation of fuzzy control rules from human operator's control action," *in IFAC Symp. Fuzzy Info.*, 1983.

[10] J. Kennedy and R. C. Eberhart, "Particle swarm optimization," *Proceedings of IEEE International Conference on Neural Networks*, Piscataway, NJ., pp. 1942-1948, 1995.

[11] EPA, "Vehicle chassis dynamometer driving schedules. Available: online: dynamometer drive schedules, vehicle and fuel emissions testing," US EPA. [Accessed Oct. 03, 2019].

Triangular Ring Patch Antenna Analysis: Neuro-Fuzzy Model for Estimating of the Operating Frequency

Ahmet Kayabasi

Department of Electrical and Electronics Engineering
University of Karamanoglu Mehmetbey, Karaman, 70100, Turkey
ahmetkayabasi@kmu.edu.tr

Abstract – In this study, a neuro-fuzzy (NF) analysis method is suggested for the estimation of the operating frequency of triangular ring patch antennas (TRPAs) that operate at ultra high band applications. Although the analysis of regular-shaped patch antennas (PAs) such as rectangular, triangle, and circle is easy, analysis of irregularly shaped patch antennas is difficult and time consuming. Here, this great effort and time has been eliminated by using an artificial intelligence technique such as NF. To create a data set for NF, 100 TRPAs with different physical and electrical properties (L, l, h, and ε_r) are simulated by using an electromagnetic simulator program. The currency and accuracy of the proposed approach is then confirmed on the measurement results of a prototype TRPA fabricated in this study. The results of NF model are compared with the simulation/measurement results and previously the method published in the literature.

Index Terms – analysis, neuro-fuzzy, operating frequency, patch antenna, triangular ring patch antenna.

I. INTRODUCTION

Patch antennas (PAs) have significant advantages such as low size, lightness, robustness, ease of production, low production cost, and physical compatibility with the surfaces. Because of these advantages, PAs are widely used in portable/non-portable wireless communication applications that require miniaturized geometry [1]. The substrates with a high dielectric constant can be used to reduce the antenna size for miniaturized mobile communication devices, but this leads to a decrease in parameters such as performance efficiency and bandwidth [1]. The miniaturized PAs can be constructed by utilizing some modifications such as shorting pins, slits or slots on the traditional rectangular, triangular, and circular geometry structures [1]. Triangular ring patch antennas (TRPAs) are constructed by triangular slot-loading in the center of the equilateral triangular patch [2, 3]. Triangular patch antennas (TPAs) with the same dimensions, the operating frequency is reduced due to slot-loading into the triangular patch. For the same operating frequency, the size of TRPA reduces compared to the TPA [2, 3].

Antenna analysis process covers the calculation of antenna performance parameters such as operating frequency, bandwidth, and gain. Several analytical and numerical methods having some disadvantages are generally used for analysis process [4]. The numerical methods give good results by using mixed mathematical operations. The numerical methods such as finite difference time domain method, finite element method, and method of moment (MoM) require much more time in solving Maxwell's equations including integral and/or differential computations. So, it becomes time consuming since it repeats the same mathematical procedure even if a minor change in geometry is carried out. Moreover, the analytical methods such as the cavity model and the transmission line model are accurate but they are based on physical assumptions. Analytical methods give a physical view of antenna radiation properties. The main difficulty of analytical models is their limited input impedance for accuracy at the resonant frequency and for non-thin substrates. According to the instantaneous phase of the signal applied to the antenna, the minimum and maximum continuously changing electric field can be mentioned. The electric field does not stop abruptly, as in the space around the patch, and stretches the outer frame of the patch somewhat. These area extensions are known as fringe areas and cause the patch to spread. These methods are more suitable for conventional MAs because of their regular shapes. In addition, these approaches require a new solution for every small change in the patch geometry [4]. For this reason, artificial intelligence techniques are widely preferred as more accurate and faster alternative methods in order to overcome these difficulties of traditional techniques in the analysis process of PAs [2–18]. The precise mathematical formulations in complex methods involve a large number of numerical operations that result in rounding errors and may require experimental adjustments to

Submitted On: June 7, 2021
Accepted On: September 9, 2021
https://doi.org/10.13052/2021.ACES.J.361104

theoretical results. Obtaining results from these methods takes a long time and these methods are not very suitable for computer aided design. Features such as learning ability, easy applicability to different problems, generalization feature, less information requirement, fast processing, and easy implementation have made artificial intelligence popular in recent years. Artificial intelligence models such as Artificial Neural Network (ANN) [19], Fuzzy Logic (FL) [20], Support Vector Machine (SVM) [20], and Neuro-Fuzzy (NF) [22] eliminate the complex mathematical procedures and time consuming for processes of antenna design. These models have been used extensively for the analysis of various PAs in the literature [5–17]. In [5–17], analysis studies were carried out to determine some performance parameters of PAs having various shapes with artificial intelligence techniques such as ANN, SVM, and NF.

In this study, an NF-based artificial intelligence model is proposed for the analysis of TRPAs in terms of operating frequency (fr). For this purpose, the simulation of 100 TRPAs was carried out by a 3D full-wave simulator based on MoM [23] and the dataset for the NF model was created. The number of 75 and 25 TRPA datasets are used to training and testing the NF model's accuracy, respectively. In addition, the NF model is verified by the measurement data of the TRPA fabricated for this study.

II. TRPA STRUCTURE AND SIMULATION PROCESS

The TRPA structure is obtained by slotting with "l" dimensional triangle in the middle of the "L" dimensional triangle as shown in Figure 1. The formed patch is placed on a substrate having dielectric constant ε_r and h as thickness. The x and y represent the feeding point of the TRPA. The triangular slotting in the center of the TPA causes a reduction in the operating frequency compared to a TPA of the same size. Also, TRPA is smaller than TPA at the same operating frequency, and these results are shown in Table 1.

Table 1: Comparative results of simulated TPA and TRPA

Antenna	**Patch Dimension (mm)**			ε_r	f_r *[GHz]*
	L	***l***	***h***		
TPA	52	0	1.6	2.33	2.432
TRPA	52	17.2	1.6	2.33	2.226
TPA	52	0	1.6	2.33	2.432
TRPA	43.3	25.8	1.6	2.33	2.432

Table 2: Comparative results of simulated TPA and TRPA

Number of Simulations	**Patch Dimensions (mm)**			**Dielectric Constant (ε_r)**
	L	***l***	***h***	
20	26	3.44, 6.88, 10.32, 13.76, 17.2	1.6, 2.5	2.33, 4.4
20	34	5.16, 10.32, 15.48, 20.64, 25.8		
20	52	8.6, 17.2, 25.8, 34.4, 43		
20	69	17.2, 25.8, 34.4, 43, 51.6		
20	86	25.8, 34.4, 43, 51.6, 60.2		

Simulations of 100 TRPAs were made according to the parameters (L, l, h, and ε_r) and the operating frequency (f_r) given in Table 2. Commonly used materials such as FR4 and Rogers RT/duroid 5870 were chosen as substrates in the simulations. The TRPA structures are modeled/simulated according to the topology in Figure 2 by the software HyperLynx® 3D EM [24] based MoM [23]. The software uses the MoM to analyze potentially any patch shape in the spectral domain. The only limitation on the potential of this method is the length of analytical and numerical computation required for analysis. The complex potential integral equation is solved by the software in the space domain using the MoM. A wave source of 1 Volt with coaxial feed is utilized for the TRPAs in the simulations. The TRPA models are meshed

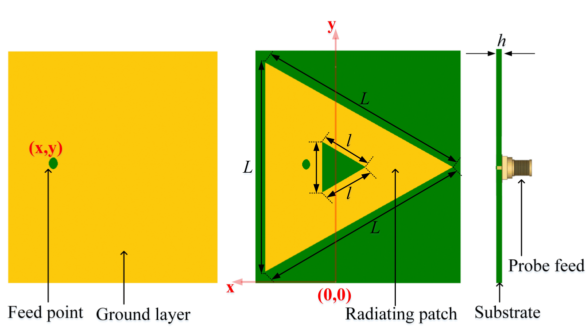

Fig. 1. Geometry of the TRPA.

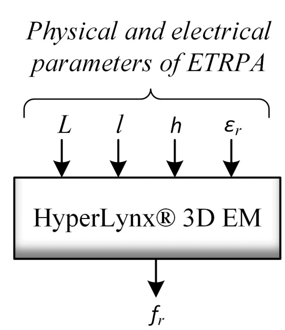

Fig. 2. Geometry of the TRPA.

with maximum frequency of 4 GHz and lines per wavelength ratio of 40. The TRPAs are simulated between the frequency of 0 GHz and 4 GHz. The feed point of TRPAs is determined (S_{11} <-10 dB) by using the HyperLynx® 3D EM's built-in optimization module.

III. PROCESS OF NF MODEL

The steps of NF model construction to determine the operating frequency of TRPAs are shown in Figure 3. The number of 75 antenna data are used to train the NF model and it is aimed to minimize the average percentage error (APE) between targets/outputs.

A. NF modeling and training

The NF is an important method that helps in accurate computation, estimation, prediction, and classification [22]. It is an integrated form of the ANN and fuzzy inference system (FIS) to merge the learning characteristic of the ANN with the expert knowledge of the FIS [22]. Seventy-five of the 100 TRPA datasets were used for training the NF model. In prediction of operating frequency, an NF based on Sugeno type FIS is designed as presented in Figure 4 and its set-parameters are given in Table 3. The algorithm of the NF model is coded in the platform of MATLAB®. Before the input data is presented to the NF model, it is normalized by dividing by 1000. Membership functions (MFs) of the NF model are Gaussian functions which are used for the input and linear function which is used for the output. The NF network is trained by hybrid-learning algorithm [22] associating the backpropagation algorithm and the least-square method. Considering the comparative results given in Figure 5, the results obtained from the simulations are compatible with the proposed NF model, and the APE for analysis in the training process was obtained as 0.259%.

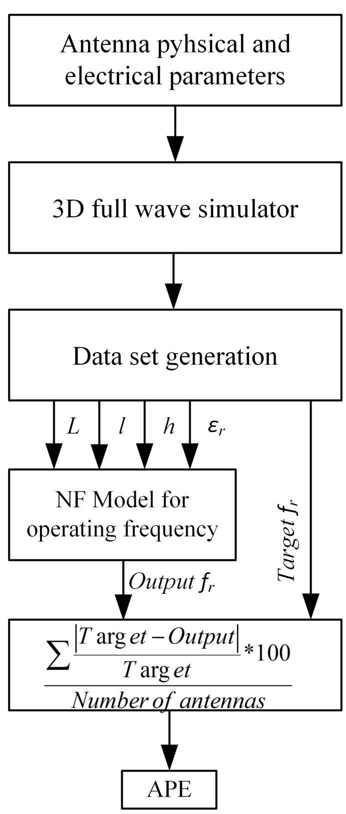

Fig. 3. The working principle of the NF model.

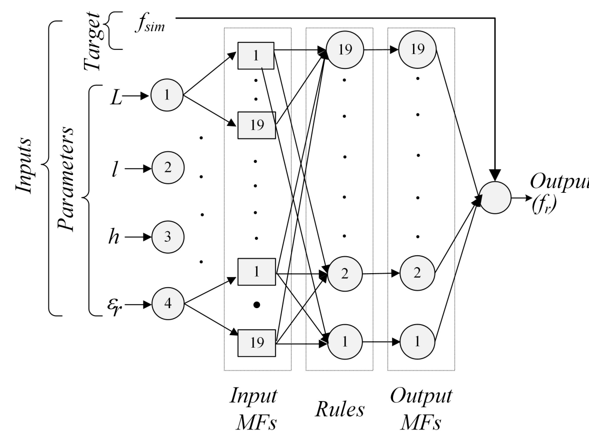

Fig. 4. The proposed NF model.

Table 3: The used NF parameters for analysis TRPA

Parameters	Set Type/Value
Input MF type	Gaussian
Output MF type	Linear
Number of inputs	4
Number of outputs	1
Number of fuzzy rules	19
Number of MFs	19
Seed value	349097429
Epochs	150
Number of nonlinear parameters	4 x 19 x 2 = 152
Number of linear parameters	5 x 19 = 95
Number of nodes	197
Number of training data pairs	75

B. Testing results of analysis for TRPA

In the last section, NF model is constructed and trained with proper parameters. The accuracy of the NF model is now tested through 25 TRPA datasets not included in the training phase. The parameters of 25 simulated antennas with respective operating frequency values and the computed operating frequency values are given in Table 4. Also, NF results are compared with the results of proposed method in the literature [2]. It is seen from the results; model successfully obtains the

Table 4: The comparative test results for operating frequencies of TRPAs

#	Inputs					Operating Frequencies [GHz]		Percentage Error (PE)	
	***L* [mm]**	***l* [mm]**	***h* [mm]**	ε_r	$f_{r\_sim.}$	f_r [2]	f_{r_NF}	**[2]**	***NF***
1	26	6.88	1.6	2.33	4.614	4.599	4.638	0.325	0.520
2	26	10.32	1.6	4.4	3.261	3.254	3.255	0.227	0.184
3	26	13.76	2.5	2.33	4.365	4.338	4.327	0.625	0.871
4	26	3.44	2.5	4.4	3.401	3.441	3.431	1.179	0.882
5	26	17.2	2.5	4.4	3.198	3.195	3.218	0.102	0.625
6	34	5.16	1.6	2.33	3.576	3.585	3.609	0.253	0.923
7	34	10.32	1.6	4.4	2.538	2.543	2.515	0.188	0.906
8	34	25.8	1.6	4.4	2.13	2.114	2.145	0.773	0.704
9	34	15.48	2.5	2.33	3.278	3.279	3.297	0.031	0.580
10	34	10.32	2.5	4.4	2.544	2.575	2.54	1.223	0.157
11	34	20.64	2.5	4.4	2.309	2.342	2.317	1.446	0.346
12	52	25.8	1.6	2.33	2.03	1.964	1.994	3.245	1.773
13	52	34.4	1.6	2.33	1.856	1.821	1.827	1.874	1.563
14	52	8.6	2.5	2.33	2.368	2.378	2.361	0.430	0.296
15	52	25.8	2.5	4.4	1.536	1.524	1.545	0.784	0.586
16	69	25.8	1.6	2.33	1.616	1.614	1.62	0.114	0.248
17	69	51.6	1.6	2.33	1.28	1.277	1.285	0.209	0.391
18	69	34.4	1.6	4.4	1.11	1.139	1.114	2.589	0.360
19	69	34.4	2.5	2.33	1.536	1.552	1.53	1.035	0.391
20	69	25.8	2.5	4.4	1.21	1.189	1.207	1.734	0.248
21	86	60.2	1.6	2.33	1.03	0.981	1.03	4.709	0.000
22	86	43	1.6	4.4	0.87	0.878	0.878	0.936	0.920
23	86	51.6	2.5	2.33	1.15	1.136	1.119	1.208	2.696
24	86	34.4	2.5	4.4	0.95	0.957	0.945	0.789	0.526
25	86	60.2	2.5	4.4	0.79	0.803	0.775	1.685	1.899
							Average percentage error (APE)	1.109	0.744

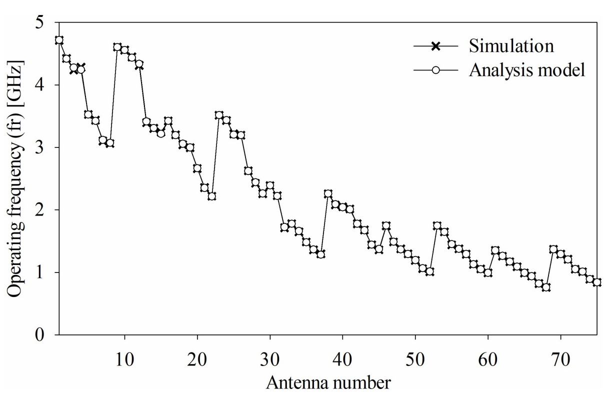

Fig. 5. Comparative results for the simulation/NF analysis model in the training process.

operating frequency with APE of 0.744%. The harmony of simulation and NF model results is seen in Figure 6. The results obtained with NF are better than the method proposed in the literature [2]. Because NF shows a better approach to nonlinear problems than SVM [2].

IV. FABRICATION OF TRPA

The TRPA fabricated in this study is used for the accuracy of the NF analysis model. TRPA printed on FR4 PCB substrate is shown in Figure 7 and the electrical/physical properties of FR4 PCB ($\varepsilon_r = 2.22$,

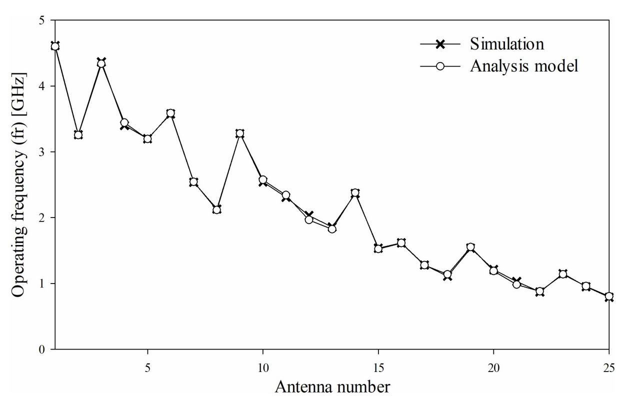

Fig. 6. Comparative results of the simulation and NF analysis model in the testing process.

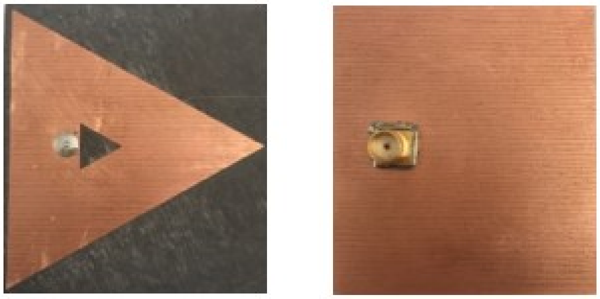

Fig. 7. The photograph of prototyped TRPA.

Table 5: The comparative operating frequencies

Inputs				Operating Frequency [GHz]			
L [mm]	*l [mm]*	*h [mm]*	ε_r	$f_{sim.}$	$f_{mea.}$	[2]	f_{NF}
52	8.6	1.6	2.22	2.438	2.468	2.391	2.425

tangent loss = 0.02) are given in Table 5. FR4 substrate is made of fiberglass. This substrate layer provides a solid foundation for PCBs, though the thickness can vary according to the uses of a given board. The Keysight Technologies N5224A PNA network analyzer is used to measure the prototyped TRPA. The measured S_{11} parameter is shown in Figure 8 in comparison with the simulated one. The results of measured and the analysis model are listed in Table 5 to evaluate the testing process in detail.

From Table 5, the result of NF model is much close to the simulated/measured results. Therefore, the NF model can be successfully used to obtain the operating frequency (f_r) of the TRPA without handling complex mathematical functions and transformations. Moreover, the proposed NF model can be modified and developed to solve similar nonlinear electromagnetic problems.

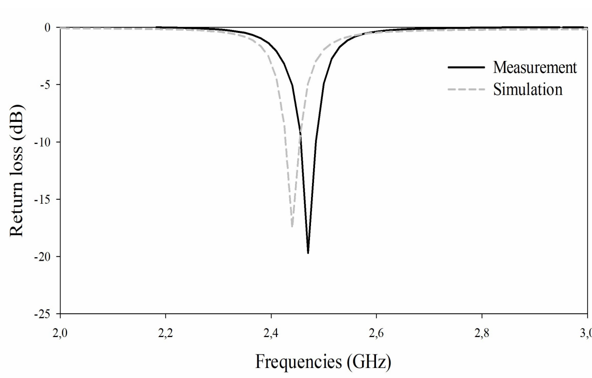

Fig. 8. The simulated and measured S11 parameters of TRPA.

V. CONCLUSION

In this study, the NF model is implemented for analysis of the TRPAs. For this, the NF model using Sugeno-type FIS is designed to compute the operating frequency of TRPAs. The number of 100 TRPAs having four antenna parameters is simulated to obtain the operating frequency. The NF model is trained and tested respectively with 75 and 25 datasets of the 100 TRPAs. The APE is computed as 0.259% for 75 training data and as 0.744% for 15 test data of TRPAs. According to the obtained results, the operating frequency of TRPAs is successfully computed using the proposed NF model. Also, the operating frequency values predicted in this work are compared with different calculated results reported in the literature. The NF technique may be preferred as a faster and accurate alternative method according to the traditional techniques in the analysis processes of PAs. On average, the simulation time is five minutes to find the operating frequency of a TRPA. However, this time is in the order of milliseconds by using the proposed method. It was concluded that the NF method may successfully be used to define any parameter of TRPA for analysis.

REFERENCES

[1] K. Wong, *Compact and Broadband Microstrip Antennas*. John Wiley & Sons, Inc., 2002.

[2] A. Kayabasi, "Analysis and synthesis of equilateral triangular ring microstrip antenna using Support vector machine," *Appl. Comput. Electromagn. Soc. J.*, vol. 33, no. 6, pp. 616-624, Jun. 2018.

[3] A. Kayabasi, "Soft computing-based synthesis model for equilateral triangular ring printed antenna," *AEU - Int. J. Electron. Commun.*, vol. l94, pp. 332-338, Sep. 2018.

[4] J. R. James, P. S. Hall, and C. Wood, *Microstrip Antenna Theory and Design*. Peter Peregrinus, 1981.

[5] A. Kayabasi and A. Akdagli, "Predicting the resonant frequency of E-shaped compact microstrip antennas by using ANFIS and SVM," *Wireless Pers. Commun.*, vol. 82, pp. 1893-1906, Jun. 2015.

[6] A. Kayabasi, A. Toktas, A. Akdagli, M. B. Bicer, and D. Ustun, "Applications of ANN and ANFIS to predict the resonant frequency of L-shaped compact microstrip antennas," *Appl. Comput. Electromagn. Soc. J.*, vol. 29, no. 6, pp. 460-469, Jun. 2014.

[7] K. Sabanci, A. Kayabasi, A. Toktas, and E. Yigit, "Notch antenna analysis: Artificial neural network-based operating frequency estimator," *Appl. Comput. Electromagn. Soc. J.*, vol. 32, no. 4, pp. 303-309, Apr. 2017.

[8] K. Guney and N. Sarikaya, "Adaptive neuro-fuzzy inference system for computing the resonant

frequency of circular microstrip antennas," *Appl. Comput. Electromagn. Soc. J.*, vol. 19, pp. 188-197, Nov. 2004.

[9] F. Güneş, N. T. Tokan, and F. Gürgen, "A consensual modeling of the expert systems applied to microwave devices," *Int. J. RF Microw. Comput.-aided Eng.*, vol. 20, pp. 430-440, 2010.

[10] Y. Tighilt, F. Bouttout, and A. Khellaf, "Modeling and design of printed antennas using neural networks," *Int. J. RF Microw. Comput.-aided Eng.*, vol. 21, pp. 228-233, Mar. 2011.

[11] A. R. Venmathi and L. Vanitha, "Support vector machine for bandwidth analysis of slotted microstrip antenna," *Int. J. Comput. Inf. Sci.*, vol. 4, no. 1, pp. 67-61, 2011.

[12] A. De Khan and M. Uddin, "Prediction of slot-size and inserted air-gap for improving the performance of rectangular microstrip antennas using artificial neural networks," *IEEE Antennas Wireless Propag. Lett.*, vol. 12, pp. 1367-1371, Oct. 2013.

[13] E. Demircioglu, M. H. Sazlı, S. T. İmeci, and O. Sengul, "Soft computing techniques on multiresonant antenna synthesis and analysis," *Microw. Opt. Technol. Lett.*, vol. 55, no. 11, pp. 2643-2648, Nov. 2013.

[14] L. Merad, F. T. Bendimerad, and S. M. Meriah, "Design and resonant frequency calculation of rectangular microstrip antennas," *Int. J. Numer. Model. El.*, vol. 24, no. 2, pp. 144-153, Feb. 2011.

[15] N. K. Saxena, M. Khan, P. K. S. Pourush, and N. Kumar, "Neural network analysis of switchability of microstrip rectangular patch antenna printed on ferrite material," *Int. J. RF Microw. Comput.-aided Eng.*, vol. 20, no. 1, pp. 1-5, 2010.

[16] N. T. Tokan and F. Gunes, "Support vector characterization of the microstrip antennas based on measurements," *Prog. Electromagn. Res. B.*, vol. 5, pp. 49-61, 2008.

[17] Z. Qi-Jun, K. C. Gupta, and V. K. Devabhaktuni, "Artificial neural networks for RF and microwave design-from theory to practice," *IEEE Trans. Microw. Theory Tech.*, vol. 51, pp. 1339-1350, Apr. 2003.

[18] A. Akdagli, A. Kayabasi, and I. Develi, "Computing resonant frequency of C-shaped compact microstrip antennas by using ANFIS," *Int. J. Elec.*, vol. 102, pp. 407-417, Mar. 2015.

[19] S. Haykin, *Neural Networks: A Comprehensive Foundation.* Macmillan College Publishing Company, New York, 1994.

[20] L. A. Zadeh, "Fuzzy logic," *Computer (Long Beach Calif),* vol. 21, pp. 83-93, 1988.

[21] V. Vapnik and A. Chervonenkis, "The necessary and sufficient conditions for consistency in the empirical risk minimization method," *Pattern Recognit. Image Anal.*, vol. 1, pp. 283-305, Jan. 1991.

[22] J. R. Jang, "ANFIS: adaptive-network-based fuzzy inference system," *IEEE Transactions on Systems, Man, and Cybernetics*, vol. 23, no. 3, pp. 665-685, 1993.

[23] R. F. Harrington, *Field Computation by Moment Methods.* IEEE Press, Piscataway, NJ, 1993.

[24] HyperLynx® 3D EM, Version 15, Mentor Graphics Corporation, 8005 SW Boeckman Road, Wilsonville, OR 97070.

Ahmet Kayabasi was born in 1980. He received his B.S. and M.S. degrees in electrical and electronics engineering from Selcuk University, Turkey, in 2001, 2005 respectively. In 2015, he received his Ph.D. degree in electrical and electronics engineering from Mersin University, Turkey. From 2001 to 2015, he was a lecturer in the Electronics and Automation Department of Selcuk University. He has been working as an Associate Professor in the Department of Electrical and Electronics Engineering at Karamanoglu Mehmetbey University. His current research interests include antennas, microstrip antennas, computational electromagnetics, and artificial intelligence.

Quad-Band MIMO Antenna System for 5G Mobile Handsets

M. Abo El-Hassan, A. E. Farahat, and K. F. A. Hussein

Electronics Research Institute (ERI), Cairo, Egypt
mayaboelhassan@yahoo.com, asmaa@eri.sci.eg, Khalid_elgabaly@yahoo.com

***Abstract* –** An efficient Multi-Input Multi-Output (MIMO) antenna system with a spatial diversity configuration for the Fifth Generation (5G) mobile handsets is constructed from a compact-size quad-band (28/45/51/56 GHz) microstrip patch antennas. The antenna is constructed as primary and secondary patches which are capacitively coupled and designed to realize impedance matching and to produce appropriate radiation patterns in the four frequency bands. The novel quad-band patch antenna includes complicated radiation mechanisms required for multiple-band operation. Two-port and four-port MIMO antenna systems that employ the quad-band patch antenna are proposed in the present work for the 5G mobile handsets. Numerical and experimental investigations are achieved to assess the performance of both the single-element antenna and the proposed MIMO antenna systems including the return loss at each antenna port and the coupling coefficients between the different ports. It is shown that the simulation results agree with the experimental measurements and both show good performance. The bandwidths achieved around 28, 45, 51, and 56 GHz are about 0.6, 2.0, 1.8, and 1.3 GHz, respectively. The radiation patterns produced when each port is excited alone are shown to be suitable for spatial diversity scheme with high radiation efficiency. It is shown that the envelope correlation coefficient (ECC) and the diversity gain (DG) are perfect over the four frequency bands.

***Index Terms* –** MIMO antenna, diversity gain, quad-band antenna.

I. INTRODUCTION

The further Fifth Generation (5G) of mobile communications will make the spectrum allocation more efficient [1–4]. The unused millimeter-wave (mm-wave) electromagnetic spectrum (30–300 GHz) has attracted the attention and has been introduced as a candidate for the 5G mobile communication to enable multi-Gbit/s transmission rate exploiting the wide available bandwidth to meet the demands of the future applications which require high quality and low latency transmission and, hence, it is able to handle much greater capacity than the available 4G networks.

The mm-wave frequency bands centered at 28, 38, 60, and 73 GHz have been allocated for 5G mobile communications by International Telecommunications Union (ITU) [2]. Bands of 59–64 GHz are allocated by the Federal Communications Commission (FCC) as an unlicensed band for short range and wireless communications of high speeds [3, 4]. Some of the expected mm-wave bands recommended for 5G mobile communications are: 27.5 – 29.5 GHz, 33.4 – 36 GHz, 37 – 40.5 GHz, 42 – 45 GHz, 47 – 50.2 GHz, 50.4 – 52.6 GHz, and 59.3 – 71 GHz [1]. Significant attenuation is caused by oxygen molecules in the atmosphere to react with mm-wave signals and reaches up to 10 dB km^{-1} especially for the frequencies higher than 45 GHz. Due to this defect, it is not recommended to operate at frequencies that are much higher than 45 GHz for communication applications and long-range radar. For cellular mobile communications, the 28 GHz band is advantageous due to its low oxygen absorption rates unlike the higher mm-wave frequencies especially in 60 GHz band. The operation in the frequency bands higher than 45 GHz is recommended for short-range communications such as the Wi-Fi (with the WiGig standard in the 60 GHz band) [1, 5].

Due to the short wavelength of the mm-waves, the employment of spatial, pattern and polarization diversity techniques, such as Multi-Input Multi-Output (MIMO) is highly recommended for future generations of wireless communication systems that enable several Gb/s communication speed. In a MIMO antenna system, high radiation efficiency and high isolation between the multiple ports are required. Recently, a lot of research work has provided many designs for single-element antenna as well as MIMO antenna systems for 5G mobile handsets are demonstrated in this paragraph. For example, the work of [3] introduces a 60 GHz antenna consisting of H-shaped and E-shaped slots on the radiating patch. The work of [1] presents a dual-band circular microstrip patch antenna with an elliptical slot. This antenna operates at frequencies of 28 GHz and 45 GHz, with bandwidths of 1.3 GHz and 1 GHz. In [6], a printed

Submitted On: March 22, 2021
Accepted On: August 1, 2021
https://doi.org/10.13052/2021.ACES.J.361105

planar Yagi–Uda antenna is introduced for dual-band operation at 28/38 GHz. In the same work, a four-port MIMO antenna system is constructed using the proposed Yagi–Uda antenna arranged at the edges of the mobile handset to provide pattern and polarization diversities. In [7], a 28 GHz four-port MIMO antenna is proposed, where each antenna has an end-fire gain of about 10 dBi to provide pattern and polarization diversities. The work of [8] introduces a compact microstrip line fed dual-band printed four-port MIMO antennas resonating at 28 GHz and 38 GHz to provide spatial diversity. In [9], a compact dual-band (38/60 GHz) microstrip patch antenna is proposed for 5G mobile handsets. In [10], a dual-band (38/54 GHz) microstrip patch antenna and a 4-element array are proposed to achieve 12 dBi gain for 5G mobile data applications. The work of [11] presents a compact MIMO antenna design with polarization and pattern diversity operating in the frequency band (34–38 GHz).

A computationally efficient electromagnetic (EM) solver can be used to solve the antenna problems such as the Method of Moments (MoM) solution of the Electric Field Integral Equation (EFIE) [12–14], or the Finite-Difference-Time-Domain (FDTD) [15]. The commercially available CST® EM simulator combines the advantages of both techniques and is used in the present work for design and simulation of the proposed patch antenna and MIMO system.

The present work proposes two-port and four-port MIMO antenna systems for operation in the quad-band (28/45/51/56 GHz). The MIMO antenna performance including the return loss at each antenna port and the coupling coefficients between the different ports is investigated and shown to be suitable for 5G mobile communications. The radiation patterns produced when each port is excited alone are shown to be suitable for an efficient diversity scheme. The performance measures such as the envelope correlation coefficient (ECC) and diversity gain (DG) are evaluated showing excellent performance of the proposed MIMO antenna systems.

The remaining part of the present paper is organized as follows. Section II provides the reduced-size patch antenna design to radiate at 28 GHz. Section III proposes two- and four-port MIMO antenna systems that employ spatial diversity for enhancement of the wireless channel performance. Section IV gives a summary of the proposed antenna performance and comparisons with some published designs. Finally, Section V provides the most important conclusions for the present work.

II. CONSTRUCTION OF QUAD-BAND PATCH ANTENNA

The geometry of the proposed quad-band antenna operating at 28, 45, 51, and 56 GHz bands is presented in Figure 1. The antenna structure can be viewed as

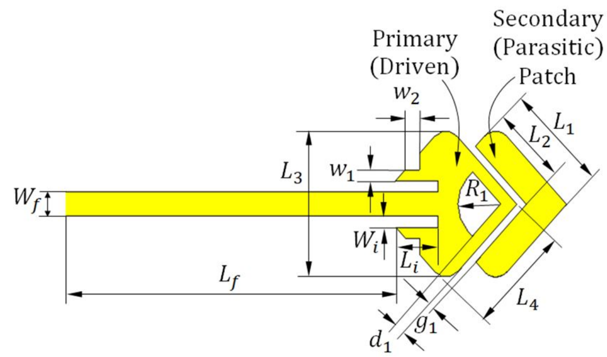

Fig. 1. Final geometry of the proposed quad-band patch antenna.

composed of primary and secondary patches. The primary patch is responsible for radiation at 28 GHz and is excited through a microstrip line with inset feed. The secondary patch is capacitively coupled to the primary patch and can be considered as parasitic radiator. The composite structure of the dual-patch antenna is responsible for radiation at the other three frequency bands around 45, 51, and 56 GHz.

First, a rhombic patch antenna with right-angle corners is designed to operate at 28 GHz. If this patch is used to radiate at its higher-order resonances the resulting radiation patterns and the gain may not be appropriate for mobile applications due to the existing nulls and sidelobes. This is because the size of the 28 GHz patch is electrically large at the mm-wave frequencies higher than 28 GHz. It is expected that the higher the order of the radiating mode the larger the number of the nulls and sidelobes of the radiation pattern. The relatively large size of the conducting patch surface allows the formation of surface current patterns that result in radiation patterns with a number of nulls and sidelobes depending on the radiating mode order. Thus, if the area of the conducting patch surface is reduced the formed surface current patterns may result in acceptable shape of the radiation pattern and the maximum gain. The reduction of the area of the conducting surface of a rhombic patch (originally designed to radiate at 28 GHz) is performed by making some cuts in its geometry to remove the regions of negligible magnitude of the patch surface current formed at 28 GHz. This modified patch should not badly affect its performance at the principal resonant frequency (28 GHz). The smaller size of the geometrically modified patch antenna allows the excitation of higher-order resonances at higher frequencies with significantly improved shapes of the radiation patterns and acceptable values of the gain. To get the higher-order resonances located at the desired frequency bands, a secondary patch is added as parasitic radiator to act as a reactively coupled element

Table 1: Dimensions of the proposed antenna

Dimension	L_1	L_2	L_3	L_4	w_1	w_2
Value (mm)	3.14	2.15	3.86	2.88	0.4	0.62
Dimension	$\mathrm{W_i}$	$\mathrm{L_i}$	$\mathrm{W_f}$	$\mathrm{L_f}$	$\mathrm{g_1}$	$\mathrm{d_1}$
Value (mm)	0.3	1.29	0.63	9.98	0.28	0.48

of the appropriate geometry. The load impedance caused by such reactively coupled patch controls the locations of the higher-order resonant frequencies.

The antenna is fabricated on Rogers RO3003 substrate of height $h = 0.25$ mm, dielectric constant $\varepsilon_r = 3$, and loss tangent tanδ =0.001. The substrate is placed over a solid ground plane. The feeding microstrip transmission line has a characteristic impedance of 50 Ω and dimensions of $W_f \times L_f$. An inset feed is used to match the antenna impedance to 50 Ω source. The corresponding values of the symbolic dimensional parameters of the antenna shown in Figure 7, are given in Table 1.

A. Numerical simulation and experimental assessment of the quad-band patch antenna

This section is concerned with the presentation of the results of numerical simulation and experimental measurements of the proposed quad-band microstrip patch antenna. To confirm the accuracy of the assessed performance for both the single-element and MIMO antennas, the experimental measurements are compared to those obtained by electromagnetic simulation using the commercially available CST® software package. The prototype shown in Figure 2 is fabricated for this purpose. The antenna size is compared to the size of a coin of standard one-inch diameter. Excluding the microstrip line feeder, the outer dimensions of antenna are 4×5 mm.

Fig. 2. Fabricated prototype of the proposed quad-band patch antenna with its size compared to a metal coin of standard size.

A1. Reflection coefficient at the antenna port

The vector network analyzer (VNA) of Rohde and Schwarz model ZVA67 is used for measuring the frequency response of the reflection coefficient magnitude $|S_{11}|$. The 1.85 mm end-launch connector from Southwest Microwave Inc. is used for connecting the antenna to the VNA as shown in Figure 3 (a).

The numerical simulation and experimental measurements for the frequency dependence of the magnitude of the reflection coefficient, $|S_{11}|$, are presented in Figure 4. The experimental measurements show good agreement with the numerical results obtained by the CST simulator. It is clear that the antenna has excellent impedance matching over four frequency bands centered at 28, 45, 51, and 56 GHz where the value of $|S_{11}|$ is less than −20 dB with respect to 50 Ω feeder.

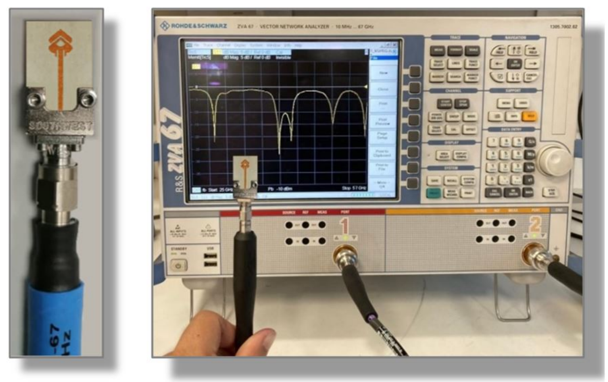

(a) (b)

Fig. 3. Measurement of the reflection coefficient $|S_{11}|$ of the proposed quad-band patch antenna: (a) The fabricated prototype is connected to the end launcher, (b) The antenna is connected to the VNA of Rohde and Schwarz model ZVA67.

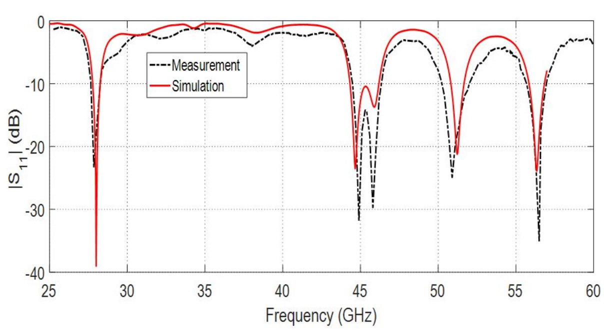

Fig. 4. Dependence of the reflection coefficient $|S_{11}|$ of the frequency for the proposed quad-band patch antenna.

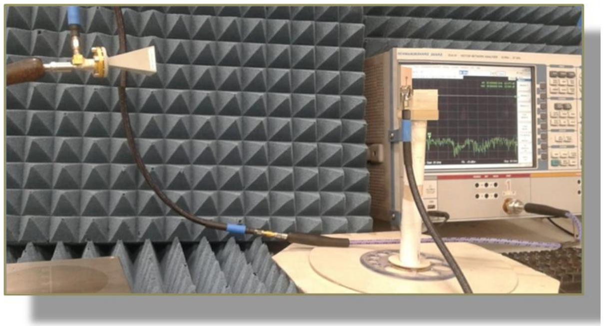

Fig. 5. Experimental setup for measuring the radiation pattern and gain of the quad-band antenna.

A2. Radiation patterns of the quad-band patch antenna

The experimental setup for measuring the radiation patterns and the maximum gain of the proposed antenna is presented in Figure 5. The VNA Rohde and Schwarz model ZVA67 operating in the two-port measurement mode is used for this purpose by measuring the transmission coefficient $|S_{21}|$ through the antenna under test and the reference-gain linearly-polarized horn antenna models LB-018400 (for $18-40$ GHz band) and LB-12-10-A (for $40-60$ GHz band). The radiation patterns of the proposed antenna at 28, 45, 51, and 56 GHz are presented in Figures 6, 7, 8, and 9, respectively, in the elevation planes $\phi=0^{\circ}$ and $\phi=90^{\circ}$. The experimental measurements show good agreement with the numerical results obtained by the CST simulation package. It is shown that the radiation patterns obtained at the four frequencies are acceptable and can be appropriate either for long-range or short-range communications.

III. MIMO ANTENNA SYSTEMS USING THE QUAD-BAND PATCH ANTENNA

In this section, two-port and four-port MIMO antenna systems are constructed using the quad-band patch antenna. Prototypes of the proposed MIMO antennas are fabricated for the purpose of experimental assessment. The results of numerical simulation are compared to those of experimental measurements for the purpose of confirmation.

A. Two-port MIMO antennas using the quad-band patch antenna

Prototypes are fabricated for two-port MIMO antenna systems constructed as two elements of the proposed quad-band patch antenna using different configurations. The patches of the first MIMO system are arranged side-by-side as shown in Figure 10 (a). The patches of the other MIMO system are arranged face-to-face as shown in Figure 11 (a). A prototype is fabricated for each type of the MIMO antenna systems as shown in

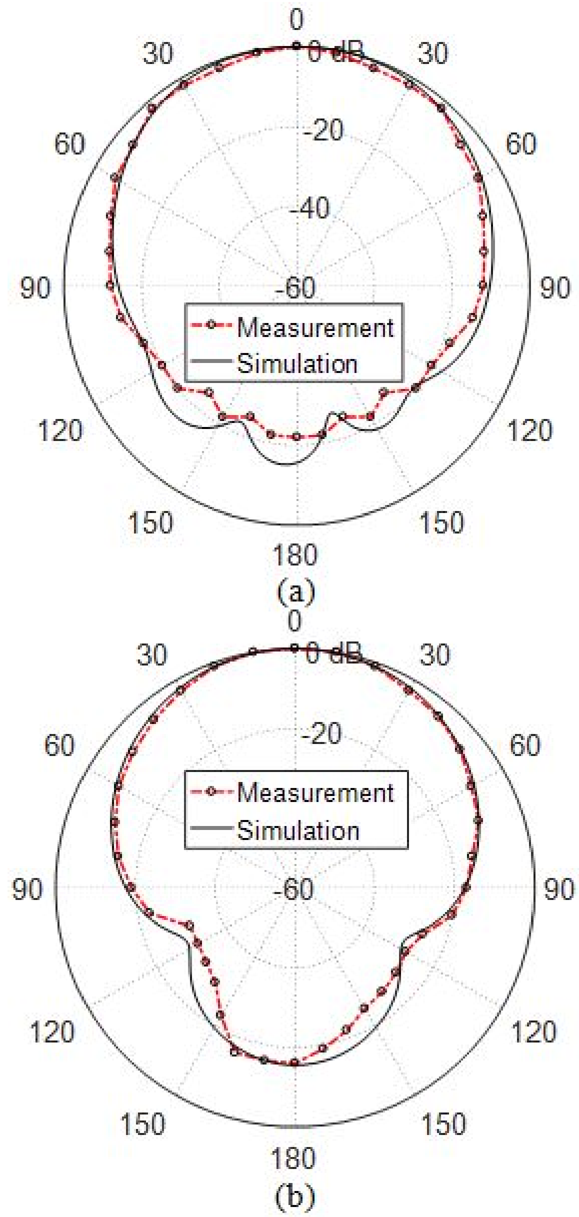

Fig. 6. Radiation patterns of the proposed quad-band patch antenna in the elevation planes (a) $\phi=0^{\circ}$ and (b) $\phi=90^{\circ}$ at 28 GHz.

Figures 10 (b) and 11 (b), respectively, and connected to a coaxial feeder using coaxial end launchers for experimental assessment. The VNA of Rohde and Schwarz model ZVA67 is used to evaluate the transmission coefficient S_{21} for the fabricated prototypes of the proposed MIMO antennas.

The frequency dependence of the coupling coefficient $|S_{21}|$ for each of the two-port MIMO configurations is presented in Figure 12. The experimental measurements show good agreement with the simulation results

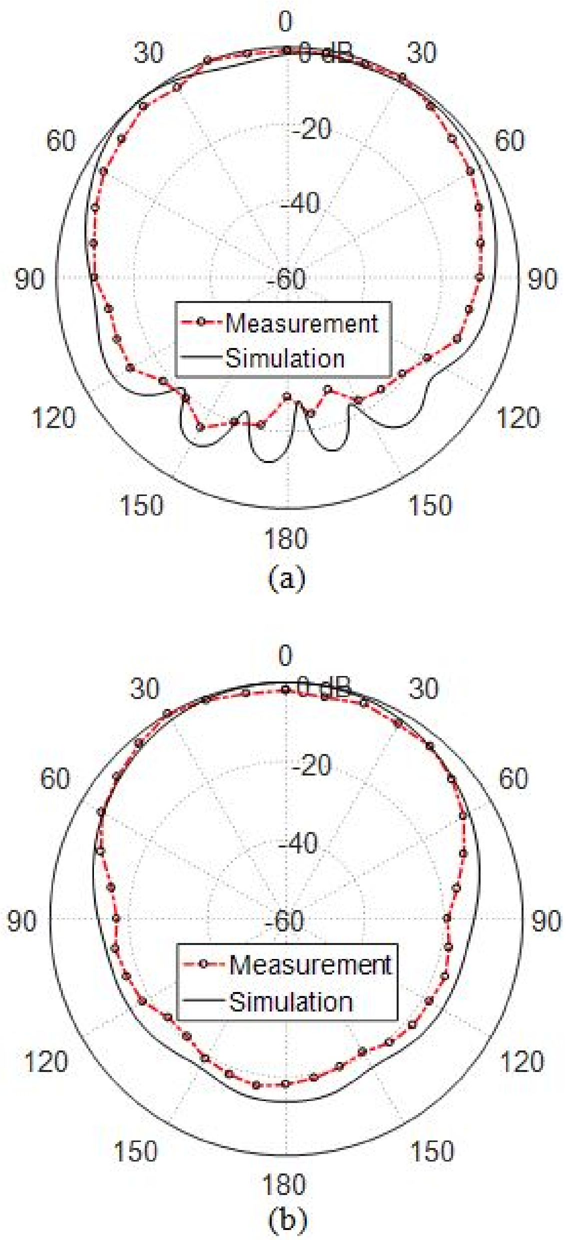

Fig. 7. Radiation patterns of the proposed quad-band patch antenna in the elevation planes (a) $\phi=0^{\circ}$ and (b) $\phi=90^{\circ}$, at 45 GHz.

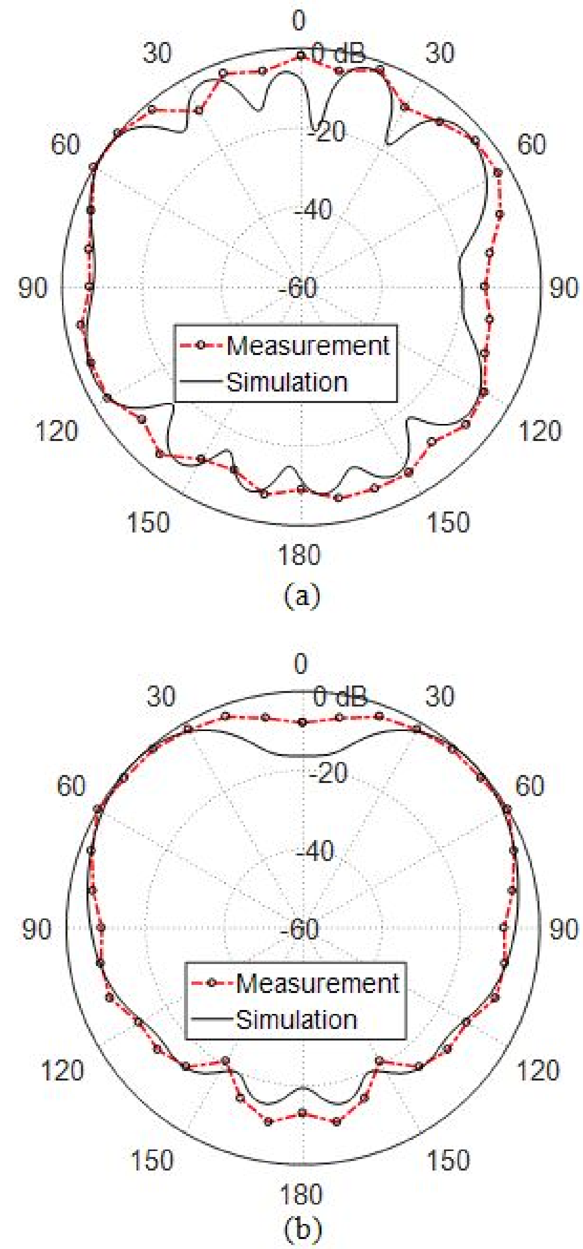

Fig. 8. Radiation patterns of the proposed quad-band patch antenna in the elevation planes $\phi=0^{\circ}$ and $\phi=90^{\circ}$ at 51 GHz.

and both of them show that the antennas of each MIMO configuration are very weakly coupled where $|S_{21}|$ does not exceed –25 dB over the entire frequency range. It is clear that the coupling coefficients, S_{21}, of the face-to-face MIMO configuration have larger magnitudes than those of the side-by-side MIMO configuration. This can be attributed to that the face-to-face configuration has narrower separation between the two antennas than that in the side-by-side configuration. Moreover, the face-to-face configuration allows higher rate of power transfer between the two antennas of the MIMO system because each antenna lies in the direction of the power flowing on the transmission line feeding the other antenna.

B. Four-port MIMO antenna system

To construct a four-port MIMO antenna system for operation at 28, 45, 51, and 56 GHz, four elements of the quad-band microstrip patch antenna with the dimensions listed in Table 1 are arranged as shown in the geomet-

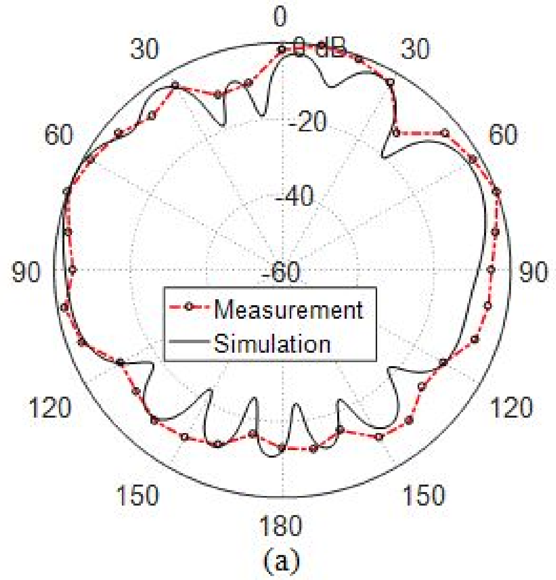

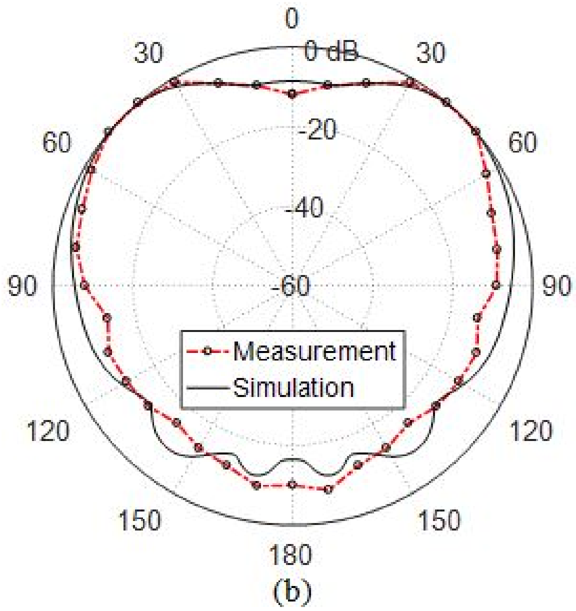

Fig. 9. Radiation patterns of the proposed quad-band patch antenna in the elevation planes $\phi=0^{\circ}$ and $\phi=90^{\circ}$ at 56 GHz.

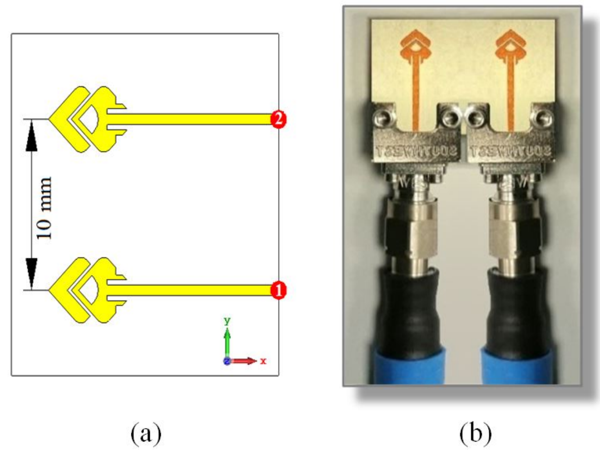

Fig. 10. Two-port MIMO antenna system constructed as two elements of the quad-band patch arranged side-by-side; (a) Model in the CST simulator, (b) Fabricated prototype is connected to end launchers and coaxial cables for measurements.

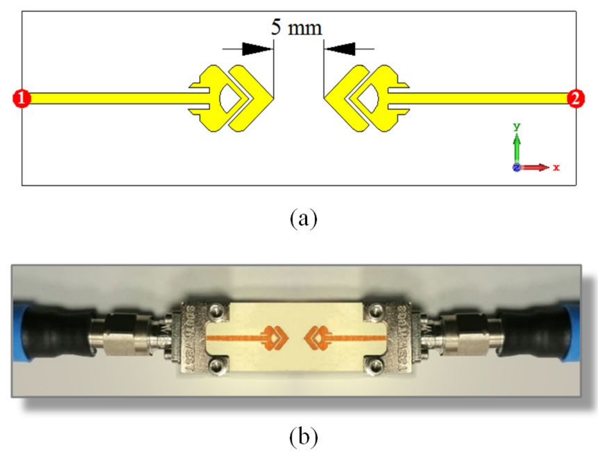

Fig. 11. Two-port MIMO antenna system constructed as two elements of the quad-band patch arranged face-to-face; (a) Model in the CST simulator, (b) Fabricated prototype is connected to end launchers and coaxial cables for measurements.

ric model presented in Figure 13 for the MIMO antenna in the CST simulator. The separations between the four antennas are set so as to achieve the spatial diversity required for the target 5G applications. This design has total dimensions of 42×20 mm^2. Such a MIMO antenna system can be practically suitable to be manufactured and integrated on a printed electronic board of a mobile handset.

The prototype shown in Figure 14 is fabricated for the purpose of experimental assessment of the performance of the proposed quad-band four-port MIMO antenna system. The VNA Rohde and Schwarz model ZVA67 is used for measuring the frequency response of the reflection coefficients S_{21}, S_{43}, S_{31}, S_{42}, S_{41}, and S_{32}. Four 1.85 mm end-launch connectors from Southwest Microwave Inc. are used for connecting the corresponding antenna ports to the VNA whereas the other two ports are connected to matched (50 Ω) loads as shown in Figure 14.

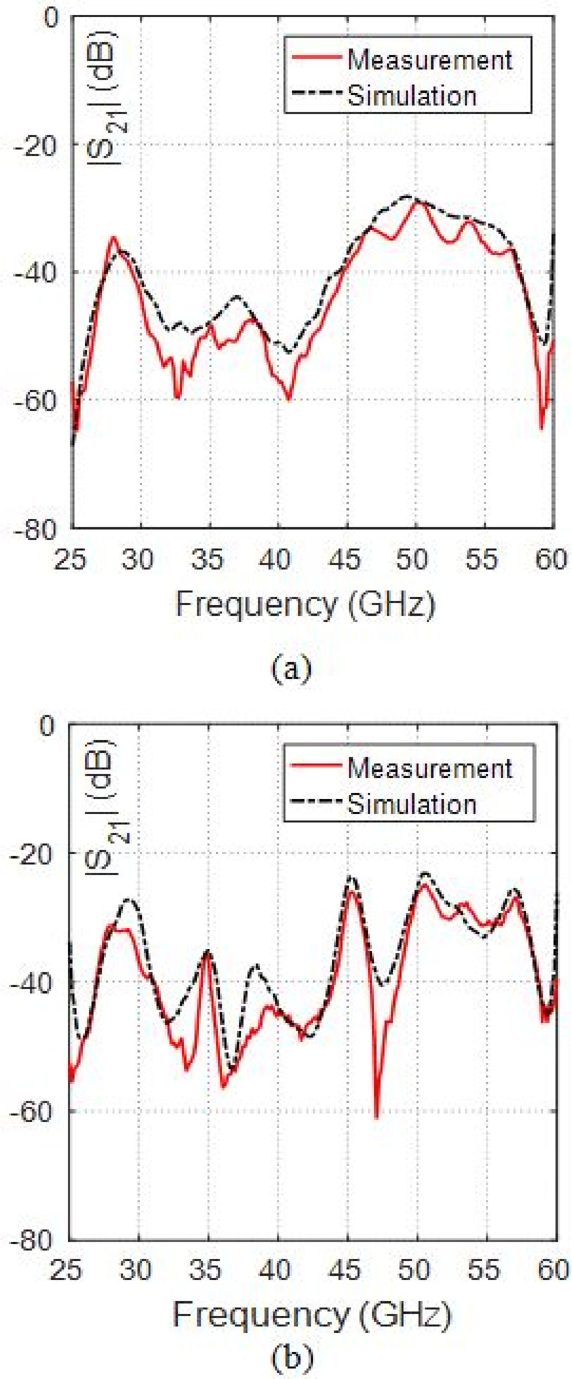

Fig. 12. Frequency responses of the coupling coefficient $|S_{21}|$ for the two-port MIMO configurations: (a) Side-by-Side configuration shown in Figure 10, (b) Face-to-face configuration shown in Figure 11.

B1. Coupling coefficients, envelop correlation coefficients, and diversity gain

The simulation results and experimental measurements describing the frequency dependence of the magnitudes of the scattering parameters S_{21}, S_{43}, S_{31}, S_{42}, S_{41}, and S_{32} representing the different coupling coefficients for the proposed quad-band four-port MIMO antenna system are presented in Figure 15. The simulation results appear to be in agreement with the results of the experimental measurements, and both of them show low values of the coupling coefficients.

The dependencies of the ECC and the DG of the proposed four-port MIMO antenna system on the frequency are presented in Figure 16. It is shown that at the operating frequencies 28, 45, 51, and 56 GHz and over the width of each of the four bands, the ECC is very low (almost 0) and, consequently, the DG is very high (almost 10). This can be considered as the optimum performance of MIMO antenna system. It should be noted that the relative positions of the antennas in the pair of ports (1,2) are the same as those in the pair of ports (3,4); this leads to identical ECC and DG as shown in Figure 16. The same applies for the antenna pairs (1,3) and (2,4) and, also, for the antenna pairs (1,4) and (2,3).

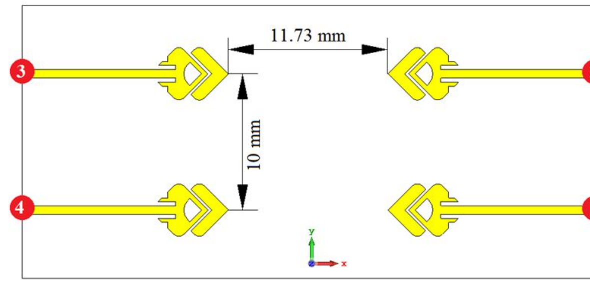

Fig. 13. Design of the quad-band four-port MIMO antenna system (total dimensions 42×20 mm^2) proposed for mobile handsets.

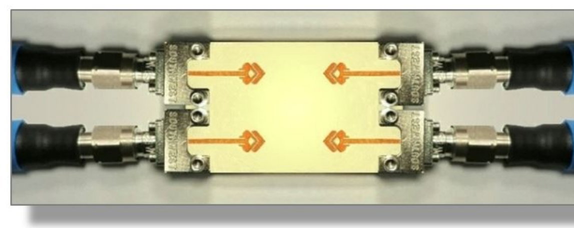

Fig. 14. Fabricated quad-band four-port MIMO system.

B2. Radiation patterns of the four-port MIMO antenna system

The radiation patterns produced at 28, 45, 51, and 56 GHz by the four-port MIMO antenna system, shown in Figure 14, are presented in Figures 17, 18, 19, and 20, respectively when the MIMO antenna system is excited at the different ports. The produced radiation patterns appear to be suitable for most

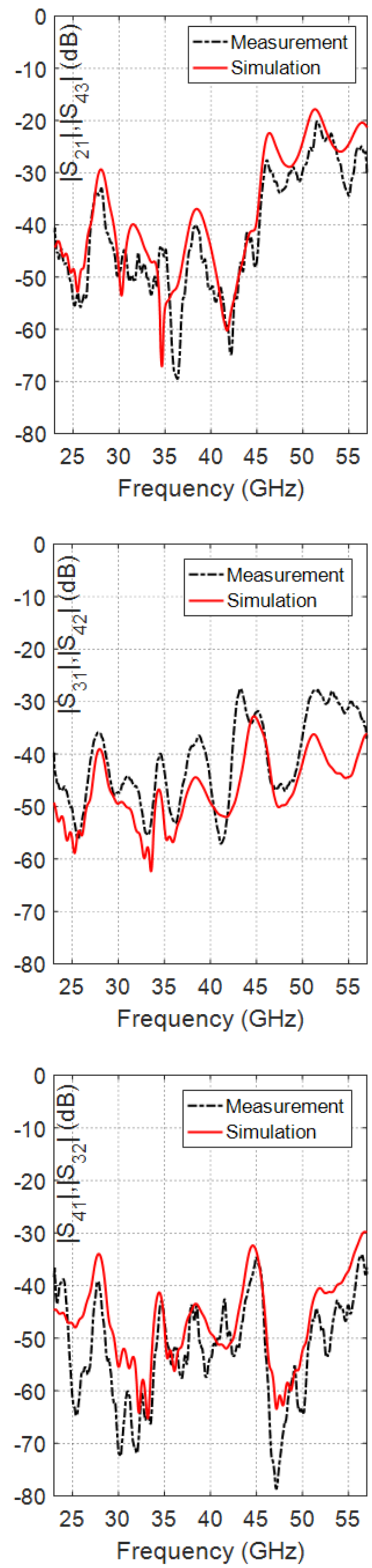

Fig. 15. The scattering parameters S_{21}, S_{43}, S_{31}, S_{42}, S_{41}, and S_{32} representing the different coupling coffiecients for the proposed MIMO antenna system.

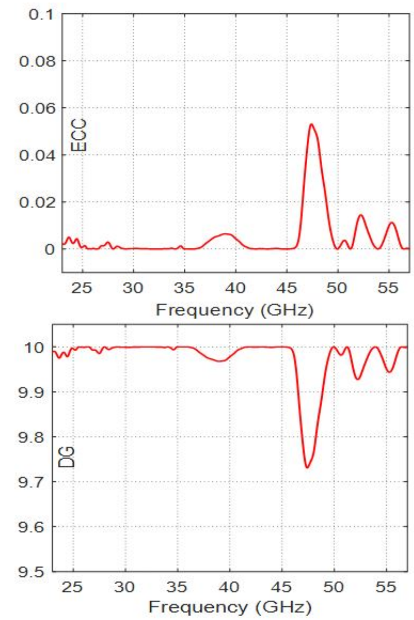

Fig. 16. Dependence of the ECC and DG on the frequency for the proposed quad-band four-port MIMO antenna system for ports (1,2) and (3,4).

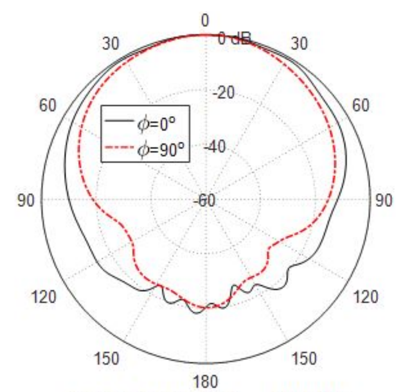

Port 1 or Port 2, $f = 28$ GHz

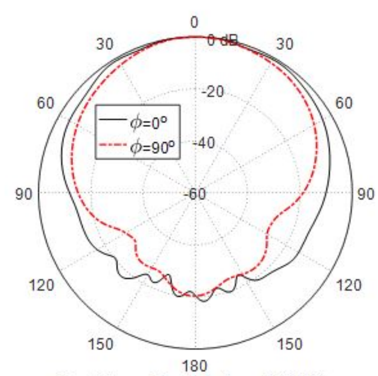

Port 3, or Port 4, $f = 28$ GHz

Fig. 17. Radiation patterns in the elevation planes for the quad-band MIMO antenna system at 28 GHz when excited at the indicated ports.

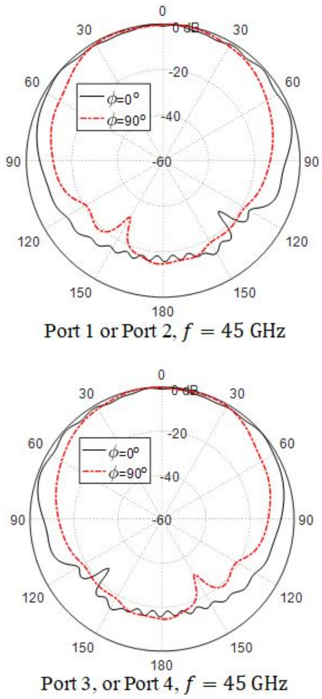

Port 1 or Port 2, f = 45 GHz

Port 3, or Port 4, f = 45 GHz

Fig. 18. Radiation patterns in the elevation planes for the quad-band MIMO antenna system at 45 GHz when excited at the indicated ports.

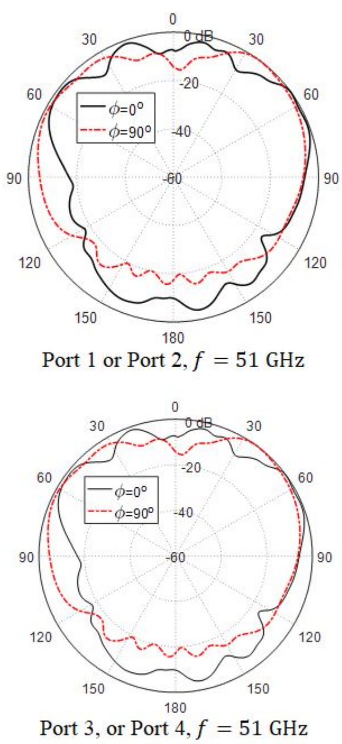

Port 1 or Port 2, f = 51 GHz

Port 3, or Port 4, f = 51 GHz

Fig. 19. Radiation patterns in the elevation planes for the quad-band MIMO antenna system at 51 GHz when excited at the indicated ports.

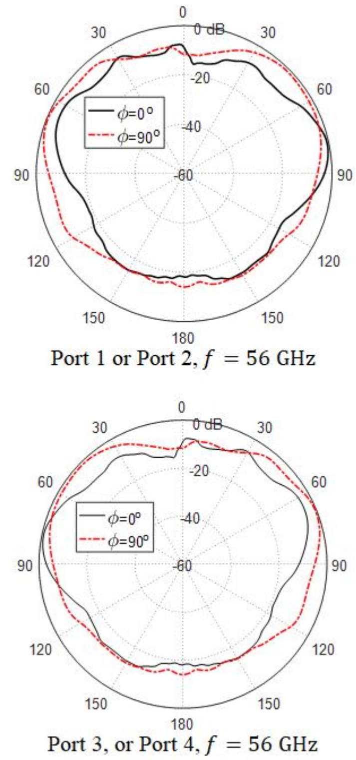

Port 1 or Port 2, f = 56 GHz

Port 3, or Port 4, f = 56 GHz

Fig. 20. Radiation patterns in the elevation planes for the quad-band MIMO antenna system at 56 GHz when excited at the indicated ports.

of the future wireless applications relevant to the mobile handsets. More specifically, the radiation patterns produced at 28 and 45 GHz are ripple-free and appear to be more appropriate for long-range cellular mobile networks. On the other hand, the radiation patterns obtained at 51 and 56 GHz have some ripples and may be more appropriate for short-range communications.

IV. SUMMARY OF THE PROPOSED ANTENNA PERFORMANCE

This section is concerned with providing a summary of the most important performance metrics for the quad-band patch antenna as well as the MIMO antenna systems proposed in the present work. Table 2 gives a summary of the single-element as well as the MIMO antenna performance at the four operational frequencies. The radiation efficiency is the percentage of radiated power to the total power accepted at the antenna port. The radiated power is the accepted power minus the Ohmic losses in the conducting and dielectric parts of the antenna. The accepted power is equal to the input power minus the reflected power at the antenna port. However, the radiation efficiency listed in Table 2 is obtained by the commercially available CST studio suite® version 2017. Table 3 gives comparative performance among

Table 2: Achieved frequency bands (obtained experimentally) by the proposed quad-band patch antenna and the corresponding gain and radiation efficiency

Fc (GHz)	Fs (GHz)	Fe (GHz)	Bandwidth (GHz)	Gain (dBi)	Radiation Efficiency
28	27.70	28.30	0.60	7.30	86.5%
45	44.50	46.50	2.00	7.03	87.5%
51	50.20	52.00	1.80	7.20	89.2%
56	55.70	57.00	1.30	8.03	90.0%

Table 3: Comparison with other published designs of mm-wave antennas

Work	Center Frequencies (GHz)	Gain (dBi)	Patch Dimensions (mm)
[8]	28, 38	7.2, 9.2	4.6×2.8
[16]	28,38	3.7, 5.1	3.7×5.1
[1]	38, 45	7.6, 7.2	6.0×6.0
[10]	38, 54	6.9, 7.4	6.3×6.0
[Present]	28, 45, 51, 56	7.3, 7.03, 7.2, 8.03	4.0×5.0

some mm-wave patch antennas available in some recent literature and the antenna proposed in the present work.

V. CONCLUSION

A novel design for a compact-size quad-band microstrip patch antenna is introduced for the 5G mobile communications in the frequency bands 28, 45, 51, and 56 GHz. The proposed quad-band antenna has primary and secondary patches which are reactively coupled and well designed to produce appropriate radiation patterns and good impedance matching in the four frequency bands of operation. Two-port and four-port MIMO antenna systems that employ the quad-band microstrip patch are investigated for operation in the 5G mobile handsets. The performance of both the quad-band patch antenna and the MIMO antenna systems are assessed including the return loss at each antenna port and the coupling coefficients between the different ports. It is shown that the simulation results agree with the experimental measurements and both show good performance. The bandwidths achieved around 28, 45, 51, and 56 GHz are, respectively, 0.6, 2.0, 1.8, and 1.3 GHz. It is shown that the ECC and the DG are perfect over the four frequency bands for the four-port MIMO antenna system.

REFERENCES

[1] K. Muhammad Irfan, A. Sohail, U. Khan, Z. Barki, and G. Witjaksono, "Elliptical slot circular patch antenna array with dual band behaviour for future 5G mobile communication networks," *Progress in Electromagnetics Research*, vol. 89, pp. 133-147, 2019.

[2] Ş. Cihat, T. Ozturk, and M. Tahir Güneşer, "A single band antenna design for future millimeter wave wireless communication at 38 GHz," *European Journal of Engineering and Formal Sciences*, vol. 2, no. 2, pp. 35-39, 2018.

[3] S. Jyoti and S. K. Agarwal, "Design a single band microstrip patch antenna at 60 GHz millimeter wave for 5G application," *2017 International Conference on Computer, Communications and Electronics (Comptelix)*, pp. 227-230, 2017.

[4] H. Wonbin, K.-H. Baek, and S. Ko, "Millimeter-wave 5G antennas for smartphones: overview and experimental demonstration," *IEEE Transactions on Antennas and Propagation*, vol. 65, no. 12, pp. 6250-6261, 2017.

[5] J. G. Andrews, S. Buzzi, W. Choi, S. V. Hanly, A. Lozano, A. C. K. Soong, and J. C. Zhang, "What will 5G be?," *IEEE Journal on Selected Areas in Communications*, vol. 32, no. 6, pp. 1065-1082, 2014.

[6] A. E. Farahat and K. F. A. Hussein, "28/38 GHz dual-band Yagi-Uda antenna with corrugated radiator and enhanced reflectors for 5G MIMO antenna systems," *Progress in Electromagnetics Research C*, vol. 101, pp. 159-172, 2020.

[7] W. Zamir, M. P. Abegaonkar, and S. K. Koul, "A 28-GHz antenna for 5G MIMO applications," *Progress in Electromagnetics Research*, vol. 78, pp. 73-79, 2018.

[8] H. M. Marzouk, M. I. Ahmed, and A.-E. Hamied Shaalan, "Novel dual-band 28/38 GHz MIMO antennas for 5G mobile applications," *Progress in Electromagnetics Research C*, vol. 93, pp. 103-117, 2019.

[9] M. H. Sharaf, A. I. Zaki, R. K., Hamad, and M. M. Omar, "A novel dual-band (38/60 GHz) patch antenna for 5G mobile handsets," *Sensors*, vol. 20, no. 9, pp. 2541, 2020.

[10] D. Imran, M. M. Farooqi, M. I. Khattak, Z. Ullah, M. I. Khan, M. A. Khattak, and H. Dar, "Millimeter wave microstrip patch antenna for 5G mobile communication," *2018 International Conference on Engineering and Emerging Technologies (ICEET)*, pp. 1-6, 2018.

[11] L. He-Sheng and Y.-C. Lin, "Millimeter-wave MIMO antennas with polarization and pattern diversity for 5G mobile communications: the corner design," *2017 IEEE International Symposium on Antennas and Propagation & USNC/URSI National Radio Science Meeting*, pp. 2577-2578, 2017.

[12] K. F. A. Hussein, "Fast computational algorithm for EFIE applied to arbitrarily-shaped conducting surfaces," *Progress in Electromagnetics Research*, vol. 68, pp. 339-357, 2007.

[13] K. F. A. Hussein, "Efficient near-field computation for radiation and scattering from conducting surfaces of arbitrary shape," *Progress in Electromagnetics Research*, vol. 69, pp. 267-285, 2007.

[14] K. F. A. Hussein, "Accurate representation of excitation and loading for arbitrarily shaped antennas composed of conducting surfaces in the method of moments," *Progress in Electromagnetics Research*, vol. 36, pp. 151-171, 2012.

[15] E. M. Eldesouki, K. F. A. Hussein, and A. M. El-Nadi, "Circularly polarized arrays of cavity backed slot antennas for X-band satellite communications," *Progress in Electromagnetics Research*, vol. 9, pp. 179-198, 2008.

[16] W. Ahmad and W. T. Khan, "Small form factor dual band (28/38 GHz) PIFA antenna for 5G applications," *2017 IEEE MTT-S International Conference on Microwaves for Intelligent Mobility (ICMIM)*, pp. 21-24, Mar. 2017.

M. Abo El-Hassan received her B.Sc., M.Sc., in Communications and Electronic Engineering, Communications Engineering from Menoufa University, Egypt, in 2007 and 2014 respectively. She received the PhD 2020. She is currently researcher at the Department of Microwave Engineering at the Electronics Research Institute.. Her current research interests include RFID, areas in Antennas, Chipless tags, SAR, Beam shaping. She has published more than 18 papers in international, regional and local scientific journals and conferences.

Asmaa E. Farahat received her B.Sc. and M.Sc. in the Department of Biomedical engineering, Faculty of Engineering, Cairo University, 2002 and 2006, respectively. She received the PhD 2012, Ain Shams University. She is currently associate professor at the Department of Microwave Engineering at the Electronics Research Institute. She has work experience in scientific research for about 17 years. She has published more than 28 papers in international, regional and local scientific journals and conferences. She has worked as secondary investigator for three research projects. Her research interests are in the areas of antennas, electromagnetic wave propagation, risk assessment of human exposure to microwave radiation, remote sensing systems, and radar systems.

Khalid F. A. Hussein received his B.Sc., M.Sc. and Ph.D. degrees in the Department of Electronics and Electrical Communications, Faculty of Engineering, Cairo University, 1990, 1995 and 2001, respectively. He is currently a professor at the Department of Microwave Engineering at the Electronics Research Institute. He has work experience in scientific research for more than 30 years. He has teaching experience in engineering colleges in many universities for more than 20 years. He has supervised more than seventy doctoral and master theses. He has published more than 100 papers in international, regional and local scientific journals and conferences. He has served as Head of Microwave Engineering Department at the Electronics Research Institute for up to four years. He has been a member of the Egyptian Space Program (currently the Egyptian Space Agency) for more than eight years. He has worked as Principal Investigator for four research projects and Head of Research Group in four other research projects. He designed and implemented several satellite antennas between prototypes and finished products. He has provided scientific consultations and conducted field measurements related to the design and distribution of mobile communication base station antennas for good signal coverage in behalf of many Egyptian and international companies. His research interests are in the areas of antennas, electromagnetic wave propagation, risk assessment of human exposure to microwave radiation, optical communications, photonics, quantum computing, radar systems, particularly ground penetrating radar (GPR), synthetic aperture radar (SAR), and remote sensing systems.

Slit-Loaded Hexagonal Patch for Body Area Network Applications at 5.8 GHz

Shaktijeet Mahapatra and Mihir Narayan Mohanty

ITER, Siksha O' Anusandhan deemed to be University, Odisha, India
shaktijeetmahapatra@gmail.com, mihir.n.mohanty@gmail.com

Abstract **–** Increasing population and expanding remote healthcare monitoring needs have provided an impetus to the research and development of wireless devices. The quest for smaller antennas for wireless devices has led to the design of the proposed antenna. In this work, we present a slit-loaded hexagonal patch antenna for body area network applications. The antenna has been designed on a 0.193λ ×0.193λ×0.03λ FR4-epoxy substrate. The radiator patch has two parallel slits. The antenna resonates at 5.8 GHz (ISM band) with a wide bandwidth of 1.15 GHz. A maximum gain of 5.81 dB and a front-to-back ratio of 11.93 dB is observed at 5.8 GHz. Radiation efficiency is observed to be 72.3%. The measured return loss values show a close agreement with the simulated results. Specific absorption rate (SAR) analysis on a simplified 2/3$^{\text{rd}}$ muscle model shows an average SAR of 0.5633 W kg^{-1}, due to the use of a full-ground plane. The simulations were done in ANSYS HFSS. The antenna is suitable for on-body communications.

Index Terms **–** hexagonal patch, inset-fed, ISM band, miniature, slit-loaded.

I. INTRODUCTION

Antennas are the reason that the market for wireless communication devices thrives. A device without an antenna cannot communicate with other devices on a physical level. Antennas are not only responsible for launching or receiving the electromagnetic waves into the space but also for filtering and providing the passive gains to the signals. The antennas have to be designed carefully to meet the requirements of the communication system they are part of.

With the increase in the number of wireless handheld devices for day-to-day monitoring for health, security, business, and military purposes, the need to connect to data-collecting devices has also risen [1, 2]. Therefore, the requirement for antennas that can be easily integrated with such devices has also risen. However, the design of antennas for portable devices has its own set of challenges. The antenna needs to be small and yet operate at ISM bands. The specific absorption rate (SAR) should remain within safe limits to avoid unnecessary heating of the tissues. The bandwidth should be wide enough to resist interference from other devices and the detuning effect of proximity to the body. Due to the less area available for the antenna, the antenna geometry, the feeding technique, and the corresponding matching technique have to be chosen carefully.

In this paper, we propose a miniaturized hexagonal microstrip patch radiator. The choice of hexagonal shape was driven by the fact that it offers longer electrical path length, and slightly better bandwidths and gains than rectangular or circular shaped radiators. The hexagonal shape also utilizes available areas more efficiently than rectangular and circular patches. The radiator has two parallel slits which bring down the resonant frequency to include the 5.8 GHz ISM band. The slits are the cuts made from the edges, and when placed close to the feed point, load the antenna with the capacitance [3]. Both the slots and the slits have been used to increase the bandwidth and lower the resonant frequency [4]. The choice of this band is motivated by the fact that the band at 2.45 GHz is already congested, and the 5.8 GHz band is relatively free and can support higher data rates [5]. The ground plane has a small circular slot for enhancing the bandwidth of the antenna. The antenna is fed through one of the edges by a microstrip line at an inset. The inset feeding helps in matching the port impedance with the input impedance of the antenna. This technique is very easy to implement and does not demand extra area outside the patch [6]. Feeding through the edge ensures better isolation between the antenna and the subject. The antenna offers very wide bandwidth and a moderate gain. SAR of the antenna is also well within limits. The antenna has been simulated using the ANSYS HFSS platform.

In the subsequent sections, some of the related works, antenna design, and results are presented and discussed. The conclusion section summarizes the work in this paper and the referred works are cited in the reference section.

II. RELATED WORKS

Antennas designed for wearable purposes should not only be compact but also have smaller back lobes.

Submitted On: July 27, 2021
Accepted On: September 15, 2021
https://doi.org/10.13052/2021.ACES.J.361106

Smaller back lobes mean lesser exposure of living tissue to the electromagnetic radiations, and hence lower SARs.

A metamaterial-based superstrate for enhancing gain by 12 dBi and bandwidth by 355 MHz at 5.8 GHz in [7]. A 2×2 element patch antenna array for unmanned aerial vehicles on a PCB substrate and a gain of 6.2 dB was obtained in [8]. designed A lightweight and optically transparent antenna using VeilShield for conducting parts and polydimethylsiloxane (PDMS) operating at 5.8 GHz was designed in [9] and a gain of 3.35 dB was reported. In [10], an antenna loaded with an artificial magnetic conductor working at 5.8 GHz for ingestible endoscopy on polyimide was designed and a gain of 1.64 dBi was reported. A MIMO antenna at 5.8 GHz with a metasurface structure for enhancing gain was designed in [11]. A dual-band antenna with electromagnetic bandgap (EBG) structure on F4B substrate was used in [12] with a gain of 9.1 dBi at 5.8 GHz. A high-gain hexagonal patch antenna for V2V communication was designed in [13]. Slot-loaded hexagonal microstrip antenna designed on FR4 by [14] operated in multiple bands. A button antenna for WBAN applications covering 2.45 and 5.8 GHz with dual-polarization by [15]. A patch antenna array designed in [16], was loaded with split ring resonators and via holes resulting in dual-band operations. Nitinol-strip–based reconfigurable fractal antenna using artificial neural network was designed in [17] that operated in 2.4 GHz and 5.2 GHz bands and four configurable modes. Antennas for wearable applications with wide bandwidth and low SAR are presented in [18, 19].

From the above literature, we find that the hexagonal antennas have not been explored for body area network. In this work, we emphasize on the reduced size that can perform better as compared to earlier designs in terms of the gain and the bandwidth. Therefore, the design is proposed and explained in the following sections. It also performs well for the SAR reduction. Finally, the comparative results are exhibited in result section.

III. ANTENNA DESIGN

The antenna has been designed on an FR4-epoxy substrate measuring 10 × 10 × 1.6 mm^3. Mechanical strength, suitable RF response, resistance to humidity and temperature, and easy availability were important factors in deciding the substrate. The dielectric constant of FR4 remains fairly close to 4.35 even up to 7 GHz [20].

The radiator patch is hexagonal. The hexagon-shaped patches have better area utilization than rectangular or circular patches. Moreover, they provide a longer radiating edge and hence can be easily used for lower frequencies. For the computation of resonant frequency for any TM_{mn} mode for a hexagonal patch with a side a, an empirical equation has been developed by curve fitting the theoretical and experimental results. The equation uses an effective value of side length a_e, to compute the resonant frequency. As a regular hexagon can be equally divided into equilateral triangles, therefore starting equations are modified versions of those used for equilateral triangular patches [21].

$$f_{mn} = \frac{c \times \sqrt{m^2+mn+n^2}}{(a_e \times \sqrt{\varepsilon_r})}, \tag{1}$$

where a_e is empirically given by

$$a_e = a\left[1+7.962\frac{h_s}{a} - 12.853\frac{h_s}{a\sqrt{\varepsilon_r}} + 16.436\frac{h_s}{a\varepsilon_r} + 6.182\left(\frac{h_s}{a}\right)^2 - 9.802\frac{1}{\sqrt{\varepsilon_r}}\left(\frac{h_s}{a}\right)^2\right]. \tag{2}$$

For 5.8 GHz and TM10 mode, a hexagonal patch of side length 15.48 mm is required. As the objective of this work is to design a miniaturized antenna, a patch with a side of 4.5 mm is chosen.

In order to meet the objective of the resonant frequency, we need to increase the capacitance of the patch antenna by increasing the electrical path length. This can be done by introducing a slit in the patch [3]. Two slits were introduced to bring down the resonant frequency to 5.8 GHz. The increase of path length produced by two slits together is larger than one slit. This allowed for the miniaturization of the antenna.

For maximum power transfer from the port to the antenna, the return loss has to be reduced. To reduce the return loss at the same frequency, we have to increase the degree of matching between the port and the antenna. The easiest method to do this is to use the inset feed technique. This introduces matching impedance. On both sides of the feedline, a gap of 0.35 mm is introduced. The feedline intersects the patch at 1.5 mm from the edge. A longer feedline introduces inductive impedance and the gaps introduce capacitive impedance. This transforms the input impedance of the patch to the characteristic impedance of the lumped port.

For the computation of the input impedance, we approximate the hexagon to the circumscribing circle of radius, r_c. If the side of a hexagon is a, then $r_c = a$. The effective radius, r_e, of the assumed circumscribing circle can be expressed as [23]:

$$r_e = r_c\left[1+\frac{2h_s}{\pi r_c \varepsilon_r}\left\{\ln\left(\frac{r_c}{2h_s}\right) + (1.4\varepsilon_r+1.768) + \left(\frac{h_s}{r_c}\right)(0.267\varepsilon_r+1.649)\right\}\right]^{-\frac{1}{2}}. \tag{3}$$

The input impedance, Z_{in} of the assumed circular disk circumscribing the hexagonal patch is the load impedance for (4). Z_{in} at any radial distance $\rho = \rho 0$

for TM11 mode for a circular disk is given by [22]

$$Z_{\text{in}}(\rho=\rho_0)=\frac{J_1^2(k\rho_0)}{(G_t \times J_1^2(kr_e)}, \tag{4}$$

where k is the wavenumber, $J_1(x)$ is the Bessel's function of the first kind of order 1, and G_t is the total conductance. The total conductance, G_t is given by

$$G_t = G_{\text{rad}} + G_c + G_d, \tag{5}$$

The conductance between the patch and the full ground plane, G_{rad} is given by:

$$G_{\text{rad}} = \frac{(k_0 r_e)^2}{480}\int_0^{\frac{\pi}{2}} [J_{02}'^2 + \cos^2\theta J_{02}^2]\, sin\theta\, d\theta. \tag{6}$$

The ohmic conductance that accounts for the ohmic loss, G_c is given by

$$G_c = \frac{\varepsilon_{m0}\pi(\pi\mu_0 f_r)^{-\frac{3}{2}}\left[(kr_e)^2 - m^2\right]}{4h^2\sqrt{\sigma}}. \tag{7}$$

The losses in dielectric are accounted by G_d, given by:

$$G_d = \frac{\varepsilon_{m0}\tan\delta\left[(kr_e)^2 - m^2\right]}{4\mu_0 h f_r}, \tag{8}$$

where $\varepsilon_{m0} = 2$ for $m = 0$, $\varepsilon_{m0} = 1$ for other m, and f_r is the resonant frequency of the *mn0* mode.

The dependence of Q factor, Q_T on bandwidth, BW is given by [23]:

$$BW = \frac{VSWR - 1}{Q_T\sqrt{VSWR}}, \tag{9}$$

where Q_T is given by

$$Q_T = \left[\tan\delta + \frac{1}{h\sqrt{\pi f \mu_0 \sigma}} + \frac{hf\mu_0 (k_0 r_e)^2 I_1}{30\left[(k_0 r_e)^2 - n^2\right]}\right]^{-1}, \tag{10}$$

and I_1 is an integral given by,

$$I_1 = \int_0^{\frac{\pi}{2}}\left[J_n'^2(k_0 r_e \sin\theta) + \frac{\cos^2\theta J_n^2(k_0 r_e \sin\theta)}{(k_0 r_e \sin\theta)^2}\right]\sin\theta\, d\theta. \tag{11}$$

To enhance the bandwidth of the antenna, we have to reduce the Q-factor of the antenna slightly. For this, we introduce a circular slot of 1 mm diameter in the ground plane.

The finalized design and dimensions of the antenna are shown in Figure 1.

Design steps

1. On a substrate measuring 10 × 10 × 1.6 mm^3, a hexagon-shaped patch of copper is created. Each side of the patch measures 4.5 mm.
2. A microstrip feed line of 3 mm is provided at one of the edges of the patch.
3. A lumped port with a characteristic impedance of 50? is assigned at the other end of the microstrip feed line.
4. Slits, 0.5 mm wide, are cut from the patch.
5. Slits, 0.35 mm wide and 1.5 mm in length, are cut on both sides of the feed line in the patch.

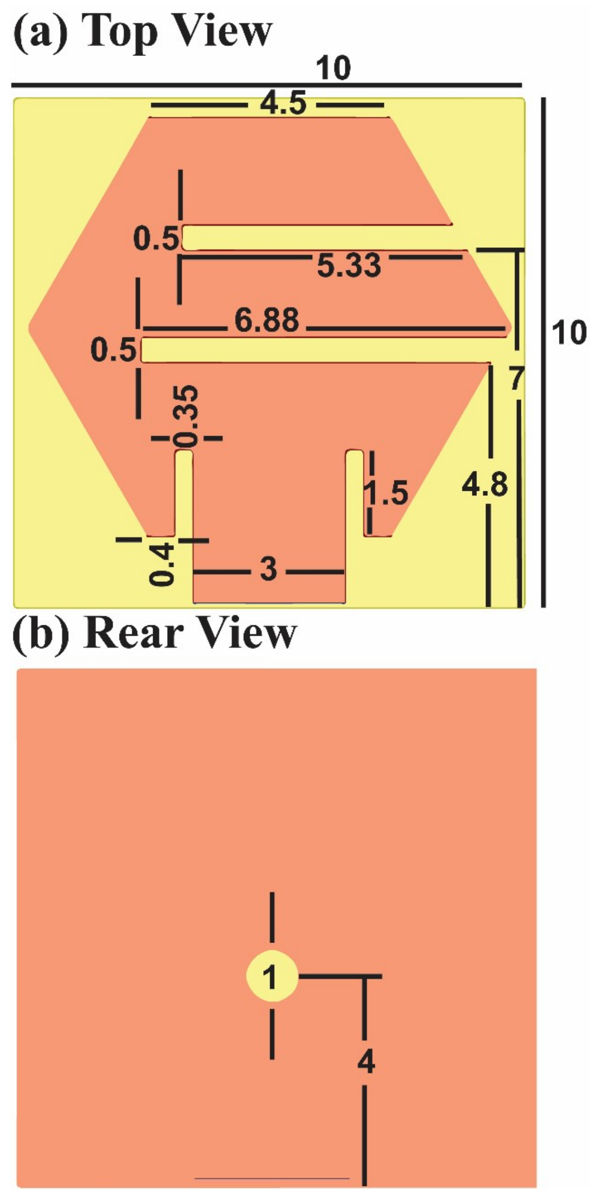

Fig. 1. Front and rear view of the proposed antenna (All dimensions are in mm).

6. A circular slot of 1 mm diameter is cut from the ground plane for enhancing the bandwidth.

IV. RESULTS AND DISCUSSIONS

The objective of this paper is to design a miniature antenna for body area network applications working at 5.8 GHz, with an impedance bandwidth of more than 1 GHz.

We start with the hexagonal patch with a side of 4.5 mm. The antenna in stage 1 in Figure 2 (a) has the resonant frequency occurring at 24.9 GHz. In stage 2, the first slit is introduced as shown in Figure 2 (b). Due to

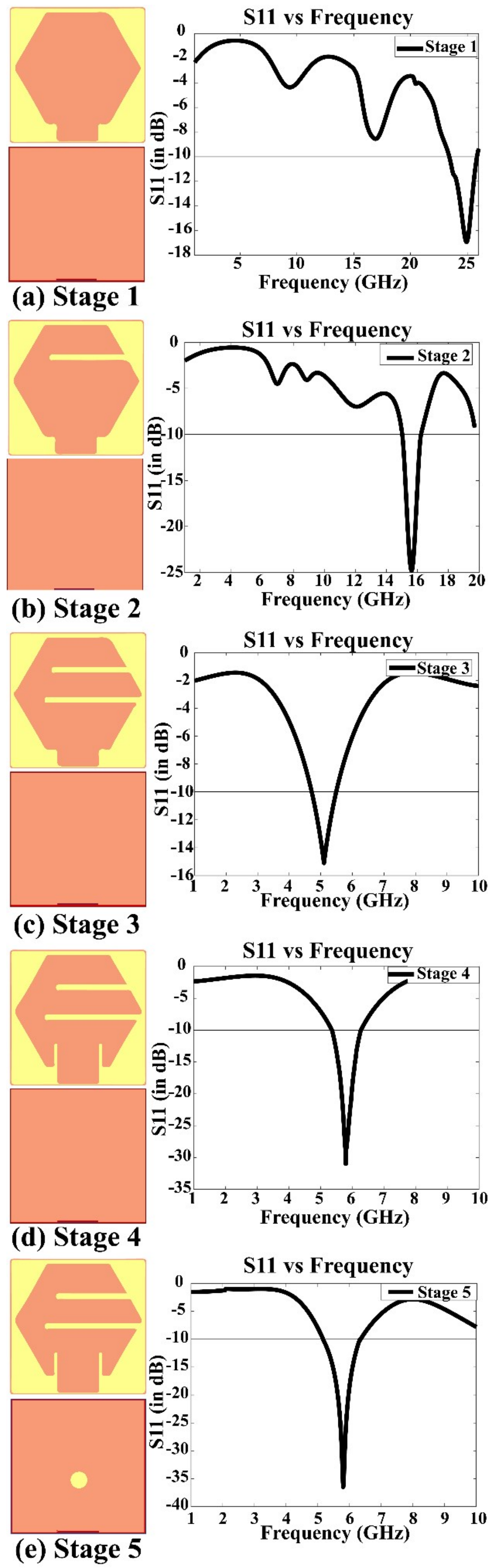

Fig. 2. Design stages of the antenna.

the increased capacitance, the resonant frequency of the stage 2 antenna comes down to 15.6 GHz. However, to further reduce the resonant frequency close to the band of interest, we introduce the second slit closer to the feed. From the return loss of antenna of stage 3 shown in Figure 2 (c), it can be seen that the resonant frequency (5.1 GHz) comes close to the required frequency, 5.8 GHz. The return loss is –15 dB. For better performance, the matching with the port should be improved. For improving the match, the inset feeding technique is used. The resulting antenna in stage 4 now resonates at 5.8 GHz with an improved return loss of –31.15 dB as can be seen from Figure 2 (d). To further enhance the bandwidth and the gain of the antenna, a circular slot is introduced in the ground plane near the feed point of the patch. The resulting antenna of stage 5 and its corresponding return loss plot is shown in Figure 2 (e). A comparison of gains of antennas of stage 4 and stage 5 is given in Figure 3. The addition of the slot in the ground plane increased the gain by at least 4 dB in the broadside direction. It is also observed that the back lobes also reduce considerably.

The antenna of stage 5 was finalized as it met our requirements and the antenna was fabricated. The fabricated antenna is shown in Figure 4. Figure 5 shows S11 or reflection coefficient plots of the simulated and the fabricated versions. The return loss at 5.8 GHz for the simulated design is –36.5 dB and for the fabricated antenna is –31.23 dB. This frequency is considered for body area network communications. The antenna covers the ISM band and is capable of handling high data rate communications. The bandwidth of the simulated design is observed to be 1.17 GHz and that of the fabricated one is found to be 1.06 GHz.

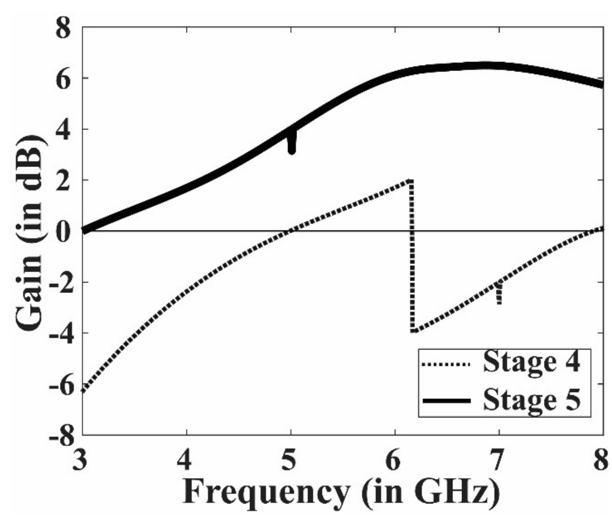

Fig. 3. Gain vs frequency plot of antenna in stage 4 and stage 5.

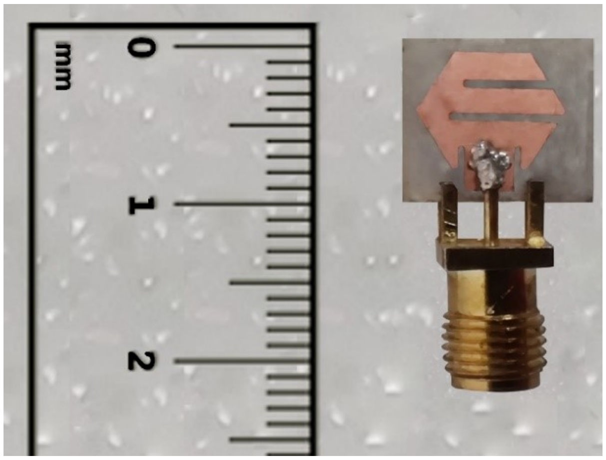

Fig. 4. Fabricated antenna.

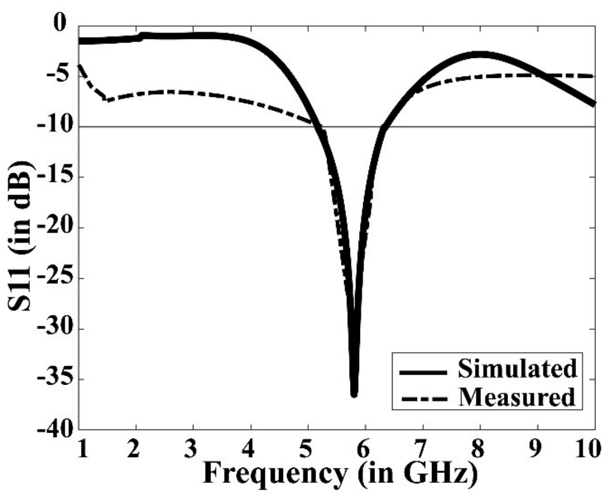

Fig. 5. A comparison of return loss characteristics of the simulated and fabricated versions.

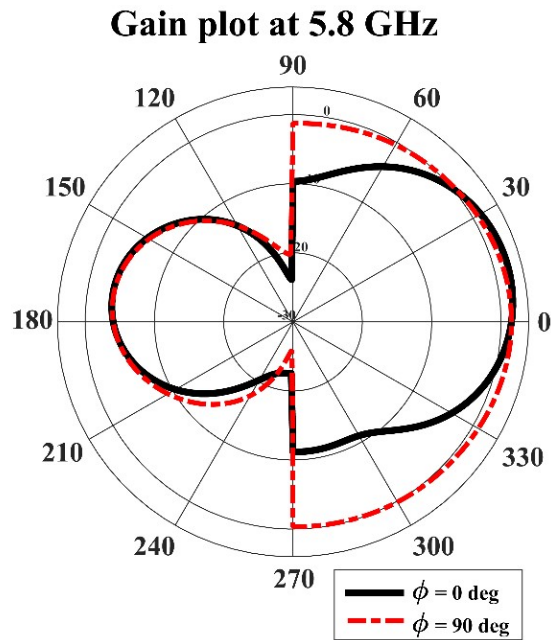

Fig. 6. Gain plot of the proposed antenna.

Table 1: Summary of results

Parameters	Simulated	Measured
Freq [GHz]	5.8	5.8
S11 [dB]	–36.5	–31.25
Bandwidth (< –10 dB)	1.17	1.06
Peak Gain [dB]	5.8	
Radiation Efficiency [%]	72.3	
Front-to-Back Ratio	11.92	

Figure 6 shows the gain of the antenna in directions at phi equal to 0 and 90 degrees, corresponding to H-plane and E-plane respectively. It can be observed seen that in the broadside direction, the gain is 5.81 dB. It can also be observed that due to the ground plane the back radiation has been reduced. A high gain is one of most characteristics for an antenna designed for wearable purposes as it compensates for various losses to some extent. The front-to-back ratio (FBR) can be computed from the gain plot by taking the ratio of maximum gain to the gain in opposite direction. *FBR, in dB = maximum gain (dB) – gain in exactly opposite direction (dB)*. The maximum gain is 5.81 dB and the gain in the opposite direction is –6.12 dB. Thus, the FBR is 11.93 dB. This is an important result as it shows how much of the radiation is in the forward direction. This gives the idea of radiation being directed away from the human body. The radiation efficiency was found to be 72.3% as a result of better matching.

Figure 7 presents the radiation pattern in the E-plane and H-plane of the antenna measured at 5.8 GHz, with 10 dBm input power. Figure 8 (a) shows the electric field distribution and 8(b) shows the surface current distribution at 5.8 GHz. It can be observed that the slits disturbed the surface current distribution resulting in better bandwidth. A high value of the electric field can be observed near the slits. This indicates a better power transfer toward the radiating edges and a reason for the better efficiency of the antenna. Table 1 summarizes the findings of this work.

Figure 9 shows the simulated evaluation of the antenna to find the SAR. The antenna was evaluated on a simplified 4-layer 2/3rd muscle model. In the 2/3rd muscle model, the muscle occupies 2/3rd of the volume of the tissue. Such tissues are mostly found on arms and thighs.

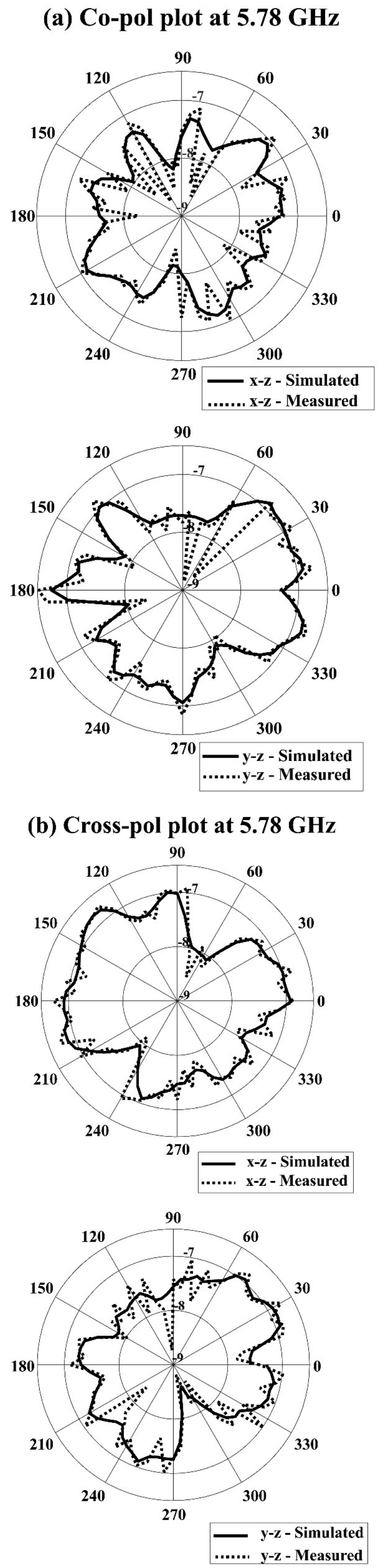

Fig. 7. Radiation pattern plots at 5.8 GHz.

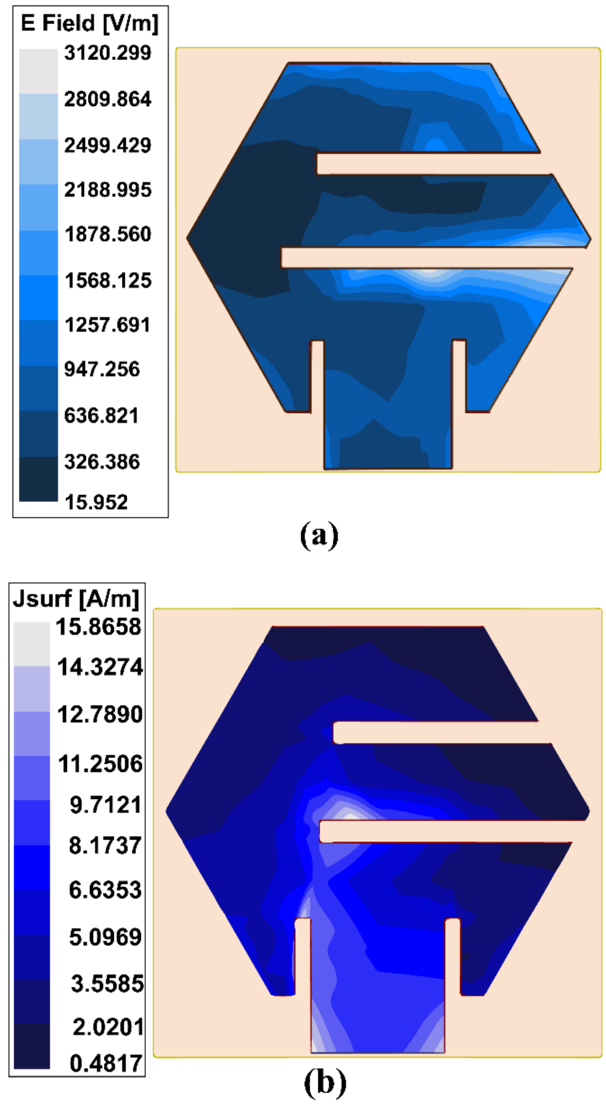

Fig. 8. (a) Electric field distribution; (b) Surface current distribution.

These areas are generally where the wireless devices for off-body communication are usually placed. Skin, fat, muscle, and bone constitute the layers of the model and each layer acts as frequency-dependent lossy dielectrics. The dielectric constants ($\varepsilon_r(\omega)$) and loss tangents of the layers were computed at 5.8 GHz using following equations and given in Table 2 [24]:

$$\varepsilon_r(\omega) = \varepsilon_\infty + \sum_{m=1}^{4} \frac{\Delta\varepsilon_m}{1+(j\omega\tau_m)^{1-\alpha_m}} + \frac{\sigma_i}{j\omega\varepsilon_0}, \qquad (12)$$

$$\tan^{-1}\delta = \frac{Im(\varepsilon)}{Re(\varepsilon)}\ . \qquad (13)$$

The antenna was placed on the model and simulated results were observed. The living tissues absorb electromagnetic waves and heat up. SAR represents the degree

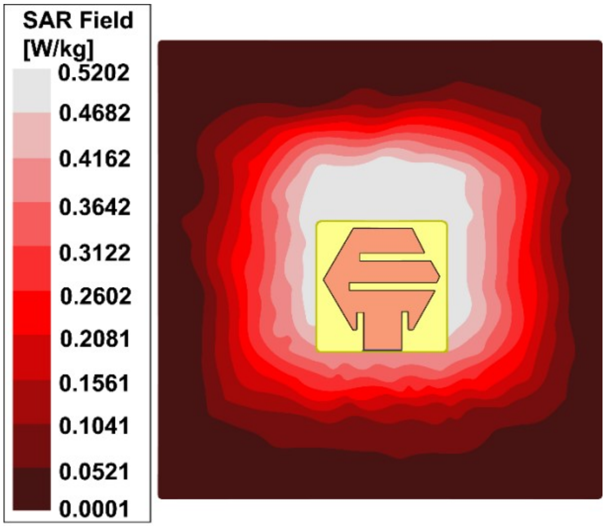

Fig. 9. Evaluation of SAR at 5.8 GHz.

Table 2: Dielectric constants and loss tangents of various layers at 5.8 GHz

Layers	Skin	Fat	Muscle	Bone
Dielectric constant	36.9549	5.0905	51.7447	10.3329
Loss Tangent	0.3281	0.2592	0.3516	0.3723

of heating produced by electromagnetic waves emitted by the antenna. The threshold value of SAR is 1.6 W kg^{-1} [25]. The SAR value of the antenna was observed to be 0.5633 W kg^{-1}. This further makes the antenna suitable for body area network applications. A comparison with some previous works has been presented in Table 3.

Table 3: Performance comparison with some previous works

Ref.	Antenna/ Substrate	Antenna Structure Dimensions [mm]	Frequency [GHz]/ Gain [dB]/ SAR[W kg^{-1}]
[10]	AMC-loaded radiator/ Polyimide	$4.6 \times 7.6 \times 0.15$	5.8/1.64/0.82505
[11]	MIMO antenna with a dipole, J-shaped balun, and metasurface/ RT5880	$140 \times 3.7 \times 35.075$	5.8/9.5/NA
[12]	Monopole with EBG/F4B	$67.71 \times 64.71 \times 10$	5.8/9.1/0.212
[14]	Slotted hexagonal patch/FR4	35×30	2.4/1.63; 5.03/1.38; 8.67/2.95;
[15]	Button antenna/Rogers RT 6006	Radius 9.4 mm and 1.27 mm thickness	2.45/2.2/1.04 5.8/8.6/0.29
[16]	Array of patch loaded with SRR and via-holes/ FR4	7.5 cm $\times$ 7.5 cm $\times$ 1.48 mm	2.45/5.6 5.0/11.4
[17]	Fractal antenna/ Nitinol-strip	3000 sq µm	2.5/22; 5.5/–6.99
This Work	Inset-fed hexagonal patch with slits	$10 \times 10 \times 1.6$	5.8/5.81/0.5633

V. CONCLUSIONS

In this work, a miniaturized hexagonal patch antenna is proposed. The miniaturization was possible due to two slits. The gain enhancement was done by a circular slot on the ground plane. The antenna is fed by a microstrip line at an inset and produced better matching results. The antenna operated in the frequency range 5.12–6.34 GHz and resonated at 5.8 GHz. The measured value of the antenna agrees closely with the simulated results. The gain was observed to be 5.81 dB and the front-to-back ratio to be 11.92 dB at 5.8 GHz. The SAR analysis yielded an average SAR of 0.5633 W kg^{-1}. These characteristics make the antenna suitable for body area communications at high data rates.

REFERENCES

[1] A. Y. I. Ashyap, S. H. B. Dahlan, Z. Z. Abidin, M. I. Abbasi, M. R. Kamarudin, H. A. Majid, M. H. Dahri, M. H. Jamaluddin, and A. Alomainy, "An overview of electromagnetic band-gap integrated wearable antennas," *IEEE Access*, vol. 8, pp. 7641-7658, Jan. 2020. doi: 10.1109/ACCESS.2020.2963997.

[2] S. Mahapatra and M. N. Mohanty, "A review on state-of-art techniques of antennas for body area networks," *Int. J. Sensors, Wirel. Commun. Control*, vol. 11, no. 6, pp. 604-618, Jul. 2021. doi: 10.2174/2210327910999201228152543.

[3] K. Siakavara, "Methods to design microstrip antennas for modern applications," in *Microstrip Antennas*, N. Nasimuddin, Ed. InTech, pp. 173-236, 2011.

[4] S. Mahapatra and M. N. Mohanty, "Investigation on effects of slotting in a microstrip-fed rectangular patch antenna," *in 2018 2nd International Conference on Data Science and Business Analytics (ICDSBA)*, pp. 241-244, Dec. 2018.

[5] S. K. Behera and N. C. Karmakar, "Wearable chipless radio-frequency identification tags for biomedical applications: A Review [Antenna Applications Corner]," *IEEE Antennas Propag. Mag.*, vol. 62, no. 3, pp. 94-104, Jun. 2020. doi: 10.1109/MAP.2020.2983978.

[6] S. Mahapatra and M. N. Mohanty, "Simulation and feed analysis of microstrip antenna for UWB communication," *in IEEE Conf. ICCPCT*, pp. 18-20, Mar. 2014.

[7] C. Arora, S. Pattnaik, and R. Baral, "Performance enhancement of patch antenna array for 5.8 GHz Wi-MAX applications using metamaterial inspired technique," *AEU-International J. Electron. Commun.*, vol. 79, pp. 124-131, May 2017.

[8] N. Majidi, G. G. Yaralioglu, M. R. Sobhani, and T. Imeci, "Design of a quad element patch antenna at 5.8 GHz," *2018 Int. Appl. Comput. Electromagn. Soc. Symp. Denver, ACES-Denver 2018*, pp. 1-2, Mar. 2018. doi: 10.23919/ROPACES.2018.8364309.

[9] A. S. Sayem and K. P. Esselle, "A unique, compact, lightweight, flexible and unobtrusive Antenna for the Applications in Wireless Body Area Networks," *in 2019 13th International Conference on Signal Processing and Communication Systems (ICSPCS)*, pp. 1-4, Dec. 2019.

[10] T. M. Neebha, M. Nesasudha, and D. K. Janapala, "A stable miniaturised AMC loaded flexible monopole antenna for ingestible applications," *Comput. Biol. Med.*, vol. 116, p. 103578, Jan. 2020. doi: 10.1016/j.compbiomed.2019.103578.

[11] L. N. Nguyen, "A MIMO antenna with enhanced gain using metasurface," *Appl. Comput. Electromagn. Soc. J.*, vol. 36, no. 4, pp. 458-464, Apr. 2021. doi: 10.47037/2020.ACES.J.360412.

[12] C. Wang, L. Zhang, S. Wu, S. Huang, C. Liu, and X. Wu, "A Dual-band monopole antenna with ebg for wearable wireless body area networks," *Appl. Comput. Electromagn. Soc. J.*, vol. 36, no. 1, pp. 48-54, Jan. 2021. doi: 10.47037/2020.ACES.J.360107.

[13] H. Singhal, S. Ashwin, V. Sharma, J. Prajapati, and M. D. Upadhayay, "High gain hexagonal patch antenna for V2V communication," *2020 7th Int. Conf. Signal Process. Integr. Networks, SPIN 2020*, pp. 687-691, Feb. 2020. doi: 10.1109/SPIN48934.2020.9071270.

[14] A. O. Fadamiro, J. D. Ntawangaheza, O. J. Famoriji, Z. Zhang, and F. Lin, "Design of a multiband hexagonal patch antenna for wireless communication systems," *IETE J. Res.*, pp. 1-8, Oct. 2019. doi: 10.1080/03772063.2019.1664340.

[15] X. Yin, S. J. Chen, and C. Fumeaux, "Wearable dual-band dual-polarization button antenna for WBAN applications," *IEEE Antennas Wirel. Propag. Lett.*, vol. 19, no. 12, pp. 2240-2244, Oct. 2020. doi: 10.1109/LAWP.2020.3028868.

[16] C. Arora, S. S. Pattnaik, and R. N. Baral, "Dual band microstrip patch antenna array loaded with split ring resonators and via holes," *AEU - Int. J. Electron. Commun.*, vol. 93, no. June, pp. 253-260, Sep. 2018. doi: 10.1016/j.aeue.2018.06.016.

[17] S. Ambigapathy and J. Paramasivam, "2.4 GHz and 5.2 GHz frequency bands reconfigurable fractal antenna for wearable devices using ANN," *Appl. Comput. Electromagn. Soc. J.*, vol. 36, no. 3, pp. 354-362, Mar. 2021. doi: 10.47037/2020.ACES.J.360315.

[18] S. Mahapatra, L. P. Mishra, and M. N. Mohanty, "Design of circular patch antenna with modified ground structure for body area communication," *in 2020 International Conference on Communication and Signal Processing (ICCSP)*, pp. 512-514, Jul. 2020.

[19] S. Mahapatra, J. Mishra, and M. Dey, "A dual-band inset-fed octagonal patch antenna for wearable applications," *in Advances in Intelligent Computing and Communication*, Springer, pp. 699-706, May 2021.

[20] J. Paleèek, M. Vestenickı, P. Vestenickı, and J. Spalek, "Frequency dependence examination of PCB material FR4 relative permittivity," *IFAC Proc. Vol.*, vol. 46, no. 28 Part 1, pp. 90-94, Jan. 2013. doi: 10.3182/20130925-3-CZ-3023.00020.

[21] K. Guney, "Input impedance of an equilateral triangular microstrip antenna," *Mediterr. Electrotech. Conf. - MELECON*, vol. 2, no. 5, pp. 414-417, Apr. 1994. doi: 10.1109/melcon.1994.381070.

[22] C. A. Balanis, *Antenna Theory - Analysis and Design*, 3rd Edition. John Wiley and Sons, 2005.

[23] R. Garg, P. Bhartia, I. Bahl, and A. Ittipiboon, *Microstrip Antenna Design Handbook*. Artech House, 2001.

[24] P. S. Hall and Y. Hao, *Antennas and Propagation for Body-Centric Wireless Communications*. Artech House, 2012.

[25] IEEE_SCC39, *IEEE Standard for Safety Levels with Respect to Human Exposure to Electric, Magnetic, and Electromagnetic Fields, 0 Hz to 300 GHz - Corrigenda 2*, vol. 2019, 2020.

Shaktijeet Mahapatra is currently working as an assistant professor in the Department of Electronics and Communication Engineering, Institute of Technical Education and Research (FET), Siksha 'O' Anusandhan (Deemed to be University), Bhubaneswar, Odisha. He received his M. Tech. degree in VLSI and Embedded System from the Biju Patnaik University of Technology, Odisha. He is currently pursuing his Ph.D. degree from Siksha ‘O’ Anusandhan (deemed to be University). His research interests include Antenna Design and IoT.

Mihir Narayan Mohanty is currently working as a Professor in the Department of Electronics and Communication Engineering, Institute of Technical Education and Research (FET), Siksha ‘O’ Anusandhan (Deemed to be University), Bhubaneswar, Odisha. He received his Ph.D. degree in Applied Signal Processing from the Biju Patnaik University of Technology, Odisha and his M. Tech. degree in Communication System Engineering from the Sambalpur University, Sambalpur, Odisha. He is the fellow of IE (I), and IETE. He is a senior member of IEEE and member of many professional societies including IET, ACES etc. He has more than 25 years of teaching and research experience. He has published more than 500 papers in different Journals, Conferences including Book Chapters. He has authored two books and edited two conference proceedings. He is the successive reviewer of manuscripts from IEEE, Elsevier, Springer, IGI Global, etc. His areas of research interests include Applied Signal and Image Processing, Wireless Communication, Antenna, and Intelligent Signal Processing.

Switched Beam Antenna System for V2V Communication in 5G Applications

Allam M. Ameen[1,2], Mohamed I. Ahmed[2], Hala Elsadek[2], and Wagdy R. Anis[1]

[1]Electronics and Communication Department, Faculty of Engineering, Ain Shams University, Cairo 11566, Egypt
allamameen@eri.sci.eg, wagdyanis51@yahoo.com

[2]Microstrip Department, Electronics Research Institute, New Nozha, Cairo 11843, Egypt
miahmed@eri.sci.eg, helsadek@eri.sci.eg

***Abstract* –** In this paper, a switched beam antenna system consists of four Vivaldi antennas for vehicle-to-vehicle communication is presented. The proposed design is realized on a substrate material of "Rogers 5880" with $\varepsilon_r = 2.2$, $\tan\delta = 0.002$, and 0.508-mm substrate thickness. The antenna is designed to operate at a center frequency of 28 GHz with operating bandwidth of 1.463 GHz. An overall realized gain of 9.78 dBi is achieved at the intended center frequency. The proposed antenna is designed and simulated using CSTMWS. It is also fabricated using photolithography techniques and measured using R&S vector network analyzer. Good agreement is obtained between both CSTMWS and measured results.

***Index Terms* –** Vivaldi antenna, intelligence transportation system (ITS), vehicle-to-vehicle (V2V) communication, switched beam antenna, 5G applications.

I. INTRODUCTION

Intelligence transportation system (ITS) is built depending on dedicated short range communication (DSRC) technology which presents a high reliability and a fast data transmission [1–7]. This system improves the road safety to avoid car accidents and reduce the traffic jam by sending all the information about the road to the drivers to make decisions. There are four classifications of V2X wireless communications: vehicle-to-vehicle (V2V), vehicle-to-personal (V2P), vehicle-to-infrastructure (V2I), and vehicle-to-network (V2N) [8–14]. A low-profile monopolar was introduced and two antenna designs were presented: low-profile and flush-mounted [15]. Both antennas were surrounded by a thin plastic radome. Four-element monocone broadband antenna for V2X wireless communication is introduced [16]. Three antennas were proposed and discussed in the cavity to offer a significant room for antennas and radio frequency [17]. A low-profile wideband monopolar antenna size is reduced by adding four tapered slots which make it applicable for vehicles and helmets [18]. Three antenna arrays consisting of 16 patches in each array were developed to operate at 61 GHz [19].

There are many techniques for beam switching that can be used to reconfigure the radiated beams [20, 21]. Some of them are traditional such as digital beamforming [22], butler matrix [23], and phased array antennas [24]. Narrow bandwidth, bulky structure, and complicated beamforming networks are disadvantages of these methods at microwave frequencies. Another method to satisfy the beam switching configuration is by using PIN diodes which are operated by DC controlled circuit [25–28]. In [25], RF switch controlled by a microcontroller to feed a 2 × 2 array antenna is introduced.

In this paper, four switched beam Vivaldi antennas with single port are designed, simulated, and fabricated for V2V wireless communication system. The proposed antenna provides a full 360^o coverage area with high gain and large distance compared with an omnidirectional one. The antenna is designed to operate at a frequency of 28 GHz for mm-wave and 5G applications.

II. PROPOSED ANTENNA DESIGN

Figure 1 introduces the configuration of the proposed antenna structure. Four symmetric microstrip Vivaldi antennas are placed at different directions with an angle of 90^o between each two antennas to cover the full 360^o area. Five PIN diodes are used to connect the single port of the structure to each antenna. A controlled circuit is applied to switch the PIN diodes to ON/OFF states. Details of the single patch antenna and the overall structure are described below.

A. Single microstrip Vivaldi antenna

Figure 2 shows the design of the proposed Vivaldi antenna and its structure. The structure of the proposed antenna is realized by subtraction of an elliptical shape from the rectangular patch antenna on each side. The antenna is placed on a substrate of type "Roger 5880" with $\varepsilon_r = 2.2$, $\tan\delta = 0.002$, and 0.508-mm thickness. The overall antenna size for a single patch is $L_{\text{sub}} = 32.25$ mm and $W_{\text{sub}} = 16$ mm. Table 1 shows the dimensions of the structure and all dimensions are in mm. The

Submitted On: June 29, 2021
Accepted On: October 10, 2021

https://doi.org/10.13052/2021.ACES.J.361107

1054-4887 © ACES

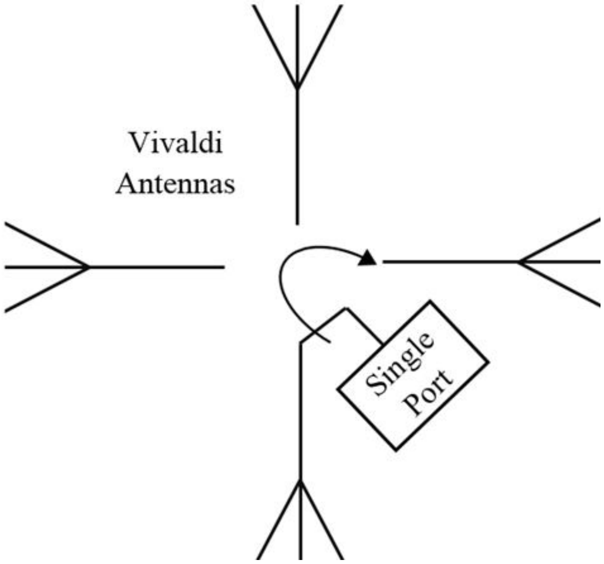

Fig. 1. Configuration of the proposed switched beam Vivaldi antennas.

Table 1: The dimensions of the proposed antenna element in the designed structure

Parameter	Length (mm)	Parameter	Length (mm)
L_{sub}	32.25	W_{sub}	16
L_P	9.581	W_P	0.705
L_f	13	W_f	1.65
L_g	8.75	R_g	4.25
R_i	9.775	R_{out}	28.825

dimension of R_g represents a minor radius of an ellipse which has a center at the edge of the substrate. Figure 3 shows the return loss of the single patch antenna.

A parametric study is obtained for each dimension individually while the other parameters are constant. Figure 4 discusses the effect of changing the length of L_P which tends to shift the resonance frequency and change the value of return loss (S_{11}). Increasing of L_P tends to increase the resonance frequency and increase the return loss while the gain decreases. In Figure 5, increasing of W_P tends to decrease the resonance frequency, while the return loss (S_{11}) approximately remains the same. Elaborating the results of all parametric studies, it is easy to choose the proper dimensions that achieve the resonant frequency at 28 GHz based on the required specifications and application. Figure 6 shows the radiation pattern of the proposed antenna at the resonant frequency. In Figure 7, the overall antenna gain for the single patch element is presented.

B. Proposed complete structure

The designed structure consists of four elements of the Vivaldi antenna designed. The four elements are con-

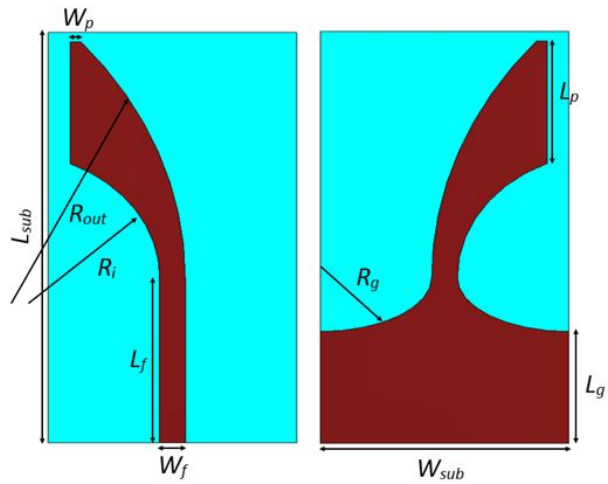

Fig. 2. The design of the proposed Vivaldi antenna and its structure.

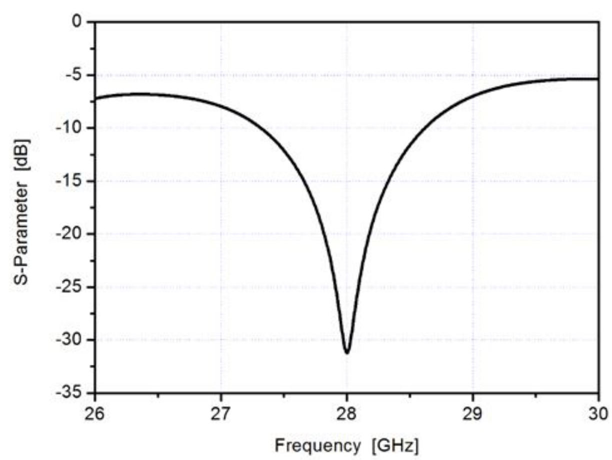

Fig. 3. The S-parameter (S_{11}) of the single patch antenna.

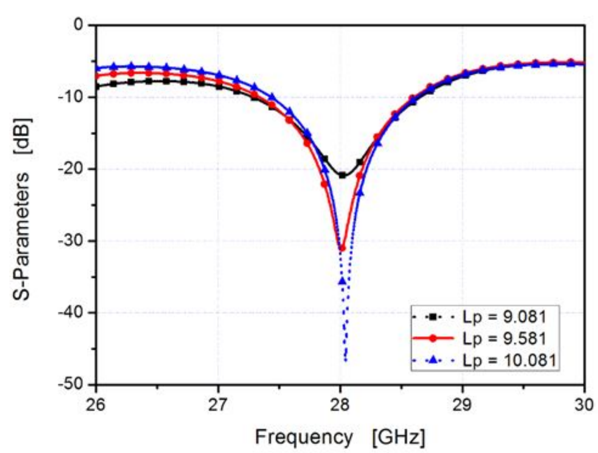

Fig. 4. A parametric study of increasing and decreasing of the length L_P.

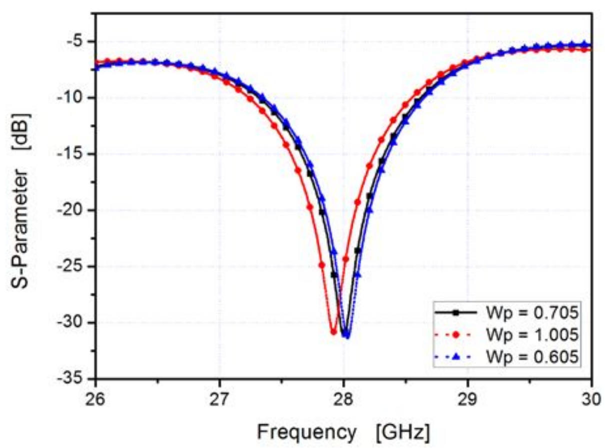

Fig. 5. A parametric study of increasing and decreasing of the length W_P.

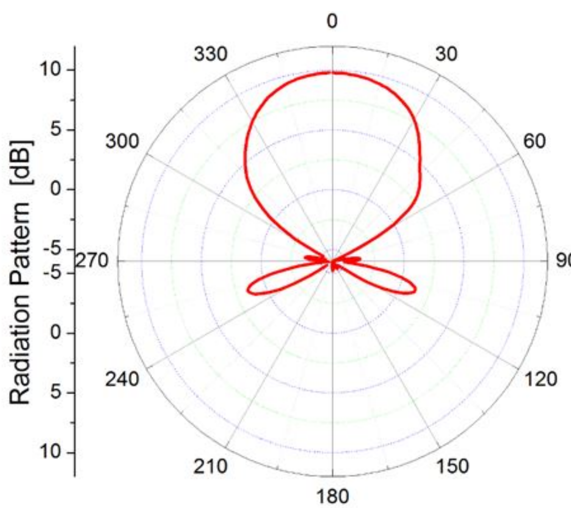

Fig. 6. The simulated radiation pattern of the single patch Vivaldi antenna.

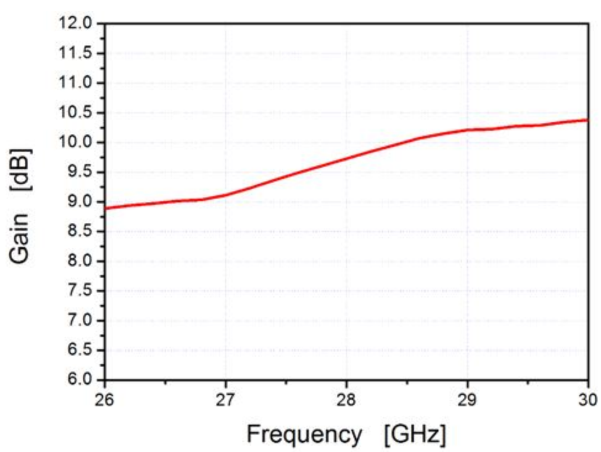

Fig. 7. The overall antenna gain for the single patch antenna.

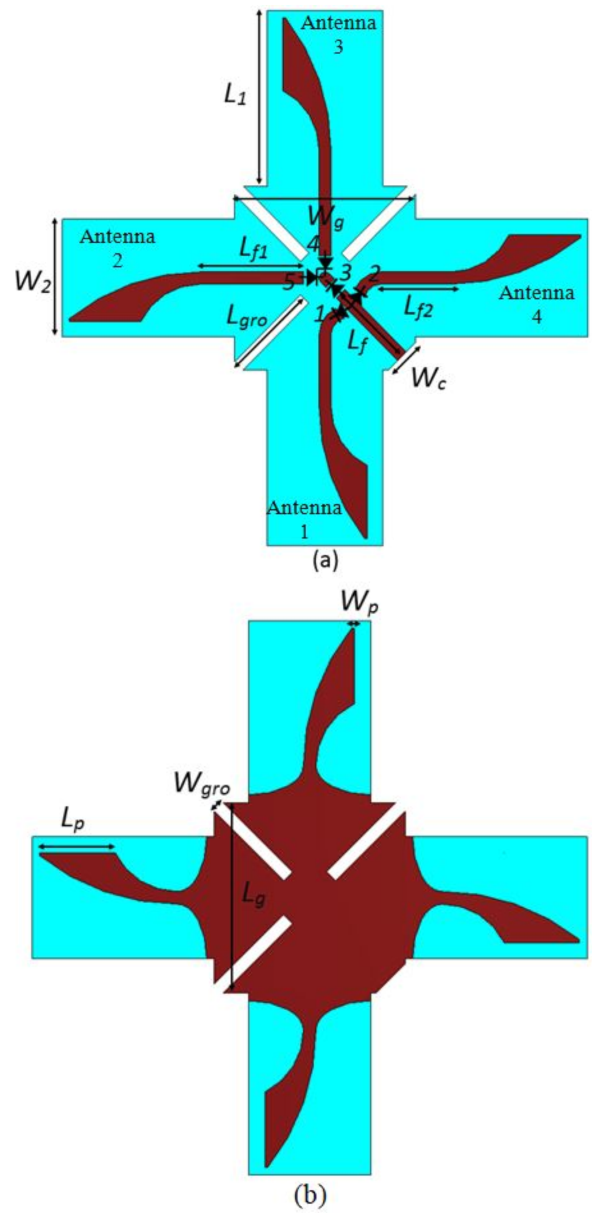

Fig. 8. The complete proposed structure with four elements.

structed to cover the overall area by making the angle between any two elements equal to 90°; so the overall coverage angle will be 360° as shown in Figure 8. The main benefit to use this structure instead of an omnidirectional antenna is the high gain and long distance that the signal can travel compared with the omnidirectional antenna. One microstrip feedline is used to feed the four elements. PIN diodes controlled by switching circuits are used to select the radiated antenna sequentially to transmit and receive the signals in all directions. PIN diodes offer a very good linearity and are applied for high power appli-

Table 2: Four configurations of the proposed antenna using switched RF diodes

State	Switched Diodes					Radiator
	D1	D2	D3	D4	D5	
1	ON	OFF	OFF	OFF	OFF	Antenna 1
2	OFF	OFF	ON	OFF	ON	Antenna 2
3	OFF	OFF	ON	ON	OFF	Antenna 3
4	OFF	ON	OFF	OFF	OFF	Antenna 4

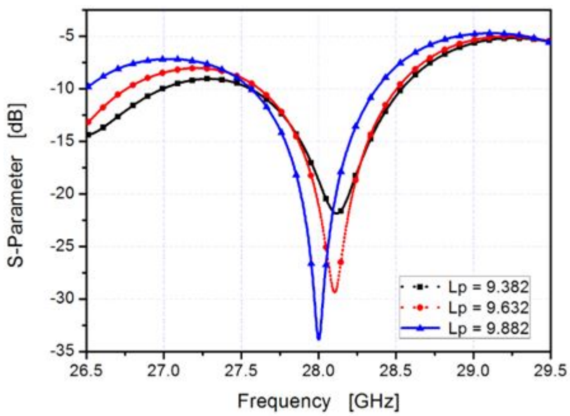

Fig. 9. A parametric study of increasing the length L_P.

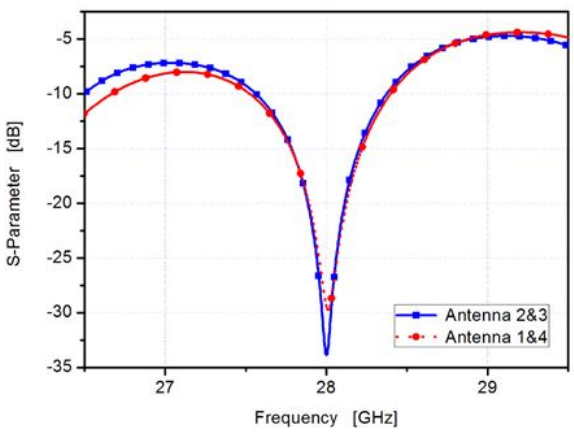

Fig. 10. The S-parameter (S_{11}) of the complete antenna structure: blue curve for antennas 2 and 3 and the red one for antennas 1 and 4.

Table 3: The dimensions of the overall proposed antenna structure

Parameter	Length (mm)	Parameter	Length (mm)
L_1	23.85	W_1	16
L_P	9.882	W_P	0.39
L_f	12	W_f	1.65
L_{f1}	14.35	L_{f2}	9.60
L_g	25	W_g	25
L_{gro}	12.85	W_{gro}	1.65
R_g	4.25	W_c	5.355
R_i	9.775	R_{out}	28.825

cations at microwave frequencies. An AlGaAs PIN diode of type "MA4AGBLP912" with a small ON-resistance, low capacitance, and significant fast switching speed is applied. The proposed structure is shown in Figure 8. The relationship between the switched RF diodes and the four radiator antenna structures is tabulated in Table 2. The shape of feedline is different in each case; so a parametric study for the shape of the feedline is presented in Figure 9. A groove between each two elements is used to enhance the system operation and improve the return loss. Table 3 shows additional dimensions for the proposed structure. In Figure 10, the return loss (S_{11}) of the four elements is shown. Figure 11 shows the radiation pattern of the proposed structure. In Figure 10 (a), for example, the diodes D3 and D5 are ON and D1, D2, and D4 are OFF, and then antenna 2 will operate and the radiation will be in the –90^o direction. In Figure 10 (b), the diodes D3 and D4 are ON and D1, D2, and D5 are OFF, and then antenna 3 will operate and the radiation will be in the 0^o direction and so on. The overall gain over the frequency range of operation for the full structure is studied.

III. RESULTS AND DISCUSSION

A. Single element

The proposed single element Vivaldi antenna is designed and simulated by CST software. This structure is operated at a resonance frequency of 28 GHz to cover

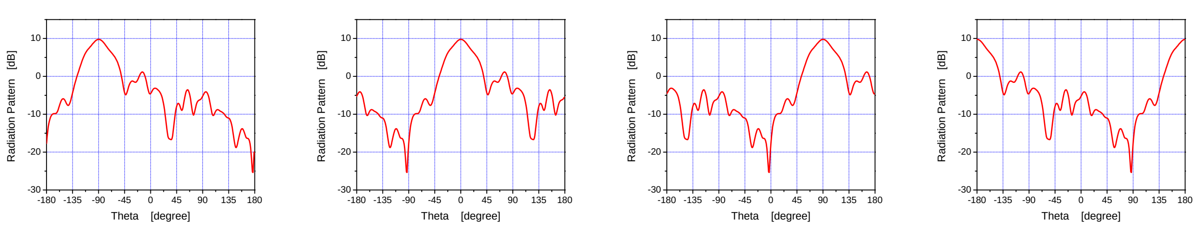

Fig. 11. The radiation pattern of the complete antenna structure: (a) antenna 2 is ON, (b) antenna 3 is ON, (c) antenna 4 is ON, and (d) antenna 1 is ON.

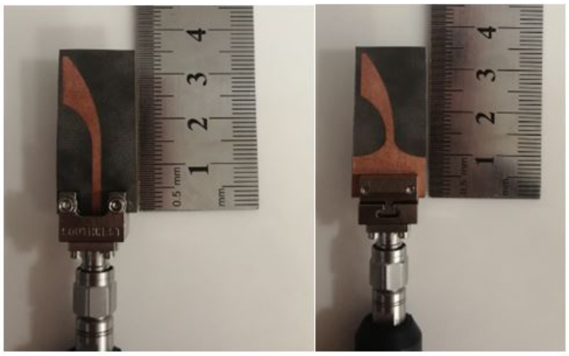

Fig. 12. The fabricated antenna design.

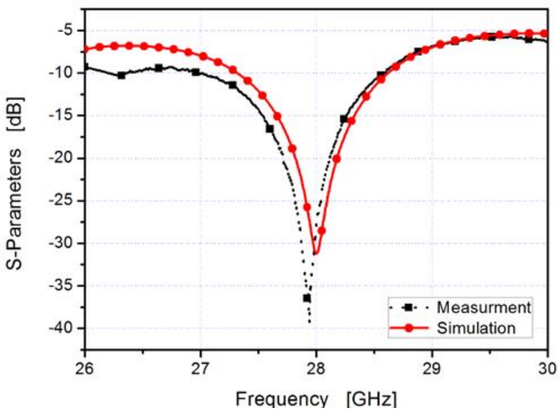

Fig. 13. The comparison of simulated and measured S_{11} results for single element antenna.

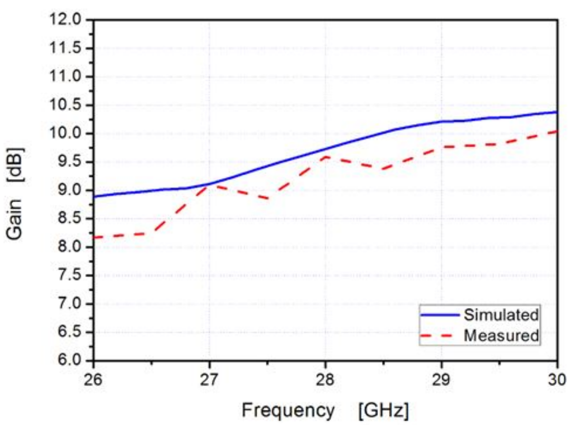

Fig. 14. The comparison between simulated and measured overall gain versus frequency results for the single element.

the ITS and 5G applications. It has a return loss of 31.5 dB at a resonance frequency. The antenna is fabricated using the photolithography method and measured using vector network analyzer (R&S ZVA 67). Figure 12

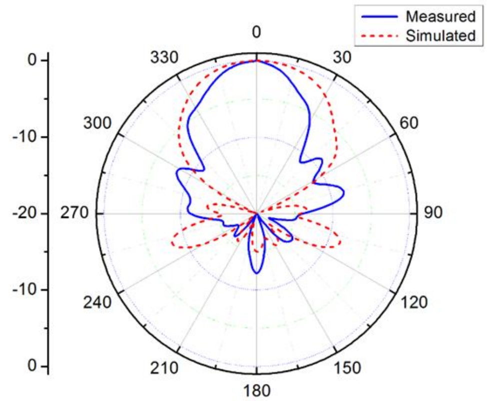

Fig. 15. The comparison between simulated and measured radiation patterns (normalized).

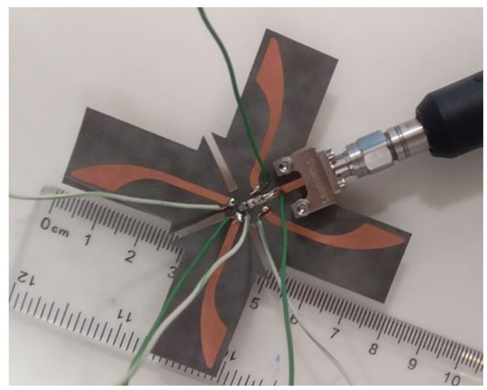

(a)

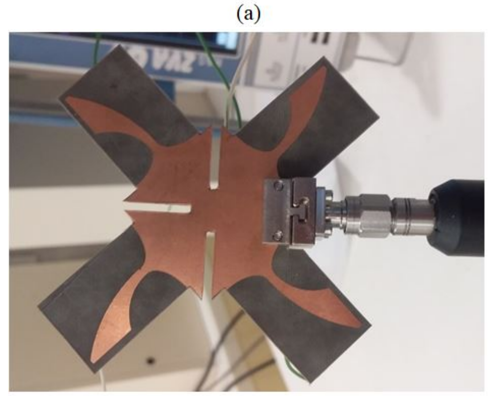

(b)

Fig. 16. The fabricated antenna structure: (a) top view; (b) bottom view.

shows the fabricated single element antenna. Good agreement is achieved between the simulated and measured results.

The return loss comparison curves are shown in Figure 13. The gain of the antenna is also measured and Figure 14 shows the comparison between measured and simulated results. The comparison between simulated

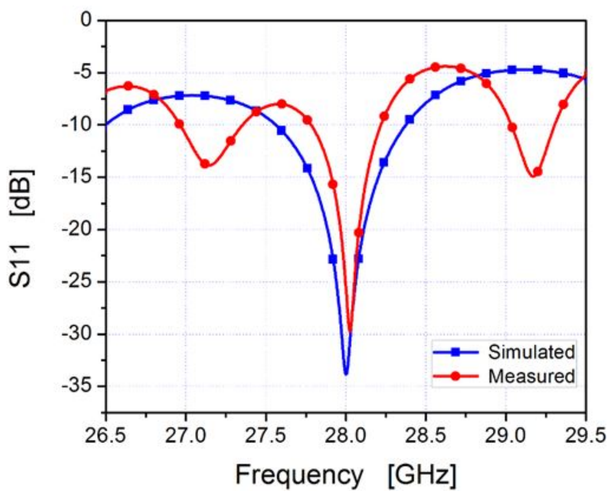

Fig. 17. The comparison of simulated and measured S_{11} results for antennas 1 and 4 in the complete structure.

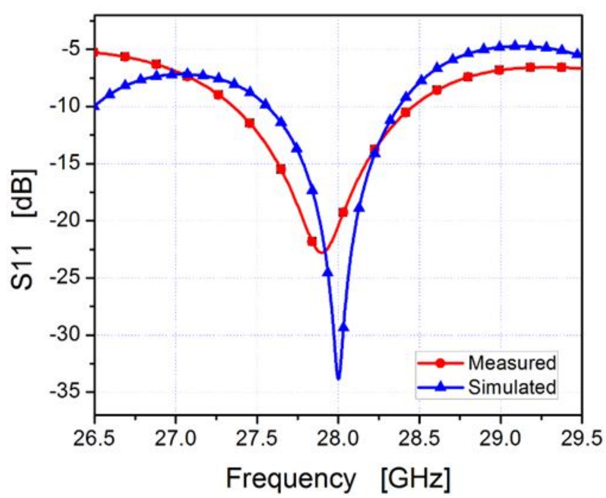

Fig. 18. The comparison of simulated and measured S_{11} results for antennas 2 and 3 in the complete structure.

and measured radiation pattern (normalized) is introduced as shown in Figure 15.

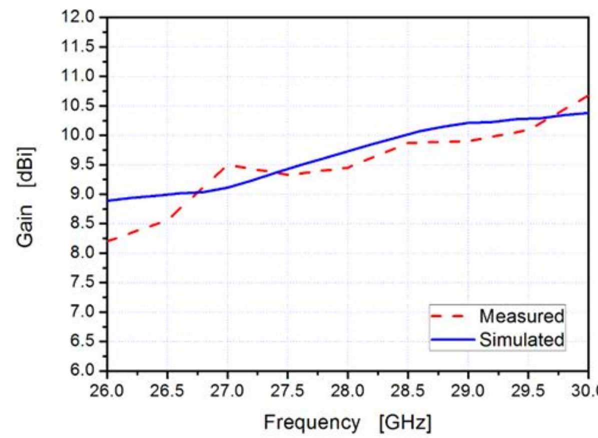

Fig. 20. The comparison between simulated and measured overall gain versus frequency results for a single element within the complete structure.

B. Complete structure

The complete antenna structure is designed on the same substrate of “Rogers 5880.” The complete antenna structure is fabricated and measured. Figure 16 shows the fabricated antenna structure. The return loss is measured and compared with the simulated one. Figure 17 shows the return loss for antennas 1 and 4 elements. The measured result is closed to the simulated one with some notches. Figure 18 shows the return loss for antennas 2 and 3 elements. The radiation pattern and the gain are also measured and compared with the simulated one. Good agreements are achieved between the simulated and measured results. Figure 19 shows the comparison between the simulated and measured radiation patterns. Figure 20 shows the overall gain versus frequency for the complete structure. The comparison between this work and previous works is tabulated in Table 4.

IV. CONCLUSION

A switched beam antenna system that consists of four elements of Vivaldi antennas for V2V communication in 5G application is introduced. The designed antenna achieves a wide bandwidth of 5.38% around the operating center frequency of 28 GHz.

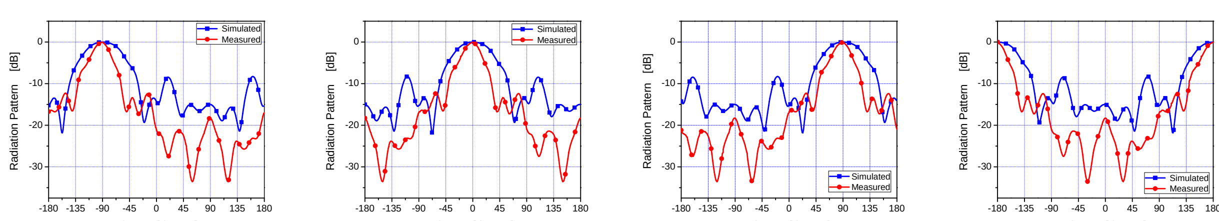

Fig. 19. The comparison between simulation and measurements of overall structure radiation pattern (normalized).

Table 4: Comparison with pervious works

Paper	[15]	[16]	[18]	[19]	[20]	**This Work**
Center frequency [GHz]	0.67	25.9	61	1	60	**28**
Bandwidth (at –10 dB) [%]	14.3	23.7	2.46	36	3.33	**5.86**
Coverage area (degree)	360	180	66	50	90	**360**
Gain (dBi)	5.8	6.1	18.7	9	3	**9.78**
Size (in mm)	144 × 144	570 × 220	46.4 ×31	250 × 250	14.7 × 11.9	**48.85 × 48.85**

The omnidirectional radiation is achieved by using the four elements of Vivaldi antennas. The antenna shows remarkable radiation characteristics and a high gain of more than 9.78 dBi. The proposed antenna has achieved a bandwidth of 1.64 GHz for the single element and 1.11 GHz for the complete structure. The antenna is fabricated and measured.

REFERENCES

[1] S. Maddio, "A compact circularly polarized antenna for 5.8 GHz intelligent transportation system," *IEEE Antennas and Wireless Propagation Letters*, vol. 16, no. 7, pp. 533-536, Jul. 2016.

[2] P. Singh, K. S. R. K. Chaitanya, and R. Kumari, "Microstrip patch antenna for application in intelligent transport systems," *TEQIP III Sponsored International Conference on Microwave Integrated Circuits, Photonics and Wireless Networks (IMICPW),* Tiruchirappalli, India, 22-24 May 2019.

[3] Z.-P. Zhong, X. Zhang, J.-J. Liang, C.-Z. Han, M.-L. Fan, G.-L. Huang, W. Xu, and T. Yuan, "A compact dual-band circularly polarized antenna with wide axial-ratio beamwidth for vehicle GPS satellite navigation application," *IEEE Trans. Veh. Technol.*, vol. 68, no. 9, pp. 8683-8692, Sep. 2019.

[4] M. Chowdhury and K. C. Dey, "Intelligent transportation systems-a frontier for breaking boundaries of traditional academic engineering disciplines," *IEEE Intelligent Transportation Systems Magazine,* vol. 8, no. 1, pp. 4-8, 2016.

[5] W. Wang, K. Guan, D. He, B. Ai, and Z. Zhong, "Channel characterization for vehicle-to-vehicle communication in urban sloped terrain," *International Applied Computational Electromagnetics Society Symposium - (ACES),* Beijing, China, 29 July-1 Aug. 2018.

[6] L. Wen, S. Gao, Q. Luo, W. Hu, and Y. Yin, "Wideband dual circularly polarized antenna for intelligent transport systems," *IEEE Transactions On Vehicular Technology*, vol. 69, no. 5, May 2020.

[7] W. Viriyasitavat, M. Boban, H. M. Tsai, and A. Vasilakos, "Vehicular communications: survey and challenges of channel and propagation models," *IEEE Veh. Technol. Mag.*, vol. 10, no. 2, pp. 55-66, Feb. 2015.

[8] C. Li, W. Chen, J. Yu, K. Yang, F. Li, and Y. Shui, "V2V radio channel properties at urban intersection and ramp on urban viaduct at 5.9 GHz," *IET Communications,* vol. 12, no. 17, pp. 2198-2205, 2018.

[9] A. Liu and Y. Lu, "Low-profile patch antennas with enhanced horizontal omnidirectional gain for DSRC applications," *in IET Microwaves*, *Antennas & Propagation*, vol. 12, no. 2, pp. 246-253, 2018.

[10] K. Wevers and M. Lu, "V2X communication for ITS-from IEEE 802.11p towards 5G," *IEEE 5G Tech Focus,* vol. 1, no. 2, Jun. 2017.

[11] L. Huang and Y. Lu, "A switchable or MIMO antenna for V2X communication," *IEEE International Conference on Computational Electromagnetics (ICCEM),* Shanghai, China, China, pp. 20-22, Mar. 2019.

[12] T. Fan, W. Chen, C. Li, X. Shu, and F. Chang, "Small scale characteristics analysis on highway V2V channel for intelligent transportation systems," *5th International Conference on Transportation Information and Safety (ICTIS),* Liverpool, United Kingdom, pp. 14-17, Jul. 2019.

[13] C.-H. Kuo, C.-C. Lin, and J.-S. Sun, "Modified microstrip franklin array antenna for automotive short-range radar application in blind spot information system," *IEEE Antennas and Wireless Propagation Letters,* vol. 16, no. 2, pp. 1731-1734, Feb. 2017.

[14] S. F. Jilani and A. Alomainy, "A multiband millimeter-wave 2-D array based on enhanced franklin antenna for 5G wireless systems," *IEEE*

Antennas and Wireless Propagation Letters, vol. 16, no. 9, pp. 2983-2986, Sep. 2017

[15] N. Nguyen-Trong, S. P. Pinapati, D. Hall, A. Piotrowski, and C. Fumeaux, "Ultralow-profile and flush-mounted monopolar antennas integrated into a metallic cavity," in *IEEE Antennas and Wireless Propagation Letters*, vol. 17, no. 1, pp. 86-89, Jan. 2018.

[16] M. W. Lee and N. S. Jeong, "Low-profile vehicle roof-top mounted broadband antenna for V2X," *Antennas and Propagation and USNC-URSI Radio Science Meeting 2019 IEEE International Symposium on*, pp. 925-926, 2019.

[17] G. Artner, R. Langwieser, and C. F. Mecklenbräuker, "Concealed CFRP vehicle chassis antenna cavity," in *IEEE Antennas and Wireless Propagation Letters*, vol. 16, pp. 1415-1418, 2017.

[18] N. Nguyen-Trong, A. Piotrowski, T. Kaufmann, and C. Fumeaux, "Low-profile wideband monopolar UHF antennas for integration onto vehicles and helmets," in *IEEE Transactions on Antennas and Propagation*, vol. 64, no. 6, pp. 2562-2568, Jun. 2016.

[19] V. Semkin, F. Ferrero, A. Bisognin, J. Ala-Laurinaho, C. Luxey, F. Devillersand, and A. V. Räisänen, "Beam switching conformal antenna array for mm-wave communications," *IEEE Antennas and Wireless Propagation Letters,* vol. 15, pp. 28-31, Apr. 2015.

[20] A. Darvazehban, S. A. Rezaeieh, and A. Abbosh, "Wideband beam-switched bow-tie antenna with inductive reflector," *IEEE Antennas and Wireless Propagation Letters,* vol. 19, no. 10, pp. 1724-1728, Oct. 2020.

[21] K. Trzebiatowski, M. Rzymowski, L. Kulas, and K. Nyka, "Simple 60 GHz switched beam antenna for 5G millimeter-wave applications," *IEEE Antennas and Wireless Propagation Letters,* vol. 20, no. 1, pp. 38-42, Jan. 2021.

[22] V. Venkateswaran, F. Pivit, and L. Guan, "Hybrid RF and digital beamformer for cellular networks: algorithms, microwave architectures, and measurements," *IEEE Trans. Microwave Theory Tech.,* vol. 64, no. 7, pp. 2226-2243, 2016.

[23] P. I. Bantavis, C. I. Kolitsidas, T. Empliouk, M. L. Roy, B. L. G. Jonsson, and G. A. Kyriacou, "A cost-effective wideband switched beam antenna system for a small cell base station," *IEEE Trans. Antennas Propag.*, vol. 66, no. 12, pp. 6851-6861, Dec. 2018.

[24] X. G. Zhang, W. X. Jiang, H. W. Tian, Z. X. Wang, Q. Wang, and T. J. Cui, "Pattern-reconfigurable planar array antenna characterized by digital coding method," *IEEE Trans. Antennas Propag.,* vol. 68, no. 2, pp. 1170-1175, Feb. 2020.

[25] Y.-X. Du, H. Liu, L. Qin, and B.-S. Li, "Integrated multimode orbital angular momentum antenna based on RF switch," *IEEE Access,* vol. 8, pp. 48599-48606, Mar. 2020.

[26] A. Darvazehban, S. A. Rezaeieh, O. Manoochehri, and A. M. Abbosh, "Two-dimensional pattern-reconfigurable cross-slot antenna with inductive reflector for electromagnetic torso imaging," *IEEE Trans. Antennas Propag.,* vol. 68, no. 2, pp. 703-711, Feb. 2020.

[27] S. A. Rezaeieh, A. Zamani, and A. M. Abbosh, "Pattern reconfigurable wideband loop antenna for thorax imaging," *IEEE Trans. Antennas Propag.,* vol. 67, no. 8, pp. 5104-5114, Aug. 2019.

[28] H.-T. Chou, Y.-S. Chang, H.-J. Huang, Z.-D. Yan, T. Lertwiriyaprapa, and D. Torrungrueng, "Two-dimensional multi-ring dielectric lens antenna to radiate fan-shaped multi-beams with optimum adjacent-beam overlapping crossover by genetic algorithm," *IEEE Access,* vol. 8, pp. 79124-79133, May 2020.

[29] CST Microwave Studio, ver. 2019, Computer Simulation Technology, Framingham, MA, 2019.

Convergence Determination of EMC Uncertainty Simulation Based on the Improved Mean Equivalent Area Method

Jinjun Bai[1], Jingchao Sun[2], and Ning Wang[1]

[1]College of Marine Electrical Engineering
Dalian Maritime University, Dalian, 116026, China
E-mail: baijinjun@dlmu.edu.cn, n.wang@ieee.org

[2]Traction & Control State Key Lab
CRRC Dalian R&D Co., Ltd, Dalian, 116052, China
sunjingchaofirst@126.com

***Abstract* –** Uncertainty analysis plays a significant role in electromagnetic compatibility (EMC) simulation, but suffers from convergence determination thereby reducing simulation accuracy and computational efficiency. In this paper, an improved mean equivalent area method is proposed to enhance calculation accuracy. It shows that, using a benchmark example, the proposed method successfully achieves the convergence determination of the stochastic reduced order models (SROMs), and realizes further promotion of uncertainty analysis method.

***Index Terms* –** EMC simulation, uncertainty analysis, convergence determination, improved mean equivalent area method, stochastic reduced order models

I. INTRODUCTION

In order to accurately describe the randomness and the uncertainty in the actual engineering environment, the uncertainty simulation methods have received extensive attention in the field of electromagnetic compatibility (EMC) in recent years [1].

Among the uncertainty analysis methods, the Monte Carlo method (MCM) is the most commonly used. The MCM uses a large number of sampling points to simulate the randomness of the simulation input, and deterministic EMC simulation is performed at each sampling point to obtain the uncertainty analysis results [2–4]. However, the computational efficiency of the MCM is extremely low, which makes it gradually lose competitiveness.

Since 2013, the stochastic Galerkin method (SGM) and the stochastic collocation method (SCM) of the generalized polynomial chaos theory have been successfully applied in EMC simulation. They use chaotic polynomials under a specific order to expand the uncertainty output, and then obtain the uncertainty analysis results through the Galerkin projection technology or the multidimensional Lagrange interpolation technology [5–8]. It is proved that the calculation accuracy of the SGM and the SCM is at the same level as the MCM, but their calculation efficiency is significantly higher than the MCM. However, when the number of random variables increases, the calculation time of the SGM and the SCM will increase exponentially, which is the so-called "dimension disaster" problem.

In 2016, the stochastic reduced order models (SROMs) have been proposed, which can completely avoid the emergence of the "dimension disaster" problem. Using the optimized algorithm for clustering, the SROM can select several feature points to represent sampling points under large number. Deterministic EMC simulation at each feature point is performed, and the final uncertainty analysis results can be obtained. The limitation of the SROM is that there is no way to judge whether the algorithm has converged, so the exact number of feature points cannot be determined [9].

In fact, for each uncertainty analysis method, how to accurately judge its convergence is a key issue that needs to be solved urgently. In other words, judging convergence is an indispensable step to determine the number of sampling points of the MCM, the order of chaotic polynomials of the SGM and the SCM, or the number of feature points of the SROM. Obviously, if the algorithm does not converge, there will be errors in the uncertainty analysis results. On the contrary, if an excessively large number of sampling points, chaotic polynomial orders or feature points are used in order to ensure convergence, it will be a waste of computing resources.

In order to solve the convergence determination problem of uncertainty simulation, the mean equivalent area method (MEAM) is proposed [10]. The MEAM draws on the idea of effectiveness evaluation in the feature selective validation (FSV) method, and applies the common area between the probability density curves of

Submitted On: April 2, 2021
Accepted On: July 29, 2021
https://doi.org/10.13052/2021.ACES.J.361108
1054-4887 © ACES

standard data and simulation data as the evaluation criterion. The effectiveness of the simulation results under adjacent orders or adjacent points is evaluated. When the evaluation result is "excellent" (the common area is greater than 0.95), it indicates that the algorithm has converged.

However, in order to achieve the purpose of standardization and generalization, the conventional MEAM uses a uniform distribution curve to replace the original probability density curve. Therefore, many details are ignored in calculating the common area, which reduces the accuracy of the algorithm.

This paper proposes the improved mean equivalent area method (Improved MEAM), which can accurately calculate the common area under the premise of ensuring standardization and generalization. Meanwhile, a convergence determination method based on the proposed method is given for the SROM, in order to determine the number of feature points.

The structure of this paper is as follows. The detailed description of the improved MEAM is provided in Section II. Section III offers the calculation accuracy verification of the improved MEAM. The convergence determination of the SROM is shown in Section IV. Discussion about convergence determination method of MCM, SGM, and SCM is given in Section V. Section VI presents the conclusion part of this paper.

II. IMPROVED MEAN EQUIVALENT AREA METHOD

Uncertainty analysis results are usually presented in the form of sampling points. Applying the statistical calculation, the expected value, the standard deviation, the worst-case estimate, or the probability density curve can be obtained. Obviously, the probability density curve is the most important result, because it can retain all the information of the uncertainty analysis. According to this feature, the conventional MEAM quantifies the difference between the simulation result and standard data by calculating the value of the common area surrounded by their probability density curves, in order to judge the accuracy of the simulation result. At the same time, in order to meet the needs of standardization and scalability, the conventional MEAM uses a uniform distribution curve to approximate the original probability density curve, and converts the calculation of the common area into the calculation of the rectangular area. This approximation ignores some details of the original PDF curve, which will bring calculation errors.

In the improved MEAM, N rectangles are used to approximate the probability density curve, aiming to ensure that the premise of standardization preserves the details of the probability density curve as much as possible, as shown in Figure 1. The specific steps of the approximate process are as follows:

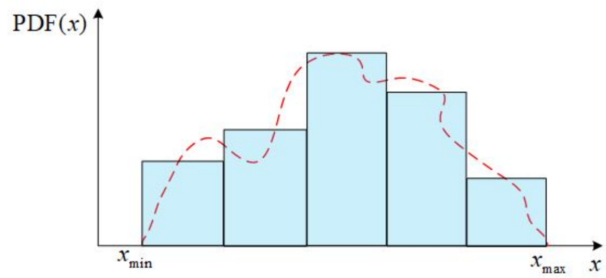

Fig. 1. Approximation of probability density curve.

1. Calculate the maximum value $x_{\max}$ and the minimum value $x_{\min}$ of M sampling points.
2. Take N–1 points at equal intervals between $x_{\min}$ and $x_{\max}$ to form N intervals, for example, N = 5 in Figure 1.
3. Count the number of sampling points in each interval M_i, and calculate the percentage$P_i = \frac{M_i}{M}$.
4. Each rectangle is regarded as a uniform distribution with a total probability of P_i.

Both standard data and simulation results can be transformed into N rectangles, as shown in Figure 2. The calculation of the common area between the probability density curves is transformed into the calculation of the common area between the rectangles. According to reference [10], conventional MEAM can calculate the common area of two rectangles, so the common area calculation of the improved MEAM can be given by the following formula:

$$Area_{\text{final}} = \sum_{i=1}^{N}\sum_{j=1}^{N} Area_{\text{MEAM}}(R_i^{\text{sta}}, R_j^{\text{sim}}), \tag{1}$$

where R_i^{sta} represents the ith rectangle of the standard data, and R_j^{sim} represents the jth rectangle of the simulation result. $Area_{\text{MEAM}}$ indicates that the common area of two rectangles is calculated using the conventional MEAM, its calculation formula is as follows:

$$Area_{\text{MEAM}}(R_i^{\text{sta}}, R_j^{\text{sim}}) = b_M \times h_M, \tag{2}$$

where b_M represents the bottom of the rectangular common area, and h_M is the height of the rectangular common area. The calculation formula for the height h_M is:

$$h_M = \min\{\frac{1}{2\sqrt{3}\sigma_i^{\text{sta}}}, \frac{1}{2\sqrt{3}\sigma_j^{\text{sim}}}\}, \tag{3}$$

where σ_i^{sta} is the standard deviation of the uniform distribution represented by R_i^{sta}, and σ_j^{sim} is the standard deviation of the uniform distribution represented by R_j^{sim}.

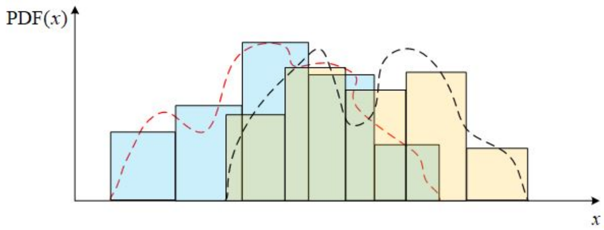

Fig. 2. The common area in the improved MEAM.

Table 1: Calculation results of b_M

	Condition	b_M
1	$m_{x,1} < m_{x,2} < m_{x,3} < m_{x,4}$	0
2	$m_{x,1} < m_{x,3} < m_{x,2} < m_{x,4}$	$m_{x,2} - m_{x,3}$
3	$m_{x,1} < m_{x,3} < m_{x,4} < m_{x,2}$	$m_{x,4} - m_{x,3}$
4	$m_{x,3} < m_{x,1} < m_{x,2} < m_{x,4}$	$m_{x,2} - m_{x,1}$
5	$m_{x,3} < m_{x,1} < m_{x,4} < m_{x,2}$	$m_{x,4} - m_{x,1}$
6	$m_{x,3} < m_{x,4} < m_{x,1} < m_{x,2}$	0

The bottom b_M is determined by Table 1. The intermediate coefficient expression is:

$$\begin{cases} m_{x,1} = m_i^{\mathrm{sta}} - \sqrt{3}\sigma_i^{\mathrm{sta}} \\ m_{x,2} = m_i^{\mathrm{sta}} + \sqrt{3}\sigma_i^{\mathrm{sta}} \\ m_{x,3} = m_j^{\mathrm{sim}} - \sqrt{3}\sigma_j^{\mathrm{sim}} \\ m_{x,4} = m_j^{\mathrm{sim}} + \sqrt{3}\sigma_j^{\mathrm{sim}} \end{cases}, \tag{4}$$

where m_i^{sta} is the average value of the uniform distribution represented by R_i^{sta}, and m_j^{sim} is the average value of the uniform distribution represented by R_j^{sim}.

Obviously, N^2 times conventional MEAM operations are required in one improved MEAM operation.

III. ACCURACY VERIFICATION OF THE IMPROVED MEAN EQUIVALENT AREA METHOD

In order to verify the accuracy of the improved MEAM, a calculation example of the common area problem is given. In calculation example, the probability density function of standard data is supposed as:

$$PDF(x) = \begin{cases} \frac{3}{8}[-2x^2 + 8x - 6], & 1 \le x \le 3 \\ 0, & x \text{ is other value} \end{cases}. \tag{5}$$

The probability density function of the simulation result is given as:

$$PDF(x) = \begin{cases} \frac{3}{8}[-2(x-k)^2 + 8(x-k) - 6], \\ \qquad 1+k \le x \le 3+k \\ 0, \qquad x \text{ is other value} \end{cases}, \tag{6}$$

where the value of k can be changed to generate different calculation examples. In this section, the value of k ranges from 0.02 to 1.5, and sampling points are taken every 0.02, for a total of 75 examples. Figure 3 shows the calculation example when k is 0.2.

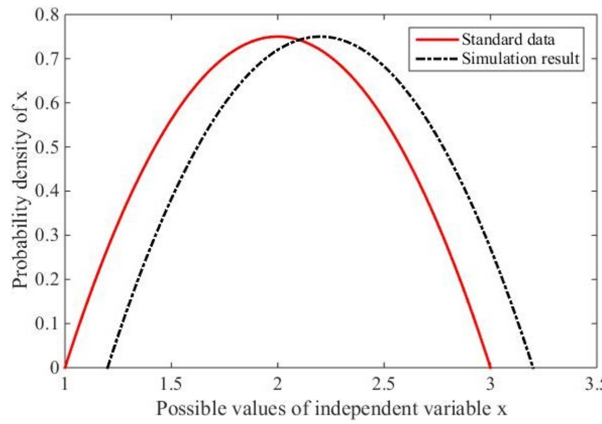

Fig. 3. Calculation example when k is 0.2.

It is worth noting that since the simulation result and the standard data are in the form of definite probability density functions, the real common area value can be obtained by directly performing integral operations.

In order to apply the conventional MEAM and the improved MEAM, the probability density function needs to be converted into the form of sampling points. Take the simulation result as an example, the distribution function is calculated first, which is shown as:

$$CDF(x) = \begin{cases} 0, & x \le 1+k \\ -\frac{1}{4}(x-k)^3 + \frac{3}{2}(x-k)^2 - \frac{9}{4}(x-k) + 1 \\ & 1+k \le x \le 3+k \\ 1, & x \ge 3+k \end{cases}. \tag{7}$$

After sampling the interval $[0,1]$ according to the uniform distribution, the following equation can be solved:

$$CDF(x) = U[0,1],\ 1+k \le x \le 3+k. \tag{8}$$

The set of solution results becomes the sampling points that characterize the probability density function. Similarly, eqn. (5) can also be transformed into the form of sampling points.

Using the conventional MEAM and the improved MEAM to calculate the common area of 75 examples, the results are shown in Figure 4. Among them, the black solid line represents the standard data, and the result is obtained by integrating the probability density function. The blue dashed line is the calculation result of the conventional MEAM, and the red dashed line is the calculation result of the improved MEAM.

Compared with standard data, Figure 5 shows the calculation errors of the conventional MEAM and the improved MEAM respectively.

Through calculation, the average error of the conventional MEAM is 12.94%, and that of the improved MEAM is 4.48%. Therefore, it is clearly proved that the proposed method has a greater improvement in the

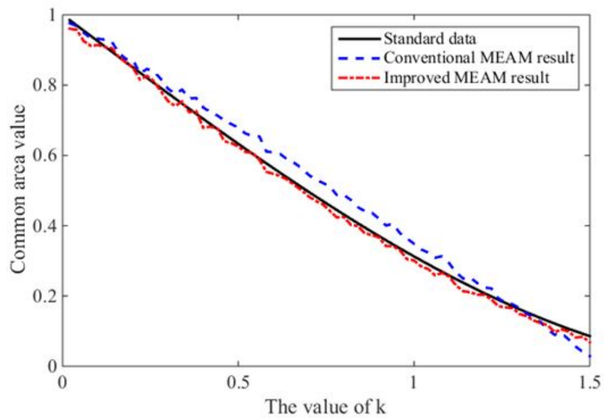

Fig. 4. Accuracy comparison of the conventional MEAM and the improved MEAM.

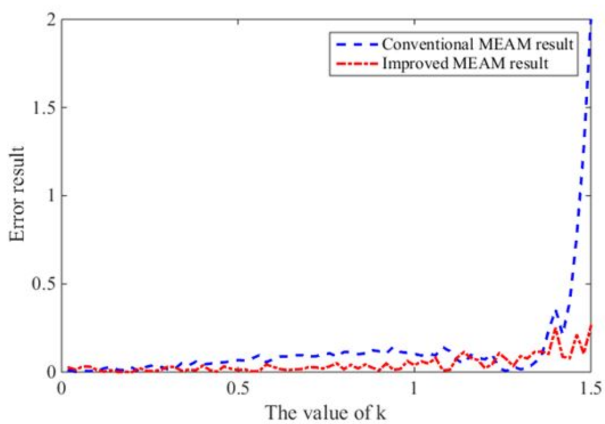

Fig. 5. Error results of the conventional MEAM and the improved MEAM.

accuracy of calculating the common area than the conventional MEAM.

IV. CONVERGENCE DETERMINATION OF THE SROM

In this section, the improved MEAM is applied to judge the convergence of SROM, which is a popular uncertainty analysis method. The convergence decision criterion is as follows:

1. SROM is used to calculate the uncertainty analysis results when the number of feature points is 2 and 2^2, and the common area value of the two results is obtained through the improved MEAM. If the area value is greater than 0.95, go to step 3., otherwise go to step 2.
2. SROM is applied to continue to calculate the uncertainty analysis result when the number of feature points is 2^3, and calculate the common area value when the feature points are 2^2 and 2^3. If it is greater than 0.95, enter step 3., otherwise continue to calculate the uncertainty analysis result when the number of feature points is 2^4, until the common area value is greater than 0.95 when the feature points are $2^{n-1}$and 2^n.
3. When the number of feature points is 2^n, the algorithm is judged to be convergent. Its corresponding uncertainty analysis result is the result of SROM.

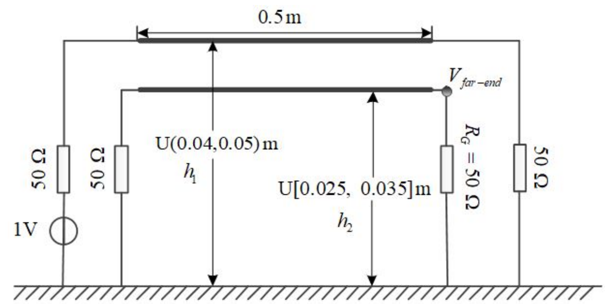

Fig. 6. The uncertainty analysis problem in the reference [8].

To verify the validity of the criterion, a typical uncertainty analysis problem in EMC simulation is presented in this section. The problem is the crosstalk calculation of the cables with the wires which are random in height, and this example is mentioned in the reference [8]. The parameters of the problem are shown in Figure 6. The amplitude of the excitation source is $1V$, the radius of the radiating conductor and the disturbed conductor are both $0.1\,mm$, the horizontal distance between the two conductors is $0.03\,m$, the length of the two conductors are both $0.5\,m$. All the loads are $50\,\Omega$.

The heights of the two conductors are uncertain, and the height of the radiating conductor h_1 obeys uniform distribution$U[0.04{,}0.05]m$while the height of the disturbed conductor h_2 obeys uniform distribution $U[0.025,\ 0.035]m$. Using a random variable model to describe this uncertainty factor, the following relationship can be obtained:

$$h_1 = 0.045{+}0.005 \times \xi_1, \tag{9}$$

$$h_2 = 0.03{+}0.005 \times \xi_2, \tag{10}$$

where $\xi_1$andξ_2 both stand for the uniform distribution $[-1,\ 1]$.

For the SROM, the random variables ξ_1 and ξ_2 are sampled first, and a fixed number of feature points are selected. Then, single deterministic EMC simulation is performed on each feature point, and the final uncertainty simulation result can be obtained. More details about the SROM can be found in reference [9]. The uncertainty analysis is realized respectively when the number of feature points is 2, 4, 8, and 16. The number

Table 2: Convergence determination process of the SROM

Number of Feature Points	The Common Area Value
2 times and 4 times	0.5337
4 times and 8 times	0.7235
8 times and 16 times	0.9606

of feature points represents the number of deterministic simulations required. Therefore, the smaller the number of feature points, the shorter the simulation time. Using the improved MEAM, Table 2 shows the convergence determination process of the SROM.

According to Table 2, the number of convergence feature points of SROM in this example is 16. It is worth noting that only two feature points will not be used in actual simulation process. In this article, this selection is to better show the convergence process of the SROM.

In uncertainty analysis field, the results of the MCM are usually regarded as the standard answer. This paper also compares the SROM results under different times with the MCM results, as shown in Figure 7 and Figure 8. Figure 7 presents the expectation results, and Figure 8 gives the standard deviation results.

In Figure 7, except two times SROM, the other results are close to the MCM results. It shows that when the number of feature points is 4, the estimate of expectation is accurate. In contrast to Figure 8, the SROM result is accurate only when the number of feature points is greater than 8. Obviously, when the feature point is 8, the algorithm is close to convergence. However, in order to ensure that the SROM completely converges, it is considered that 16 is the number of true convergent feature points.

In order to further describe the convergence process, the FSV method is introduced to quantify the difference between the MCM results and the SROM results in

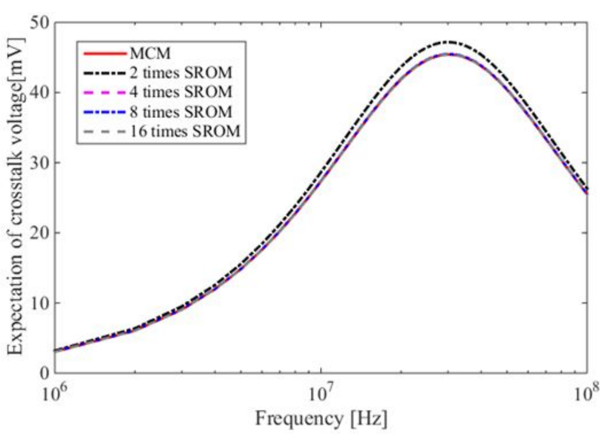

Fig. 7. Expectation results of the SROM.

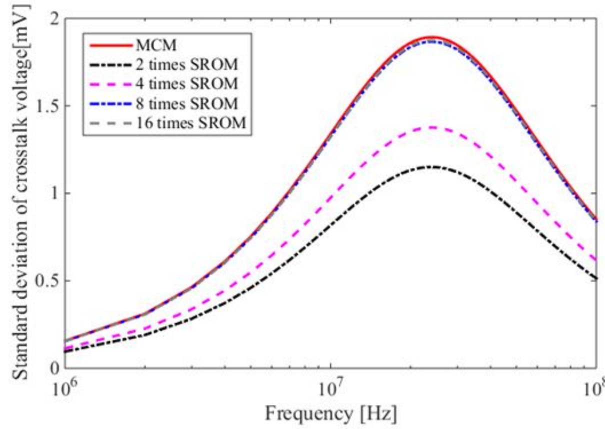

Fig. 8. Standard deviation results of the SROM.

Table 3: FSV results of the SROM under different times

	Expectation	Standard Deviation
MCM and 2 times SROM	0.0492	0.7615
MCM and 4 times SROM	0.0003	0.4763
MCM and 8 times SROM	0.0017	0.0205
MCM and 16 times SROM	0.0005	0.0144

Figure 7 and Figure 8, as shown in Table 3. More details about the FSV method can be obtained in the references [11] and [12].

According to the FSV results in Table 3, it is clearly shown that 16 is the number of convergent feature points.

In this example, the simulation time of the MCM is 642.57 s, while that of the SROM is only 1.68 s. It proves the unique advantage of the SROM in computational efficiency.

In summary, the improved MEAM can accurately determine the convergence of the SROM.

V. DISCUSSION

A. Convergence decision of the MCM

The number of basic sampling points N is determined first, and usually N is several hundred times. Then, the uncertainty analysis is respectively performed by using the MCM when the number of sampling points is N and $2N$. Based on the improved MEAM, the common area value between the uncertainty analysis results is calculated. If the area value is greater than 0.95, $2N$ is the number of convergent sampling points. Otherwise, MCM must be used for simulation under the sampling points 2^2N, 2^3N and so on, until the common area value between the uncertainty analysis results of adjacent sampling points is greater than 0.95.

In the calculation example of Section IV, N is selected as 800, and the algorithm has converged when the number of sampling points is 6400.

B. Convergence decision of the SGM and the SCM

Whether it is the SGM or the SCM, the uncertainty analysis results are calculated first when the chaotic polynomial orders are 2 and 3. The improved MEAM is applied to calculate the common area value between adjacent order results. If the area value is greater than 0.95, the convergence order is 3. Otherwise, the uncertainty analysis result must continue to calculate with chaotic polynomial order 4, 5, and so on, until the common area value between adjacent order results is greater than 0.95.

VI. CONCLUSION

In this paper, the improved MEAM is proposed to solve the problem of convergence determination of uncertainty analysis methods in the EMC simulation field. It is certified that the proposed method not only retains the advantages of the conventional MEAM in standardization and generalization, but also calculates the common area values more accurately. Using a calculation example in published reference, the improved MEAM successfully achieves the convergence determination of the SROM. Finally, the promotion of the improved MEAM in convergence determination for three famous uncertainty analysis methods (MCM, SGM, and SCM) is also described.

REFERENCES

[1] C. F. M. Carobbi, S. Lalléchère, and L. R. Arnaut, “Review of uncertainty quantification of measurement and computational modeling in EMC part I: measurement uncertainty,” *IEEE Transactions on Electromagnetic Compatibility*, vol. 61, no. 6, pp. 1690-1698, Dec. 2019.

[2] A. Kriz, “Uncertainty calculation for AMN impedance contribution using the Monte Carlo Method,” *2019 IEEE International Symposium on Electromagnetic Compatibility, Signal & Power Integrity*, pp. 565-569, Jul. 2019.

[3] E. Amador, C. Lemoine, and P. Besnier, “Optimization of immunity testing in a mode tuned reverberation chamber with Monte Carlo simulations,” *2012 ESA Workshop on Aerospace EMC, Venice*, pp. 1-6, Jul. 2012.

[4] S. K. Goudos, E. E. Vafiadis, and J. N. Sahalos, “Monte Carlo simulation for the prediction of the emission level from multiple sources inside shielded enclosures,” *IEEE Transactions on Electromagnetic Compatibility*, vol. 44, no. 2, pp. 291-308, May 2002.

[5] P. Manfredi, D. Vande Ginste, D. De Zutter, and F. G. Canavero, “Generalized decoupled polynomial chaos for nonlinear circuits with many random parameters,” *IEEE Microwave and Wireless Components Letters*, vol. 25, no. 8, pp. 505-507, Aug. 2015.

[6] P. Manfredi and F. G. Canavero, “Numerical calculation of polynomial chaos coefficients for stochastic per-unit-length parameters of circular conductors,” *IEEE Transactions on Magnetics*, vol. 50, no. 3, pp. 74-82, Mar. 2014.

[7] X. Wu, F. Grassi, P. Manfredi, and D. Vande Ginste, “Efficiency of the perturbative stochastic Galerkin method for multiple differential PCB lines,” *2018 IEEE Electrical Design of Advanced Packaging and Systems Symposium*, pp. 1-3, Dec. 2018.

[8] J. Bai, G. Zhang, D. Wang, A. P. Duffy, and L. Wang, “Performance comparison of the SGM and the SCM in EMC simulation,” *IEEE Transactions on Electromagnetic Compatibility*, vol. 58, no. 6, pp. 1739-1746, Dec. 2016.

[9] Z. Fei, Y. Huang, J. Zhou, and Q. Xu, “Uncertainty quantification of crosstalk using stochastic reduced order models,” *IEEE Transactions on Electromagnetic Compatibility*, vol. 59, no. 1, pp. 228-239, Feb. 2017.

[10] J. Bai, L. Wang, D. Wang, A. P. Duffy, and G. Zhang, “Validity evaluation of the uncertain EMC simulation results,” *IEEE Transactions on Electromagnetic Compatibility*, vol. 59, no. 3, pp. 797-804, Jun. 2017.

[11] A. P. Duffy, A. Orlandi, and G. Zhang, “Notice of retraction: review of the feature selective validation method (FSV). Part I—Theory,” *IEEE Transactions on Electromagnetic Compatibility*, vol. 60, no. 4, pp. 814-821, Aug. 2018.

[12] A. Orlandi, A. P. Duffy, and G. Zhang, “Notice of retraction: review of the feature selective validation method (FSV). Part II - Performance analysis and research fronts,” *IEEE Transactions on Electromagnetic Compatibility*, vol. 60, no. 4, pp. 1029-1035, Aug. 2018.

Jinjun Bai received the B.Eng. degree in electrical engineering and automation in 2013, and Ph.D. degree in electrical engineering in 2019 from the Harbin Institute of Technology, Harbin, China. At present, Mr. Bai is a lecturer at Dalian Maritime University. His research interests include uncertainty analysis methods in EMC simulation, EMC problem of electric vehicles, and the validation of CEM.

Jingchao Sun received the B.Eng. and M.Eng. degrees in electrical engineering from Dalian Maritime University, Dalian, China, in 2009 and 2012, respectively, where she is currently pursuing the Ph.D. degree. She is currently an Electrical Engineer with the Dalian Electric Traction Research and Development Center, China CNR Corporation Ltd., Dalian. Her current research interests include unmanned crafts and their intelligent modeling and control.

Ning Wang received his B.Eng. degree in Marine Engineering and the Ph.D. degree in control theory and engineering from the Dalian Maritime University, Dalian, China in 2004 and 2009, respectively. From September 2008 to September 2009, he was financially supported by China Scholarship Council to work as a joint-training PhD student at the Nanyang Technological University (NTU), Singapore. In view of his significant research at NTU, he received the Excellent Government-funded Scholars and Students Award in 2009. From August 2014 to August 2015, he worked as a Visiting Scholar at the University of Texas at San Antonio. His research interests include self-learning modeling and control, unmanned (marine) vehicles, machine learning, and autonomous systems. Dr. Wang received the Nomination Award of Liaoning Province Excellent Doctoral Dissertation, and also won the State Oceanic Administration Outstanding Young Scientists in Marine Science and Technology, the China Ocean Engineering Science and Technology Award (First Prize), the Liaoning Province Award for Technological Invention (First Prize), the Liaoning Province Award for Natural Science (Second Prize), the Liaoning Youth Science and Technology Award (Top10 Talents), the Liaoning BaiQianWan Talents (First Level), the Liaoning Excellent Talents (First Level), the Science and Technology Talents the Ministry of Transport of the P. R. China, the Youth Science and Technology Award of China Institute of Navigation, and the Dalian Leading Talents. He has authored three books, and more than 100 SCI-indexed journal papers. He currently serves as a member of IEEE TC on Industrial Informatics, the American Society of Mechanical Engineers (ASME), the Society of Naval Architects and Marine Engineers (SNAME), the Chinese Association of Automation (CAA), and the China's Society of Naval Architecture and Marine Engineering (CSNAME). He has been Leading Guest Editors of the International Journal of Fuzzy Systems, the International Journal of Advanced Robotics System, the Advances in Mechanical Engineering, and the International Journal of Vehicle Design. He currently serves as Editorial Board Members and Associate Editors of the International Journal of Fuzzy Systems, the Electronics (MDPI), the Journal of Electrical Engineering & Technology, the Cyber-Physical Systems (Taylor-Francis), the Frontiers in Robotics and AI, and the International Journal of Aerospace System Science and Engineering.

Design of Microstrip Filter by Modeling with Reduced Data

Ahmet Uluslu

Department of Electronics and Automation, Istanbul University-Cerrahpaşa, Istanbul 34500, Turkey
auluslu@iuc.edu.tr

Abstract **–** Many design optimization problems have high-scale problems that require the use of a fast, efficient, accurate, and reliable model. Recently, artificial-intelligence-based models have been used in the field of microwave engineering to model complex microwave stages. Here, an eight-layer symmetrical microstrip low-pass filter (LPF) is modeled using a multi-layer perceptron (MLP) with reduced data with Latin hypercube sampling. It is used to obtain target−test relationships in the MLP model along the frequency band whose electrical length in each layer determines the performance of the microstrip filter. Electrical length lower and upper limits were preferred in the widest range. The study presents the design and analysis of a non-uniform symmetrical microstrip LPF with a cutoff frequency of 2.4 GHz. Next, different network models are compared to find the variation of the non-uniform microstrip LPF around 2.4 GHz along the specified frequency band S_{11} and S_{22} (dB) for different electrical lengths. It has been observed that the network models of the microstrip LPF are both more computationally efficient and as accurate and reliable as the electromagnetic simulator.

Index Terms **–** Microstrip low-pass filter, MLP, deep learning, non-uniform microstrip filter.

I. INTRODUCTION

Microstrip low-pass filters are two-port elements that pass signals below the specified cutoff frequency but do not pass signals above or reduce their amplitude. This reduction amount varies according to the filter design. For example, the filter used in audio applications is called the treble cut or high cut filter. High-pass filters are the opposite of low-pass filters. Band-pass filters are a combination of low- and high-pass filters. The main application areas of low-pass filters are electronic circuits, image processing, sound processing, and acoustic problems. Low-pass filters are frequently used in millimeter-wave and microwave systems to pass below and above the desired cutoff frequency [1, 2]. The most striking features of microstrip low-pass filters are their small size and low interlayer losses. For this reason, its use in the fields of cellular mobile communication, especially in electronic circuits, has become quite widespread [1]. Embedded techniques and artificial neural networks (ANNs) [3], transmission lines [4, 6], waveguides [7], etc., examples are also available. In addition to all these, there are also spiral and FET amplifier studies [8, 10]. In recent years, artificial intelligence algorithms have been used in many high-performance circuit designs. They have been frequently used in many different microwave circuit designs [11], such as unit cell models [12, 13] for large-scale reflective array antenna designs and modeling of microstrip transmission lines [14, 15]. The algorithm and architectural structures used in the study are available in the multi-layer perceptron (MLP) modeling study for a similar antenna design problem [16]. This confirms the success of the algorithm and architecture. All these studies show that scientists working in the field of RF and microwave cannot remain indifferent to this developing technology. In addition, the fact that ANN can learn complex and non-linear training−test relationships and make predictions with them has revealed the idea that a study can be done by combining these two subjects. In a study, a three-element filter was designed with ANN [17]. The same author has other works on this work [18]. In a modeling study with user-preference-based range and step width, the total number of samples was specified as 55,450 [4]. In another recent study, artificial-intelligence-based modeling of the microstrip filter is available [19]. However, in this study, choosing *W-L* as the input parameter increases the total number of samples used and causes it to be 27,300.

One of the most important points in the design of surrogate models is to determine the optimum amount of training data. Failure to select the optimum amount of training data may result in poor results or poor performance due to high-dimensional samples. For this, a sampling technique called Latin hypercube sampling (LHS) was used to reduce data. The data used in surrogate models are usually obtained using the 3D electromagnetic (EM) simulation tool. The proposed non-uniform microstrip low-pass filter is modeled in the CST microwave studio program. By using the created surrogate model, the data of the scattering parameters (S_{11} and

Submitted On: May 21, 2021
Accepted On: October 30, 2021
https://doi.org/10.13052/2021.ACES.J.361109

S_{21}) of the proposed non-uniform microstrip low-pass filter depending on the design variables were obtained. These obtained data were then used as training and test data for the creation of an ANN-based proxy model. MLP structure, which is one of the most widely used structures, was used in the development of the ANN-based proxy model. Briefly, within the scope of this study, the variation of S_{11} and S_{21} (dB) parameters of a non-uniform microstrip low-pass filter at 2.4 GHz cutoff frequency of layers with different electrical lengths along the determined frequency band is discussed using ANN. The novelty of the study is that the S_{11} and S_{21} (dB) parameters of the microstrip low-pass filter can be found quickly, practically, and safely without costly computation and optimization processes with reduced data.

In the next part of the study, the analysis of the parameters for the design of the microstrip low-pass filter and the selection of the input parameters to be used in the modeling are mentioned. In the third part, a network model design example is presented and information about MLP training algorithms is given. Subsequently, an exemplary study was carried out. Finally, the study was completed with the conclusion and the suggested part.

II. DESIGN OF MICROSTRIP LOW-PASS FILTERS

A. Design parameters and analysis

As a design problem, low-pass filters basically consist of two stages. The first step is to identify a suitable low-pass prototype. Here, the passband fluctuation and the number of layers must be within the specified specifications. All of this includes filter sorting between layers. The conversion from electrical length (g_i) parameters to line lengths (Weight-Length) used in the EM simulator is available in detail in Chapter 8 of the microwave engineering book [20]. These lengths can also be calculated using any microstrip line calculator [21]. The second step is to determine the most suitable model for the determined microstrip low-pass filter [20]. The impedance value Z_0 value is 50 Ω and the electrical length g_i is taken as normalized values. The filter design is designed on the layer with the substrate thickness (h) in mm and the dielectric constant (ε_r) [22]. The number of layers is determined during design. The design and modeling process are performed for the determined value.

The characteristics of the designed microstrip low-pass filter are given in Table 1. The circuit model for the microstrip low-pass filter is shown in Figure 1.

Table 1: Filter design parameters

Definition	Parameter	Value
Dielectric constant	ε_r	4.4
Layer height	h	1.6 (mm)
Cutting frequency	f_{cut}	2.4 (GHz)
Filter impedance	Z_0	50 (Ω)
Lowest line impedance	Z_{0L}	20 (Ω)
Highest line impedance	Z_{0H}	120 (Ω)

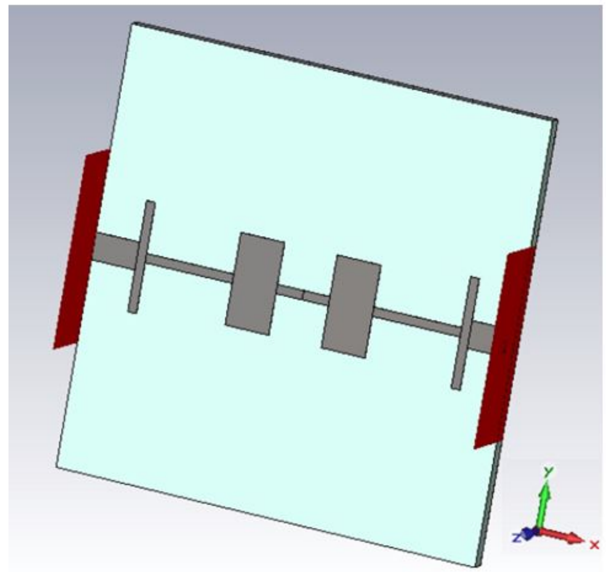

Fig. 1. 3D circuit model for eight-layer symmetrical microstrip low-pass filter.

B. Modeling parameter detection

The low training cost to be obtained is achieved by determining the optimum connection weights of the network. The selection of the input data set is very important for the determination of these optimum connection weights. The input parameter (electrical length g_i) ranges to be used in order to train the network in the widest range with the most optimum results were selected in the range of $0.5-2.6$ from the results of an optimization study [23]. These values are in the widest range band and include the ranges used in other studies [23, 24]. As it is known, optimization processes are long and costly processes. For this reason, the modeling process with the appropriate data set in many subjects provides a convenient and low-cost opportunity in terms of time. In addition, data reduction is frequently used in such applications in a way that does not change the result obtained from the analysis. For this, a sampling technique called LHS was chosen and modified according to the objectives of the present study. Data reduction method was used by taking the widest range selected for each layer as a reference.

LHS is a popular stratified sampling technique first proposed by MacKay [25] and further developed by Iman and Conover [26]. It is a sampling method of random designs that try to be evenly distributed in the

Table 2: Data set

Parameter	Range	Sampling Method	Number of Samples
g_i	0.50−2.6	LHS	225
Frequency (GHz)	0.05−5.0	Linear	100
Train sample	–	–	(225/2) × 100
Validation sample	–	–	(225/2) × 100

design space. With the LHS, one must first decide how many sample points to use and remember in which row and column the sample point is taken for each sample point. This configuration is similar to having N rooks on a chessboard without threatening each other [25, 26]. Here, the electrical lengths (g_i) of the eight-layer symmetrical filter are selected in the ranges given in Table 2. Equal step spacing was chosen as 0.05 so that there are 100 frequency samples in total.

III. MLP MODEL FOR MICROSTRIP LOW-PASS FILTER ANALYSIS

MLP-type multi-layer ANNs consist of input, hidden, and output layers. The structure of the network allows multi-element input/output modeling [27]. The MLP model used in this design is designed for different parameters consisting of two, three, and four hidden layers and consisting of 5, 10, 15, and 20 neurons. Similar structures have given successful results for a different study before [16]. Neurons input/output layers have different weight coefficients. In the training phase, modeling continues until the resulting training error rate is minimized [27]. For this purpose, a combination of two different activation functions was used between the layers. As the activation function in the hidden layer, logsis is preferred in the last neuron and tansig is preferred for the other layers. The output obtained as a result of each iteration is compared with the target, and depending on the error given, the network training is continued with the weight renewal process or the training process is terminated. The total input to the neurons of each layer is obtained by weighting the neuron outputs in a lower layer. The training success of the network can be achieved by adjusting these different weight coefficients correctly. This adjustment is compared with the output values in the previous step and corrected in the next step. Of course, besides these, it is very important to create the accurate network model. While creating the network model, there are a total of five input parameters, including four electrical length (g_i) parameters and frequency, which are different because the filter has a symmetrical structure. The black box model of the proposed network structure is given in Figure 2.

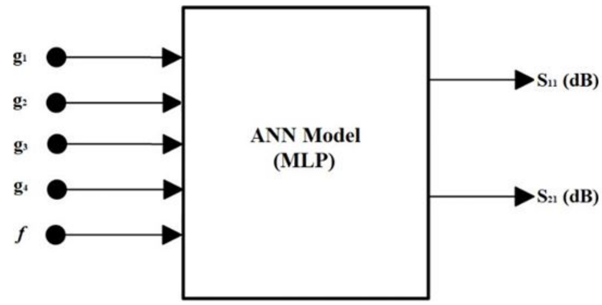

Fig. 2. ANN model for training S_{11} and S_{21} (dB) parameters of microstrip low-pass filter.

A. Activation functions

In this study, the activation functions used between layers for MLP type ANNs are, respectively, tangent-sigmoid (tansig) and logarithmic-sigmoid (logsig).

Tansig: The neuron input−output expression for this activation function is given in eqn (1) and the change of the function is given in Figure 3 (a). The dynamic range of change of the function is the range [−1 1], and the function neuron shows a non-linear change in this range depending on the total input. This function is also called the hyperbolic-tangent function in the literature

$$a = 2/(1+e^{(-2n)}) - 1. \tag{1}$$

Logsig: The input−output expression of this activation function, which is also called the sigmoid function, and the change of the function according to the input are given in eqn (2) and Figure 3 (b), respectively. The dynamic range of the function is the range [0 1], and the function exhibits a non-linear change in this range

$$a = 1/(1+e^{-n}). \tag{2}$$

B. Training algorithms

There are various training algorithms used to train the selected network. Here, we will explain three dif-

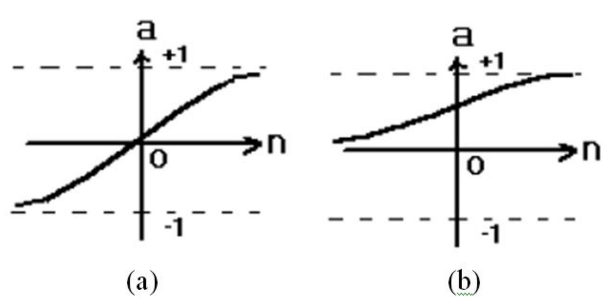

Fig. 3. (a) Tangent-sigmoid function input−output curve. (b) Logarithmic-sigmoid function input−output curve.

ferent neural network algorithms that we used while creating the algorithm. These algorithms are trainbr (Bayesian regularization), trainlm (quasi-Newton), and trainrp (gradient descent) [28].

Trainbr: Bayesian regression algorithm is a network training function in which the weight values and bias corresponding to the Levenberg−Marquardt optimization are updated. It reduces the combination of weights and squared errors to determine the appropriate combination that will help develop an important generalized quality network, and this whole process is known as Bayesian editing. Also, this function has some disadvantages such as using Jacobian for calculations; where performance is assumed to be the mean or sum of squared errors. Therefore, all structures/networks trained with the trainbr function should use either the mean of squared errors or the sum of squared errors [29].

Trainlm: Quasi-Newton algorithm provides preferred and fast optimization over conjugate gradient algorithms. It is based on the Hessian matrix (second derivatives) of the performance function with respect to the current values of the weights and deviations. It provides faster convergence than conjugate gradient methods. Because of its complexity, it takes a lot of time to find the Hessian matrix for FFNN. It is also known as the secant method and does not need any quadratic calculations. The Hessian matrix is updated very closely in all iterations of the algorithms. Trainlm is an iterative approach where the performance function will always be reduced in all iterations of the algorithm. Therefore, it becomes the fastest training algorithm for networks with a modest size. It also detects the minimum of a multi-variate function, which is the sum of the squares of non-linear real-valued functions. Besides its advantages, it has some limitations such as storage problem and computational overhead [30].

Trainrp: Gradient descent algorithms are popularized training algorithms that perform the basic gradient descent algorithm that changes the weights and biases toward the negative gradient of the performance function. The elasticity back propagation (trainrp) training algorithm cancels out the results of the weights of the partial derivatives [31]. In this algorithm, the derivative sign is used to decide whether to update the weights, and the size of the derivative does not affect the weight update. The weight change amount is learned with an independent update value. If the first derivative of the performance function by weight is of equal magnitude for two consecutive iterations [32], the update value is raised by a factor for each weight and deviation, and the same weight changes from the previous iteration. If the derivative is zero, the update will stay the same, and if the weights are flickering, they will be reduced.

IV. CASE STUDY

In the study part, a modeling study will be made for the ISM band application of the MLP-based eight-layer non-uniform microstrip filter. The proposed eight-layer microstrip filter is formed with a symmetrical structure. In this symmetric model, there are eight microstrip transmission lines, four of which are different. Therefore, based on the ANN model in Figure 2, the microstrip filter consists of five variables in total, including the frequency that will directly affect the output parameters S_{11} and S_{21} (dB). Training and validation data sets (Table 1) to construct the proposed MLP-based microstrip filter model are obtained using the EM simulation tool for the selected substrate FR4 (h = 1.6 mm; ε_r = 4.4). For the intervals given in Table 2, the data set is created using the LHS method. Here, the number of training and test data reduced for training is 225×100 in total. This input data is sized with the aid of a microstrip line calculator to obtain the results of S_{11} and S_{22} (dB) at each sample frequency. The resulting data sets are randomly divided into half as training and test data. This training and test data are processed with predetermined MLP algorithms and architectures (a total of 21 different types). All these applied processes are presented in Figure 4 as a flow chart. Since MLP algorithms are based on randomly initiated conditions and processes, the microstrip filter design is evaluated for 10 different runs to determine the best, worst, and mean performance of each MLP model

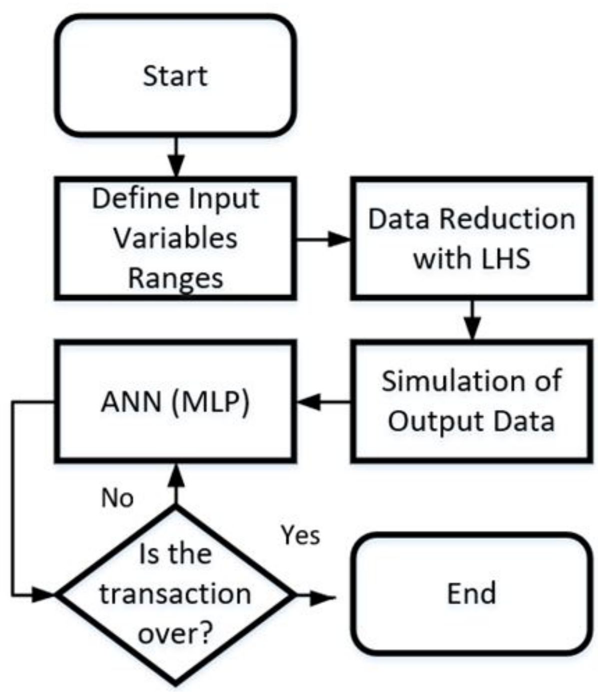

Fig. 4. Flow chart of modeling process of LHS- and MLP-based low-pass filter.

Table 3: Performance comparison of ANN models based on MAE

	Architecture	**Max.**	**Min.**	**Mean**
trainbr	5 10	2.09	1.96	2.01
	10 15	1.58	1.32	1.47
Algorithm	15 20	1.40	0.98	1.17
	5 10 15	0.93	0.81	0.88
	5 15 20	1.00	0.76	0.90
	10 15 20	0.91	0.55	0.74
	5 10 15 20	**0.66**	**0.49**	**0.62**
trainlm	5 10	2.21	2.09	2.16
	10 15	1.76	1.20	1.47
	15 20	1.32	1.09	1.12
	5 10 15	4.17	0.66	2.60
	5 15 20	1.17	0.76	0.97
	10 15 20	0.79	0.67	0.69
	5 10 15 20	1.06	0.63	0.80
trainrp	5 10	2.92	2.76	2.83
	10 15	2.46	2.34	2.38
	15 20	2.41	2.18	2.28
	5 10 15	2.66	2.43	2.55
	5 15 20	2.75	2.35	2.41
	10 15 20	2.12	1.81	1.99
	5 10 15 20	2.37	2.26	2.34

to determine the most stable architecture for the optimization problem.

The following are the commonly used error metrics used for performance evaluation of MLP models: mean absolute error (MAE) (eqn (3)); relative mean absolute error (RMAE) (eqn (4))

$$\mathrm{MAE} = \frac{1}{N}\sum_{i=1}^{N}|T_i - P_i| \tag{3}$$

$$\mathrm{RMAE} = \frac{1}{N}\sum_{i=1}^{N}\frac{|T_i - P_i|}{|T_i|} \tag{4}$$

where N is the total number of samples, T is the target value, and P stands for predicted value.

The performance measures obtained in 10 different runs for the 21 different ANN models identified are given in Table 3. Here, the MAE value is used in the overall comparison of the models during the validation process. The error value decreases with the increase in the number of hidden layers in the architecture used. However, among the algorithms used, trainbr (Bayesian regression) has the best results. As a result, among the results in Table 3, {5-10-15-20} trained with the trainbr method and the model trained with four hidden layers and hidden neurons has the best performance criteria in terms of both minimum error and narrow max−min range. The results selected from {5-10-15-20} trained with Bayesian regression method and the model trained with four hidden layers and hidden neurons. In Figure 5

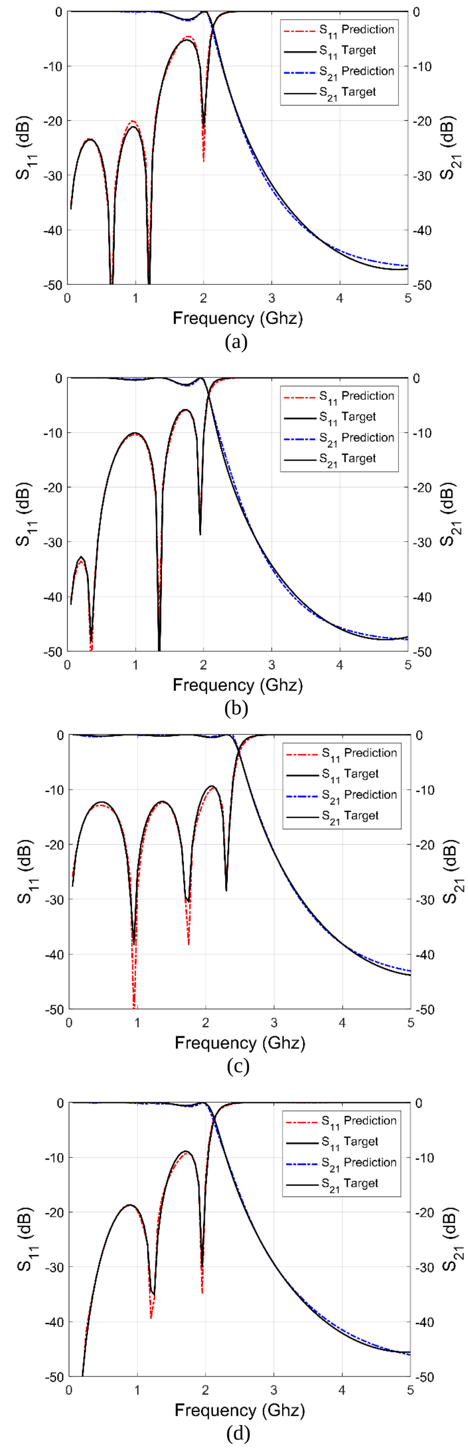

Fig. 5. Result of EM simulation and MLP-based modeling with the trainbr algorithm, {5-10-15-20} with hidden layers for eight-layer low-pass filter as S_{11} and S_{21} parameters: (a) g_{1-7} = 1.48; g_{2-6} = 1.97; g_{3-5} = 2.18; g_4 = 1.7; g_8 = 1. (b) g_{1-7} = 1.71; g_{2-6} = 2.04; g_{3-5} = 1.91; g_4 = 2.28; g_8 = 1. (c) g_{1-7} = 1.68; g_{2-6} = 1.19; g_{3-5} = 2.45; g_4 = 1.23; g_8 = 1. (d) g_{1-7} = 1.17; g_{2-6} = 2.06; g_{3-5} = 1.9; g_4 = 2.11; g_8 = 1.

Table 4: Performance comparison with other ANN models based on MEA

Model	Hyperparameter	Test Error
MLP	Hidden layer = 4neuron = [5 10 15 20]	0.49
RBF	Spread = 0.215	1.42
GRNN	Spread = 0.181	1.67
Ensemble	Method: bag, Number of cycles: 488, Min. leaf size: 1 Max. number of splits: 3344	1.8 ± 0.2

(a)−(d), S_{11} and S_{21} (dB) values were obtained by ANN. The estimated prediction is shown with the MATLAB program as target data obtained with the 3D EM simulation tool CST. As can be seen in the graphics, a high success has been achieved.

Finally, performance comparisons were made with other ANN models, especially XGBoosting-based ensemble learning, which has been popular recently in the best result surrogate model designs found with the proposed model. The parameters and results used in XGBoosting, radial basis function (RBF), and general regression neural network (GRNN) models are given numerically in Table 4. As can be seen from the results, the proposed model has the lowest error result.

V. CONCLUSION

Here, the modeling of the fast, practical, and reliable S_{11} and S_{21} (dB) parameters of the non-uniform microstrip filter is discussed using MLP for certain design features. The total number of samples was kept to a minimum by using the LHS method in the selection of training and test data. The proposed model is also low-cost in terms of total number of samples and computation [4, 19]. Performance comparisons were made for different algorithms and architectures using the created data sets. Thus, the most successful algorithm and architecture were determined. Algorithms and architectures used in the proposed MLP model have been chosen from those that have proven successful for a different design problem [16]. As a result of the study, it was seen that the ANN modeling used and 225 samples were used as accurately as an EM simulator for other electrical lengths (g_i) parameters in a wide range selected. In addition, the proposed model is not only limited to a non-uniform microstrip filter but can also be successfully applied to other microwave circuit design problems by changing the design optimization aim.

REFERENCES

[1] J-S. G. Hong and M. J. Lancaster, *Microstrip Filters for RF/Microwave Applications*, *1st Edition*. John Wiley & Sons Inc., 2001.

[2] R. E. Zich, M. Mussetta, F. Grimaccia, A. Gandelli, H. M. Linh, G. Agoletti, M. Bertarini, L. Combi, P. F. Scaramuzzino, and A. Serboli, "Comparison of different optimization techniques in microstrip filter design," *IEEE Asia-Pacific International Microwave Symposium on Electromagnetic Compatibility (APEMC)*, pp. 549-552, May 2012.

[3] Y. Jiang and X. Nong, "A radar filtering model for aerial surveillance base on kalman filter and neural network," *IEEE 11th International Conference on Software Engineering and Service Science (ICSESS)*, pp. 57-60, Oct. 2020.

[4] T. Mahouti, N. Kuşkonmaz, and T. Yıldırım, "Modelling of non-planar microstrip lines via artificial neural networks," *Innovations in Intelligent Systems and Applications Conference (ASYU)*, Nov. 2019.

[5] N. Türker and F. Güneş, "An artificial neural model of the microstrip lines," *Proceedings of the IEEE 12th Signal Processing and Communications Applications Conference*, pp. 657-660, Apr. 2004.

[6] L. Sorokosz and W. Zieniutycz, "Electromagnetic modeling of microstrip elements aided with artificial neural network," *Baltic URSI Symposium (URSI)*, pp. 85-88, Nov. 2020.

[7] P. T. Selvan and S. Raghavan, "A CAD neural analysis for conductor backed asymmetric CPW with one lateral ground plane," *International Conference on Computer, Communication and Electrical Technology (ICCCET)*, pp. 266-270, May 2011.

[8] G. L. Creech, B. J. Paul, C. D. Lesniak, T. J. Jenkins, and M. C. Calcatera, "Artificial neural networks for fast and accurate EM-CAD of microwave circuits," *IEEE Trans. Microwave Theory Tech.*, vol. 45, no. 5, pp. 794-802, May 1997.

[9] A. H. Zaabab, Q. J. Zhang, and M. S. Nakhla, "A neural network modeling approach to circuit optimization and statistical design," *IEEE Trans Microwave Theory Tech.*, vol. 43, no. 6, pp. 1349-1358, Jun. 1995.

[10] M. C. E. Yagoub, "Active device modeling methodologies for RF/microwave system-level CAD," *25th Annual Review of Progress in Applied Computational Electromagnetics,* pp. 155-160, Mar. 2009.

[11] F. Güneş, P. Mahouti, S. Demirel, M. A. Belen, and A. Uluslu, "Cost-effective GRNN-based modeling of microwave transistors with a reduced number of measurements," *International Journal of Numerical Modelling: Electronic Networks, Devices and Fields*, vol. 30, no. 3-4, May 2017.

[12] F. Güneş, S. Demirel, and S. Nesil, "A novel design approach to XBand Minkowski Reflectarray antennas using the full-wave EM simulation-based com-

plete neural model with a hybrid GA-NM algorithm," *Radioengineering*, vol. 23, no. 1, pp. 144-153, Apr. 2014.

[13] P. Mahouti, F. Gunes, A. Caliskan, and M. A. Belen, "A novel design of non-uniform Reflectarrays with symbolic regression and its realization using 3-D printer," *Applied Computational Electromagnetics Society Journal*, vol. 34, no. 2, pp. 280-285, Feb. 2019.

[14] D. Krishna, J. Narayana, and D. Reddy, "ANN models for microstrip line synthesis and analysis," *World Academy of Science, Engineering and Technology, International Science Index 22, International Journal of Electrical, Computer, Energetic, Electronic and Communication Engineering*, vol. 2, no. 10, pp. 2343-2347, Nov. 2008.

[15] P. Mahouti, F. Güneş, M. A. Belen, and S. Demirel, "Symbolic regression for derivation of an accurate analytical formulation using "Big Data" an application example," *Applied Computational Electromagnetics Society Journal*, vol. 32, no 5, pp. 372-380, May 2017.

[16] P. Mahouti, "Design optimization of a pattern reconfigurable microstrip antenna using differential evolution and 3D EM simulation-based neural network model," *International Journal of RF and Microwave Computer-Aided Engineering*, vol. 29, no. 8, Aug. 2019.

[17] G. S. Tomar, V. S. Kushwah and S. Saxena, "Design of microstrip filters using neural network," *Second International Conference on Communication Software and Networks*, pp. 568-572, Feb. 2010.

[18] V. S. Kushwah, G. S. Tomar and S. S. Bhadauria, "Designing stepped impedance microstrip low-pass filters using artificial neural network at 1.8 GHz," *International Conference on Communication Systems and Network Technologies*, pp. 11-16, Apr. 2013.

[19] T. Mahouti, T. Yıldırım, and N. Kuşkonmaz, "Artificial intelligence–based design optimization of nonuniform microstrip line band pass filter," *International Journal of Numerical Modelling*, vol. 34, no. 6, Apr. 2021.

[20] D. M. Pozar, *Microwave Engineering*, *2nd Edition,* John Wiley, 2000.

[21] https://www.emtalk.com/mscalc.php

[22] J-S. G. Hong and M. J. Lancaster, *Microstrip Filters for RF/ Microwave Applications*. John Wiley & Sons Inc, 2001.

[23] A. Uluslu, "Microstrip low pass filter analysis and design," *Research & Reviews in Engineering,* Gece Publishing, vol. 1, pp. 35-52, May 2021.

[24] H. Bohra and A. Ghosh, "Design and analysis of microstrip low pass and bandstop filters," *International Journal of Recent Technology and Engineering (IJRTE)*, vol. 8, no. 3, pp. 6944-6951, Sep. 2019.

[25] M. MaKa, R. Beckman, and W. Conover, "A comparison of three methods for selecting values of input variables in the analysis of output from computer code," *Technimeterics*, vol. 21, no. 1, pp. 239-245, May 1979.

[26] R. Iman and W. Conover, "Small sample sensitivity analysis techniques for computers models, with an application to risk assessment," *Communications in Statistics - Theory and Methods,* vol. 9, no. 17, pp. 1749-1842, Jan. 1980.

[27] Z. Şen, *Yapay Sinir Ağları İlkeleri*, Su Vakfı Yayınları, İstanbul, 2004.

[28] S. Ali and K. A. Smith, "On learning algorithm selection for classification," *Applied Soft Computing*, vol. 6, no. 2, pp. 119-138, Jan. 2006.

[29] http://in.mathworks.com/help/nnet/ref/trainbr.html

[30] D. Pham and S. Sagiroglu, "Training multilayered perceptrons for pattern recognition: a comparative study of four training algorithms," *International Journal of Machine Tools and Manufacture*, vol. 41, no. 3, pp. 419-430, Feb. 2001.

[31] A. D. Anastasiadis, G. D. Magoulas, and M. N. Vrahatis, "New globally convergent training scheme based on the resilient propagation algorithm," *Neurocomputing*, vol. 64, pp. 253-270, Mar. 2005.

[32] http://www-rohan.sdsu.edu/doc/matlab/toolbox/nnet/backpr57.html

Ahmet Uluslu received the Ph.D. degree from the Electronics and Communication Engineering Department, Istanbul Yıldız Technical University, Istanbul, Turkey, in 2020. He received the master's degree from the Department of Electromagnetic Fields and Microwave Techniques, Istanbul Yıldız Technical University. He is currently working as a Lecturer with Istanbul University - Cerrahpaşa Electronics and Automation Department. His current research areas are microwave circuits, especially optimization techniques of microwave circuits, antenna design, and antenna optimization and modeling.

A Compact Bandstop Filter Design Using DMS-DGS Technique for Radar Applications

Burak Dokmetas[1], Galip Orkun Arican[2], Nursel Akcam[1], and Erdem Yazgan[3]

[1]Department of Electrical and Electronics Engineering, Gazi University, Ankara, Turkey
burakd@gazi.edu.tr, ynursel@gazi.edu.tr

[2]ASELSAN Inc., Communication and Information Technologies Division, Ankara, Turkey
goarican@aselsan.com.tr

[3]Department of Electrical and Electronics Engineering, TED University, Ankara, Turkey
erdem.yazgan@tedu.edu.tr

Abstract – In this study, a novel compact bandstop filter (BSF) by utilizing the defected ground structure (DGS) and defected microstrip structure (DMS) techniques are presented. DGS, DMS, and compensated capacitors are used on both bottom and top layers to obtain sharp transition and wider stopband. The operating frequency bandwidth of the filter can be comfortably regulated by tuning the dimensions of the etched structures. In addition to parametric studies, an equivalent circuit model of the proposed filter is extracted. The BSF has an insertion and return losses better than –1.6 and –17 dB in the passband, respectively. Moreover, the developed filter covers X-band frequency range and has stop bandwidth of 10.8–11.8 GHz with the rejection of better than 20 dB. Furthermore, the measurement and simulation results are in compliance with the suggested method. The proposed BSF has a very small size of 14.28 mm $\times$ 4 mm $\times$ 0.508 mm and has the potential to be used for radar applications with its high compactness, low cost, and high harmonic rejection performance.

Index Terms – Bandstop filter (BSF), defected ground structure (DGS), X-band application.

I. INTRODUCTION

In recent years with the advancement of wireless communication and wireless power transfer technology, the requirement to microwave devices with high performances is increased. One of the most significant components of these devices are microwave filters. Microstrip filters are important passive elements for the attenuation of unwanted signals and noise in communication technology [1, 2]. Therefore, the development of compact and low cost microstrip filters with out-of-band rejection feature is getting more attention in modern communication systems. So to accomplish these requirements, many filtering structures have been investigated [3].

In addition, several defected ground structure (DGS) studies for microstrip applications have been reported during these decades. The DGS is realized by adding defected resonator on the ground plane to change the values of the distributed capacitance and inductance of the transmission line [4, 5]. In the previously reported studies, DGS technique was implemented to miniaturize the circuit size. In addition, a miniaturization up to 50% was reported by using DGS technique in the literature [6]. Moreover, a miniaturized dual-band triangle-shaped DGS bandstop filter (BSF) for energy harvesting applications is fabricated [7]. Furthermore, resonant frequency can be controlled by changing the dimension and shapes of the etched slots [8, 9]. This technique is evitable for both periodic and non-periodic structures.

Defected microstrip structure (DMS) is realized by etching specific slots in the transmission line and it exhibits the properties of slow wave [10]. The bandstop response and selectivity behaves are akin to the DGS but without any damage on the ground plane. As opposed to the DGS technique, the frequency response of the DMS structure is almost the same when the microstrip length varies [11]. Moreover, in the literature, it is reported that DMS and DGS techniques are used at the same time for different microwave applications. T-shaped DMS and U-shaped DGS were used to create dual-band BSF [12]. Hexagonal fractal antenna was designed for UWB applications based on DGS-DMS technique [13]. A bandpass filter with narrow bandwidth for WLAN applications was fabricated [14].

In this study, a novel compact microstrip BSF for X-band application is proposed. The prominent features of this study are the usage of DGS-DMS technique to accomplish a much more compact structure with

Submitted On: June 7, 2021
Accepted On: October 18, 2021
https://doi.org/10.13052/2021.ACES.J.361110

a unique design compared to the studies in the literature and the development of the equivalent circuit model (ECM) to be able to design higher order filters. In addition, a three-stage design procedure is presented to explain the proposed topology. In the first stage, the characteristics of the suggested modified meander DGS shape are analyzed. In the second stage, the effects of the rectangular DMS shapes on frequency response are investigated. In the final stage, the compensated capacitors are added on the strip line. Moreover, an ECM of the final design is extracted based on lumped elements [15] and the values of each circuit component is theoretically calculated. Agilent ADS circuit simulator is used to simulate the ECM results and CST software is used for 3D electromagnetic (EM) analysis. Furthermore, the BSF is modeled and manufactured on a Rogers RT5880 substrate with a dielectric constant of 2.2 and electric loss tangent of 0.0009. Substrate and copper metallization thicknesses are chosen as 0.508 and 0.035 mm, respectively. The proposed filter has a compact size compared to reported works with an area of 57.12 mm^2.

II. MICROSTRIP FILTER DESIGN

In the first stage, the two layered filter design with meandered DGS slot is presented. On the top layer, there is a transmission line, whose characteristic impedance is 50 Ω with a width of w = 1.6 mm. In addition, on the bottom layer, the proposed meandered DGS slot is etched on the ground plane. Figure 1 shows the detailed layouts of the proposed filter (Step-1).

The 3D-EM simulation of the filter is performed using the CST Microwave Studio [16]. Table 1 shows the optimized values of the BSF (Step-1).

The DGS ensures a cutoff frequency (f_C) and attenuation pole frequency (f_0). Cutoff frequency is defined as the frequency where the insertion loss is 3 dB below the passband. Attenuation pole can be achieved with the combination of inductance and capacitance elements.

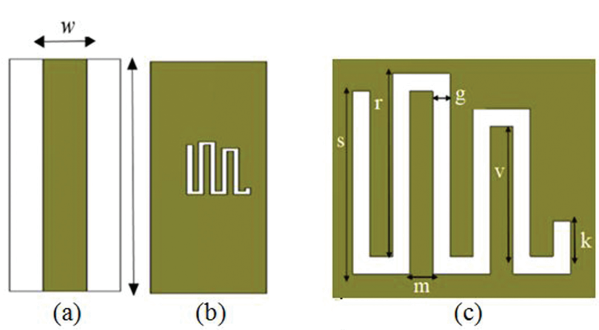

Fig. 1. Geometry of the microstrip filter design (Step-1). (a) Top layer. (b) Bottom layer. (c) Proposed DGS structure.

Table 1: Optimized dimensions of the filter

Parameter	Value (mm)	Parameter	Value (mm)
w	1.60	d	6.10
l	14.50	f	1.10
k	0.20	L_x	0.80
m	0.20	L_y	2.90
v	2.54	W_x	0.40
g	0.20	W_y	1.80
s	3.10	p_x	0.50
r	3.10	p_y	7.40

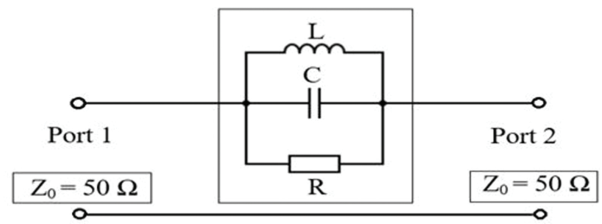

Fig. 2. Circuit model of the proposed DGS shape.

Therefore, the equivalent circuit of the DGS unit can be formulated by an *RLC* network [15] as shown in Figure 2. In addition, the frequency-independent components are utilized to simplify the ECM to be able to easily design a higher order filters up to Ku-band. However, there would be slight discrepancies at the frequency band that is higher than X-band.

As investigated in [15], the microstrip line exhibits bandstop response by using DGS section and its frequency characteristics can be calculated with effective inductance and capacitance using the following equations:

$$L = \frac{1}{4\pi^2 f_0^2 C}, \tag{1}$$

$$C = \frac{f_c}{2Z_0} \cdot \frac{1}{2\pi(f_0^2 - f_c^2)}, \tag{2}$$

$$R = \frac{2Z_0}{\sqrt{\frac{1}{|S_{11}(w_0)|^2} - \left(2Z_0\left(w_0 C - \frac{1}{w_0 L}\right)\right)^2 - 1}}. \tag{3}$$

Z_0 denotes the characteristic impedance of the transmission line in this equation. According to the equations, R, L, and C are calculated as 4.4 kΩ, 0.26 nH, and 0.82 pF, respectively.

Figure 3 shows the ECM and full wave EM simulation results. As shown in the figure, the ECM results show a unison with the EM simulation results at "f_0 = 10.81 GHz" and "fc = 9.8 GHz." On the other hand, a slight discrepancy has observed above 11 GHz. These discrepancies can be caused by the frequency-independent components in the ECM.

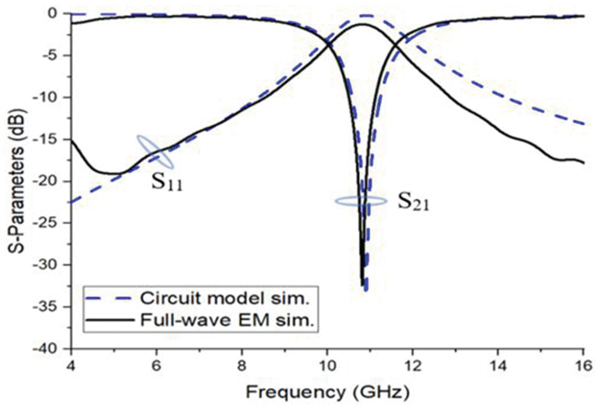

Fig. 3. Comparison between circuit model and EM simulation of the proposed microstrip filter (Step-1).

III. PARAMETRIC STUDY

So to investigate the response of different dimensions on the resonator, parametric analysis of the design of Step-1 is carried out. Figure 4 shows the effect of various dimensions of "*k*" on *S*-parameters. At this stage, "*k*" changes while other parameters remain constant. As observed in Figure 4, with the increase of "*k*," the insertion loss shifts to the lower frequency band.

The obtained results for different "*k*" values are calculated and summarized in Table 2. As observed in Table 2, with the increase of "*k*," the maximum point of the insertion loss (S_{21max}), f_C, and f_0 decreases. Moreover, the capacitance and resistance decrease with the increase of "*k*," while inductance increases. Moreover, the same procedure was similarly done for the other parameters and the obtained results were summarized in Tables 3 and 4.

According to Table 3, the length of "*m*" is increased with a period of 0.2 mm and the obtained changes are

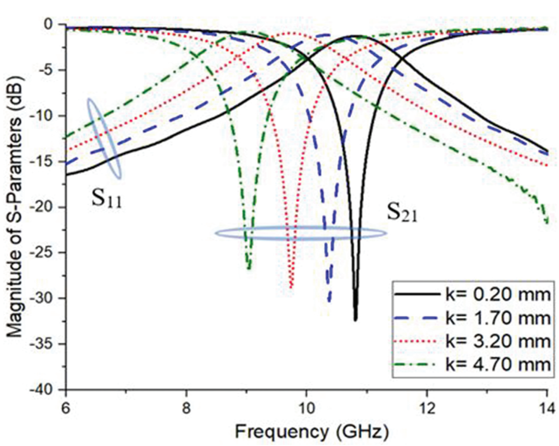

Fig. 4. Simulated *S-P*arameter results for different *k* values.

Table 2: Effect of the proposed DGS shape with different *k* values (m = 0.2 mm; g = 0.2 mm)

***k* (mm)**	**f_0(GHz)**	**f_c (GHz)**	**$S_{21\,\max}$ (dB)**
0.20	10.81	9.88	–32.79
1.70	10.36	9.38	–30.04
3.20	9.74	8.73	–28.94
4.70	9.03	8.06	–27.12
BW_{20dB} (GHz)	***L* (nH)**	***C* (pF)**	***R* (kΩ)**
0.18	0.26	0.82	4.40
0.19	0.30	0.77	3.27
0.18	0.35	0.74	2.85
0.22	0.40	0.77	2.15

Table 3: Effect of the proposed DGS shape with different *m* values (k = 0.2 mm, g = 0.2 mm)

***m* (mm)**	**f_0 (GHz)**	**f_c (GHz)**	**$S_{21\,\max}$ (dB)**
0.20	10.81	9.88	–32.79
0.40	9.54	8.18	–24.58
0.60	7.62	6.46	–12.24
0.80	6.93	5.80	–12.04
BW_{20dB}(GHz)	***L* (nH)**	***C* (pF)**	***R* (kΩ)**
0.18	0.26	0.82	4.40
0.25	0.54	0.51	1.86
0	0.63	0.69	0.65
0	0.64	0.82	0.34

investigated. The results show that the increase of "*m*" causes a decrease in f_c, f_0, S_{21max}, and stopband width (BW_{20dB}). In addition, inductance increases from 0.26 to 0.64 nH in this period. Capacitance and resistance values are in downward trend.

According to Table 4, it is interpreted that the increase of "*g*," the width of the proposed DGS pattern, causes almost no change on f_0 except the g = 0.1 mm dimension. Further f_c, resistance, and capacitance values are decreasing with the increase of "*g*" dimension. However, inductance and BW_{20dB} progressively increase. It is obvious from Table 4 that by tuning the "*g*" dimension, the desired attenuation pole frequency can be obtained.

IV. DGS-DMS BANDSTOP FILTER: DESIGN CONCEPT

The DGS-DMS BSF configuration is presented in this stage (Step-2). As shown in Figure 5, the filter design consists of two 0.8 mm × 2.9 mm identical rectangular DMS shapes which are placed with 6.1 mm distance on the strip line. These resonators are connected to connectors with the transmission line. The rectangular DMS structures behave as a bandstop element. This is an

Table 4: Effect of the proposed DGS shape with different g values (m = 0.2 mm; k = 0.2 mm)

g (mm)	f_0 (GHz)	f_c (GHz)	$S_{21\,max}$ (dB)
0.1	10.16	9.77	–25.51
0.2	10.81	9.88	–32.79
0.3	10.81	9.32	–32.42
0.4	10.86	8.53	–28.09
BW$_{20dB}$(GHz)	**L (nH)**	**C (pF)**	**R (kΩ)**
0.04	0.12	2.00	3.95
0.18	0.26	0.82	4.40
0.28	0.46	0.45	3.86
0.44	0.70	0.30	2.73

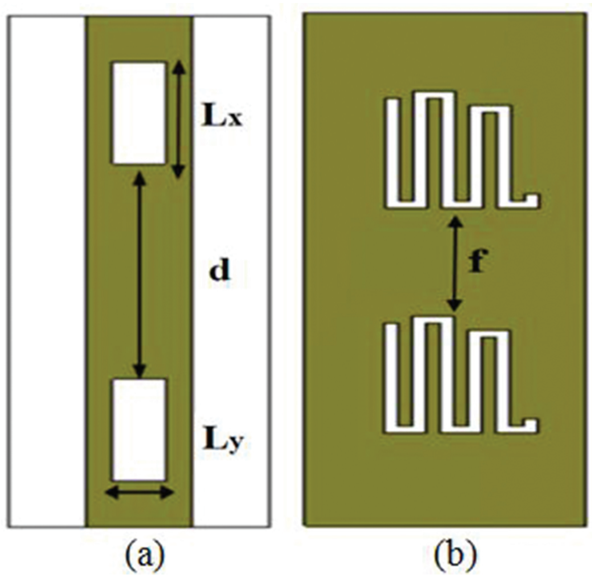

Fig. 5. Layout of the DMS-DGS structure (Step-2): (a) top layer; (b) bottom layer.

intended response from the filter. With this approach, the desired band stopping feature is achieved in the desired X-band frequency range.

In order to test the accuracy of the proposed model, the EM simulation result and the measurement results were compared. As shown in Figure 6, by using the combination of two rectangular DMS and two identical DGS shapes, there occurs a BSF behavior with 960 MHz stopband width (SBW$_{20dB}$).

In these results, the situation that can be evaluated as negative is the passband region between 4–8 GHz and 12–16 GHz. This issue will be discussed in the next section.

V. BSF USING COMPENSATED CAPACITORS

In order to enhance the performance of the passband of the filter Step-2, three compensated capacitors

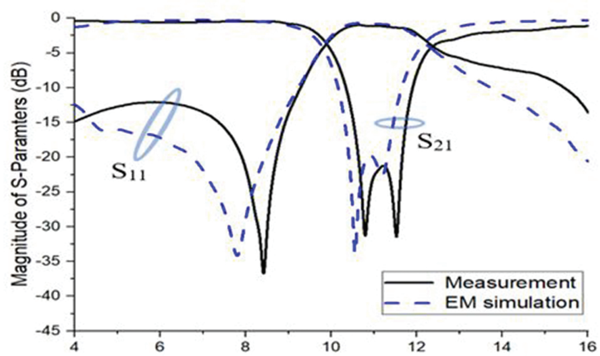

Fig. 6. Comparison of simulated and measured results of DMS-DGS bandstop filter (Step-2).

are added as shown in Figure 7. This new final design is called Step-3. The two DMS shapes and the added parallel microstrip capacitors are directly connected with the SMAs. Figure 8 shows the 3D layout of the proposed BSF filter.

Figure 9 indicates the comparison of the EM simulation results of the designed filters in Step-2 and Step-3. In the EM simulation results, it is seen that insertion loss characteristics of Step-2 and Step-3 are almost similar to each other. On the other hand, Step-3 has a better bandpass performance in the frequency bandwidths of 4–7.1 GHz and 12.2–16 GHz. The added conductors with the size ($w_x \times w_y$ and $p_x \times p_y$) on the strip line allows to increase the coupling capacitance between 50 Ω microstrip line and proposed DGS shape [17]. For this reason, the characteristic of the filter is related to the

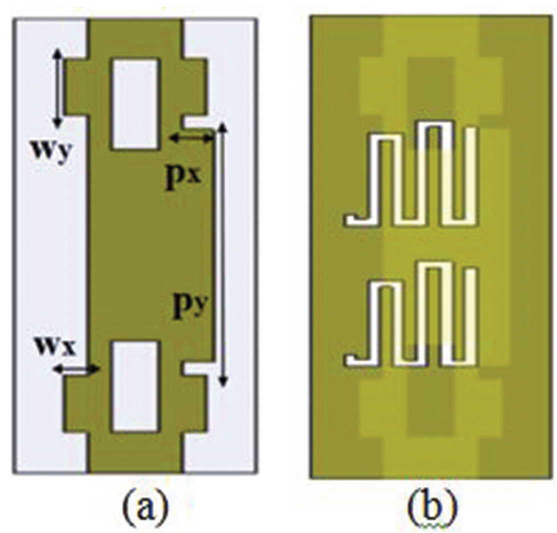

Fig. 7. Layout of the final bandstop filter structure: (a) top layer; (b) bottom layer.

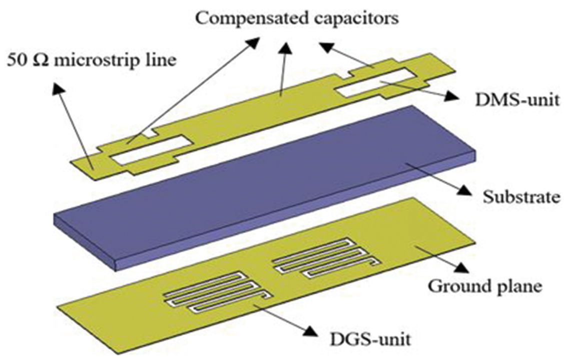

Fig. 8. 3D layout of the proposed bandstop filter.

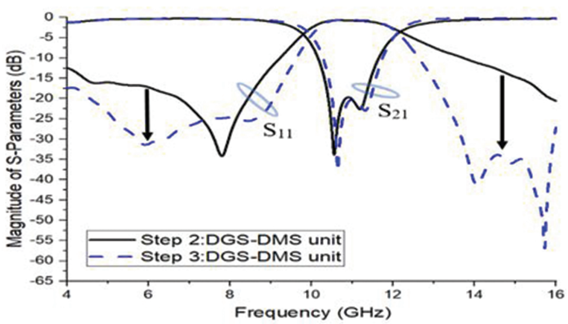

Fig. 9. Comparison of simulated results of the structures presented in Step-2 and Step-3.

physical dimensions of the added capacitors and DGS shape.

According to the proposed theory, the proposed BSF can be modeled as two cascaded DGS shapes along with three shunt capacitors C_m and C_x. Figure 10 represents the equivalent circuit of the proposed BSF. In the design, two identical DGS shapes are used to enhance the stop-band rejection attributions of the filter. The values of the L_1, C_1, and R_1 parameters were extracted by utilizing eqn (1)–(3), which were explained in Section II. The equivalent capacitance can be obtained from [18] as

$$w_c C = \frac{1}{Z_{0C}} \sin\left(\frac{2\pi l_C}{\lambda_{gC}}\right) + 2 * \frac{1}{Z_{0L}} \tan\left(\frac{\pi l_L}{\lambda_{gL}}\right). \quad (4)$$

In this equation, Z_{0C}, l_C, l_L, w_c, λ_{gC}, and λ_{gL} correspond to characteristic impedance, physical length of the added capacitor, physical width of the series reactance, width of the added capacitance, and guided wavelengths, respectively. From this equation, the values of C_m and C_x were calculated as 0.04 and 0.3 pF, respectively. Figure 11 shows the S-parameter results of the extracted ECM. The circuit model simulation results are unison with the EM results in the 4–12 GHz frequency bandwidth. However, there is a difference in the higher

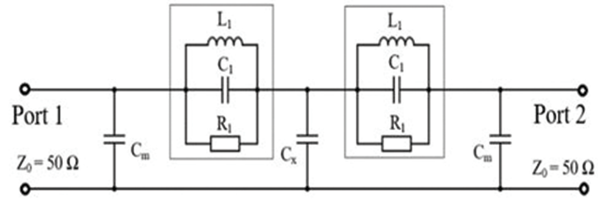

Fig. 10. Equivalent circuit model of the BSF.

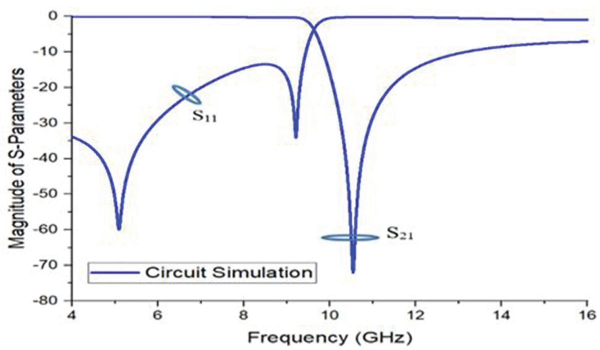

Fig. 11. S-parameter results of the circuit model.

frequency (>12 GHz). The difference between the equivalent model and measurement results in the higher frequencies can be caused by the frequency-independent components that are utilized in the ECM.

The magnetic field distribution of the proposed filter was investigated for the passband frequency of 6 GHz and stopband frequency of 11 GHz. As noticed from Figure 12, the current is mainly concentrated along the edges of the modified meander DGS pattern. The green color illustrates large values, whereas the blue color illustrates the small values of the magnetic field. The signal is blocked in Port 1 (the input feed port) on the stopband region at 11 GHz, with no energy flow around

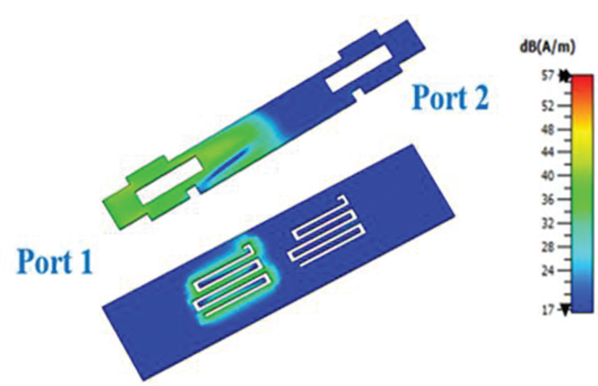

Fig. 12. EM field distribution results at 11 GHz (stopband).

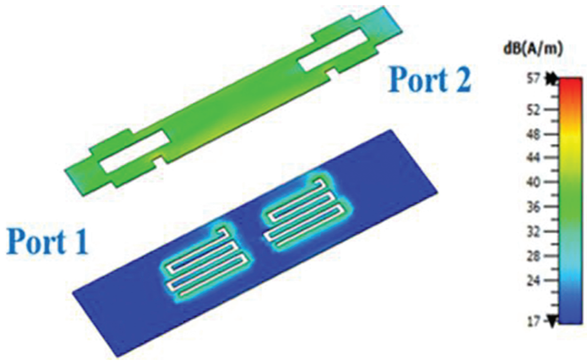

Fig. 13. EM field distribution results at 6 GHz (passband).

port 2. The field was mainly focused over one DGS element as two identical electric and magnetic energies [19]. On the other hand, in passband region at 6 GHz, the RF power was transmitted from port 1 to port 2 as shown in Figure 13. The magnetic-field patterns declare compatible coupling between the feeds and the DGS structures.

VI. FABRICATION AND MEASUREMENT

Figure 14 presents the photograph of the manufactured compact BSF. The S-parameter measurements were performed by utilizing Anritsu 3680K universal test fixture and Keysight N5224B Network Analyzer as shown in Figure 15.

As shown in Figure 16, in the measurement, the suppression level of the proposed BSF filter (Step-3) was better than 20 dB in the frequency bandwidth of 10.8–11.8 GHz as given in Figure 16. The return loss (S_{11}) was less than –17 dB in the passbands. The measured *S*-parameter results were shifted approximately 250 MHz to higher frequencies with respect to the EM simulation results.

Fig. 14. Photograph of the manufactured DMS-DGS BSF.

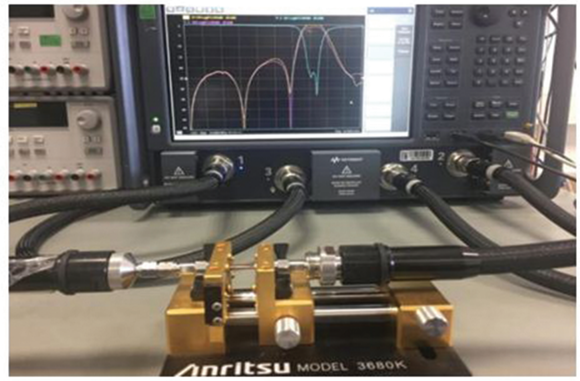

Fig. 15. Photograph of the measurement setup.

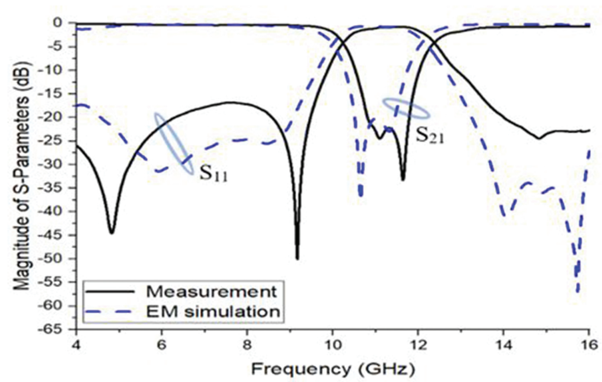

Fig. 16. Measured and simulated *S*-parameters of the proposed BSF (Step-3).

The detailed summary of different BSFs suggested for the same frequency range is listed in Table 5. N/A denotes "not available" and E.C denotes "equivalent circuit."

The proposed filter has a very compact size of 57.12 mm^2 with respect to other reported works. This work has the best $|S_{11}|$ value except [20]. The insertion loss in stopband was compared and good results were achieved except [23]. The values in [23] include the simulation results. Rejection bandwidth (RB) is the bandwidth of insertion loss $|S_{21}|$ at –3 dB and stopband bandwidth (SBW) is defined as the bandwidth of insertion loss $|S_{21}|$ at –20 dB. The obtained SBW and RB values were suitable for X-band applications with its compact size. This work also focuses on circuit analysis in addition to the production and simulation of design.

Table 5: Comparison of the designed BSF with the reported works

Ref. no.	Area (mm^2)	SBW (GHz)	RB (GHz)	S_{11} (dB)	S_{21} (dB)	E.C.
[20]	210	0.5	1.1	–20	–24	X
[21]	150	3.3	4	–10	–19	X
[22]	150	2.6	5.3	N/A	–27	X
[23]	90.11	2.55	4	–15	–52	X
This work	57.12	1	2	–17	–23	X

VII. CONCLUSION

A novel design of bandstop microstrip filter has been presented. The gradual DMS-DGS technique in combination with added compensated capacitors was utilized to achieve the desired stopband characteristic. The results were shown that the proposed filter has a bandstop effect that includes from 10.3 to 12.3 GHz. A prototype of the proposed BSF was manufactured, and it was observed that EM simulation results are in compliance with the measurement results. Due its compactness, low cost, and high suppression performance, the proposed filter is a good candidate for radar applications.

ACKNOWLEDGMENT

The authors would like to thank ASELSAN Inc. for the support provided in the fabrication and measurement of the data used in this work.

REFERENCES

[1] D. Lu, M. Yu, N. S. Barker, Z. Li, W. Li, and X. Tang, "Advanced synthesis of wide-tuning-range frequency-adaptive bandpass filter with constant absolute bandwidth," *IEEE Trans. Microw. Theory Techn.*, vol. 67, no. 11, pp. 4362-4375, Nov. 2019.

[2] D. Psychogiou and R. Gomez-Garcia, "Multi-mode-cavity-resonator-based bandpass filters with multiple levels of transfer-function adaptivity," *IEEE Access*, vol. 7, pp. 24759-24765, 2019.

[3] X. Cao, Z. X. Tang, and F. Wang, "A method of designing dual-band bandpass filter using the hexagon CRLH resonators and cascaded defected ground structure," *Microw. Opt. Technol. Lett.*, vol. 57, no. 8, pp. 1876-1879, Aug. 2015.

[4] Y. Han, Z. Liu, C. Zhang, C. Mei, Q. Chen, K. Hu, and S. Yuan, "A flexible microstrip low-pass filter design using asymmetric pi-shaped DGS," *IEEE Access*, vol. 7, pp. 49999-50006, 2019.

[5] F.-C. Chen, H.-T. Hu, J.-M. Qiu, and Q.-X. Chu, "High-selectivity low-pass filters with ultrawide stopband based on defected ground structures," *IEEE Trans. Compon., Packag., Manuf. Technol.*, vol. 5, no. 9, pp. 1313-1319, Sep. 2015.

[6] H. Elftouh, N. A. Touhami, M. Aghoutane, S. E. Amrani, A. Tazon, and M. Boussouis, "Miniaturized microstrip patch antenna with defected ground structure," *Progress in Electromagnetics Research C*, vol. 55, pp. 25-33, 2014.

[7] S. Verma, E. Sareen, and M. S. Hashmi, "A miniaturized dual-band right triangle defected ground structure band stop filter for energy harvesting applications," *in Proc. IEEE MTT-S Int. Microwave and RF Conf.*, Kolkata, India, pp. 1-3, 2018.

[8] A. Kumar and M. V. Kartikeyan, "Design and realization of microstrip filters with new defected ground structure (DGS)," *Engineering Science and Technology, an International Journal.*, vol. 20, pp. 679-686, Apr. 2017.

[9] M. K. Khandelwal, B. K. Kanaujia, and S. Kumar "Defected ground structure: fundamentals, analysis, and applications in modern wireless trends," *International Journal of Antennas and Propagation*, pp. 1-22, 2017.

[10] D. S. La, Y. H. Lu, S. Y. Sun, N. Liu, and J. L. Zhang, "A novel compact band stop filter using defected microstrip structure," *Microw. Opt. Technol. Lett.*, vol. 53, pp. 433-435, Feb. 2011.

[11] J. A. Tirado-mendez and H. Jardon-aguilar, "Comparison of defected ground structure (DGS) and defected microstrip structure (DMS) behavior at high frequencies," *Electrical and Electronics Engineering, 2004. (ICEEE). 1st International Conference*, pp. 7-10, 2004.

[12] T. Praludi, Y. Y. Maulana, E. R. Yuliasih, D. P. Kurniadi, and Y. Taryana "Dual-band bandstop filter microstrip using T-DMS and U-DGS," *2019 International Conference on Radar, Antenna, Microwave, Electronics, and Telecommunications (ICRAMET)*, 2019.

[13] D. Upadhyay, I. Acharya, and A. K. Gupta, "DGS & DMS based hexagonal fractal antenna for UWB applications," *2015 International Conference on Communications and Signal Processing (ICCSP)*, pp. 0176-0179, 2-4 Apr. 2015.

[14] A. Kumar and M. V. Kartikeyan, "A design of microstrip bandpass filter with narrow bandwidth using DGS/DMS for WLAN," *IEEE Conference Publications*, 2013.

[15] X. Chen, L. Wang, L. Weng, and X. Shi, "Compact low pass filter using novel elliptic shape DGS,"

Microwave Opt Technol Lett., vol. 51, pp. 1088-1091, 2009.

[16] CST Microwave Studio, ver. 2008, Computer Simulation Technology, Framingham, MA, 2008.

[17] A. Boutejdar, A. A. Ibrahim, and E. P. Burte, "Design of a novel ultrawide stopband lowpass filter using a DMS-DGS technique for radar applications," *International Journal of Microwave Science and Technology.*, Article ID 101602, Hindawi Publishing Corporation, 2015.

[18] J. S. Hong and M. J. Lancaster, *Microstrip Filters for RF/Microwave Applications*. John Wiley & Sons, Inc., New York, 2001.

[19] M. Challal, A. Boutejdar, and A. Azrar, "Design of compact low-pass filter with large reject band using open circuit stubs and two cascaded DGS quasitriangular resonator," *Microwave Opt Technol Lett.*, vol. 55, pp. 122-127, 2013.

[20] B. Shrestha and N.-Y. Kim, "Compact and miniaturized bandstop filter developed using slot spurline technique," *Microwave and Optical Technology Letters*, vol. 56, no. 5, pp. 1029-1031, Mar. 2014.

[21] H. Keivani, N. Adlband, and Y. Ojaroudi, "Compact band-stop X-band filter using triple meanderline-ring defected ground structures," *Applied Computational Electromagnetics Society (ACES) Journal*, vol. 30, no. 8, Aug. 2015.

[22] M. Pourbagher, N. Ojaroudi, C. Ghobadi, and J. Nourinia, "Compact band-stop filter for X-band transceiver in radar applications," *Applied Computational Electromagnetics Society (ACES) Journal*, vol. 30, no. 4, Apr. 2015.

[23] A. O. Ertay, and S. Simsek, "A compact bandstop filter design for X-band applications," *International Symposium on Fundamentals of Electrical Engineering (ISFEE)*, *IEEE*, June 30-July 2, 2016.

Burak Dokmetas received the B.S. degree in electrical and electronic engineering from Inonu University, Malatya, Turkey, in 2010, and the M.S. degree in electrical and electronic engineering from Gazi University, Ankara, Turkey, in 2016. He is currently working toward the Ph.D. degree in electrical and electronic engineering with the Gazi University.

His main interests are microwave antennas, microwave filters, electromagnetic theory, and radar systems.

Galip Orkun Arican received the B.S. degree from Bilkent University, Ankara, Turkey, in 2010, the M.S. degree from Middle East Technical University, Ankara, Turkey, in 2014, and the Ph.D. degree from Gazi University, Ankara, Turkey, in 2021.

From 2010 to 2015, he worked as a MMIC Design Engineer with Nanotechnology Research Center, Bilkent University. Since 2015, he has been working as a RF/Microwave Design Engineer with ASELSAN Inc. His research interests include high frequency applications, GaN/GaAs MMICs, satellite communication, microwave antennas, filters, and electromagnetic theory.

Nursel Akcam received the M.S. and Ph.D. degrees in electrical and electronics engineering from the University of Gazi, Ankara, Turkey, in 1993 and 2001, respectively.

She has been a Professor of Electrical and Electronics Engineering with University of Gazi. Her research interests include asymptotic high-frequency methods, numerical methods in electromagnetic theory, blocking aperture in reflector antennas, communication theory, radar systems, microwave antennas, and microwave filters.

Erdem Yazgan received the B.S. and M.S. degrees from the Middle East Technical University, Ankara, Turkey, and the Ph.D. degree from Hacettepe University, Ankara, Turkey, in 1980, all in electrical and electronics engineering.

In 1989, she was a Visiting Professor with Essex University, Essex, U.K. From 1994 to 1995, she was with the Electroscience Laboratory, The Ohio State University, Columbus, OH, USA. Between 1990 and 2015, she was a Professor with the Department of Electrical and Electronics Engineering, Hacettepe University. She joined the Engineering faculty of TED University as Chair for Electrical-Electronics Engineering in 2015. She was a Fulbright Researcher. Her research interests include HF propagation, low altitude radar systems, mobile communications, antennas, MICs, reflector and microstrip antennas, Gaussian beam solutions, conformal mapping, satellite communication, and medical electronics.

Mainlobe Interference Suppression via Eigen-Projection Processing and Covariance Matrix Reconstruction in Array Antenna

Bin Yang[1], **Wenxing Li**[1], **and Si Li**[2]

[1]College of Information and Communication Engineering, Harbin Engineering University, Harbin, Heilongjiang 150001, China

[2]School of Electronics and Information, Jiangsu University of Science and Technology, Zhenjiang, Jiangsu 212003, China
yb_alonline@126.com, liwenxing@hrbeu.edu.cn, lisi0511@just.edu.cn

Abstract – When the received data contains the desired signal, the performance of most mainlobe interference suppression methods is seriously degraded. To solve this problem, a novel mainlobe interference suppression method based on eigen-projection processing and covariance matrix reconstruction for array antenna is proposed in this paper. The method constructs the sidelobe interference plus noise covariance matrix (SINCM) and remove the mainlobe data of the covariance matrix. Then, it uses eigen-projection technology to remove the mainlobe interference in the received data and correct the SINCM to make the proposed method has better ability to suppress the mainlobe interference and sidelobe interference when the received data contains the desired signal. Simulation results demonstrate the superior performance of the proposed beamformer relative to other existing methods.

Index Terms – array antenna, eigen-projection, mainlobe interference, reconstruction

I. INTRODUCTION

The purpose of robust adaptive beamforming technology is to suppress other signals except the desired signal under the irrational environment, so as to improve the output performance of the beamformer. As a basic implementation to achieve spatial filtering, adaptive beamforming has been applied to several areas, such as array antenna, radar, sonar, remote sensing, seismology, wireless communication, etc. [1, 2]. Usually, traditional adaptive beamformer mainly focused on the suppression of sidelobe interference [3]. However, for array antenna, interference would distort the mainlobe thus significantly decrease performance once it fell into the mainlobe area. To solve this problem, many approaches of mainlobe interference suppression have been proposed [4–16].

The block matrix preprocessing (BMP) method is developed in [4], which works well when the direction of mainlobe interference is known. However, it also gives rise to the reduction of the degrees of freedom. For the problem of mainlobe direction shifting caused by the mainlobe interference suppression based on blocking matrix preprocess, a modified BMP method is proposed in [5]. But its performance improvement is limited. The eigen-projection matrix preprocessing (EMP) method is proposed in [6], which suppresses the mainlobe interference by eigen-projection method. However, this method is prone to mainlobe offset and sidelobe rise. To solve this problem, various modified EMP methods are proposed in [7–9]. In order to suppress multiple mainlobe interferences, a new method based on EMP method and similarity constraints is proposed in [10]. The above methods can suppress the mainlobe interference effectively only when there is no desired signal in the received data, otherwise they are invalid. But in fact, it is difficult for us to get such data. In order to overcome this problem, a robust mainlobe interference suppression method is proposed in [11], which achieves high accuracy of the direction of arrival and power estimation of source. However, its computational complexity is very high. To further improve the array antenna performance, modified EMP methods are proposed in [12, 13]. Both methods reconstruct the sidelobe interference plus noise covariance matrix (SINCM) and calculate the eigen-projection matrix to remove the mainlobe interference in the received data of array antenna. However, once the received data was processed via eigen-projection, the original sampling covariance matrix would change. Hence, the weight vector obtained from SINCM cannot suppress the sidelobe interference of the processed data. Sidelobe null shifts, which reduce the ability of array antenna to suppress sidelobe interference, and the output performance is far from the optimal value. A mainlobe interference suppression method for bistatic airborne radar is proposed in [14], the core idea of this method is based on BMP method to remove the mainlobe

Submitted On: November 3, 2020
Accepted On: October 21, 2021
https://doi.org/10.13052/2021.ACES.J.361111

interference. This means that this method wastes a degree of freedom. In [15, 16], the methods for distributed array to suppress mainlobe interference are proposed. In order to facilitate the construction of the signal model, this paper only considers the uniform linear array (ULA) as the research object.

In this paper, a novel mainlobe interference suppression method based on eigen-projection processing and covariance matrix reconstruction for array antenna is proposed. The proposed method first calculates the eigen-projection matrix through the reconstructed mainlobe interference plus noise covariance matrix (MINCM). Then, the SINCM is reconstructed and processed using the eigen-projection matrix to form null at the direction of sidelobe interference accurately. Finally, we obtain the weight vector. Simulation results show that the proposed method has higher output signal-to-interference-plus-noise ratio (SINR) when the desired signal is contained in the received data.

The advantages of the proposed method are as follows:

1. The output SINR of the proposed method is higher when the array antenna suffers from the mainlobe interference.
2. The array antenna has better ability to suppress mainlobe interference and sidelobe interference when the received data contains desired signal.

The rest of this paper is summarized below. The signal model is described in Section II. Section III describes the proposed method. Simulation results are described in Section IV. In Section V, we make a conclusion.

II. SIGNAL MODEL OF ARRAY ANTENNA

Consider a ULA, which is composed of N omnidirectional antennas spaced by half a wavelength, receiving uncorrelated far-field narrowband signals. The sample data of array antenna at the k^{th} snapshot is modeled as:

$$\begin{aligned}\mathbf{x}(k) &= \mathbf{x}_s(k)+\mathbf{x}_i(k)+\mathbf{x}_n(k)\\ &= \mathbf{a}(\theta_0)s_0(k)+\sum_{m=1}^{M+S}\mathbf{a}(\theta_m)s_m(k)+\mathbf{n}(k),\end{aligned} \tag{1}$$

where $\mathbf{x}_s(k)=\mathbf{a}(\theta_0)s_0(k)$, $\mathbf{x}_i(k)=\sum_{m=1}^{M+S}\mathbf{a}(\theta_m)s_m(k)$ and $\mathbf{x}_n(k)=\mathbf{n}(k)$ denote the desired signal, interference and noise, respectively. M and S represent the number of mainlobe interferences and sidelobe interferences, respectively. Moreover, these components are mutually independent. $\mathbf{n}(k)$ is the additive spatially Gaussian white noise with zero mean and variance σ_n^2. $\mathbf{a}(\theta_0)$ and $\mathbf{a}(\theta_m)$ denote the steering vector of the desired signal and the interferences, respectively. For the signal with the direction of θ, the steering vector of the signal can be expressed as:

$$\mathbf{a}(\theta)=\left[1,e^{-j\frac{2\pi d}{\lambda}\sin\theta},\cdots,e^{-j\frac{2\pi(N-1)d}{\lambda}\sin\theta}\right]^T, \tag{2}$$

where $(\bullet)^T$ is the transpose product, λ is the wavelength of the signal, and $d=\lambda/2$ is the distance between two adjacent antennas of the ULA. The output of the array antenna is given as:

$$y(k)=\sum_{i=1}^{N}w_i^*x_i(k)=\mathbf{w}^H\mathbf{x}(k), \tag{3}$$

where $\mathbf{w}=[w_1,w_2,\cdots,w_N]^T$ is the weight vector of the array antenna. The minimum variance distortionless response (MVDR) beamformer is obtained by minimizing the variance of the interference and noise at the output while constraining the target response to be unity. It can be formulated as:

$$\begin{aligned}&\min_{\mathbf{w}}\ \mathbf{w}^H\mathbf{R}_{i+n}\mathbf{w}\\ &\text{subject to } \mathbf{w}^H\mathbf{a}(\theta_0)=1,\end{aligned} \tag{4}$$

where $\mathbf{a}(\theta_0)$ is the desired signal steering vector, $\mathbf{R}_{i+n}$ is the interference plus noise covariance matrix (INCM) matrix. In practice, $\mathbf{R}_{i+n}$ is unavailable, so replace it with the following sample covariance matrix (SCM):

$$\mathbf{R}_x=\frac{1}{K}\sum_{k=1}^{K}\mathbf{x}(k)\mathbf{x}^H(k), \tag{5}$$

where K is the number of snapshots. Therefore, by solving the above problems, the weighted vector of the beamformer can be obtained as:

$$\mathbf{W}_{\text{opt}}=\frac{\mathbf{R}_x{}^{-1}\mathbf{a}(\theta_0)}{\mathbf{a}^H(\theta_0)\mathbf{R}_x{}^{-1}\mathbf{a}(\theta_0)}. \tag{6}$$

It is the sample matrix inversion (SMI) beamformer.

III. THE PROPOSED METHOD

In this section, a mainlobe interference suppression method via eigen-projection processing and covariance matrix reconstruction for array antenna is proposed.

A. The construction of eigen-projection matrix

For a ULA, the mainlobe width M_{width} can be expressed as:

$$M_{\text{width}}=2\arcsin\left(\frac{\lambda}{Nd}+\sin\theta_0\right), \tag{7}$$

where θ_0 is the direction of the desired signal. Therefore, the mainlobe angle area Θ_m of the array antenna can be expressed as:

$$\Theta_m=\left[\theta_0-\frac{M_{\text{width}}}{2},\theta_0+\frac{M_{\text{width}}}{2}\right]. \tag{8}$$

It is assumed that the desired signal angle area Θ_0 is:

$$\Theta_0=[\theta_0-\Delta\theta_0,\theta_0+\Delta\theta_0]. \tag{9}$$

There is no mainlobe interference in Θ_0. The incident angle area of mainlobe interference Θ_{mi} is as follow:

$$\begin{aligned}\Theta_{mi}=&\left[\theta_0-\tfrac{M_{\text{width}}}{2},\theta_0-\Delta\theta_0\right]\bigcup\\ &\left[\theta_0+\Delta\theta_0,\theta_0+\tfrac{M_{\text{width}}}{2}\right].\end{aligned} \tag{10}$$

Process the SCM with eigen-decomposition.

$$\begin{aligned}\mathbf{R}_x &= \sum_{i=1}^{N} \tilde{\lambda}_i \tilde{\mathbf{u}}_i \tilde{\mathbf{u}}_i{}^H \\ &= \tilde{\mathbf{U}}_\mathbf{s} \tilde{\Lambda}_\mathbf{s} \tilde{\mathbf{U}}_s{}^H + \tilde{\mathbf{U}}_\mathbf{n} \tilde{\Lambda}_\mathbf{n} \tilde{\mathbf{U}}_n{}^H,\end{aligned} \tag{11}$$

where $\tilde{\mathbf{U}}_s$ is $N \times (M+S+1)$ signal subspace, $\tilde{\Lambda}_s$ is the matrix of corresponding larger eigenvalues, $\tilde{\mathbf{U}}_n$ is the $N \times (N-M-S-1)$noise subspace, and $\tilde{\Lambda}_n$ is the corresponding eigenvalue matrix.

In the above angle area Θ_{mi}, the MINCM $\mathbf{R}_{\text{Min}}$ of the mainlobe interference region is then reconstructed by using MUSIC spatial spectrum estimation, such that:

$$\mathbf{R}_{\text{Min}} = \sum_{i=1}^{\Theta_{mi}/\Delta\theta} \frac{\mathbf{a}(\theta_i)\mathbf{a}^H(\theta_i)}{\mathbf{a}^H(\theta_i)\tilde{\mathbf{U}}_\mathbf{n}\tilde{\mathbf{U}}_n{}^H\mathbf{a}(\theta_i)}\Delta\theta. \tag{12}$$

By eigen-decomposing the matrix, $\mathbf{R}_{\text{Min}}$ can then be expressed as:

$$\mathbf{R}_{\text{Min}} = \sum_{i=1}^{N} \frown{\lambda}_i \frown{\mathbf{u}}_i \frown{\mathbf{u}}_i{}^H, \tag{13}$$

where $\frown{\lambda}_i$ is the eigenvalue in order of value, $\frown{\lambda}_1 > \frown{\lambda}_2 > \cdots > \frown{\lambda}_M > \cdots > \frown{\lambda}_N$, $\frown{\mathbf{u}}_i$ is the corresponding eigenvector. Meanwhile, the mainlobe interference subspace $\frown{\mathbf{U}}_M$ can be expressed as:

$$\frown{\mathbf{U}}_M = \left[\frown{\mathbf{u}}_1, \cdots, \frown{\mathbf{u}}_M\right]. \tag{14}$$

The eigen-projection matrix which can suppress the mainlobe interference can be formulated as:

$$\frown{\mathbf{B}} = \mathrm{I} - \frown{\mathbf{U}}_M \left(\frown{\mathbf{U}}_M^H \frown{\mathbf{U}}_M\right)^{-1} \frown{\mathbf{U}}_M^H. \tag{15}$$

B. The reconstruction of SINCM

According to eqn. (8), the sidelobe angle area Θ_s can be expressed as:

$$\begin{aligned}\Theta_s = &\left[-90^\circ, \theta_0 - \tfrac{M_{\text{width}}}{2}\right] \cup \\ &\left[\theta_0 + \tfrac{M_{\text{width}}}{2}, 90^\circ\right].\end{aligned} \tag{16}$$

In this angle area, the simple spatial spectrum estimation method is used to determine the approximate angle regions of sidelobe interference $\Theta_{I_1}, \Theta_{I_2}, \cdots, \Theta_{I_S}$. The Capon spatial spectrum method [17] is used to determine the power at each position of the spatial spectrum:

$$P(\theta) = \frac{1}{\boldsymbol{a}^H(\theta)\mathbf{R}_x{}^{-1}\boldsymbol{a}(\theta)}. \tag{17}$$

The INCM in each sidelobe interference angle area is expressed as following:

$$\bar{\mathbf{R}}_i = \sum_{l=1}^{\Theta_I/\Delta\theta} \frac{\boldsymbol{a}(\theta_l)\boldsymbol{a}^H(\theta_l)}{\boldsymbol{a}^H(\theta_l)\mathbf{R}_x{}^{-1}\boldsymbol{a}(\theta_l)}\Delta\theta. \tag{18}$$

Then the SINCM of the whole sidelobe region can be expressed as follows:

$$\begin{aligned}\bar{\mathbf{R}}_{\text{Sin}} &= \sum_{i=1}^{S} \bar{\mathbf{R}}_i \\ &= \sum_{i=1}^{s} \sum_{l=1}^{\Theta_i/\Delta\theta} \frac{\boldsymbol{a}(\theta_l)\boldsymbol{a}^H(\theta_l)}{\boldsymbol{a}^H(\theta_l)\mathbf{R}_x{}^{-1}\boldsymbol{a}(\theta_l)}\Delta\theta\end{aligned}. \tag{19}$$

According to eqn. (15), process the receiving data using the eigen-projection matrix. The processed data can be expressed as:

$$\bar{\mathbf{x}}(k) = \frown{\mathbf{B}}\mathbf{x}(k). \tag{20}$$

When desired signal of array antenna is contained in the received signal, the MVDR beamforming algorithm will be easily disturbed by the desired signal direction error, resulting a poor output performance. Assume that there is no desired signal in the received signal, eqn. (20) became:

$$\begin{aligned}\bar{\mathbf{x}}(k) &= \frown{\mathbf{B}}\left(\mathbf{x}_{\text{Mi}}(k) + \mathbf{x}_{\text{Si}}(k) + \mathbf{x}_n(k)\right) \\ &= \frown{\mathbf{B}}\mathbf{x}_{\text{Mi}}(k) + \frown{\mathbf{B}}\mathbf{x}_{\text{Si}}(k) + \frown{\mathbf{B}}\mathbf{x}_n(k) \\ &\approx \frown{\mathbf{B}}\mathbf{x}_{\text{Si}}(k) + \frown{\mathbf{B}}\mathbf{x}_n(k).\end{aligned} \tag{21}$$

The corresponding covariance matrix can be formulated as:

$$\begin{aligned}\bar{\mathbf{R}}_x &= \frac{1}{K}\sum_{k=1}^{K} \bar{\mathbf{x}}(k)\bar{\mathbf{x}}^{\mathrm{H}}(k) \\ &= \sum_{i=1}^{S} \sigma_i^2 \frown{\mathbf{B}}\mathbf{a}(\theta_i)\mathbf{a}^H(\theta_i)\frown{\mathbf{B}}^H + \sigma_n^2 \frown{\mathbf{B}}\frown{\mathbf{B}}^H \\ &= \frown{\mathbf{B}}\mathbf{R}_{\text{Si}}\frown{\mathbf{B}}^H + \sigma_n^2 \frown{\mathbf{B}}\frown{\mathbf{B}}^H,\end{aligned} \tag{22}$$

where σ_i^2 is the power of i^{th} sidelobe interference, σ_n^2 is the power of noise. $\mathbf{R}_{\text{Si}}$ is the sidelobe interference covariance matrix. Then, the reconstructed SINCM can be expressed as:

$$\mathbf{R}_{\text{Sin}} = \bar{\mathbf{R}}_x + \sigma_n^2\left(\mathbf{I} - \frown{\mathbf{B}}\frown{\mathbf{B}}^H\right). \tag{23}$$

In the proposed method, the power of noise $\hat{\sigma}_n^2$ can be expressed as:

$$\hat{\sigma}_n^2 = \frac{\sum_{n=1}^{N-M-S-1}\tilde{\Lambda}_n}{N-M-S-1}. \tag{24}$$

According to eqn. (19), (23), and (24), the SINCM $\hat{\mathbf{R}}_{\text{Sin}}$ can be reconstructed as:

$$\hat{\mathbf{R}}_{\text{Sin}} = \frown{\mathbf{B}}\left(\bar{\mathbf{R}}_{\text{Sin}} - \hat{\sigma}_n^2\mathbf{I}\right)\frown{\mathbf{B}}^H + \hat{\sigma}_n^2\mathbf{I}. \tag{25}$$

C. Calculate the weight vector of array antenna

Based on the previous discussion, replace the SCM in eqn. (6) with $\hat{\mathbf{R}}_{\text{Sin}}$ in eqn. (25), then the adaptive weight vector of array antenna can be expressed as:

$$W = \frac{\hat{\mathbf{R}}_{\text{Sin}}{}^{-1}a(\theta_0)}{a^{\mathrm{H}}(\theta_0)\hat{\mathbf{R}}_{\text{Sin}}{}^{-1}a(\theta_0)}. \tag{26}$$

Therefore, the output data of array antenna can be expressed as:

$$y(k) = \mathbf{W}^H\frown{\mathbf{B}}\mathbf{x}(k) \tag{27}$$

D. Summary of proposed method

The proposed algorithm can be implemented by several steps and summarized as follows:

1. Construct the covariance matrix $\mathbf{R}_{\text{Min}}$ as eqn. (12);
2. Eigen-decompose $\mathbf{R}_{\text{Min}}$ as eqn. (13) and construct the eigen-projection matrix as eqn. (15);

3. Reconstruct the SINCM $\hat{\mathbf{R}}_{\mathrm{Sin}}$ with eqn. (19) and (25);
4. Calculate the adaptive weight vector of array antenna by eqn. (26).

IV. SIMULATIONS AND COMPARISONS

Consider a ULA with 16 antennas spaced half-wavelength. The desired signal direction is 0° with signal-to-noise ratio (SNR) 0 dB. Two sidelobe interferences impinge on the ULA from $-25°$ and 35° with interference-to-noise ratio (INR) 25 dB and 30 dB respectively. A mainlobe interference impinge from 4° with INR 5 dB. The snapshots of received data is 100. The signal and interference are statistically independent, and the added noise is Gaussian white noise. All experimental results are from 100 independent Monte Carlo experiments. The proposed method in this paper is compared to SMI, EMP-CMR [7], EMP-SC [10], MIS-CIE [11], EMP-CMIR [12], and EMP-CMSR [13]. For the case of EMP-CMR and EMP-CMIR methods, there is no desired signal in the received data.

A. Adaptive beampatterns of array antenna

In Figure 1, the beam patterns of every method are compared. It is obvious that the beampattern of SMI method is affected, while other methods can form nulls at the direction of interference effectively.

B. Output data comparison of array antenna

Figure 2 compares the output data of every method with desired signal. It is observed from Figure 2 that the output data of EMP-CMR, EMP-SC, MIS-CIE, and the proposed method are more similar to the desired signal. Table 1 shows the correlation coefficient between the output data of every method and the real desired signal. It is obvious that the correlation coefficient of the proposed method is the highest.

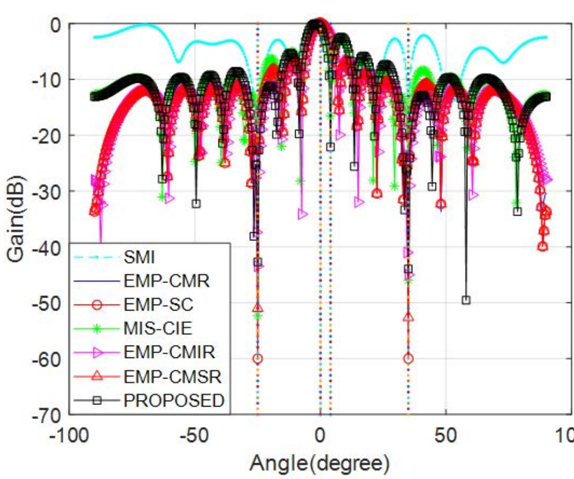

Fig. 1. Adaptive beampatterns of array antenna comparison.

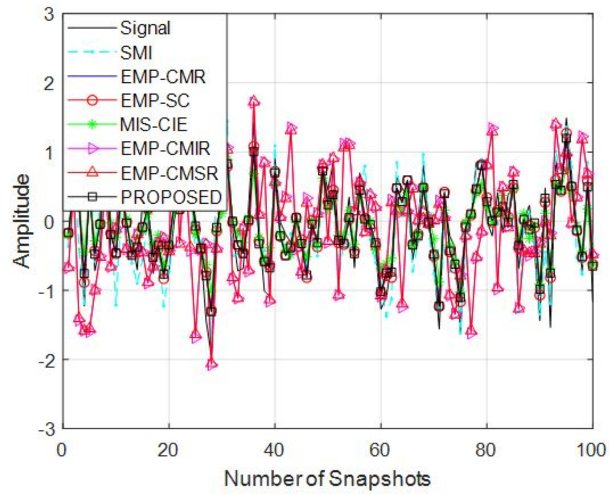

Fig. 2. Output data comparison of array antenna comparison.

Table 1: Correlation coefficient comparison

Methods	Correlation Coefficient
SMI	0.8833
EMP-CMR	0.9584
EMP-SC	0.9584
MIS-CIE	0.9328
EMP-CMIR	0.3606
EMP-CMSR	0.3799
PROPOSED	0.9589

C. Output SINR versus the input SNR

In this section, we compare the output SINR of every method when the input SNR varies from -10 dBto 40 dB**.**

In Figure 3, the output SINR versus the input SNR are compared. From this figure, it is observed that the output SINR of the proposed method and EMP-SC are very close and perform better than other methods. It is worth noting that the desired signal was not contained for the cases of EMP-CMR and EMP-SC methods.

D. Output SINR versus the number of snapshots

In this section, we compare the output SINR of every method when the number of snapshots varies from 10 to 100. Figure 4 displays the output SINR versus the number of snapshots. It is clearly shown that the output SINR of the proposed method is closer to the optimal value after the number of snapshots is 20. This shows that the convergence speed of this method is very fast.

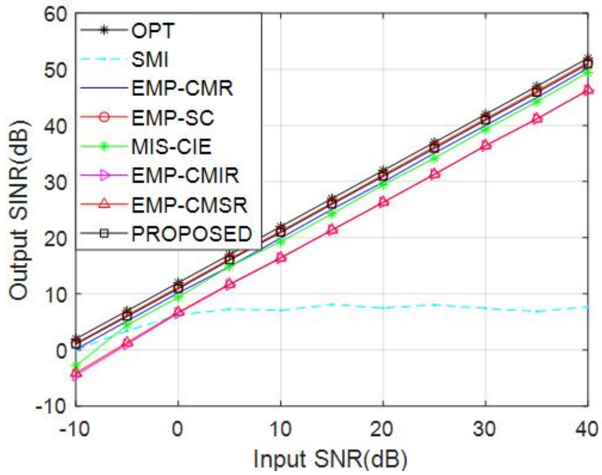

Fig. 3. Output SINR versus the input SNR.

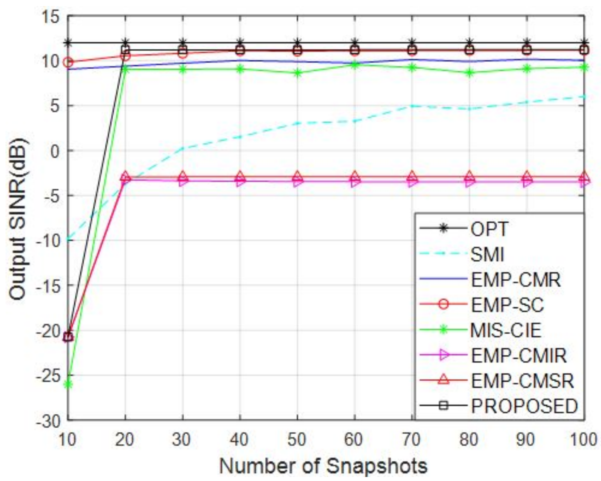

Fig. 4. Output SINR versus the number of snapshots.

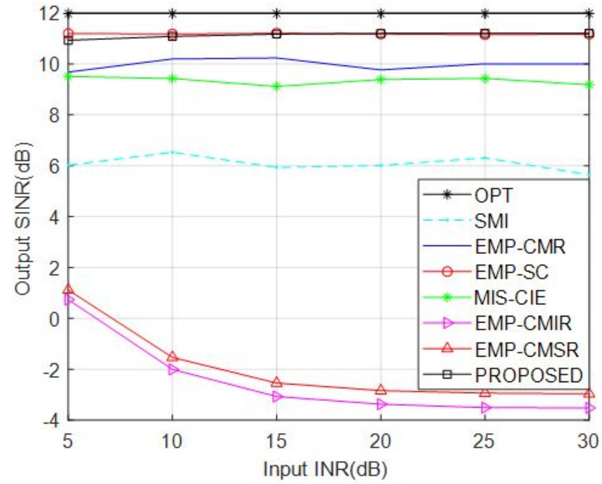

Fig. 5. Output SINR versus INR of the mainlobe interference.

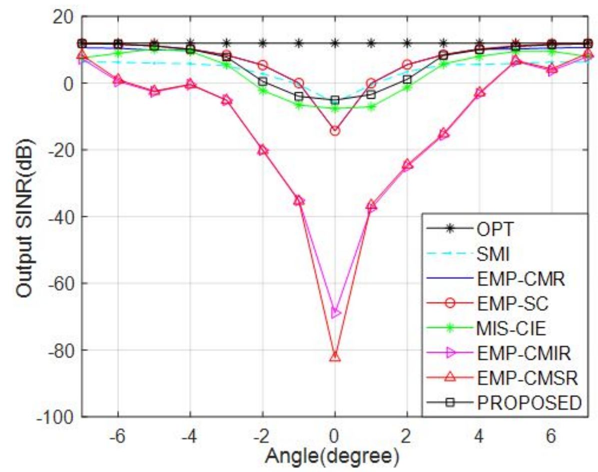

Fig. 6. Output SINR versus the direction of mainlobe interference.

E. Output SINR versus INR of mainlobe interference

In this section, we compare the output SINR of every method when the INR of the mainlobe interference varies from 5 dB to 30 dB. Figure 5 shows the variation curve of the output SINR versus INR of the mainlobe interference. Compared with other methods, the output SINR of the proposed method and EMP-SC are similar and higher than other methods obviously. It should be noticed that for this case, when the proposed method is employed, the received data contains the desired signal.

F. Output SINR versus the direction of mainlobe interference

In this section, we compare the output SINR of every method when the mainlobe interference direction varies from -7° to 7°.

Figure 6 compares the output SINR of every method versus the direction of mainlobe interference. In this figure, it is obvious that the output SINR of the proposed method is higher and closer to the optimal value.

V. CONCLUSION

This paper proposed a novel mainlobe interference suppression method for array antenna beamforming based on eigen-projection processing and covariance matrix reconstruction specified for the problem when desired signal is contained in the received data, which can not only suppress the mainlobe interference impinge but also the sidelobe interference effectively. Compared with other existing methods, simulation results demonstrated that the proposed method can achieve better performance when the mainlobe interference and sidelobe interference are co-existent and the desired signal exists in the received data of array antenna.

ACKNOWLEDGMENT

This paper is supported by the Natural Science Foundation of Jiangsu province of China (BK20190956).

REFERENCES

[1] S. Mohammadzadeh and O. Kukrer, "Robust adaptive beamforming with improved interferences suppression and a new steering vector estimation based on spatial power spectrum," *Circuits Syst Signal Process*, vol. 38, pp. 4162-4179, 2019.

[2] A. Hassanien, M. G. Amin, Y. D. Zhang, and F. Ahmad, "Dual-function radar-communications: Information embedding using sidelobe control and waveform diversity," *IEEE Transactions on Signal Processing*, vol. 64, no. 8, pp. 2168-2181, 2016.

[3] Y. Gu and A. Leshem, "Robust adaptive beamforming based on interference covariance matrix reconstruction and steering vector estimation," *IEEE Transactions on Signal Processing*, vol. 60, no. 7, pp. 3881-3885, 2012.

[4] R. Li, Y. Wang, and S. Wan, "Robust adaptive beam forming under main lobe interference conditions," *System Engineering and Electronics*, vol. 24, no. 7, pp. 4-7, 2002.

[5] J. Yang and C. Liu, "Improved mainlobe interference suppression based on blocking matrix preprocess," *Journal of Electrical and Computer Engineering*, 2015, pp. 1-8, 2015.

[6] R. Li, Y. Wang, and S. Wan, "Research of reshaping adapted pattern under mainlobe interference conditions," *Modern Radar*, vol. 24, pp. 50-55, 2002.

[7] X. Yang, Z. Zhang, T. Zeng, L. Teng, and T. K. Sarkar, "Mainlobe interference suppression based on eigen-projection processing and covariance matrix reconstruction," *IEEE Antennas & Wireless Propagation Letters*, vol. 13, pp. 1369-1372, 2014.

[8] L. Lu and Y. Liao, "Improved algorithm of mainlobe interference suppression based on eigensubspace," *2016 International Conference on Communication and Signal Processing (ICCSP)*, pp. 0133-0137, 2016.

[9] J. Qian, Z. He, F. Jia, and X. Zhang, "Mainlobe interference suppression in adaptive array," *2016 IEEE 13th International Conference on Signal Processing (ICSP)*, pp. 470-474, 2016.

[10] J. Qian and Z. He, "Mainlobe interference suppression with eigenprojection algorithm and similarity constraints," *Electronics Letters*, vol. 52, no. 3, pp. 228-230, 2016.

[11] Y. Wang, Q. Bao, and Z. Chen, "Robust mainlobe interference suppression for coherent interference environment," *EURASIP Journal on Advances in Signal Processing*, vol. 135, no. 1, pp. 1-7, 2016.

[12] Z. Luo, H. Wang, W. Lv, and H. Tan, "Mainlobe anti-jamming via eigen-projection processing and covariance matrix reconstruction," *ICE Transactions on Fundamentals of Electronics Communications and Computer ences*, vol. E100.A, no. 4, pp. 1055-1059, 2017.

[13] L. Xin, Y. Baoguo, and H. Ping, "Mainlobe interference suppression via eigen-projection processing and covariance matrix sparse reconstruction," *ICE Electronics Express*, vol. 15, no. 17, pp. 20180683-20180683, 2018.

[14] D. Xia, L. Zhang, T. Wu, and X. Meng, "A mainlobe interference suppression algorithm based on bistatic airborne radar cooperation," *2019 IEEE Radar Conference (RadarConf)*, pp. 1-6, 2019.

[15] J. Chen, X. Chen, H. Zhang, K. Zhang, and Q. Liu, "Suppression method for main-lobe interrupted sampling repeater jamming in distributed radar," *IEEE Access*, vol. 8, pp. 139255-139265, 2020.

[16] Q. Sun, Q. Zhang, X. Huang, and Q. Gao, "Target detection and localization method for distributed monopulse arrays in the presence of mainlobe jamming," *Journal on Advances in Signal Processing*, vol. 1, 2020.

[17] Y. Gu, N. A. Goodman, S. Hong, et al., "Robust adaptive beamforming based on interference covariance matrix sparse reconstruction," *Signal Processing*, vol. 96, pp. 375-381, Mar. 2014.

Planar Magnetic Integration Design Based on LLC Resonant Converter

Xianming Deng, Kang Zheng, Yanxing Gu, Ankang Zhang, and Zhen Jia

Jiangsu Province Laboratory of Mining Electric and Automation, China University of Mining and Technology, Xuzhou 221116, China
xmdengcumt@126.com, K_Zheng@cumt.edu.cn

Abstract **–** High power density and high efficiency is a major trend in the development of power converters. The main measure to reduce the size of power converter is to improve the working frequency, and the limiting factor is the size of magnetic components. With the development of new semiconductor devices, the working frequency of power converters has been significantly improved, which gives us the opportunity to apply printed circuit board (PCB) winding planar magnetics. Compared with the traditional high frequency magnetics, planar magnetics not only reduce the size of the magnetic components effectively but also improve reliability through repeatable automated manufacturing, which is convenient for large-scale production. Magnetic integration is another method to reduce the size of the power converter. In this paper, a new magnetic structure based on PCB winding is proposed, which integrates inductance and transformer into one component. And the inductor can be independent of the transformer. In this structure, the inductance of inductor and excitation inductance of transformer can be easily controlled by changing the number of winding turns or the length of the air gap. A 20-W 200-kHz half-bridge LLC resonant converter with a peak efficiency of 94.9% is built to verify the feasibility of the designed planar magnetic integrated structure.

Index Terms **–** High frequency, printed circuit board (PCB) transformer, magnetic integration, LLC resonant converter.

I. INTRODUCTION

Nowadays, power electronic converters with high power density and high efficiency play a significant role in data center, aerospace, communication, and other fields. As an important part of power converter, the magnetic components including inductor and transformer are actually the limitation to reduce the size and weight of the power converter system. In addition, the production process of traditional magnetic components is complex and labor-intensive, which has become an impediment to the automatic production of power electronic converters.

In recent years, with the rapid development of printed circuit boards (PCBs), low-altitude power electronic converter has become a research hotspot. Planar magnetic structure can not only reduce the size of magnetic components but also improve the reliability through repeatable automatic manufacturing and better control of parasitic parameters. However, at low operating frequency, the cost and excessive winding turns limit the application of PCB magnetic components in power converters [1–5].

With the development of power electronics, the working frequency of the power converter increases to hundreds of kilohertz, even megahertz. At higher switching frequency, it can not only reduce the size of magnetic components but also reduce the coil turns of magnetic components, making PCB winding planar magnetic components more practical. In [6], the transformer on 65-W flyback circuit adopts PCB planar transformer. In [7] and [8], the application of PCB transformer in LLC resonant converter can significantly reduce the size of the converter and improve the power density.

Although planar magnetic components have many advantages, there are still many problems, such as multiple magnetic components and large volume. Fortunately, magnetic integration technology is an effective method to solve the above problems. Through magnetic integration, multiple magnetic components can be integrated into one magnetic component, which can effectively reduce the number of magnetic components of power converter and improve the power density.

In order to reduce the number of magnetic components and the size of the power converter, several methods of magnetic integration are often adopted. A common method is to realize the inductance function through the leakage inductance of the transformer. Several theoretical methods have been proposed to design leakage inductance of transformers. Some of them use low permeability materials as additional magnetic circuit, resulting in increased leakage inductance [9–11]. However, this will change the structure of the transformer and make its production process more complex. Due to the

Submitted On: March 30, 2021
Accepted On: September 29, 2021
https://doi.org/10.13052/2021.ACES.J.361112

characteristics of low permeability materials, the core loss of magnetic components will increase and the overall efficiency of the converter will decrease. In addition, it is also popular to wind the primary winding and the secondary winding separately to obtain the required leakage inductance [12–14]. This method can lead to serious electromagnetic interference (EMI) problems, additional eddy current losses, and increased AC losses in the windings. In addition, due to the low profile characteristics of the winding transformer on PCB, this structure is difficult to be applied to it [15].

In this paper, a novel winding structure based on planar core is proposed. The inductor and transformer are integrated through an EI planar core, and they are decoupled. With this structure, the excitation inductance of the transformer and the inductance of the inductor can be adjusted by the air gap of the core or the number of turns of the winding. Because the leakage inductance of the transformer is not used as inductance, the EMI and eddy current loss are effectively reduced.

The structure of this paper is as follows. In Section II, a new type of magnetic integrated structure including inductor and transformer is proposed, the equivalent model is established, and the decoupling mechanism and calculation formula are deduced. In Section III, magnetic integrated components are applied to half-bridge LLC resonant transformer and the selection formula of planar core size is derived. In Section IV, simulation parameters of half-bridge LLC resonant converter are determined, and the simulation analysis of magnetic integrated components is carried out. In Section V, the experimental verification is carried out. Section VI summarizes the whole paper.

II. STRUCTURE AND ANALYSIS OF PLANAR MAGNETIC INTEGRATION

A. Planar magnetic integration of inductor and transformer

The structure of the inductor integrated with the transformer is shown in Figure 1. In order to effectively use the magnetic core and decouple the inductor and transformer, the resonant inductor is wound around the side legs of the magnetic core, the primary and secondary sides of transformer are wound around the middle leg of the magnetic core, and air gaps of the same length are opened for the three magnetic legs.

In Figure 1, N_P and N_S are the turns of primary and secondary windings of the transformer, N_{r1} and N_{r2} are the turns of the inductor windings around the left and right poles of the magnetic core, L_P and L_S are the self-inductance of the primary and secondary windings of the transformer, respectively, L_{r1} and L_{r2} are the inductance of windings around the respective side legs, the sum of L_{r1} and L_{r2} inductance is the inductance of resonant inductance L_r, V_{Lr1} and V_{Lr2} are the inductance voltages of the left and right legs, respectively, V_P and V_S are the voltages of primary and secondary windings of the transformer, respectively, R_{m1}, R_{m2}, and R_{m3} are the magnetoresistance of two side legs and the middle leg, respectively, and Φ_{Lr1}, Φ_{Lr2}, and Φ_T are the magnetic flux generated by the left and right column windings and the magnetic flux generated by the transformer winding, respectively.

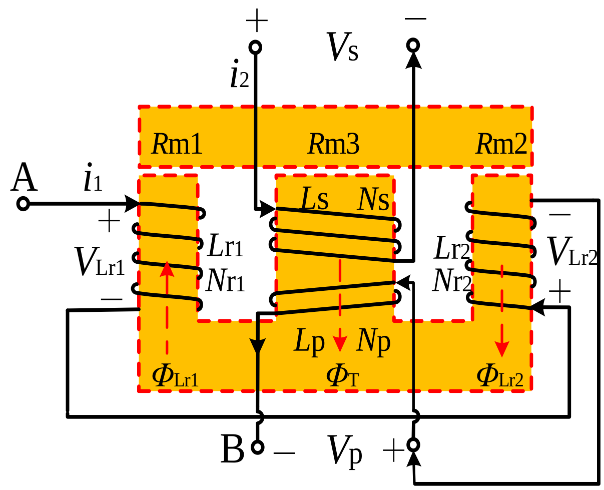

Fig. 1. Structure diagram of planar magnetic integration.

In the design, three cylinders of the magnetic core have air gaps with the same length. For the EI-type magnetic core, the area of the column is the sum of the areas of the two side legs:

$$R_{m1} = R_{m2} = 2R_{m3} = 2R_m. \tag{1}$$

In formula (1), R_m is the air gap magnetoresistance of the middle leg of the magnetic core. According to the magnetic circuit of the magnetic integrated element, the equivalent magnetic circuit diagram is obtained, as shown in Figure 2. In this figure, Φ_1, Φ_2, and Φ_3, respectively, represent the magnetic flux of the two side legs and the center leg of the magnetic core. $N_{Lr1}i_{Lr1}$, $N_{Lr2}i_{Lr2}$, N_pi_p, and N_si_s, respectively, represent the magnetic potential of the inductor windings of the two side legs, and the magnetic potential of the primary and secondary side windings of the transformer.

As shown in the above design structure, the total magnetic flux generated by the inductor winding on the side leg of the core does not affect the magnetic flux of the transformer winding and vice versa. In this structure, the inductor and the transformer can be completely decoupled.

B. Principal analysis of integrated magnetic element

According to the equivalent diagram of magnetic circuit in Figure 2, combined with Ohm's law of magnetic circuit and Faraday's law of electromagnetic induc-

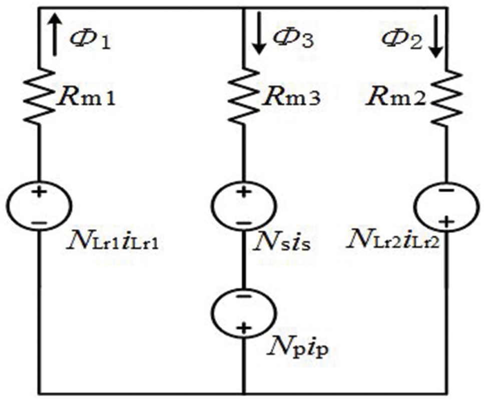

Fig. 2. Equivalent diagram of magnetic circuit.

tion, the following formulas are deduced. First, the magnetic flux generated by each winding is as follows [16]:

$$\begin{cases} \Phi_{Lr1} = \dfrac{N_{Lr1} i_{Lr1}}{R_{m1} + R_{m2}//R_{m3}} = \dfrac{N_{Lr1} i_{Lr1} (R_{m2} + R_{m3})}{8R_m} \\ \Phi_{Lr2} = \dfrac{N_{Lr2} i_{Lr2}}{R_{m2} + R_{m1}//R_{m3}} = \dfrac{N_{Lr2} i_{Lr2} (R_{m1} + R_{m3})}{8R_m} \\ \Phi_T = \dfrac{N_p i_p - N_s i_s}{R_{m3} + R_{m1}//R_{m2}} = \dfrac{(N_p i_p - N_s i_s)(R_{m1} + R_{m2})}{2R_m} \end{cases}. \tag{2}$$

According to the magnetic circuit diagram of the planar magnetic integrated structure shown in Figure 2, the magnetic flux of each cylinder of the magnetic core is obtained as follows:

$$\begin{cases} \Phi_1 = \Phi_{Lr1} + \Phi_T \dfrac{R_{m2}}{R_{m1} + R_{m2}} + \Phi_{Lr2} \dfrac{R_{m3}}{R_{m1} + R_{m3}} \\ \Phi_2 = \Phi_{Lr2} - \Phi_T \dfrac{R_{m1}}{R_{m1} + R_2} + \Phi_{Lr1} \dfrac{R_{m3}}{R_{m2} + R_{m3}} \\ \Phi_3 = \Phi_T + \Phi_{Lr1} \dfrac{R_{m2}}{R_{m2} + R_{m3}} + \Phi_{Lr2} \dfrac{R_{m1}}{R_{m1} + R_{m3}} \end{cases}. \tag{3}$$

And because the voltage V_{Lr} of the inductance L_r is the sum of V_{Lr1} and V_{Lr2}, and the current i_{Lr} flowing through the inductance L_r is equal to i_{Lr1} and i_{Lr2}, where i_{Lr1} and i_{Lr2} are the current flowing through the left and right side column inductance windings respectively. And according to the law of electromagnetic induction, primary winding voltage V_p, secondary winding voltage V_s, and inductance winding voltage V_{Lr} are as follows:

$$\begin{cases} V_p = N_p \dfrac{d\Phi_3}{dt} \\ V_s = -N_s \dfrac{d\Phi_3}{dt} \\ V_{Lr} = V_{Lr1} + V_{Lr2} = N_{Lr1} \dfrac{d\Phi_1}{dt} + N_{Lr2} \dfrac{d\Phi_2}{dt} \end{cases}. \tag{4}$$

According to all the above equations, the relationship between voltage and current of planar magnetic integrated components is derived

$$\begin{bmatrix} V_{Lr} \\ V_p \\ V_s \end{bmatrix} = \begin{bmatrix} L_r & M_{pLr} & M_{sLr} \\ M_{pLr} & L_p & -M_{ps} \\ M_{sLr} & -M_{ps} & L_s \end{bmatrix} \begin{bmatrix} \dfrac{di_{Lr}}{dt} \\ \dfrac{di_p}{dt} \\ \dfrac{di_s}{dt} \end{bmatrix}. \tag{5}$$

In formula (5), i_p and i_s are, respectively, the current flowing through the primary and secondary windings of the transformer, and M_{pLr}, M_{sLr}, and M_{ps}, respectively, represent the mutual inductance between the primary winding N_p of the transformer and the inductance L_r, the mutual inductance between the winding N_s on secondary side of the transformer and the inductance L_r, and the mutual inductance between the primary winding N_p of the transformer and the secondary winding N_s of the transformer. Formula (6) is obtained by solving the above formula

$$\begin{cases} L_s = \dfrac{N_s^2}{2R_m} \\ L_s = \dfrac{N_s^2}{2R_m} \\ L_r = \dfrac{3N_{Lr1}^2 + 3N_{Lr2}^2}{8R_m} + \dfrac{N_{Lr1} N_{Lr2}}{4R_m} \\ M_{pLr} = \dfrac{N_p (N_{Lr1} - N_{Lr2})}{4R_m} \\ M_{sLr} = \dfrac{N_s (N_{Lr2} - N_{Lr1})}{4R_m} \\ M_{ps} = \dfrac{N_p N_s}{2R_m} \end{cases}. \tag{6}$$

By simplifying formula (6), formula (7) is obtained as follows:

$$\begin{cases} k_{ps} = \dfrac{-M_{ps}}{\sqrt{L_p L_s}} = -1 \\ k_{pLr} = \dfrac{M_{pLr}}{\sqrt{L_r L_p}} = \dfrac{N_{Lr2} - N_{Lr1}}{\sqrt{3N_{Lr1}^2 + 3N_{Lr2}^2 + 6N_{Lr1} N_{Lr2}}} \\ k_{sLr} = \dfrac{-M_{sLr}}{\sqrt{L_r L_s}} = \dfrac{N_{Lr1} - N_{Lr2}}{\sqrt{3N_{Lr1}^2 + 3N_{Lr2}^2 + 6N_{Lr1} N_{Lr2}}} \end{cases}. \tag{7}$$

In formula (7), k_{ps}, k_{pLr}, and k_{sLr}, respectively, represent the coupling coefficients between L_P and L_S, L_P and L_r, and L_S and L_r.

According to the above formula, the coupling coefficient k between the inductor and the transformer can be obtained by changing the turns of the windings N_{Lr1} and N_{Lr2} around the two side legs of the planar transformer core. When N_{Lr1} = N_{Lr2}, the coupling coefficient k_{pLr} = k_{sLr} = 0 between the primary and secondary windings and the inductance of the transformer is 0. At this time, they will not affect each other in the working process, and the decoupling integration between the inductance and the transformer is realized.

III. ANALYSIS AND DESIGN OF INTEGRATED MAGNETIC ELEMENT

A. Structure of LLC resonant converter based on magnetic integration

For half-bridge LLC resonant converter, the back stage rectifier can be divided into full wave rectifier with central tap of transformer and bridge rectifier without central tap of transformer. The first scheme is suitable for the application of low voltage and high current, and the second scheme is suitable for the application of high voltage and low current. The planar transformer integration based on inductors completely decoupled from transformers is suitable for both schemes, and the primary and secondary sides of the inductor and transformer can be completely decoupled [17–19]. The structure diagram of LLC resonant converter using the designed magnetic integrated elements is shown in Figure 3.

The planar magnetic integrated transformer is applied to the half-bridge LLC series resonant converter. There are two resonant frequencies in the half-bridge LLC resonant converter, f_{r1} and f_{r2}. f_{r1} is the resonant frequency of inductance L_r and capacitor C_r, and f_{r2} is the frequency at which the sum of inductance L_r and excitation inductance L_m of the transformer resonates with the capacitor. In order to maximize efficiency, the working range of the frequency is set between f_{r2} and f_{r1}, and the current works in a discontinuous mode (DCM). In this case, not only ZVS of the switch can be turned on, but also the rectifier diode on the secondary side can be turned off at zero current. The main waveforms of the converter operating between f_{r2} and f_{r1} are shown in Figure 4.

B. Design and selection of integrated magnetic elements

Figure 5 shows the air gap and cross-section of the integrated magnetic elements; l_g is the length of the air gap of the planar transformer magnetic core. For the convenience of the design, the three cylinders of the EI core have the same air gap. S_1, S_2, and S_3 represent the core

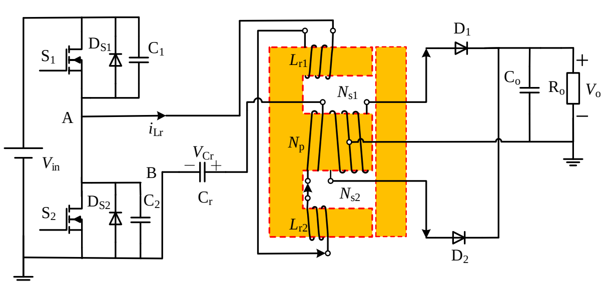

Fig. 3. Half-bridge LLC resonant converter based on magnetic integration.

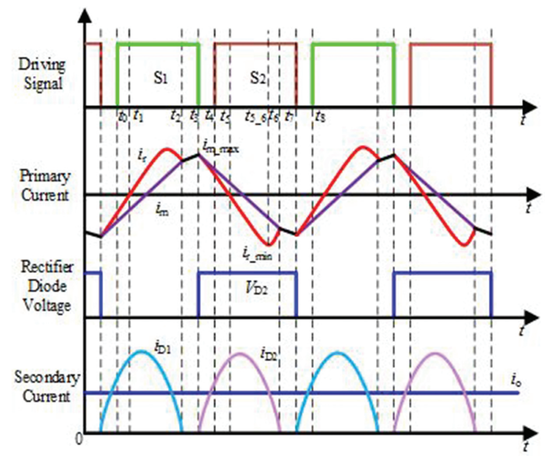

Fig. 4. Main waveforms of LLC when $f_{r2} < f_s < f_{r1}$.

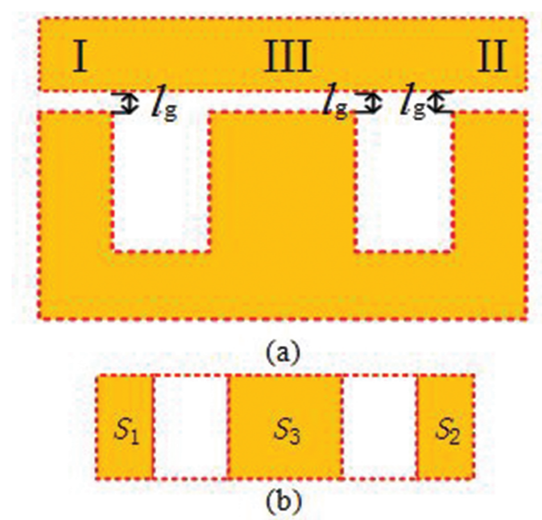

Fig. 5. Air gap and cross-section of planar integrated magnetic elements. (a) Air gap of EI core. (b) Cross-sectional area of magnetic core.

cross-sectional area of two side columns and a central column of the planar transformer, respectively. Since EI magnetic core is selected, $S_3 = 2S_1 = 2S_2$.

Formula (8) represents the magnetoresistance of each cylinder of the integrated magnetic element, where μ_0 represents the air permeability

$$\begin{cases} R_{g1} = \dfrac{l_g}{\mu_0 S_1} \\ R_{g2} = \dfrac{l_g}{\mu_0 S_2} \\ R_{g3} = \dfrac{l_g}{\mu_0 S_3} \end{cases} . \tag{8}$$

In order to analyze the magnetic density variation of the integrated magnetic element applied in the LLC resonant converter, we select the continuous phase in Figure 4 because the magnetic element of LLC resonant converter is bidirectionally excited and has periodicity. In t_3–t_6, the rectifier diode of the secondary side of the transformer is switched on, the voltage of the primary winding of the transformer is clamped to nV_0, and the voltage of the secondary winding is $-V_0$; so V_s can be expressed as

$$V_\mathrm{s} = -V_0 = -N_\mathrm{s}\frac{\mathrm{d}\Phi_3}{\mathrm{d}t} \quad (t_3 \le t \le t_6). \tag{9}$$

For the center leg III of the core, the magnetic flux of both sides of the cylinder will not pass through, and the magnetic flux density of the center column reaches the maximum value during t_3–t_6. According to formula (9), the maximum magnetic density B_{3max} of the middle column is

$$B_{3\max} = \frac{\Phi_{3\max}}{S_3} = \frac{V_0}{2S_3N_\mathrm{s}}(t_6 - t_3). \tag{10}$$

When the half-bridge LLC converter operates in modes 3, 4, 5, and 6, there are

$$\begin{aligned} V_{L\mathrm{r}} &= V_\mathrm{in} - V_\mathrm{p} - V_{C\mathrm{r}} \\ &= N_{Lx1}\frac{\mathrm{d}\Phi_1}{\mathrm{d}t} + N_{Lx2}\frac{\mathrm{d}\Phi_2}{\mathrm{d}t} \quad (t_2 \le t \le t_6). \end{aligned} \tag{11}$$

At t_6, the magnetic density of core side leg I reaches the maximum value, and because Φ_1=Φ_2+Φ_3, the maximum magnetic density B_{1max} is obtained as follows:

$$B_{1\max} = \frac{\Phi_{1\max}}{S_1} = k_1\frac{[\frac{V_\mathrm{o}(N_\mathrm{p}-N_{L\mathrm{r}2})}{N_\mathrm{s}}](t_6-t_2)}{2S_1(N_{L\mathrm{r}1}+N_{L\mathrm{r}2})}. \tag{12}$$

In the calculation, the voltage of the winding is equal to the DC voltage. In practical application, the voltage will change due to resonance and the actual flux density will be slightly less than the obtained flux density. Therefore, the coefficient k_1 is introduced to obtain the real flux density, and the value of k_1 is about 0.7–0.9.

For the maximum flux density B_{2max} of the magnetic leg II, when the resonant current of the inductor reaches the maximum or minimum value, the flux density reaches the maximum value and the converter operates at $t_5 < t < t_{5\_6}$. The magnetic density began to increase at t_{5_6}. According to formula (12) and Φ_1=Φ_2+Φ_3, B_{2max} can be obtained as follows:

$$B_{2\max} = \frac{\Phi_{2\max}}{S_2} = k_2\frac{\left[\frac{V_0(N_\mathrm{p}+N_{L\mathrm{r}2})}{2N_\mathrm{s}}\right](t_{5\_6}-t_3)}{2S_2(N_{L\mathrm{r}1}+N_{L\mathrm{r}2})}. \tag{13}$$

In the same way as formula (12), the voltage of the winding is equal to the DC voltage. Therefore, the coefficient k_2 is introduced to obtain the real flux density of cylinder II, and the value of k_2 is about 0.7–0.9.

Through the above formula, we can verify whether the selected magnetic core is reasonable. Because the magnetic flux cancelation effect will occur in cylinder III and cylinder II, the magnetic flux density of cylinder I and cylinder III will not be offset but will be superimposed. Therefore, it is only necessary to ensure that cylinder I is not saturated and the other two cylinders will not be saturated. In formula (11), t_6–t_2 is about half of a cycle; so formula (11) can be simplified as follows:

$$B_{1\max} = \frac{\Phi_{1\max}}{S_1} = k_1\frac{[\frac{V_\mathrm{o}(N_\mathrm{p}-N_{L\mathrm{r}2})}{N_\mathrm{s}}]}{2S_1(N_{L\mathrm{r}1}+N_{L\mathrm{r}2})f}. \tag{14}$$

In formula (14), f is the working frequency of half-bridge LLC resonant converter. In the calculation, the minimum value of working frequency should be selected.

For the selection of the magnetic core size under the determined power, first, select the type under the worst working conditions. According to formula (14), ensure that the maximum magnetic flux density will not saturate the magnetic core at this time, and the coefficient k_1 in the formula has guaranteed the magnetic flux density margin.

Table 1: Main parameters of converter

Specifications	Values
Resonant frequency	200 kHz
Input voltage range	60–80 V
Output voltage	10 V
Power	20 W
Turn ratio of transformer	4:1
Resonant inductor	20 μH
Excitation inductance	56 μH
Resonant capacitor	33 nF

IV. SIMULATION ANALYSIS OF PLANAR MAGNETIC INTEGRATION

A. Parameter setting

In the design, we make LLC resonant converter work between f_{r2} and f_{r1}, which can not only realize soft switching but also realize ZCS of secondary rectifier diode. According to the input voltage range, the working frequency range of LLC resonant converter is 125–180kHz. The main parameters of half-bridge LLC resonant converter are shown in Table 1.

The planar EI core is made of PC95 ferrite EI22/8/16. The structure of E core and I core is shown in Figure 6, and the specific core parameters are shown in Table 2.

For the method of setting air gap, we use 0.06-mm air gap gasket to ensure that the air gap of each cylinder is the same. According to formulas (6) and (7), the number of turns of the inductor on the side leg of the planar magnetic core is calculated as 4 turns, the number of original side turns of the transformer is 8 turns, and the number of secondary side turns of the transformer is 2 turns.

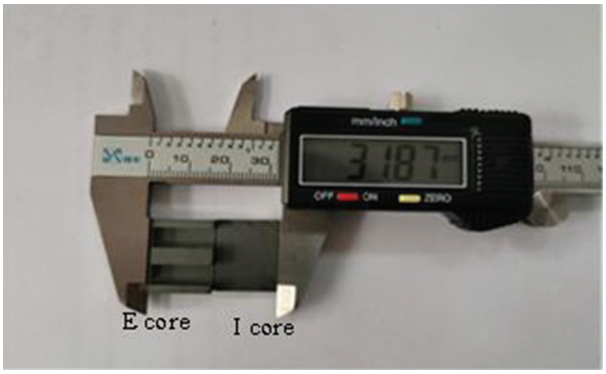

Fig. 6. Structure and size of E core and I core.

Table 2: Core parameters

Cylinder	Area/mm^2	Air gap/mm	Reluctance/10^6H^{-1}
I	40	0.06	1.193
II	80	0.06	0.598
III	40	0.06	1.193

According to the formula deduced in Section III and the design parameters of LLC resonant converter, the maximum magnetic flux density is only 0.27T, while the saturated magnetic flux density of PC95 EI22/8/16 magnetic core is 0.55T, which verifies the rationality of the selected magnetic core.

B. Simulation analysis

According to the design parameters of the planar magnetic integrated elements, the finite element analysis model of the magnetic integrated elements is established in Ansys Maxwell electromagnetic field simulation software. Considering the influence of simulation accuracy and computer performance, the mesh is divided based on the edge length of the inside element of the model, and the set length is 0.5 mm. According to a series of parameters of half-bridge LLC resonant converter design, an open-loop circuit is built in Maxwell circuit design and imported into Ansys Maxwell, the external circuit structure is shown in Figure 7. In the figure, Lwinding1 and Lwinding2 are the resonant inductance of the resonant cavity, Lwinding3 is the excitation inductance of the primary side of the transformer, and Lwinding4 and Lwinding5 are the excitation inductance of the secondary side of the transformer. This circuit is used as the external excitation source of the planar magnetic integrated model, and its parameters are set as input 60 V, switching frequency 125 kHz, and output rated load. After the simulation, observe whether the soft switching and zero current shutdown of the secondary side are realized and obtain the resonant current and driving waveforms of the down transistor and the current and voltage waveforms of

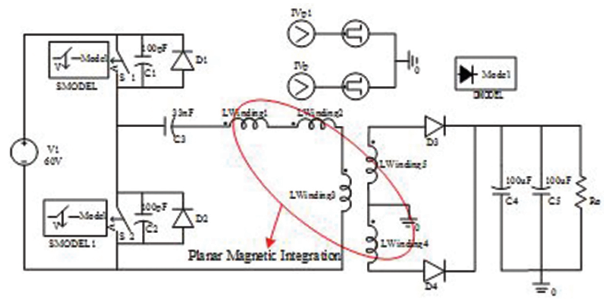

Fig. 7. External circuit structure diagram of simulation.

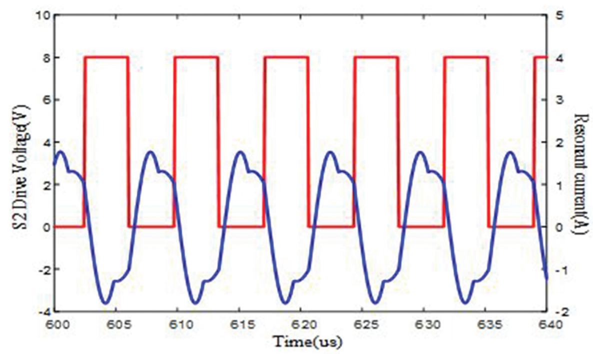

Fig. 8. Resonant current and S_2 driving waveforms.

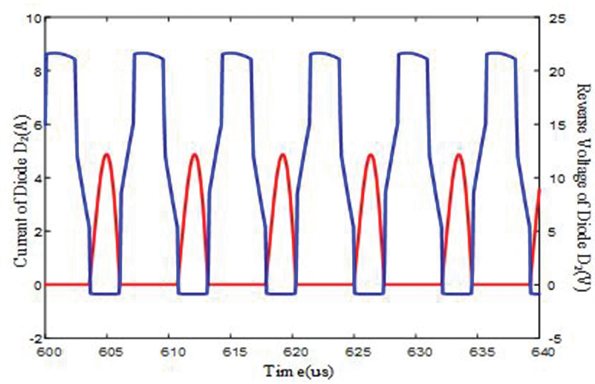

Fig. 9. Current and voltage waveforms of rectifier D_2.

the secondary rectifier tube. These waveforms are shown in Figures 8, and 9.

According to Figure 8, when S_2 starts to turn on, the resonant current is positive. At this time, the body diode of S_2 has conducted the freewheeling current, realizing ZVS of MOSFET. In Figure 9, when the current flowing through the rectifier diode is 0, the reverse voltage begins to increase. Therefore, the zero current shutdown of the rectifier diode is realized. In the figure, when the diode is on, it has a negative voltage because of the voltage drop. When analyzing the iron loss of the magnetic integrated structure, the parameters of PC95 material are imported

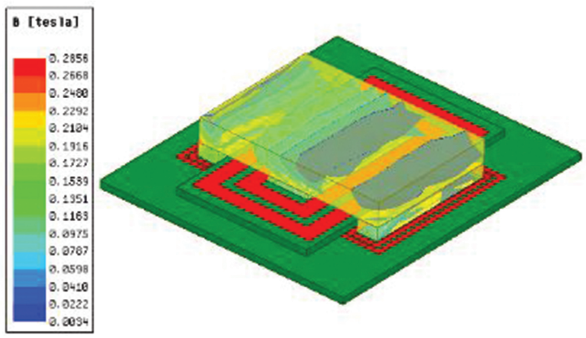

Fig. 10. Magnetic flux density of planar magnetic integrated elements.

into the software, and it is concluded that the core loss changes periodically. According to the calculation, the average core loss is about 0.41 W.

In the Ansys Maxwell-3D simulation environment, the model of planar magnetic integrated components is established, the external circuit is drawn, and the flux density distribution of planar magnetic integrated components is obtained by co-simulation. As shown in Figure 10, the maximum magnetic flux density of the magnetic integrated component is 0.285T, which is not different from the maximum magnetic flux density deduced from the formula. The rationality of the magnetic core selection is proved.

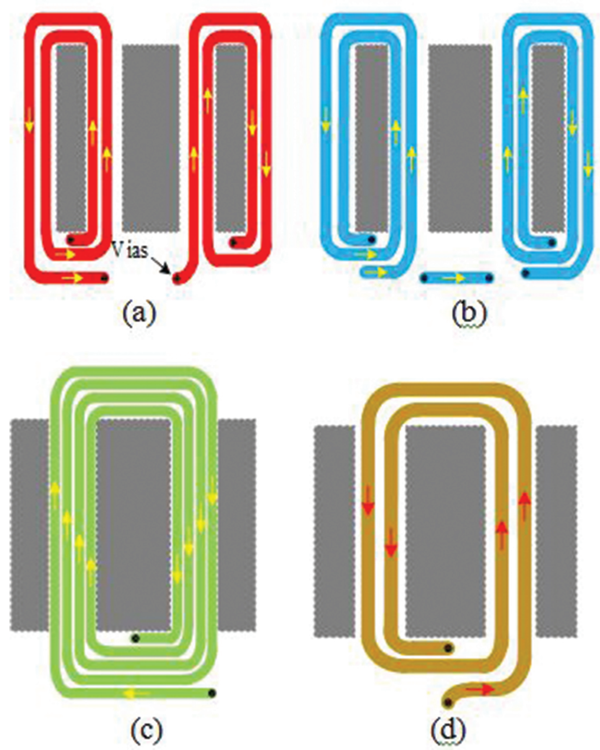

Fig. 12. Partial winding arrangement. (a) Layer 1. (b) Layer 2. (c) Layer 3. (d) Layer 4.

V. EXPERIMENTAL VERIFICATION

In order to verify the correctness and superiority of the structure design of planar magnetic integrated magnetic elements, an experimental prototype is built as shown in Figure 11.

Some winding configurations are shown in Figure 12, where (a) and (b) are the windings of the inductor, (c) is the primary winding of the transformer, and (d) is the secondary winding of the transformer. Each layer is connected through vias. The yellow arrow indicates the flow direction of the current in the primary winding and the red arrow indicates the flow direction of the current in the secondary winding.

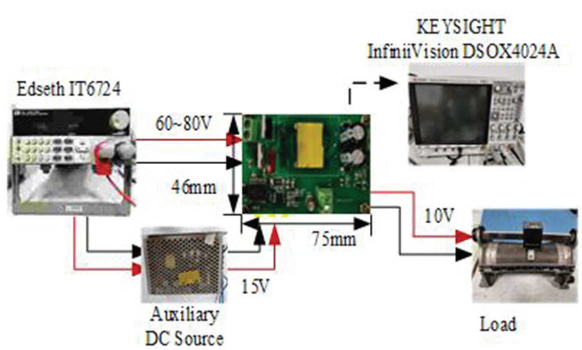

Fig. 11. Testing system of LLC resonant converter.

When the input voltage is 60 V and the output voltage is 10 V, the resonant current and the waveform of switching tube S_2 and the current and voltage waveforms of rectifier diode D_2 are shown in Figure 13. When the input voltage is 80 V and the output voltage is 10 V, the current and voltage waveforms of rectifier diode D_2 are shown in Figure 14.

According to Figures 13 and 14, when the driving voltage of the lower tube S_2 increases, that is, when the lower tube is on, the resonant current is positive. At this time, the body diode of S_2 has been turned on, realizing ZVS of the switching tube. When the current of rectifier diode is 0, the reverse voltage of the diode begins to increase, and ZCS of the secondary diode is realized. According to the oscilloscope, the working frequency is between 133 and 169 kHz, and the effective value of resonant current is 0.594–0.939A, which is basically consistent with the design parameters.

In order to compare the integrated magnetic components with the discrete magnetic components, the geometric dimensions and parameters of each magnetic component are given in Table 3. The volume of the integrated magnetic component is 2040 mm^3 and the mass is 10.5 g. Compared with the discrete magnetic

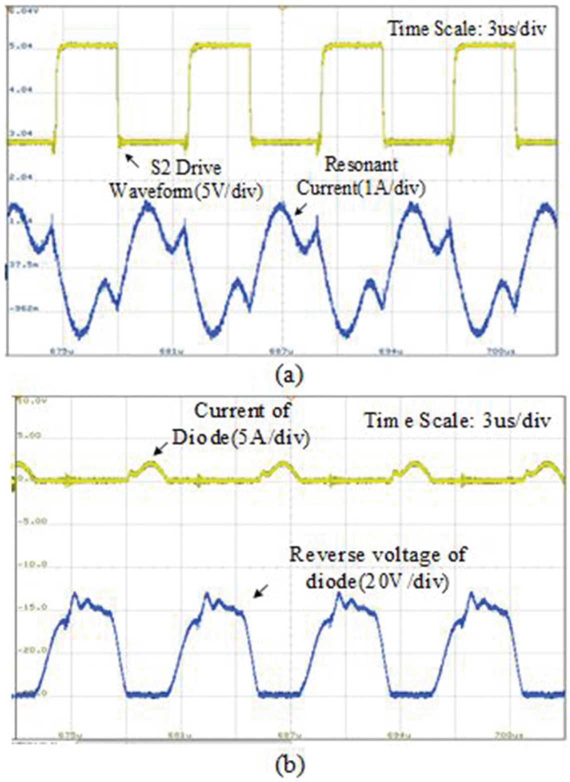

Fig. 13. Waveforms at 60-V input. (a) Resonant current and driving voltage waveforms. (b) Waveforms of diode current and reverse voltage.

Table 3: Comparison of core size and mass

Magnetic Parts		Core	Volume/mm^3	Quality/g
Discreteness	Inductance	EE19	910	4.9
	Transformer	EE20	1450	7.6
Integration		EI22	2040	10.5

elements, the volume and weight of the planar integrated magnetic elements are reduced by 13.56% and 16%, respectively. For the whole circuit board, the power density is increased by 15%.

Under the same conditions, the efficiency comparison curve of half-bridge LLC resonant transformer is obtained by testing the discrete magnetic devices and integrated devices, as shown in Figure 15. Compared with the traditional discrete magnetic components, the planar core has a larger body ratio and is more conducive to heat dissipation. Due to the magnetic flux cancelation effect, the core loss is reduced. When the output current is 2.2 A, the efficiency reaches the maximum in both cases. At this time, the corresponding efficiency of the discrete magnetic components is 94.2%, and the efficiency of the integrated magnetic components is 94.9%. Within full load range, the efficiency of planar

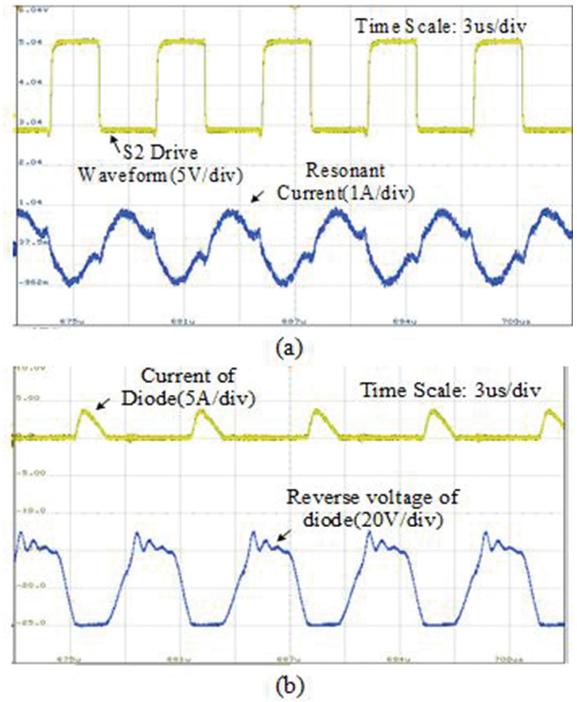

Fig. 14. Waveforms at 80-V input. (a) Resonant current and driving voltage waveforms. (b) Waveforms of diode current and reverse voltage.

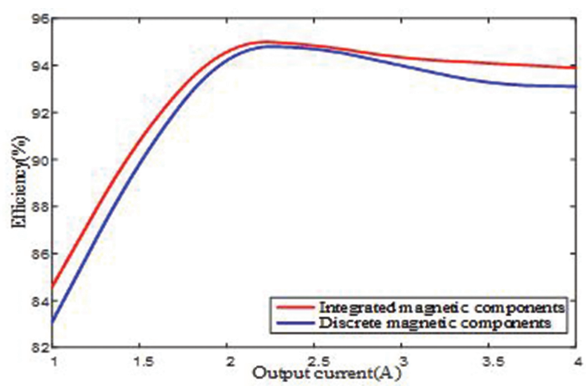

Fig. 15. Efficiency comparison curve.

integrated magnetic components is significantly higher than that of discrete magnetic components, and the efficiency curves have the same trend.

VI. CONCLUSION

In this paper, a planar magnetic integrated component based on independent inductance is proposed. The inductor and transformer are integrated on a planar magnetic core by the decoupling integration method and the inductor and transformer are decoupled completely. It is applied to half-bridge LLC resonant converter. It is proved that there is no coupling between the inductor and transformer by the formula derivation, and the design and selection methods of magnetic integrated components are proposed. The excitation inductance of the inductor and transformer can be easily controlled by changing the air gap and winding turns. In addition, the electromagnetic field characteristics of planar magnetic integrated components are analyzed in the simulation software. Finally, a 20-W 200-kHz half-bridge LLC resonant converter is built, which achieves good soft switching performance in the whole load range, and the peak efficiency reaches 94.9%.

ACKNOWLEDGMENT

This work was supported by the Natural Science Foundation of Jiangsu Province under Grant BK20190634 and Postgraduate Research & Practice Innovation Program of Jiangsu Province under Grant KYCX21_2226.

REFERENCES

[1] C. Fei, R. Gadelrab, Q. Li, and F. C. Lee, "High-frequency three-phase interleaved LLC resonant converter with GaN devices and integrated planar magnetics," *IEEE J. Emerg. Sel. Topics Power Electron.*, vol. 7, no 2, pp. 653-663, Jun. 2019.

[2] C. Fei, F. C. Lee, and Q. Li, "High-efficiency high-power-density LLC converter with an integrated planar matrix transformer for high-output current applications," *IEEE Trans Ind Electron.*, vol. 64, no. 11, pp. 9072-9082, Nov. 2017.

[3] R. X. Liu, Y. F. Wang, Q. Chen, F. Q. Han, and Z. Meng, "Entire magnetic integration method of multi-transformers and resonant inductors for cltlc resonant converter," *Electronics.*, vol. 9, no. 9, 1386, Sep. 2020.

[4] Z. W. Ouyang, O. C. Thomsen, and M. A. E. Andersen, "Optimal design and tradeoff analysis of planar transformer in high-power DC-DC converters," *IEEE Trans Ind Electron.*, vol. 59, no. 7, pp. 2800-2810, Jul. 2012.

[5] Y. C. Yang, M. K. Mu, Z. Y. Liu, F. C. Lee, and Q. Li, "Common mode EMI reduction technique for interleaved MHz critical mode PFC converter with coupled inductor," *IEEE Energy Convers. Congr. Expo.*, pp. 233-239, Sep. 2015.

[6] X. C. Huang, J. J. Feng, W. J. Du, F. C. Lee, and Q. Li, "Design consideration of MHz active clamp flyback converter with GaN devices for low power adapter application," *IEEE Appl. Power Electron. Conf.*, pp. 2334-2341, May. 2016.

[7] Y. C. Liu, C. Chen, K. D. Chen, Y. L. Syu, D. J. Lu, K. A. Kim, and H. J. Chiu, "Design and implementation of a planar transformer with fractional turns for high power density LLC resonant converters," *IEEE Trans Power Electron.*, vol. 36, no. 5, pp. 5191-5203, May 2021.

[8] K. W. Kim, Y. Jeong, J. S. Kim, and G. W. Moon, "Low common-mode noise full-bridge LLC resonant converter with balanced resonant tank," *IEEE Trans Power Electron.*, vol. 36, no. 4, pp. 4105-4115, Apr. 2021.

[9] J. Biela, and J. W. Kolar, "Electromagnetic integration of high power resonant circuits comprising high leakage inductance transformers," *IEEE Power Electron.*, pp. 4537-4545, Jun. 2004.

[10] M. X. Li, Z. W. Ouyang, and M. A. E. Andersen, "High-frequency LLC resonant converter with magnetic shunt integrated planar transformer," *IEEE Trans Power Electron.*, vol. 34, no. 3, pp. 2405-2415, Mar. 2019.

[11] J. Zhang, Z. W. Ouyang, M. C. Duffy, M. A. E. Andersen, and W. G. Hurley, "Leakage inductance calculation for planar transformers with a magnetic shunt," *IEEE Trans Ind Appl.*, vol. 50, no. 6, pp. 4107-4112, Dec. 2014.

[12] S. S. Gao, Y. J. Wang, Y. S. Guan, and D. G. Xu, "A high step up SEPIC-based converter based on partly interleaved transformer," *IEEE Trans Ind Electron.*, vol. 67, no. 2, pp. 1455-1465, Feb. 2020.

[13] L. X. Xue, M. K. Mu, D. Boroyevich, and P. Mattavelli, "The optimal design of GaN-based dual active bridge for bi-directional plug-in hybrid electric vehicle (PHEV) charger," *IEEE Appl. Power Electron. Conf.*, pp. 602-608, Mar. 2015.

[14] L. Wu, L. Xiao, J. Zhao, and G. Z. Chen, "Modelling and optimisation of planar matrix transformer for high frequency regulated LLC converter," *IET Power Electron.*, vol. 13, no. 3, pp. 516-524, Feb. 2020.

[15] M. H. Ahmed, F. C. Lee, and Q. Li, "Wide voltage range high-efficiency sigma converter 48V VRM with integrated magnetics," *IEEE Ener Conv.*, pp. 4701-4707, Oct. 2019.

[16] S. Q. Li, Q. Y. Min, E. G. Rong, R. Zhang, X. Du, and S. Z. Lu, "A magnetic integration half-turn planar transformer and its analysis for LLC resonant DC-DC converters," *IEEE Access.*, pp. 128408-128418, Sep. 2019.

[17] Y. Jin, W. Xie, N. Yang, and H. Y. Liu, "High efficiency resonant DC/DC converter based on GaN Device and planar transformer," *IEEE 5th Information Technology and Mechatronics Engineering Conference.*, pp. 358-362, Jun. 2020.

[18] F. C. Lee, Q. Li, and A. Nabinh, “High frequency resonant converters: an overview on the magnetic design and control methods,” *IEEE J. Emerg. Sel Topics Power Electron.*, vol. 9, no. 1, pp. 11-23, Feb. 2021.

[19] M. C. Dai, X. J. Zhang, H. Li, D. B. Zhou, Y. J. Wang, and D. G. Xu, “LLC converter with an integrated planar matrix transformer based on variable width winding,” *Intermationl Conference on Electrical Machines and System.*, pp. 229-232, Aug. 2019.

Xianming Deng was born in Sichuan, China. He received the B.S., M.S., and Ph.D. degrees in electrical engineering from the China University of Mining and Technology, Jiangsu, China.

He is currently a Professor with the School of Electrical and Power Engineering, China University of Mining and Technology. His current research fields include power electronics and motor drive.

Kang Zheng received the B.S. degree in electrical engineering from the China University of Mining and Technology, Xuzhou, China, in 2019, where he is currently working toward the M.S. degree with the School of Electrical and Power Engineering.

His current research interests include high frequency transformer and DC/DC converters.

Yanxing Gu received the B.S. degree in electrical engineering from the Xu Zhou University of Technology, Xuzhou, China, in 2019. She is currently working toward the M.S. degree with the China University of Mining and Technology.

Her current research direction is in motor design.

Ankang Zhang was born in Jiangsu, China. He received the B.S. degree in electrical engineering and intelligent control from Nantong University, Jiangsu, China. He is currently working toward the master’s degree with the China University of Mining and Technology.

His current research interests include motor control and transformer design.

Zhen Jia was born in Xinjiang, China. He received the B.S. degree in electrical engineering from Chongqing University, Chongqing, China. He is currently working toward the master’s degree with the China University of Mining and Technology.

His current research interests include power electronics and motor drive.

A Compact and High-Performance Shielding Enclosure by Using Metamaterial Design

Keyi Cui, Dan Shi, Chi Sun, and Xiaoyong Liu

Department of Electronic Engineering, Beijing University of Posts and Telecommunications, Beijing 100876, China
cuikeyi@buptemc.com, shidan@buptemc.com, sunchi@buptemc.com, liuxiaoyong@srtc.org.cn

Abstract – A compact and high-performance shielding enclosure designed by metamaterial structure based on frequency selective surface (FSS) is proposed. The enclosure has large holes for convenience of airflow and cable access. However, it can achieve great shielding performance by maintaining more than 40 dB attenuation. The shield is composed of $n \times n$ unit cells, and each unit cell is designed by knitting the 2.5-dimensional loop-type elements interconnected through vias. This design shows promising capability of size reduction, bandwidth expansion, and shielding effectiveness enhancement. Moreover, the enlarged holes on the FSS are helpful for the ventilation and heat dissipation. The size of the proposed 2.5-D FSS is only $0.097\lambda_0 \times 0.097\lambda_0$, where λ_0 corresponds to free space wavelength of resonance frequency. The proposed structure provides 3.38 GHz (3.21–6.59 GHz) wide shielding bandwidth. Furthermore, it has stable response to the wide-angle incident wave ranging from 0° to 85° with more than 40 dB attenuation at 4.83 GHz for both *x*-polarization and *y*-polarization. The proposed FSS is practically useful for the shielding of fifth generation (5G) wireless systems, WiMAX, and WLAN.

Index Terms – Electromagnetic shielding, fifth generation (5G) wireless systems, frequency selective surfaces (FSSs), metamaterial, ventilation.

I. INTRODUCTION

A metallic enclosure is often used as a shield to protect sensitive and critical electronic devices from electromagnetic interference. It is indispensable as a part of electronic products to block against unwanted electromagnetic signals [1–3]. The high-frequency signals in the fifth generation (5G) communication bring a challenge to the shielding design of electronic products. The wireless signals will be coupled into the interior through the holes on the metallic enclosure and cause electromagnetic interference [4]. In some cases, metallic shields are huge and heavy, which are inapplicable for compact and lightweight electronic products [5–7].

The influence of holes on shielding effectiveness (SE) of a shield has been widely investigated [8–10]. The literature shows that the size of hole significantly affects the SE. The ventilation may degrade severely due to blockage of deposit dust in smaller holes. The relationship among SE, the diameter of holes, and the frequency (wavelength) is given as follows [11]:

$$\mathrm{SE} = 20\log\left(\lambda/2d\right), \tag{1}$$

where SE represents shielding effectiveness, λ denotes free space wavelength, and d is hole diameter. When the SE remains unchanged, the smaller hole diameter is required for higher frequency. For example, if the SE is required to be more than 26 dB for 5G signal, the hole diameter should be smaller than 1.5 mm. However, the small hole is more likely to deposit dust due to blockage, which may threaten the security of electronic equipment. Therefore, well-performed shielding designs with holes are in demand, and frequency selective surface (FSS) is an optimal choice.

FSS is a periodic structural array printed on a dielectric substrate. In some frequency bands, FSS can act as a band-stop or band-pass filter [12–14]. The frequency selective behavior of FSS depends on the geometry of cells and resonance frequency. Recently, FSS for shielding has been proposed. In [5], a reconfigurable metamaterial for electromagnetic interference shielding is proposed, and PIN diodes are used to interconnect components to control the specific polarization properties. In [15], a compact dual band-stop FSS is proposed. It consists of a modified double square loop with folded strips into the inner space at the four corners of square loops to control resonant wavelengths. In [16], knitting the loop-type FSS elements in 2.5-D is proposed, where segments of the loop are placed alternately on the top and bottom surfaces of the substrate and then interconnected through metallic vias. In [17], a dual-frequency miniaturized FSS with a closely spaced band of operation is proposed, and its SE is less than 20 dB. In [18], the new miniaturized FSS is based on interconnecting the convoluted segments, which are arranged alternately on both sides of the substrate. The SE does not exceed 30 dB. In [19], a compact FSS based on the 2.5-D Jerusalem cross is designed whose SE is less than 40 dB. A compact FSS composed of a swastika unit cell with the smallest

Submitted On: June 29, 2021
Accepted On: October 18, 2021
https://doi.org/10.13052/2021.ACES.J.361113
1054-4887 © ACES

dimension of 7 mm × 7 mm is described in [20]. The SE is less than 35 dB. Very closely located dual-band FSSs are discussed in [21]. And the SE is less than 20 dB. A novel dual-band FSS designed by [22] with closely spaced frequency response is proposed. The SE is less than 35 dB. A convoluted and connection FSS unit cell is reported in [23] for shielding 5G electromagnetic signals. The SE is less than 40 dB. In the above literature, the maximum angular stability does not exceed 75°, and the heat dissipation is poor due to the seamless structure. Although so many FSSs for electromagnetic interference shielding have been proposed, high SE, stable incidence angle, and sufficient heat dissipation are still tricky problems. Therefore, a miniaturized FSS with high shielding performance and vent holes is in demand.

In [4], an FSS with holes is proposed. Although the SE is more than 40 dB, the unit cell size ($0.46\lambda_0 \times 0.46\lambda_0$, where λ_0 corresponds to free space wavelength of resonance frequency) is too large for miniaturized electronic devices. Therefore, a novel compact FSS for shielding 5G signals is proposed in this paper. The FSS unit cell has a large square aperture with 3.2 mm length. However, the SE is more than 40 dB and the heat dissipation is better than metallic enclosure and other FSSs in published literature. In addition, the unit cell of the proposed FSS has a compact size of $0.097\lambda_0 \times 0.097\lambda_0$ through knitting the square loop in 2.5-D. The resonance frequency of the proposed FSS is stable as the incidence angle increases from 0° to 85°.

The paper is organized as follows. The details of the FSS geometry design and performance are described in Section II. The parameter analysis and equivalent circuit model is introduced in Section III. Section IV provides the conclusion.

II. FSS DESIGN AND PERFORMANCE

The structure of the unit cell of the proposed FSS is shown in Figure 1.

Compared with plane FSS, the proposed 2.5-D FSS is improved by square-loop unit consisting mainly of three parts. The first part is metal vias, which connect metallic split rings across two sides of substrate. Vias are an important part of FSS for miniaturization, which elongate total loop perimeter and increase equivalent inductance and capacitance [16]. The second part is the metallic segments at the top and bottom layers. The resonance frequency can be adjusted by extending the loop perimeter through inward convolution. The square loop is selected because of its excellent performance in the stability for various incidence angles, cross-polarization, bandwidth, and band separation [24]. The third part is the substrate, which is FR-4 lossy layer with relative permittivity of 4.3 and loss tangent of 0.025. The effective

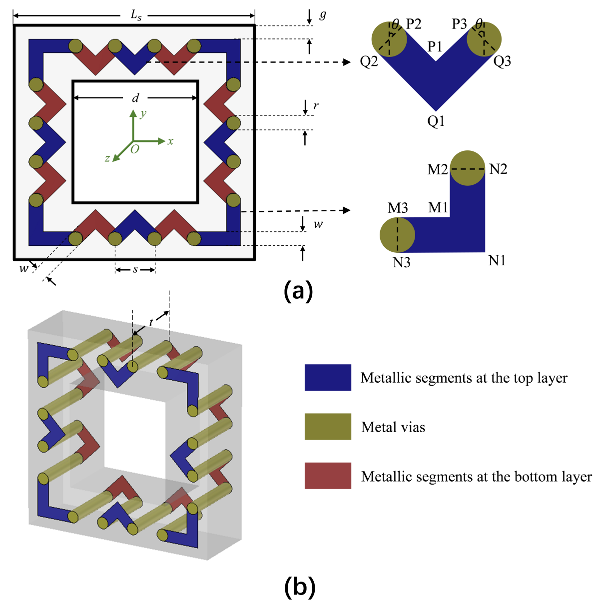

Fig. 1. Structure of the unit cell of the proposed FSS. (a) Top view. (b) Perspective view.

Table 1: Parameters of the unit cell

No.	Parameters	Value
1	L_s	6 mm
2	g	0.32 mm
3	w	0.36 mm
4	r	0.36 mm
5	s	1 mm
6	d	3.2 mm
7	t	2 mm
8	θ	45°

dielectric constant is calculated as follows [25]:

$$\varepsilon_{\text{eff}} = \sqrt{(\varepsilon_r + 1)/2}. \quad (2)$$

The resonance frequency will decrease as the dielectric permittivity increases. Therefore, it is very important to consider the dielectric properties of the substrate in FSS design. In addition, the thickness of the substrate can also significantly affect the shielding performance, which will be analyzed in Section III.

For sufficient heat dissipation and wiring, the diameter (d) of the hole is set to 3.2 mm and the thickness (t) is 2 mm. Finally, the proposed FSS is designed to provide more than 40 dB shielding attenuation at the center frequency of 4.83 GHz. The width of the loop, the gap (g) between adjacent loops, the side length (L_s) of the whole unit, and the radius (r) of vias of loops are given in Table 1. The design details of one of the triangular strips and right-angled strips are given in Table 2

Table 2: Design details of triangular and right-angled strips

Point Name	Coordinate
P1	(0, 2.25456, 0)
P2	(–0.372721, 2.62728, 0)
P3	(0.372721, 2.62728, 0)
Q1	(0, 1.7455, 0)
Q2	(–0.627279, 2.37272, 0)
Q3	(0.627279, 2.37272, 0)
M1	(2.32, –2.32, 0)
M2	(2.32, –1.5, 0)
M3	(1.5, –2.32, 0)
N1	(2.68, –2.68, 0)
N2	(2.68, –1.5, 0)
N3	(1.5, –2.68, 0)

and other strips can be obtained by means of rotation or translation.

The array of the proposed FSS is shown in Figure 2. The entire model is simulated in CST Microwave Studio based on finite integral technique (FIT) method and ANSYS HFSS based on finite element method (FEM), respectively. FIT method describes Maxwell's equations on a grid space with no restriction on grid type, which is widely applied in solving electromagnetic field problems in both time and frequency domains. By discretizing a large system into finite elements, FEM method converts some complex boundary value problems to a system of simple equations, which is also a common numerical method in the electromagnetic field. In two simulation softwares, the periodic boundary conditions are set in the x-axis and y-axis to represent the infinite periodic FSS array and the proposed FSS is excited by Floquet ports in the z-axis. Besides, the open (add space) boundaries are required to be set in the z-axis in CST simulation.

Here, the transmission coefficient is chosen to evaluate the shielding performance of the proposed FSS and smaller transmission coefficient represents better shielding performance. The transmission coefficients at normal incidence of the proposed FSS simulated by CST and HFSS are shown in Figure 3. The results of two electromagnetic simulators are basically consistent, which

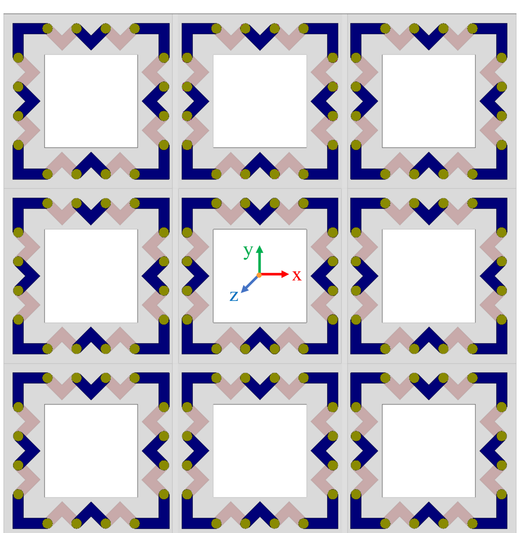

Fig. 2. Array of the proposed FSS.

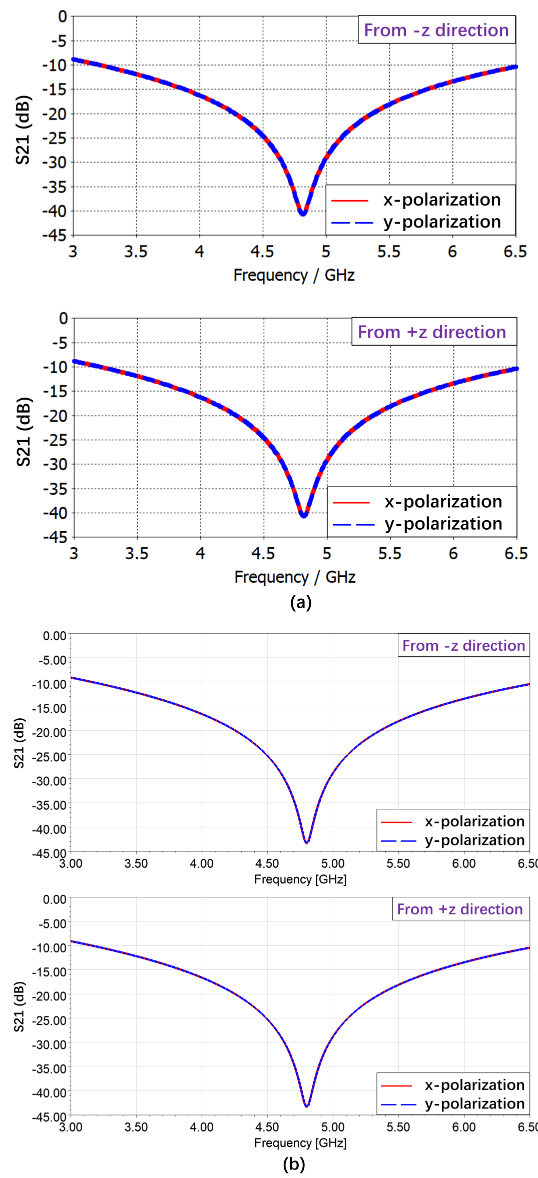

Fig. 3. Transmission coefficients at normal incidence from $-z$ and $+z$ directions for x-polarization and y-polarization simulated by (a) CST and (b) HFSS.

further verifies the validity of the proposed FSS. Simulation results show that the proposed FSS provides more than 40.74 dB attenuation for a bandwidth of 3.38 GHz (3.21–6.59 GHz) at the center frequency of 4.83 GHz and can fully meet the shielding requirement. It can be seen that the results with excitation from both $+z$ and $-z$ directions are the same. In addition, the proposed FSS behaves identically for both x-polarization and y-polarization, which provides stability in shielding.

The angular stability is also investigated. The S21 at different incidence angles from $-z$ and $+z$ directions for x-polarization and y-polarization is shown in Figures 4 and 5. Simulation results show that the S21 with excitation from both $+z$ and $-z$ directions is the same. It can also be seen that the resonance frequency of the proposed FSS deviates less than 0.5% at various incident angles. Therefore, for x-polarization and y-polarization, the proposed FSS can provide a stable S21 up to 85° incident angle at the frequency of 4.83 GHz. As shown in Figures 4 and 5, the S21 for x-polarization decreases when the incidence angle increases. However, the S21 for y-polarization increases when the incidence angle increases. The phenomenon is mainly attributed to wave impedance change, which validates the basic theory of FSS mentioned in [25].

III. PARAMETER ANALYSIS

The distribution of surface current at the resonance frequency of 4.83 GHz is illustrated in Figure 6.

The substrate thickness t is much less than free space wavelength of resonance frequency. The surface current flows through the metal vias, which provide additional inductance due to elongation of the loop conductor. Moreover, vias also enhance the capacitance due to coupling between adjacent elements. The equivalent circuit model is shown in Figure 7 and the resonance frequency is calculated as follows:

$$f = 1/2\pi\sqrt{(L+L_t)(C+C_t)}, \tag{3}$$

where L and C represent the inductance and capacitance of metallic strip, respectively. L_t and C_t are introduced by the metallic vias. L_t is contributed by vias itself and C_t is generated by the adjacent vias in two neighboring units. According to formula (3), the resonance frequency of 2.5-D structure decreases compared with the plane structure with the same size. Thus, vias show a capability for reducing the size of FSSs.

Because transmission coefficients with excitation from $-z$ and $+z$ directions are the same, the results for $-z$ direction are used in the following discussion and analysis. The comparison of transmission coefficients between 2.5-D FSS and plane FSS with the same size for normally incident plane wave is represented in Figure 8. As shown in Figure 8, the resonance frequency of the 2.5-D FSS is lower than that of plane square-loop FSS,

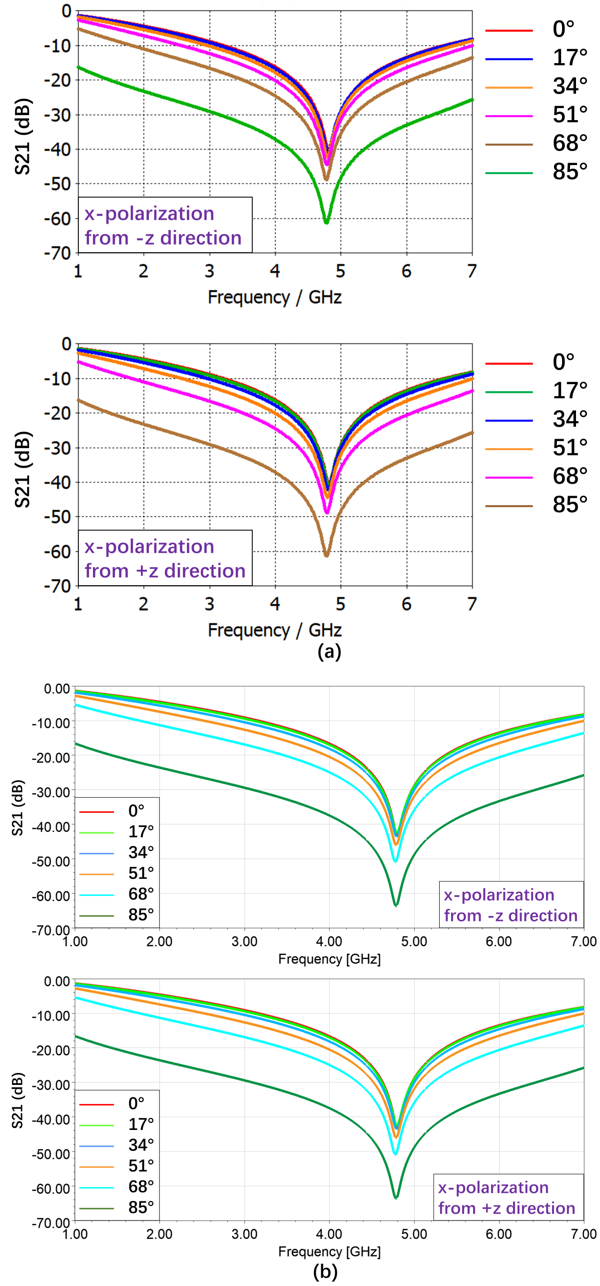

Fig. 4. Transmission coefficients at different incident angles from $-z$ and $+z$ directions for x-polarization simulated by (a) CST and (b) HFSS.

which validates the previous analysis. Hence, the band characteristics can be adjusted by changing the total perimeter of the 2.5-D square loop. Compared with the design in [4] with size of $0.46\lambda_0 \times 0.46\lambda_0$, the unit cell of the proposed FSS has a more compact size of $0.097\lambda_0 \times 0.097\lambda_0$. This indicates that the proposed FSS achieves the structure miniaturization.

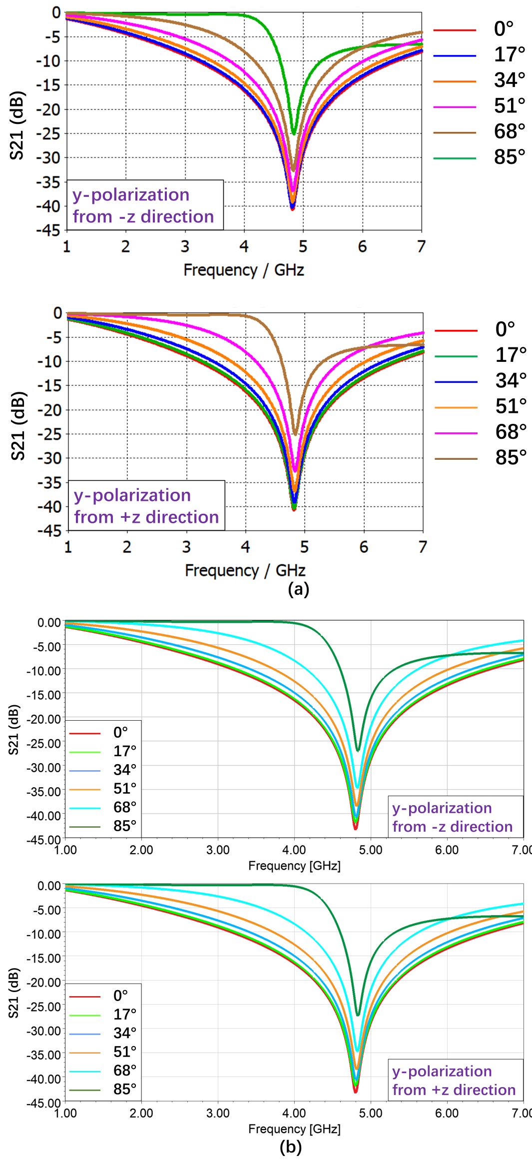

Fig. 5. Transmission coefficients at different incident angles from –z and +z directions for y-polarization simulated by (a) CST and (b) HFSS.

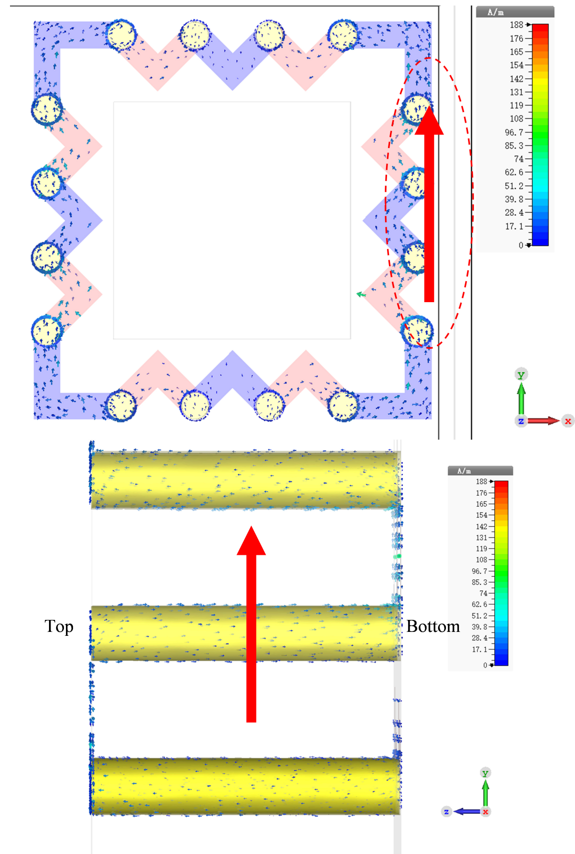

Fig. 6. Distribution of the surface current.

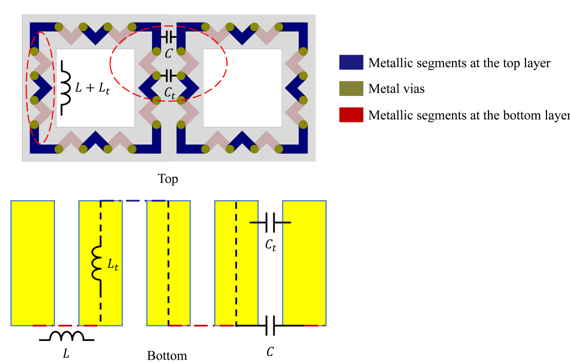

Fig. 7. The equivalent circuit of the unit cell of the proposed FSS.

The comparison of transmission coefficients between 2.5-D FSS and a metal plate with hole at normal incidence with excitation from –z direction is illustrated in Figure 9. It can be seen that there is not much difference between two S21 values at 4.83 GHz. However, in the case of similar shielding performance, the proposed FSS with FR-4 lossy substrate is much lighter than a metal plate with the same size, which is more suitable for small lightweight electronic products.

The relative dielectric constant ε_r of the dielectric substrate is 4.3, and the thickness t of the dielectric substrate changes from 1.8 to 2.2 mm at 0.2-mm intervals to investigate the influence of dielectric substrate thickness. Because the results for x-polarization and y-polarization at normal incidence from –z and +z directions are the same, the results for x-polarization at normal incidence from –z direction are taken as an example to be analyzed and shown in Figure 10. When the thickness of the dielectric substrate increases, the resonance frequency

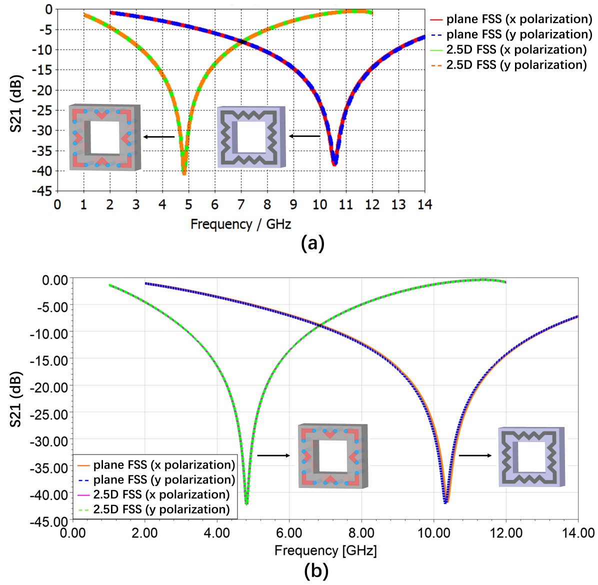

Fig. 8. Comparison of transmission coefficients between 2.5-D FSS and plane FSS at normal incidence simulated by (a) CST and (b) HFSS.

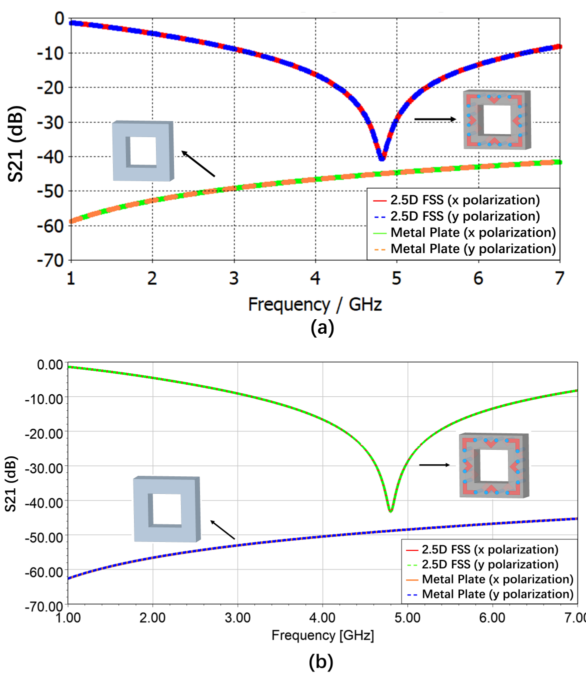

Fig. 9. Comparison of transmission coefficients between 2.5-D FSS and a metal plate at normal incidence simulated by (a) CST and (b) HFSS.

will decrease due to the inductance and capacitance contributed by vias.

Table 3: Comparison with other structures in published literature

FSS	Holes	Size (λ_0)	Attenuation	Bandwidth	Stability
[26]	Without	0.30	40 dB	Not reported	45°
[17]	Without	0.08	20 dB	Not reported	60°
[18]	Without	0.037	30 dB	Not reported	60°
[20]	Without	0.125	35 dB	400 MHz (–20 dB)	60°
[21]	Without	0.216	20 dB	Not reported	45°
[22]	Without	0.088	35 dB	315 MHz (–15 dB)	60°
[23]	Without	0.069	40 dB	950 MHz (–10 dB)	60°
[4]	With	0.458	40 dB	2 GHz (–30 dB)	60°
Proposed	With	0.097	40.74 dB	3.38 GHz (–10 dB)	85°

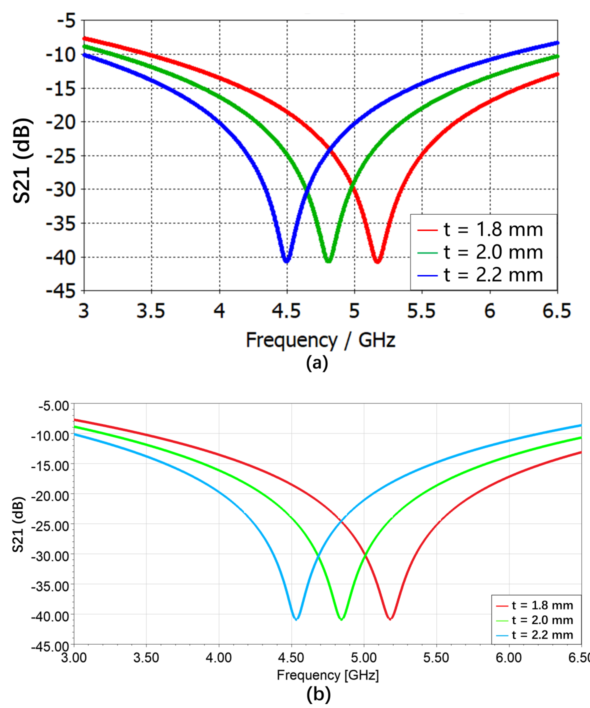

Fig. 10. Influence of dielectric thickness on transmission coefficients simulated by (a) CST and (b) HFSS simulator.

Finally, the comparison between the proposed 2.5-D FSS and the results from published literature are listed in Table 3. It can be seen from Table 3 that the proposed 2.5-D FSS shows excellent performance in miniaturization. Especially compared with the FSS with holes [4], the unit cell size is significantly reduced. The proposed FSS has a large attenuation bandwidth, which is about 3.56 times larger than that in [23]. A Compact and High-Performance Shielding Enclosure by Using Metamaterial Design. In addition, the proposed 2.5-D FSS has small S21 and the angular stability is up to 85°.

IV. CONCLUSION

An effective and novel metamaterial structure is proposed for 5G electromagnetic shielding. It provides 40.74 dB attenuation and 3.38-GHz bandwidth to suppress interference signals operating near 4.83 GHz. In particular, the proposed FSS overcomes the difficulty that the heat dissipation of the metal shielding deteriorates significantly for small apertures. It demonstrates the advantage of high shielding performance, small size, and excellent heat dissipation. This design can be further extended to the application of WLAN, ISM, GSM, and Wi-Fi shielding.

ACKNOWLEDGMENT

This work was supported by the National Natural Science Foundation of China under Grant 61771069 and National Key Laboratory on Electromagnetic Environment Effects under Grant A03B07C01-202002D0.

REFERENCES

[1] C. R. Paul, *Introduction to Electromagnetic Compatibility*, John Wiley & Sons, vol. 184, pp. 3-48, Jan. 2006.

[2] L. H. Hemming, *Architectural Electromagnetic Shielding Handbook: A Design and Specification Guide*, pp. 7-11, John Wiley & Sons, Aug. 2000.

[3] H. W. Ott, *Electromagnetic Compatibility Engineering*, John Wiley & Sons, pp. 238-300, Sep. 2011.

[4] L. Yan, L. Xu, X. Zhao, and R. X.-K. Gao, "An angularly stable frequency selective surface with vent holes for 5G electromagnetic shielding," *in 2019 IEEE International Symposium on Electromagnetic Compatibility-EMC EUROPE*, pp. 366-369, Sep. 2019.

[5] M. Masud, B. Ijaz, A. Iftikhar, M. Rafiq, and B. Braaten, "A reconfigurable dual-band metasurface for EMI shielding of specific electromagnetic wave components," *in 2013 IEEE International Symposium on Electromagnetic Compatibility*, pp. 640-644, Aug. 2013.

[6] F. Li, J. Han, and C. Zhang, "Study on the influence of PCB parameters on the shielding effectiveness of metal cavity with holes," *in 2019 IEEE 3rd Information Technology, Networking, Electronic and Automation Control Conference (ITNEC)*, pp. 383-387, Mar. 2019.

[7] J. Bai, Y. Gao, Y. Shen, and D. Shi, "Shielding effectiveness of an enclosure with PCB," *in 2009 IEEE 5th Asia-Pacific Conference on Environmental Electromagnetics*, pp. 130-134, Sep. 2009.

[8] T. Otoshi, "A study of microwave leakage through perforated flat plates (short papers)," *IEEE Transactions on Microwave Theory and Techniques*, vol. 20, no. 3, pp. 235-236, Mar. 1972.

[9] B. Archambeault and C. Brench, "Shielded air vent design guidelines for EMI modeling," *in 1993 IEEE International Symposium on Electromagnetic Compatibility*, pp. 195-199, Aug. 1993.

[10] M. Li, J. Nuebel, J. L. Drewniak, R. E. DuBroff, T. H. Hubing, and T. P. Van Doren, "EMI from airflow aperture arrays in shielding enclosures-experiments, FDTD, and MoM modeling," *IEEE Transactions on Electromagnetic Compatibility*, vol. 42, no. 3, pp. 265-275, Aug. 2000.

[11] H. W. Ott and H. W. Ott, *Noise Reduction Techniques in Electronic Systems*, Wiley, New York, vol. 442, pp. 4-16, May 1988.

[12] R. Natarajan, M. Kanagasabai, S. Baisakhiya, R. Sivasamy, S. Palaniswamy, and J. K. Pakkathillam, "A compact frequency selective surface with stable response for WLAN applications," *IEEE Antennas and Wireless Propagation Letters*, vol. 12, pp. 718-720, May 2013.

[13] H. AlKayyali and N. Qasem, "Convoluted frequency selective surface wallpaper to block the industrial, scientific, and medical radio bands inside buildings," *American Academic & Scholarly Research Journal*, vol. 5, no. 3, p. 106, Apr. 2013.

[14] R. Sivasamy, L. Murugasamy, M. Kanagasabai, E. F. Sundarsingh, and M. G. N. Alsath, "A low-profile paper substrate-based dual-band FSS for GSM shielding," *IEEE Transactions on Electromagnetic Compatibility*, vol. 58, no. 2, pp. 611-614, Feb. 2016.

[15] Y. Mannaa and R. W. Aldhaheri, "New dual-band frequency selective surface for GSM shielding in secure-electromagnatic buildings using square loop fractal configurations," *in 2016 16th Mediterranean Microwave Symposium (MMS)*, pp. 1-4, IEEE, Nov. 2016.

[16] T. Hussain, Q. Cao, J. K. Kayani, and I. Majid, "Miniaturization of frequency selective surfaces using 2.5-D knitted structures: design and synthesis," *IEEE Transactions on Antennas and Propagation*, vol. 65, no. 5, pp. 2405-2412, Feb. 2017.

[17] C.-N. Chiu and W.-Y. Wang, "A dual-frequency miniaturized-element FSS with closely located

resonances," *IEEE Antennas and Wireless Propagation Letters*, vol. 12, pp. 163-165, Feb. 2013.

[18] D. Li, T. Li, and E. Li, "Implementation of ultra-miniaturised frequency-selective structures based on 2.5 D convoluted segments," *Electronics Letters*, vol. 54, no. 8, pp. 476-478, Apr. 2018.

[19] P. Zhao, Y. Zhang, R. Sun, W.-S. Zhao, Y. Hu, and G. Wang, "Design of a novel miniaturized frequency selective surface based on 2.5-dimensional Jerusalem cross for 5G applications," *Wireless Communications and Mobile Computing*, vol. 2018, Apr. 2018.

[20] R. Natarajan, M. Kanagasabai, S. Baisakhiya, R. Sivasamy, S. Palaniswamy, and J. K. Pakkathillam, "A compact frequency selective surface with stable response for WLAN applications," *IEEE Antennas and Wireless Propagation Letters*, vol. 12, pp. 718-720, May 2013.

[21] F.-C. Huang, C.-N. Chiu, T.-L. Wu, and Y.-P. Chiou, "Very closely located dual-band frequency selective surfaces via identical resonant elements," *IEEE Antennas and Wireless Propagation Letters*, vol. 14, pp. 414-417, Oct. 2014.

[22] R. Sivasamy and M. Kanagasabai, "A novel dual-band angular independent FSS with closely spaced frequency response," *IEEE Microwave and Wireless Components Letters*, vol. 25, no. 5, pp. 298-300, Apr. 2015.

[23] H. Wang, S. Qu, J. Wang, M. Yan, and L. Zheng, "Dual-band miniaturised FSS with stable resonance frequencies of 3.4/4.9 GHz for 5G communication systems applications," *IET Microwaves, Antennas & Propagation*, vol. 14, no. 1, pp. 1-6, Jan. 2020.

[24] T.-K. Wu, *Frequency Selective Surface and Grid Array*, Wiley-Interscience, vol. 40, pp. 27-70, Jul. 1995.

[25] B. A. Munk, *Frequency Selective Surfaces: Theory and Design*, John Wiley & Sons, pp. 1-48, Apr. 2005.

[26] W. Kiermeier and E. Biebl, "New dual-band frequency selective surfaces for GSM frequency shielding," *in 2007 European Microwave Conference, IEEE*, pp. 222-225, Oct. 2007.

Keyi Cui was born in Heze, Shandong, China, in 1998. She is currently working toward the master's degree in electronic engineering from the Beijing University of Posts and Telecommunications, Beijing, China. Her main research interests include metamaterial, metalens, and machine learning.

Dan Shi (Member, IEEE) received the Ph.D. degree in electronic engineering from the Beijing University of Posts & Telecommunications, Beijing, China, in 2008. She has been a Professor with the Beijing University of Posts & Telecommunications. Her interests include electromagnetic compatibility, electromagnetic environment, and electromagnetic computation.

Chi Sun was born in Xi'an, Shanxi, China, in 1996. He received the master's degree in electronic engineering from the Beijing University of Posts and Telecommunications, Beijing, China, in 2021. His main research content is electromagnetic compatibility and theory, mainly in FSS design for shielding.

Xiaoyong Liu received the bachelor's degree in radio technology and information system from Tsinghua University, Beijing, China, in 2002. He is currently working toward the Ph.D. degree in electronic science and technology from the Beijing University of Posts & Telecommunications, Beijing, China. His research interests include electromagnetic compatibility, testing and measurement, and radio frequency spectrum technology.

Interaction Magnetic Force of Cuboidal Permanent Magnet and Soft Magnetic Bar Using Hybrid Boundary Element Method

Ana N. Vučković[1], Mirjana T. Perić[1], Saša S. Ilić[1], Nebojša B. Raičević[1], and Dušan M. Vučković[2]

[1]Department of Theoretical Electrical Engineering, University of Niš, Faculty of Electronic Engineering, 18000 Niš, Serbia
{ana.vuckovic, mirjana.peric, sasa.ilic, nebojsa.raicevic}@elfak.ni.ac.rs

[2]Department of Computer Science, University of Niš, Faculty of Electronic Engineering, 18000 Niš, Serbia
dusan.vuckovic@elfak.ni.ac.rs

Abstract **–** The hybrid boundary element method for solving a three-dimensional magnetostatic problem is presented in this paper for the first time. The interaction force between the cuboidal permanent magnet and the bar, made of soft magnetic material, is calculated. Results of the presented approach are confirmed using COMSOL Multiphysics as well as with the results of the image theorem that is applicable when the dimensions of the bar are large enough; so it could be considered an infinite soft magnetic plane.

Index Terms **–** Hybrid boundary element method (HBEM), magnetization charges, magnetic force, cuboidal permanent magnet.

I. INTRODUCTION

In order to precisely calculate performance parameters of different electronic devices, various mathematical methods can be applied. Efficiency of the most common ones in the analysis of the problems involving electromagnetic fields of very thin electrodes [1] is debatable. Some of these applications were analyzed in the cable terminations having a thin deflector [2], strip lines with perfect conducting plates [3], or floating stripes used for electrostatic field modeling [4].

Since there is a constant need for size reduction and optimization of electrical devices and gadgets, the development of new mathematical approaches for their performance's calculation is a necessity. The hybrid boundary element method (HBEM) developed at the Department of Theoretical Electrical Engineering was initially made for solving electromagnetic field distribution in the vicinity of cable joints and terminations [5, 6], but it finds its application in solving numerous electromagnetic problems. As a combination of the boundary element method (BEM) [7], the equivalent electrodes method (EEM) [8], and the point-matching method (PMM), until now, it was applied for permanent magnets (PMs) configuration modeling [9, 10], characteristic parameters of transmission lines calculation [11–13], and for the grounding system analyses [14]. Also, a line inductance of two-wire in the vicinity of magnetic material composites was successfully calculated using this approach [15]. All the structures that are analyzed using HBEM are either planar or axially symmetrical, but the method can be used for solving 3D electromagnetic problems too. The advantage of the method is that equivalent electrodes, equivalent currents, or magnetic sources, depending on the problem that is being solved, are located on the body surface, or boundary surface between two different materials, while in the case of the charge simulation method (CSM), sources are placed within the volume.

The application of HBEM for 3D magnetostatic problems is presented here for the first time. It will be applied to a PM configuration modeling because, due to the low production cost, PMs have become a primary choice in many instances. The absence of a power supply unit also goes in favor of PMs. Perfect examples are magnetic couplings, bearings, different assemblies, sensors, or actuators. Cuboidal, cylindrical, and ring magnets are the most common shapes of PMs and many scientists around the world are calculating the field, force, and torque of different configurations that contain them [16–21]. Since Akoun presented his study of cuboidal PMs [22], many papers were published that were dealing with the force and torque between cuboidal magnets using Ampere's current [23, 24] or magnetic charges approach [16, 19, 20, 25–27]. Also, the calculation of the interaction between a cuboidal magnet and current carrying conductor [28] or a cuboidal magnet and infinite magnetic plate are the topics of interest [29]. The HBEM was applied for calculating the force between ring and cylindrical PM and the object of the finite dimension made of soft magnetic material [9, 10].

Submitted On: June 16, 2021
Accepted On: October 30, 2021
https://doi.org/10.13052/2021.ACES.J.361114
1054-4887 © ACES

This method is used in the paper for the force calculation between cuboidal magnet and the bar made of soft magnetic material. The advantages of this approach are its simplicity and low computation time. The results presented could prove important in the modeling and manufacturing process of different devices that incorporate PMs.

II. METHODOLOGY

The basic idea of the HBEM is that either the conductor surface or the boundary surfaces between two dielectric layers or even boundary surface between two different magnetic materials should be divided first into number of small segments. For the electrostatic problems, equivalent electrodes or electric charges should be placed right in the center of each segment. Influence of the magnetic materials of different magnetic permittivity can be replaced by equivalent currents that are located on the boundary surface of the magnetic layers. Using the boundary condition for tangential components of magnetization vector on boundary surface of two magnetic materials, $M_{2\mathrm{t}} - M_{1\mathrm{t}} = J_{\mathrm{s}}$, a system of linear equations can be formed with microscopic Ampere's currents, J_{s}, as the unknown values [5].

The system of magnetic sources placed along the boundary surface also substitutes the influence of two different magnetic materials. In that case, the system of linear equations is formed using the boundary condition for the normal component of magnetization vector on the boundary surface, $M_{2\mathrm{n}} - M_{1\mathrm{n}} = \eta_{\mathrm{m}}$ [9, 10].

The geometry of the sources depends on the problem that is being solved. In case of axial symmetry, the magnetic sources are toroidal [9, 10], for the planar problems, they are line charges [13, 14], and for 3D problems, magnetic sources are spherically shaped.

A. Model definition

Using HBEM, the system of cuboidal PM and the bar made of soft magnetic material is modeled (Figure 1).

The PM magnetized in the axial direction is modeled using the fictitious magnetic charges approach. Since the boundary conditions for the surface and volume charge density have to be satisfied [30]

$$\eta_{\mathrm{m}} = \hat{n} \cdot \boldsymbol{M}, \tag{1}$$

$$\rho_{\mathrm{m}} = -\nabla \cdot \boldsymbol{M} = 0, \tag{2}$$

it is obvious that the magnetic charges exist on the bottom and the top faces of the magnet, with the surface density $\eta_{\mathrm{m}1} = \hat{n} \cdot \boldsymbol{M} = M$ for the top face, and $\eta_{\mathrm{m}2} = \hat{n} \cdot \boldsymbol{M} = -M$, for the bottom one [25]. The volume charge density is equal to zero.

On the other hand, since the bar is made of soft magnetic material of magnetic permeability $\mu = \mu_0 \mu_{\mathrm{r}2}$, its influence can be replaced with a system of small airborne

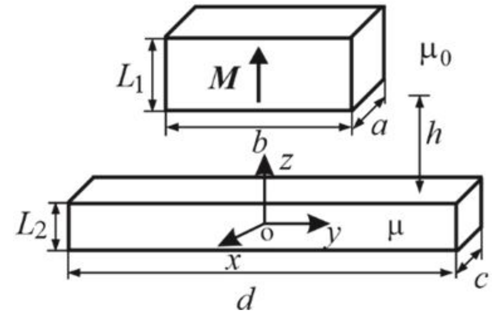

Fig. 1. Cuboidal magnet placed above soft magnetic bar.

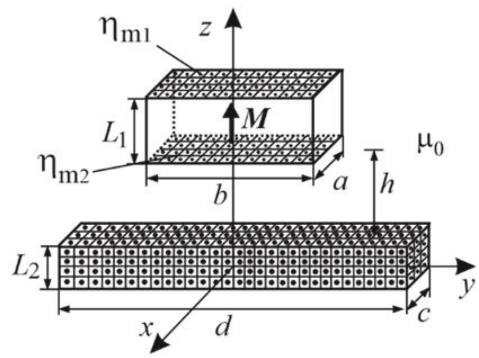

Fig. 2. Discretization model for the considered system.

spherical magnetic sources. Boundaries between the soft magnetic bar and the air (all faces of the magnetic bar) are divided into a large number of square-shaped segments. Each magnetic source is located in the center of a segment. The discretization model of the system is presented in the Figure 2.

B. HBEM application

The magnetic scalar potential of magnetic sources system

$$\varphi_{\mathrm{m}} = \sum_{n=1}^{N} Q_n G(\boldsymbol{r}, \boldsymbol{r_n}) \tag{3}$$

can be calculated starting from the Green's function of an isolated point magnetic charge

$$G(\boldsymbol{r}, \boldsymbol{r_n}) = \frac{1}{4\pi |\boldsymbol{r} - \boldsymbol{r_n}|}, \tag{4}$$

where $\boldsymbol{r}$ is the field point radius vector and $\boldsymbol{r_n}$ is the radius vector of the spherical magnetic source center.

After the discretization (Figure 2), the magnetic scalar potential of the considered system becomes

$$\varphi_{\mathrm{m}} = \sum_{k=1}^{N_a N_b} \left(\frac{Q_{\mathrm{k}}^{\mathrm{m}}}{4\pi \sqrt{(x-x_k)^2 + (y-y_k)^2 + (z-z_{k1})^2}} - \frac{Q_{\mathrm{k}}^{\mathrm{m}}}{4\pi \sqrt{(x-x_k)^2 + (y-y_k)^2 + (z-z_{k2})^2}} \right) +$$

$$+\sum_{i=1}^{N_{\text{tot}}} \frac{Q_i}{4\pi} \frac{1}{\sqrt{(x-x_i)^2+(y-y_i)^2+(z-z_i)^2}}. \quad (5)$$

The first sum in eqn (5) is the magnetic scalar potential of the PM. The magnetic charges of the PM segments are $Q_{\mathrm{k}}^{\mathrm{m}} = M\frac{ab}{N_{\mathrm{a}}N_{\mathrm{b}}}$.

The positions of the top face elements are $(x_k, y_k, z_{k1} = h+L_1+L_2/2)$ and for the bottom ones are $(x_k, y_k, z_{k2} = h+L_2/2)$.

$N_a \cdot N_b$ is the total number of the surface charges on the PM face. N_a and N_b are the number of the segments along the edges a and b, calculated from the initial number of segments (magnetic point charges) N. They depend on the PM dimensions, $N_a = \sqrt{aN/b}$ and $N_b = N\Big/\sqrt{aN/b}$.

The second sum in eqn (5) represents the magnetic scalar potential of the bar made of soft magnetic material. Each face of the bar is discretized into square segments with corresponding spherical magnetic sources, Q_i, placed in the center of each segment.

The radii of the spherical sources placed along the faces of the bar are

$a_{\mathrm{ez}} = \sqrt{\frac{\Delta x \Delta y}{2\pi}}$, for the bottom and the top faces,

$a_{\mathrm{ex}} = \sqrt{\frac{\Delta z \Delta y}{2\pi}}$, for the front and back faces,

$a_{\mathrm{ey}} = \sqrt{\frac{\Delta x \Delta z}{2\pi}}$, for the right and left faces,

where $\Delta x = \frac{N_d}{d}, \Delta y = \frac{N_c}{c}, \Delta z = \frac{N_L}{L_2}$.

$N_d, N_c,$ and N_L are the number of the segments along the edges $d, c,$ and L_2 that are calculated starting from the initial number of the elements, N_{s}. So, the total number of segments (or unknown magnetic sources Q_i) is $N_{\text{tot}} = 2N_cN_d + 2N_cN_L + 2N_dN_L$.

Magnetic field strength vector can be expressed as

$$\boldsymbol{H} = -\operatorname{grad}(\varphi_{\mathrm{m}}). \quad (6)$$

The relation that the normal component of the magnetic field vector and surface charges must complete is

$$\hat{n}_k \cdot H_k = -\frac{\mu_{\mathrm{r}2}}{\mu_{\mathrm{r}1}-\mu_{\mathrm{r}2}} \eta_{\mathrm{m}i}, \quad (7)$$

$$\eta_{\mathrm{m}i} = \frac{Q_i}{S_i},\ i = 1,2,\ldots,N_{\text{tot}}, k = 1,...,6,$$

where $\hat{n}_k$ is the outgoing unit normal vector and S_i is the surface of the ith segment.

The system of the linear equations is formed after the point matching method is applied for the normal component of the magnetic field. The solution of the linear equations system gives the values of unknown boundary sources of the bar Q_i. After the magnetic sources are calculated, the magnetic scalar potential of the bar becomes

$$\varphi_{\mathrm{mb}} = \frac{1}{4\pi}\sum_{i=1}^{N_{\text{tot}}} \frac{Q_i}{\sqrt{(x-x_i)^2+(y-y_i)^2+(z-z_i)^2}}. \quad (8)$$

The magnetic field vector can be determined by the expression (6), and magnetic flux density vector in the vicinity of the bar is

$$\boldsymbol{B^{ext}} = \mu_0 \boldsymbol{H^{ext}}. \quad (9)$$

Finally, when magnetic flux density vector generated by the bar is determined, the interaction force can be calculated using the superposition of the force obtained between all sources of the bar and all magnetic charges of the PM:

$$\boldsymbol{F} = \sum_{k=1}^{N_aN_b} Q_k^m \boldsymbol{B^{ext}}. \quad (10)$$

Substituting eqn (9) in eqn (10), the force is calculated, and its components are

$$F_x = \frac{\mu_0}{4\pi}\frac{Mab}{N_aN_b}\times \sum_{k=1}^{N_aN_b}\sum_{i=1}^{N_{\text{tot}}} Q_i \left(\frac{x_k-x_i}{\left((x_k-x_i)^2+(y_k-y_i)^2+(z_{k1}-z_i)^2\right)^{\frac{3}{2}}} - \frac{x_k-x_i}{\left((x_k-x_i)^2+(y_k-y_i)^2+(z_{k2}-z_i)^2\right)^{\frac{3}{2}}} \right), \quad (11)$$

$$F_y = \frac{\mu_0}{4\pi}\frac{Mab}{N_aN_b}\times \sum_{k=1}^{N_aN_b}\sum_{i=1}^{N_{\text{tot}}} Q_i \left(\frac{y_k-y_i}{\left((x_k-x_i)^2+(y_k-y_i)^2+(z_{k1}-z_i)^2\right)^{\frac{3}{2}}} - \frac{y_k-y_i}{\left((x_k-x_i)^2+(y_k-y_i)^2+(z_{k2}-z_i)^2\right)^{\frac{3}{2}}} \right), \quad (12)$$

$$F_z = \frac{\mu_0}{4\pi}\frac{Mab}{N_aN_b}\times \sum_{k=1}^{N_aN_b}\sum_{i=1}^{N_{\text{tot}}} Q_i \left(\frac{z_{k1}-z_i}{\left((x_k-x_i)^2+(y_k-y_i)^2+(z_{k1}-z_i)^2\right)^{\frac{3}{2}}} - \frac{z_{k2}-z_i}{\left((x_k-x_i)^2+(y_k-y_i)^2+(z_{k2}-z_i)^2\right)^{\frac{3}{2}}} \right). \quad (13)$$

The x and y components of the force are equal to zero; so the calculated z component represents the interaction force.

III. NUMERICAL RESULTS

The expression for the interaction force, developed using HBEM, is easily handled in the Wolfram Mathematica environment and enables parametric studies of

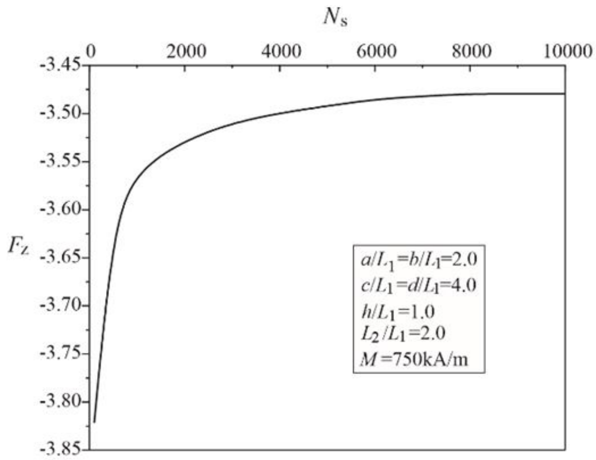

Fig. 3. Convergence results.

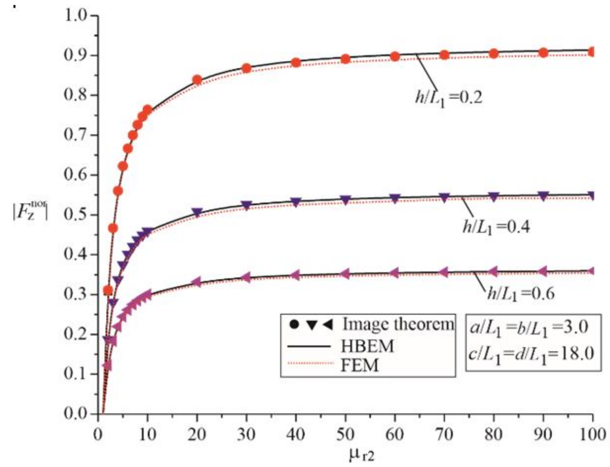

Fig. 4. Interaction force versus relative magnetic permeability μ_{r2}.

Table 1: Computational time

	HBEM	Image Theorem	FEM
CPU time [s]	39.4	28.6	129

the force. The results are presented graphically for the different configuration parameters.

Convergence of the results is tested, and the results are compared with the finite-element method (FEM) (COMSOL Multiphysics) computations in order to determine the optimal number of magnetic sources. For the system parameters: $a/L_1 = b/L_1 = 2.0, h/L_1 = 1.0, c/L_1 = d/L_1 = 4.0$, $L_2/L_1 = 2.0$, $M = 750kA/m$, $\mu_r = 100$, $N = 3000$, the attraction force is calculated for various numbers of bar segments, N_s, as it is presented in Figure 3. The same configuration is modeled in COMSOL Multiphysics and the obtained intensity of the force is 3.4617 N. In the case when the initial number of segments is $N_s = 7000$, the relative deviation between FEM and HBEM result is 0.58%. It is confirmed that the HBEM results are compliant with the value obtained with FEM. In the further calculations, the number of PM segments is limited to $N = 3000$ and the initial number of the bar segments is $N_s = 7000$.

The results of the presented approach are also compared with the ones obtained using the method of images [23, 25] for the case where the dimensions of the bar, $c/L_1, d/L_1$ are large enough; so it could be considered an infinite soft magnetic plane. Figure 4 presents comparative results of three different methods. The normalized magnetic force, $F_z^{nor} = F_z/\mu_0 M^2 L_1^2$, versus relative permeability of the bar, for various axial displacements of the magnet is shown. Configuration parameters are: $a/L_1 = b/L_1 = 3.0$, $c/L_1 = d/L_1 = 18.0$. Results shown in Figure 4 also prove the accuracy of the method. HBEM results coincide with the image theorem results, with relative deviation lower than 0.6%. FEM results, on the other hand, have a relative deviation below 1.5%.

Table 1 presents the computational time in case where HBEM, image theorem, and FEM were applied. The computational time is the lowest in case of the image theorem, but a disadvantage of this approach is that it is not applicable when the bar is of finite dimension.

The comparative results of HBEM and FEM are presented in Figures 5–9 with the satisfactory alignment.

Normalized axial force between PM and soft magnetic bar versus normalized axial displacement of PM, h/L_1, for variable relative permeability of the bar, μ_{r2}, is presented in Figure 5. The analysis is per-

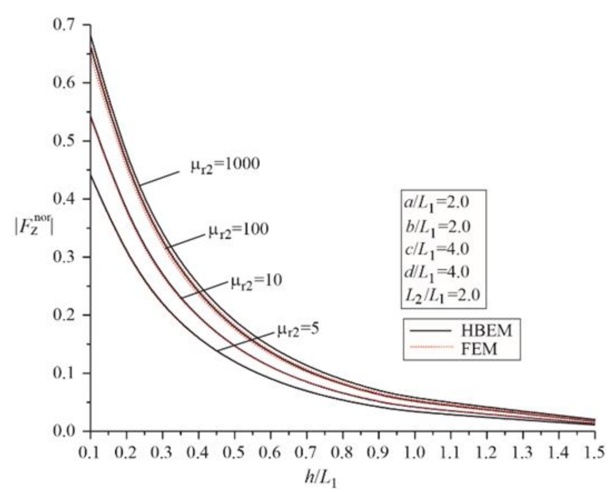

Fig. 5. Interaction force versus h/L_1 for variable magnetic permeability μ_{r2}.

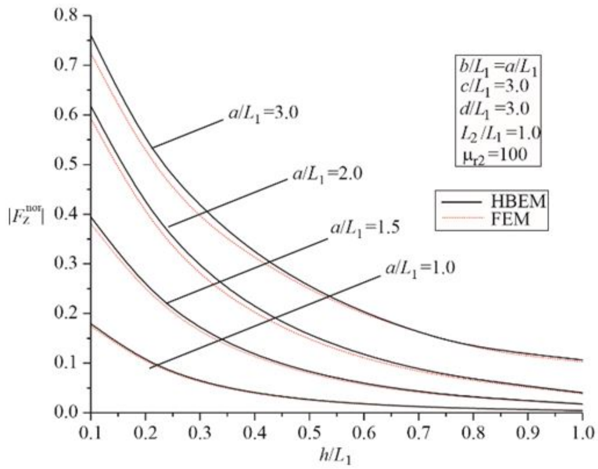

Fig. 6. Interaction force versus h/L_1 for different values of PM dimensions.

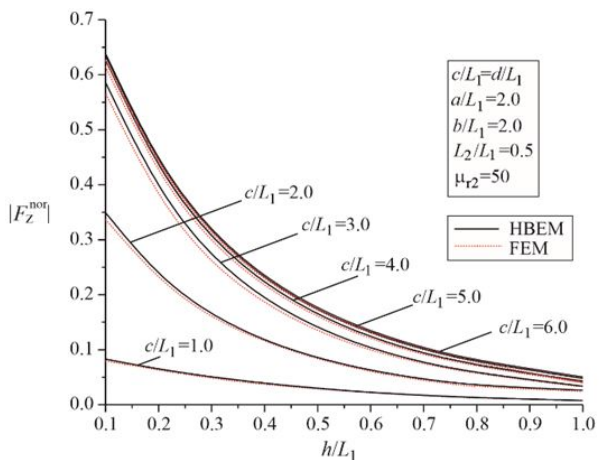

Fig. 7. Interaction force versus h/L_1 for different values of bar's dimensions.

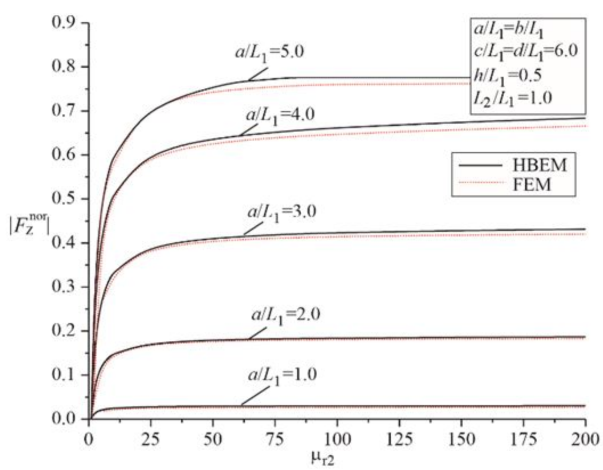

Fig. 8. Interaction force versus relative magnetic permeability of the bar for variable PM dimensions.

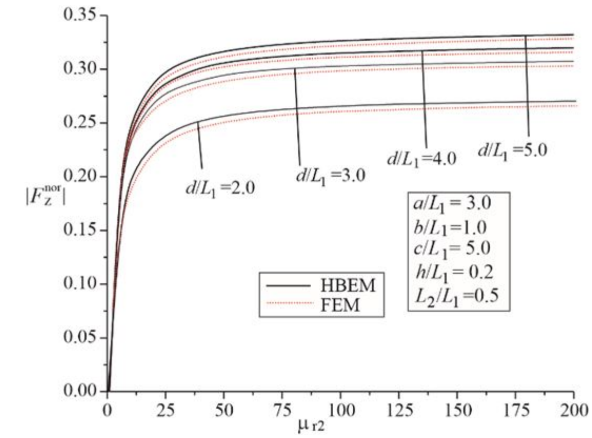

Fig. 9. Interaction force versus relative magnetic permeability μ_{r2} for variable bar's dimensions.

formed for $a/L_1 = b/L_1 = 2.0$, $c/L_1 = d/L_1 = 4.0$, $L_2/L_1 = 2$.

Figures 6 and 7 present interaction force distribution versus the distance h/L_1 for different values of PM dimensions and for various bar's dimensions, respectively. The system parameters in the first case are: $c/L_1 = d/L_1 = 3.0$, $L_2/L_1 = 1$, $\mu_{r2} = 100$, while in the second example: $\mu_{r2} = 50$, $a/L_1 = b/L_1 = 2.0$, $L_2/L_1 = 0.5$.

Force distribution versus relative permeability of the bar is presented in Figures 8 and 9 with the configuration parameters: $c/L_1 = d/L_1 = 6.0$, $L_2/L_1 = 1.0$, $h/L_1 = 0.5$ and $a/L_1 = 3.0$, $b/L_1 = 1.0$, $c/L_1 = 5.0$, $h/L_1 = 0.2$,$h/L_1 = 0.5$, respectively.

IV. CONCLUSION

The HBEM is applied for the calculation of the interaction force between cuboidal PM and the bar made of soft magnetic material. The three-dimensional electromagnetic problem is solved for the first time using this approach. The accuracy of the method is confirmed using COMSOL Multiphysics software and the image theorem. The solution for the magnetostatic problem is derived here, and, similarly, using analogous procedure, the wide variety of multilayer 3D electromagnetic problems can be solved. The advantage of this method is its simplicity. Since the discretization of the surface is applied, it is also very time efficient. As expected, the number of segments grows with the increase in dimensions of the bar. For the examples presented in the paper, it is not greater than $N_s = 7000$. Calculation done using Intel i7 processor and 32 GB of RAM took around 15 minutes of run time for a distribution curve. Parametric studies and design of the devices that incorporate PMs could be improved using the obtained expression of the force.

ACKNOWLEDGMENT

This work has been supported by the Ministry of Education, Science and Technological Development of the Republic of Serbia.

REFERENCES

[1] C. A. Brebbia, J. C. F. Telles, and L. C. Wrobel, *Boundary Element Techniques. Theory and Applications in Engineering*, Springer, Berlin, 1984.

[2] N. B. Raičević, "Conformal mapping and equivalent electrodes method application of electric field determination at cable accessories," *Discrete and Computational Mathematics*, Nova Publishers, New York, USA, chapter 14, pp. 205-214, 2008.

[3] N. B. Raičević and S. S. Ilić, "Equivalent electrode method application on anisotropic micro strip lines calculations," *Int. Conf. on Electromagnetics in Advanced Applications ICEAA 07*, Torino, Italy, paper 122 (CD), Sep. 2007.

[4] N. B. Raičević, "One method for multilayer dielectric system determination," *8th Int. Conf. on Applied Electromagnetics PES 2007*, Niš, Serbia, Sep. 2007.

[5] N. B. Raičević, S. R. Aleksić, and S. S. Ilić, "A hybrid boundary element method for multi-layer electrostatic and magnetostatic problems," *Journal of Electromagnetics*, no. 30, pp. 507-524, 2010.

[6] N. B. Raičević, S. S. Ilić, and S. R. Aleksić, "Application of new hybrid boundary element method on the cable terminations," *14th International IGTE Symposium*, Graz, Austria, pp. 56-61, Sep. 2010.

[7] D. Li and L. Di. Rizenzo, "Boundary element computation of line parameters of on-chip interconnects on lossy silicon substrate," *Applied Computational Electromagnetics Society (ACES) Journal*, vol. 26, no. 9, pp. 716-722, Sep. 2011.

[8] D. M. Veličković, "Equivalent electrodes method," *Scientific Review*, no. 21-22, pp. 207-248, 1996.

[9] A. N. Vučković, D. M. Vuckovic, M. T. Perić, and N. B. Raičević, "Influence of the magnetization vector misalignment on the magnetic force of permanent ring magnet and soft magnetic cylinder," *International Journal of Applied Electromagnetics and Mechanics*, vol. 65, no. 3, pp. 417-430, Mar. 2021.

[10] A. N. Vučković, N. B. Raičević, and M. T. Perić, "Radially magnetized ring permanent magnet modelling in the vicinity of soft magnetic cylinder," *Safety Engineering*, vol. 8, no. 1. pp. 33-37, Jun. 2018.

[11] S. Ilić, M. Perić, S. Aleksić, and N. Raičević, "Hybrid boundary element method and quasi-TEM analysis of 2D transmission lines – generalization," *Electromagnetics*, vol. 33, no. 4, pp. 292-310, Apr. 2013.

[12] M. T. Perić, S. S. Ilić, S. R. Aleksić, and N. B. Raičević, "Application of hybrid boundary element method to 2D microstrip lines analysis," *International Journal of Applied Electromagnetics and Mechanics*, vol. 42, no. 2, pp. 179-190, 2013.

[13] M. T. Perić, S. S. Ilić, A. N. Vučković, and N. B. Raičević, "Improving the efficiency of hybrid boundary element method for electrostatic problems solving," *Applied Computational Electromagnetics Society (ACES) Journal*, vol. 35, no. 8, pp. 872-877, Aug. 2020.

[14] S. S. Ilić, N. B. Raičević, and S. R. Aleksić, "Application of new hybrid boundary element method on grounding systems," *14th International IGTE Symposium*, Graz, Austria, pp. 160-165, Sep. 2010.

[15] S. Ilić, D. B. Jovanović, A. N. Vučković, and M T. Perić, "External inductance per unit length calculation of two wire line in vicinity of linear magnetic material," *14th Int. Conf. on Applied Electromagnetics PES 2019*, Niš, Serbia, Sep. 2019.

[16] H. Allag, J.P. Yonnet, H. Bouchekara, M. Latreche, and C. Rubeck, "Coulombian model for 3D analytical calculation of the torque exerted on cuboidal permanent magnets with arbitrary oriented polarizations," *Applied Computational Electromagnetics Society (ACES) Journal,* vol. 30, no. 4, pp. 351-356, Apr. 2015.

[17] J. Ren, L.Yang, and J. Ren, "Study on spatial magnetic field intensity distribution of rectangular permanent magnets based on Matlab," *Applied Computational Electromagnetics Society Conference,* vol. 46, no. 1, pp. 255-269, 2014.

[18] A. N. Vučković, N. B. Raičević, S. S. Ilić, and S. R. Aleksić, "Interaction magnetic force calculation of radial passive magnetic bearing using magnetization charges and discretization technique," *International Journal of Applied Electromagnetics and Mechanics*, vol. 43, no. 4, pp. 311-323, 2013.

[19] W. S. Robertson, B. S. Cazzolato, and A. C. Zander, "A simplified force equation for coaxial cylindrical magnets and thin coils," *IEEE Transactions on Magnetics*, vol. 47, pp. 2045-2049, Aug. 2011.

[20] R. Ravaud, G. Lemarquand, and V. Lemarquand, "Force and stiffness of passive magnetic bearings using permanent magnets. Part 1: Axial magnetization," *IEEE Transactions on Magnetics*, vol. 45, pp. 2996-3002, Jul. 2009.

[21] M. Lahdo, T. Strohla, and S. Kovalev, "Magnetic propulsion force calculation of a 2-DoF large stroke actuator for high-precision magnetic levitation system," *Applied Computational Electromagnetics Society (ACES) Journal,* vol. 32, no. 8, pp. 663-669, Aug. 2017.

[22] G. Akoun and J. P. Yonnet, "3D analytical calculation of the forces exerted between two cuboidal magnets," *IEEE Transactions on Magnetics,* vol. 20, pp. 1962-1964, Sep. 1984.

[23] Ana N. Vučković, Saša S. Ilić, and Slavoljub R. Aleksić, "Interaction magnetic force calculation of ring permanent magnets using Ampere's microscopic surface currents and discretization technique," *Electromagnetics*, vol. 32, no. 2, pp. 117-134, Jan. 2012.

[24] M. Braneshi, O. Zavalani, and A. Pijetri, "The use of calculating function for the evaluation of axial force between two coaxial disk coils," *Third International PhD Seminar on Computational Electromagnetics and Technical Application*, Banja Luka, Bosnia and Hertzegovina, pp. 21–30, Aug. 2006.

[25] A. N. Vučković, S. R. Aleksić, and S. S. Ilić, "Calculation of the attraction and levitation forces using magnetization charges," *10th Int. Conf. on Applied Electromagnetics PES 2011*, *CD Proceedings,* Niš, Serbia, pp. 33-55, Sep. 2011.

[26] J. L. G. Janssen, J. J. H. Paulides, and E. A. Lomonova, "3-D analytical calculation of the torque between perpendicular magnetized magnets in magnetic suspension," *IEEE Trans. on Magnetics*, vol. 47, no. 10, pp. 4286-4289, Oct. 2011.

[27] H. Allag and J. P. Yonnet, "3-D Analytical calculation of the torque and force exerted between two cuboidal magnets," *IEEE Trans. on Magnetics*, vol. 45, no. 10, pp. 3969-3972, Oct. 2009.

[28] M. Aissaoui, H. Allag, and J. P. Yonnet, "Mutual inductance and interaction calculation between conductor or coil of rectangular cross section and-parallelepiped permanent magnet," *IEEE Trans. on Magnetics*, vol. 50, no. 11, Nov. 2014.

[29] M. Beleggia, D. Vokoun, and M. D. Graef, "Forces between a permanent magnet and a soft magnetic plate," *IEEE Magnetics Letters*, vol. 3, 2012.

[30] E. P. Furlani, *Permanent Magnet and Electromechanical Devices: Materials, Analysis and Applications*, Academic Press, London, 6th edition, 2001.

Comparative Study on Improved and Traditional Equivalent Circuit of Long Primary Double-Sided Linear Induction Motor

Qian Zhang, Hui-juan Liu, Zhen-yang Zhang, Teng-fei Song, and Yu Wang

School of Electrical Engineering, Beijing Jiaotong University, Beijing 100044, China
qianzh@bjtu.edu.cn, hjliu@bjtu.edu.cn, 16117375@bjtu.edu.cn, 18117020@bjtu.edu.cn, 20121498@bjtu.edu.cn

Abstract **–** Based on the quasi-two-dimensional (2D) field model of long primary double-sided linear induction motor (LPDLIM), an improved equivalent circuit model is proposed. First, the traditional equivalent circuit of LPDLIM is reviewed. Second, the skin effect correction coefficients for the secondary equivalent resistance and excitation reactance, and the secondary leakage inductance are derived. Moreover, an improved equivalent circuit model for LPDLIMs is presented, in which the leakage reactance of the secondary is considered, and the excitation reactance and secondary resistance are modified by the correction coefficients independently. Then, the slip frequency characteristics of various effect forces and variations of forces under different operations and mechanical air gap width are presented. Finally, the calculated forces by the proposed equivalent circuit are validated by the finite element method results and also compared with that of the traditional equivalent circuit model.

Index Terms **–** Double-sided linear induction motor, end effect, equivalent circuit, long primary, skin effect.

I. INTRODUCTION

Because the linear induction motor (LIM) has a wide range of speed and acceleration, it avoids the intermediate transmission mechanism of linear motion, reduces the mechanical loss and stress, and its system has high reliability [1]. The LIMs have been widely used in aircraft electromagnetic launch or accelerator system [2], transportation system [3, 4], loading and unloading system [5], etc.

The LIM has a different structure from the rotating induction motor (RIM), and the unique structure produces special effects, such as the longitudinal end effect, transverse edge effect, and so on, which will affect the thrust characteristics of the motor. The most commonly used methods to solve the thrust characteristics of LIM are finite element method (FEM) [6], numerical calculation method [7], equivalent circuit (or equivalent magnetic circuit) method [8, 9], and so on.

The FEM software is not only convenient for the optimization design of LIMs [10] but also provides convenience for the performance calculation of motor with special structure or with abnormal secondary position [11, 12]. However, due to the longitudinal end effect, it cannot build a partial pole pair FEM model of LIM like a RIM; a full model means that more computer resources and longer computing time are needed [13].

Among the analytical methods for solving the performance of linear motor, one-dimensional (1D) field analytical method is the most used [14], while two-dimensional (2D) and three-dimensional (3D) fields are more accurate to solve the performance [15–17].

The analytical solution is helpful to understand the field distribution clearly, but it cannot directly reflect the impedance of the motor as the equivalent circuit. The end and edge effects, which play a significant role in the performance of a LIM, are reflected in the equivalent circuit by modifying factors on the impedance [9]. In addition to Duncan's equivalent circuit [18], T-type equivalent circuit based on field theory is another common model. The equivalent circuit of SLIM has been deeply studied because of its application as traction motor [9]. However, because the secondary of double-sided LIM (DLIM) is usually only a conductive plate, while that of SLIM has back iron, their equivalent circuits are different.

The research of the equivalent circuit of DLIM is far less extensive than that of SLIM for its limited application. In the conventional equivalent circuit of the long primary double-sided LIM (LPDLIM), the longitudinal end effect and transverse edge effect of motor are demonstrated by correction factors of secondary resistance and excitation reactance, and the secondary leakage reactance is neglected [14, 19]. In the high-speed applications, an equivalent circuit with only longitudinal end effect may be enough to analyze the performance of the LPDLIM [14, 20].

In addition to the end/edge effect, the secondary leakage reactance and the skin effect of the secondary

Submitted On: July 13, 2021
Accepted On: October 18, 2021
https://doi.org/10.13052/2021.ACES.J.361115

will have an important impact on the performance of the low-speed LPDLIM with the large air gap. Although the impedance parameters with skin effect of the equivalent circuit can be obtained by 2D and 3D field analyses, their expressions are very complex [21]. In the above equivalent circuit model for LPDLIM, few papers take the skin effect into the equivalent circuit.

In this paper, quasi-2D model is built to analyze the inhomogeneous distribution of air gap flux density in vertical direction, that is, the skin effect and secondary leakage reactance are considered in the equivalent circuit to make it more perfect. In Section II, the correction factors of longitudinal end and transverse edge effects on the equivalent circuit impedance are given. And then the conventional equivalent circuit in the coupling region of the LPDLIM is presented. In Section III, the skin effect factors of modified secondary equivalent resistance and excitation reactance, and secondary leakage reactance are derived. And the improved equivalent circuit model for LPDLIMs is proposed. In Section IV, the slip frequency characteristics of various effect forces are presented. The results of 3D FEM are used to verify the proposed equivalent circuit model, and also compared with that of the traditional equivalent circuit model. Finally, the conclusions are summarized in Section V.

II. TRADITIONAL T-TYPE EQUIVALENT CIRCUIT

The 3D LPDLIM was developed and is presented in Figure 1. The model is usually decomposed into two independent analytical models, namely, the longitudinal (x-axis) analysis model (Figure 1 (b)) considering the longitudinal end effect, and the transversal (z-axis) analysis model (Figure 1 (c)) considering the transverse edge effect. In the 1D field analysis theory for LPDLIMs, the longitudinal end effect and transverse edge effect can be considered to act independently or be neglected.

A. Longitudinal end effect

The longitudinal 1D analysis model is shown in Figure 1 (b). In order to simplify the analysis model considering longitudinal end effects, the assumptions are presented as [14].

Taking the secondary as the motion reference coordinate [22], according to the fact that the equal complex power between the magnetic field and the electrical circuit, the secondary resistance and excitation reactance per phase with end effect neglected can be calculated by the following equation [14]:

$$\left.\begin{aligned} r_2 &= \frac{4m_1(W_1k_{w1})^2a}{p\tau\sigma_s} \\ x_m &= G\cdot r_2 \end{aligned}\right\}, \tag{1}$$

where m_1 is the number of primary phases, W_1 is the number of turns of the primary per phase winding in series, k_{w1} is the primary winding coefficient, a is the

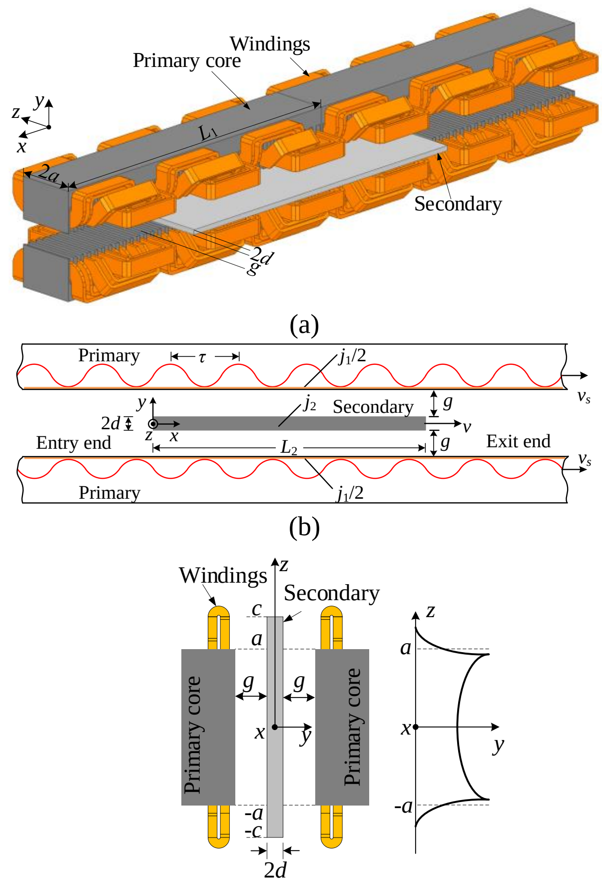

Fig. 1. (a) 3D model of LPDLIM. (b) Longitudinal analysis model. (c) Transversal analysis model.

half width of primary core, p is the number of the pole pairs, τ is the pole pitch, σ_s is the surface conductivity of the secondary, and G is the quality factor.

The longitudinal end effect factors are denoted as eqn (2) [14], where K_r and K_x are the correction factors for the secondary resistance and the magnetizing reactance, respectively

$$\left.\begin{aligned} K_r &= \frac{sG}{L_2\sqrt{1+s^2G^2}}\frac{k_1^2+k_2^2}{k_1} \\ K_x &= \frac{1}{L_2\sqrt{1+s^2G^2}}\frac{k_1^2+k_2^2}{k_2} \end{aligned}\right\}, \tag{2}$$

where k_1 and k_2 are the functions of slip s and quality factor G and L_2 is the secondary length, which is the same as the segmented primary length $L_1 = 2p\tau$ in this paper.

B. Transversal edge effect

The transversal analysis model is shown in Figure 1 (c). The longitudinal end effect is neglected in solving the transverse edge effect, and some assumptions are made in deriving the field equations [19].

Table 1: Specifications of the LPDLIM

Quantity	Symbol	Value
Number of phases	m_1	3
Number of poles	$2p$	6
Number of slots per phase per pole	q_1	2
Pole pitch	τ	66 mm
Segmented primary length	L_1	396 mm
Primary width	$2a$	70 mm
Mechanical air gap length	g	27 mm
Secondary thickness	$2d$	3 mm
Secondary width	$2c$	140 mm
Secondary length	L_2	396 mm

The correction factors of the transverse edge effect C_r and C_x are given by [19, 21]

$$\left.\begin{array}{l} C_r = sG\cdot\left(\mathrm{Re}^2[T]+Im^2[T]\right)/\mathrm{Re}[T] \\ C_x = \mathrm{Re}^2[T]+Im^2[T]/Im[T] \end{array}\right\}. \tag{3}$$

These correction factors of transverse edge effect are also used to modify the secondary resistance and excitation reactance, respectively, where T is the function of the slip, quality factor, and motor structure parameters [19].

$$T = \mathrm{j}\left(r^2+\left(1-r^2\right)\lambda\tanh(\alpha a)/\alpha a\right), \tag{4}$$

where r, λ, and α are given as eqn (5) [19], and $k = \pi/\tau$,

$$\left.\begin{array}{l} r^2 = (1+\mathrm{j}sG)^{-1} \\ \lambda = \left(\tanh(\alpha a)\tanh(kc-ka)/r+1\right)^{-1} \\ \alpha = k\sqrt{1+\mathrm{j}sG} \end{array}\right\}. \tag{5}$$

The transverse edge effect may be accounted for by introducing a larger equivalent primary stack width $2a_e$ instead of actual width $2a$, and $a_e = a + k_g \cdot (d+g)$, and range of the coefficient k_g is 0.6−1 [23]. The new correction factors C_{er} and C_{ex} of transverse edge effect can be obtained by replacing the actual core width with the new equivalent stack width in eqn (3)−(5).

C. Traditional equivalent circuit

The specifications of the LPDLIM are listed in Table 1, and frequency of operation is 60 Hz.

The longitudinal end effect and transverse edge effect factors are calculated in Figure 2. The factor of secondary resistance corrected by the longitudinal end effect increases with slip frequency, while the factor of modified excitation reactance decreases with slip frequency, that is, the longitudinal end effect increases the secondary resistance and reduces the excitation reactance. The distribution of transverse edge effect factors is similar to that of longitudinal end effect but have smoother trend. In the new correction factors of transverse edge effect calculated by equivalent primary width $2a_e$, the factor of modified secondary resistance C_{er} is reduced, while the correction factor of excitation reactance C_{ex} is basically unchanged, compared with the traditional ones.

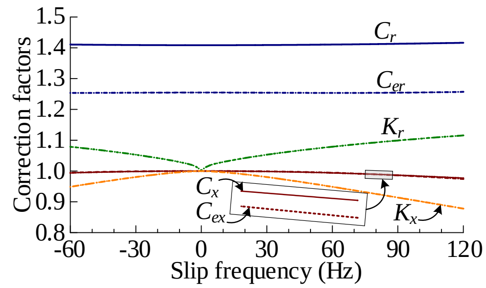

Fig. 2. Correction factors for longitudinal end effect and transverse edge effect.

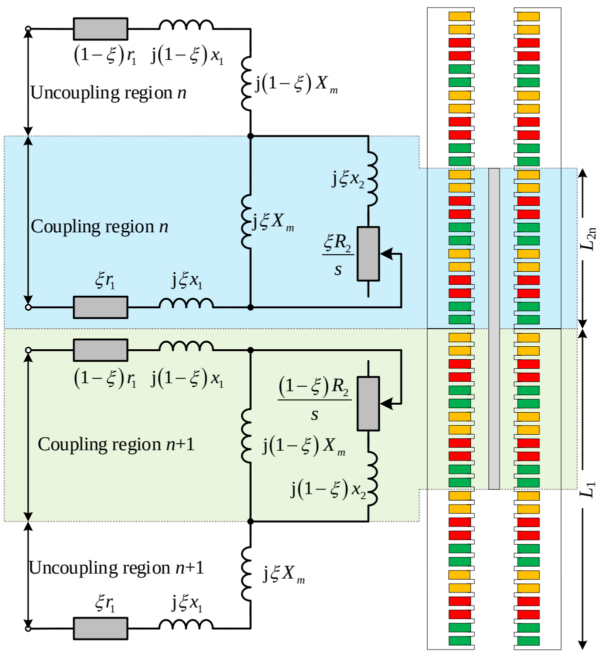

Fig. 3. Equivalent circuit of LPDLIM with primary windings in series.

The T-model equivalent circuit is shown in Figure 3 since the LPDLIM is usually segmented supplied. The coupling coefficient between the secondary and the nth primary is defined as

$$\xi = L_{2n}/L_1, \tag{6}$$

where L_{2n} is the coupling length between the secondary and the nth primary. Because the length of the secondary is equal to that of the primary, the coupling coefficient between the secondary and the $(n+1)$th primary is $1-\xi$.

Here, r_1 and x_1 are the phase resistance and leakage reactance of one segment primary, X_m is the excitation reactance of primary and secondary fully coupled ($\xi = 1$), and R_2 and x_2 are the equivalent phase resistance and leakage reactance of secondary. The excitation reactance

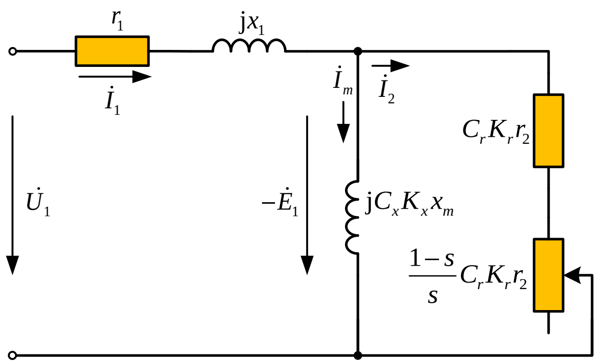

Fig. 4. Traditional equivalent circuit with longitudinal end effect and transverse edge effect (EC-LT).

and secondary resistance in Figure 3 can be end/edge effect considered or not.

When the windings of the LPDLIM with segmented supplied are in series, the equivalent circuit of the coupling region introducing the longitudinal end effect and the transverse edge effect correction factors can be simplified as shown in Figure 4 due to the same currents of the two stator windings. The excitation reactance and secondary resistance without end (edge) effect of the coupling region are x_m and r_2, respectively. In the traditional equivalent circuit, the secondary leakage reactance is usually ignored, i.e., $x_2 \approx 0$.

When factors C_{er} and C_{ex} are used to replace the traditional transverse edge effect correction factors C_r and C_x in Figure 4, a new equivalent circuit (EC-LTe) can be used to calculate the characteristics of a LPDLIM.

III. IMPROVED EQUIVALENT CIRCUIT MODEL

In the traditional equivalent circuit of LPDLIMs, longitudinal end effect and transverse edge effect, or one of them, are usually considered.

As it knows, the field distribution of linear motor is 3D. In order to consider the influence of field distribution in each direction on the impedance parameters of equivalent circuit, the 3D motor model is divided into three independent direction models, namely longitudinal, transversal, and vertical analysis models. Each model is analyzed separately to obtain the corresponding correction coefficient of impedance. A full equivalent circuit model considering the longitudinal, transverse, and vertical field distribution is obtained.

A. Correction factors for skin effect and secondary leakage reactance

As in Section II, for example, when solving the longitudinal end effect, it is considered that the transverse edge effect does not exist, that is, the transverse width (y-direction) is infinite, and the air gap magnetic field is

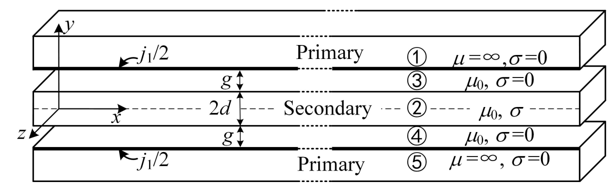

Fig. 5. Vertical analysis model of skin effect.

evenly distributed in the vertical direction (z-axis). In this section, the longitudinal and transverse end effects are negligible; only the influence of inhomogeneous distribution of the air gap magnetic field in the vertical direction (y-axis), i.e., the skin effect on the thrust characteristics of the motor, is further considered. The correction factors of the excitation reactance and secondary resistance caused by the inhomogeneous distribution of the air gap flux vertically are solved based on the quasi-2D electromagnetic field.

The quasi-2D representation of the LPDLIM is shown in Figure 5. To simplify the analytical model, the following assumptions are made [7, 9, 15].

1. The primary core is not saturated, and the resistivity of the primary core is infinite.
2. The primary and secondary are infinitely long in the motion direction and wide enough transversally.
3. Both primary and secondary currents have only z-component, and the primary currents flow in infinitesimally thin sheets.

Based on the theory of the LPDLIM and the Maxwell's equations, the vector magnetic potential equation of the electromagnetic field of the motor is [21]

$$\nabla^2 \boldsymbol{A} = \mu_0 \sigma \left[\frac{\partial \boldsymbol{A}}{\partial t} - v \left(\nabla \times \boldsymbol{A} \right) \right], \tag{7}$$

where $\boldsymbol{A}$ is the vector magnetic potential, μ_0 is the air magnetic permeability, σ is the conductivity of the secondary, and v is the relative velocity of primary and secondary. According to the above assumptions, $\boldsymbol{A}$ has only the z-direction component and can be defined as

$$\boldsymbol{A}_z = A_i(y) \cdot e^{j(\omega t - kx)}. \tag{8}$$

In regions 2 (secondary) to 4 (air gap), the following equation is obtained:

$$\left. \begin{array}{l} \frac{\partial^2 A_2(y)}{\partial y^2} - \left(k^2 + j\mu_0 \sigma s \omega \right) A_2(y) = 0 \\ \frac{\partial^2 A_3(y)}{\partial y^2} - k^2 A_3(y) = 0 \\ \frac{\partial^2 A_4(y)}{\partial y^2} - k^2 A_4(y) = 0 \end{array} \right\} . \tag{9}$$

Undetermined magnetic potential A_i (i = 2, 3, 4) are solved by the satisfactions of the boundary conditions among primary, air gap, and secondary.

The electric field intensity in the air gap and the secondary is denoted by

$$\boldsymbol{E}_{zi} = -\frac{\partial \boldsymbol{A}_{zi}}{\partial t} \quad i = 2, 3, 4 . \tag{10}$$

The electromagnetic complex power transferred from the primary to the air gap and secondary can be calculated as follows [21]:

$$\boldsymbol{S}_{23} = 2 \times \int_{-a}^{a} \int_{0}^{L_2} \frac{1}{2} \left(-\frac{\boldsymbol{j}^*{}_1}{2} \right) \left(\boldsymbol{E}_{z3}|_{y=g_e} \right) dxdz, \quad (11)$$

where $\boldsymbol{j}_1$ is the primary surface current density, g_e is the electromagnetic air gap width, and $g_e = d + g$, d is the half thickness of secondary, and g is the mechanical air gap width.

There is no active power and reactive power in the secondary when slip is 0, and the complex power calculated by eqn (11) only has the reactive power on the exciting reactance, i.e., $\boldsymbol{S}_{23} = \mathrm{j}Q_{30}$. Therefore, the excitation reactance with inhomogeneous air gap magnetic field in the vertical direction considered can be obtained by the following expression:

$$x_{ms} = \frac{Q_{30}}{m_1 I_1^2} = x_m \cdot K_m, \quad (12)$$

where K_m is the correction factor of the skin effect on excitation reactance with end effect neglected

$$K_m = \frac{k\delta \cosh(kg_e)}{2 \cdot \sinh(kg_e)}. \quad (13)$$

When the slip is not 0, in the T-type equivalent circuit, the following relationship is satisfied [21]:

$$\left.\begin{array}{l} -\dot{E}_1 = \frac{S_{23}}{m_1 I_1} \\ Q_3 = \frac{m_1 \left|-\dot{E}_1\right|^2}{x_{ms}} \\ \boldsymbol{S}_2 = \boldsymbol{S}_{23} - \mathrm{j}Q_3 = P_2 + \mathrm{j}Q_2 \\ \dot{I}_2^* = \frac{S_2}{m_1(-\dot{E}_1)} \end{array}\right\}, \quad (14)$$

where P_2 and Q_2 are the active power and reactive power in the secondary, respectively, and $\dot{I}_2^*$ is the conjugate current of the secondary branch reduced to the primary.

The secondary resistance and leakage reactance considering inhomogeneous air gap magnetic field in the vertical direction can be calculated by

$$R_2 = \frac{P_2}{m_1 \left|\dot{I}_2^*\right|^2} = \frac{r_2}{s} \cdot K_f, \quad (15)$$

$$x_2 = \frac{Q_2}{m_1 \left|\dot{I}_2^*\right|^2} = \frac{x_m k\delta}{2} \frac{D_1 M + D_2 N}{M^2 + N^2}, \quad (16)$$

where K_f is the correction factor of the secondary resistance without end effect. The secondary leakage reactance x_2 can be expressed by the excitation reactance without end effect

$$K_f = \frac{sG \cdot \frac{1}{2} k\delta (C_2 D_1 - C_1 D_2)}{M^2 + N^2}, \quad (17)$$

$$\left.\begin{array}{l} M = C_1 - D_1 \tanh(kg_e) \\ N = C_2 - D_2 \tanh(kg_e) \end{array}\right\}, \quad (18)$$

where the constants C_1, C_2, D_1, and D_2 are the functions of slip frequency, and motor parameters, such as secondary thickness $2d$, mechanical air gap width g, pole pitch τ, etc.

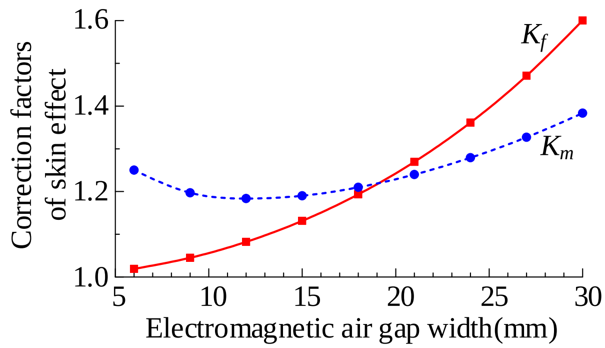

Fig. 6. Correction factors for skin effect.

The calculation results show that these two correction factors (K_m and K_f) are determined by the parameters of the LPDLIM, e.g., the electromagnetic air gap width, and independent of slip frequency. With the secondary thickness of 3 mm, these two factors versus the width of the electromagnetic air gap g_e are shown in Figure 6. They both increase the secondary resistance and excitation reactance although their trends are different.

B. Improved equivalent circuit

Based on the traditional equivalent circuit in Figure 4, the derived correction factors K_m and K_f are used to modify the excitation reactance and secondary resistance, respectively, and the secondary leakage reactance is connected in series with the modified secondary resistance in the secondary branch circuit; an improved equivalent circuit (EC-LTS) for LPDLIM as shown in Figure 7 is obtained. Similarly, if the traditional transverse edge effect factors C_r and C_x in Figure 7 are replaced with the C_{er} and C_{ex}, respectively, another T-type equivalent circuit (EC-LTeS) can be obtained to solve the performance of the LPDLIM.

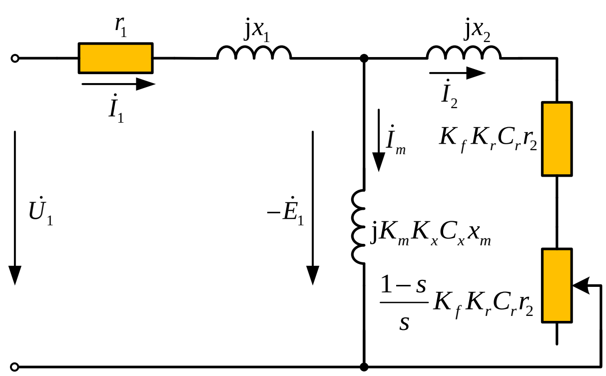

Fig. 7. Improved equivalent circuit with longitudinal end effect, transverse edge effect, inhomogeneous air gap magnetic field in vertical direction, and secondary leakage reactance (EC-LTS).

In the improved equivalent circuit, the end effect in the longitudinal direction, the edge effect in the transverse direction, and the inhomogeneous air gap magnetic field in the vertical direction are considered. The mechanical power of LPDLIM with all effects considered is expressed as follows [24]:

$$P_M = (1-s)\cdot \mathrm{Re}\left[m_1 \dot{I}_1^2 Z_{\mathrm{LTS}}\right], \tag{19}$$

$$Z_{\mathrm{LTS}} = \frac{\left(K_f K_r C_r \frac{r_2'}{s} + \mathrm{j}x_2\right)\cdot K_m K_x C_x \cdot \mathrm{j}x_m}{K_f K_r C_r \frac{r_2'}{s} + \mathrm{j}x_2 + K_m K_x C_x \cdot \mathrm{j}x_m}. \tag{20}$$

IV. COMPARATIVE STUDY ON IMPROVED AND TRADITIONAL EQUIVALENT CIRCUIT

A. Circuit parameters

The excitation reactance and secondary resistance without any end effect, as shown in eqn (1), are only functions of the parameters of the motor, while they are also functions of the slip frequency after considering the longitudinal end effect, transverse edge effect, and vertical magnetic field distribution

$$\left.\begin{array}{l} R_{2\mathrm{LT}} = K_r C_r \cdot r_2 \\ X_{m\mathrm{LT}} = K_x C_x \cdot x_m \end{array}\right\}, \tag{21}$$

$$\left.\begin{array}{l} R_{2\mathrm{LTS}} = K_r C_r K_f \cdot r_2 \\ X_{m\mathrm{LTS}} = K_x C_x K_m \cdot x_m \end{array}\right\}, \tag{22}$$

where the one with "LT" in the subscript is the equivalent impedance including longitudinal end and transverse edge effects, and the impedance with "LTS" in the subscript also takes into account the inhomogeneous magnetic field vertically.

Figure 8 (a) shows the calculation curves for the rectified excitation inductance and secondary resistance versus the slip frequency. The longitudinal end and transverse edge effects reduce the excitation inductance and increase the secondary resistance in the equivalent circuit, and the skin effect increases both the excitation inductance and secondary resistance.

The parameter with "LTe" and "LTeS" in the subscript represents the equivalent resistance or excitation inductance calculated by using the equivalent primary width $2a_e$. The new transverse edge effect factors mainly reduce the secondary resistance, while the excitation inductance remains unchanged, which is compared with the corresponding impedance calculated by the actual primary width $2a$.

The secondary leakage inductance with respect to the secondary thickness $2d$ and air gap width $2g$ is given in Figure 8 (b). The secondary leakage inductance increases with the increase of mechanical air gap and secondary thickness. For the DLIM with large mechanical air gap, the secondary leakage reactance may not be ignored in the equivalent circuit.

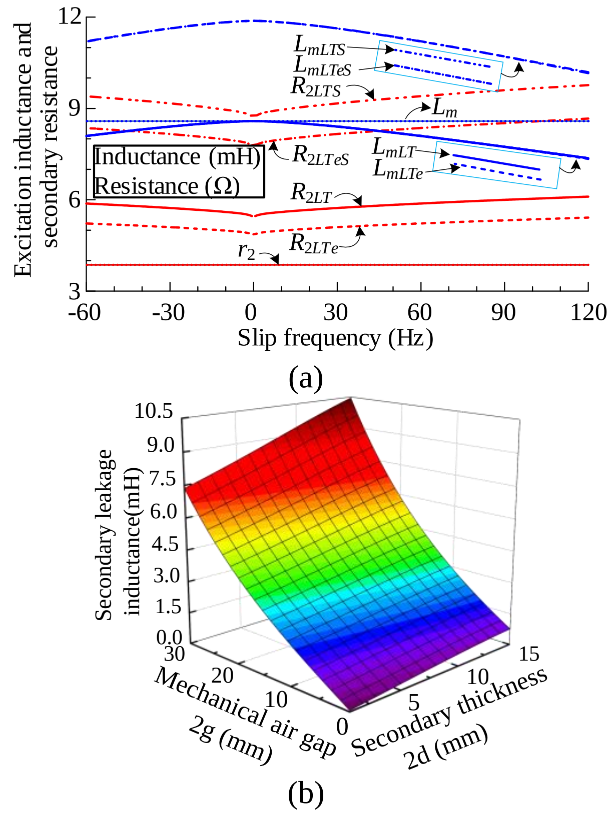

Fig. 8. (a) Modified excitation inductance and secondary resistance under different slip frequencies. (b) Secondary leakage inductance with different secondary thickness $2d$ and air gap width $2g$.

B. End effect and skin effect force

It has been proved that the longitudinal end effect can produce a certain braking force or thrust in the motoring region by the thrust analytical calculation [22]. If the correction factors of the longitudinal end effect and the transverse edge effect in Figure 4 are 1, the normal traveling wave thrust without any end effects can be calculated. When the transverse edge effect factors are 1, the thrust with longitudinal end effect can be calculated. The longitudinal end effect force varies with slip frequency in the whole operation region, as shown in Figure 9 (a), in which the secondary thickness is 3 mm and the mechanical air gap width changes from 9 to 27 mm.

In the motoring region (0−60 Hz), the longitudinal end effect force is the braking force, and the force reaches the peak and then decreases with an increase of the slip frequency; in the generating region (−60 to 0 Hz), the longitudinal end effect force becomes a kind of thrust; when it enters the negative braking region (60−120 Hz), the force is mainly a braking force, and the descending slope is smoother. When the slip frequency is 0 Hz, there is no end longitudinal effect, and the longitudinal end effect force is 0 N.

The transverse edge effect force can be calculated by a similar method. The transverse edge effect force and longitudinal end effect force have similar distribution characteristics. It is shown as braking force in motoring region and thrust force in generating region. The force reaches the peak rapidly and then decreases with an increase of the slip frequency, in the region of high slip frequency, the force changes gently. The new transverse edge effect factors reduce the transverse edge effect force in most slip frequency range, compared with the traditional ones.

The force produced by the inhomogeneous distribution of the vertical air gap magnetic field, i.e., the skin effect force, is basically opposite to the longitudinal end effect force in the whole slip frequency range. That is, in the generating region, the skin effect force is the braking force, and in the motoring region, it is the thrust force. At high slip frequency, for the motor with large air gap, it is the braking force that increases approximately linearly with the slip frequency. The new transverse end effect coefficient has little effect on the skin effect force basically.

The maximum values of longitudinal end effect force, transverse end effect force, and skin effect force decrease with the increase of air gap, which is due to the decrease of magnetic flux density at the secondary surface with the increase of air gap width.

The frequency characteristics of total force (i.e., the sum of longitudinal end effect force, transverse end effect force, and skin effect force) generated by various effects are shown in Figure 9 (d). For the LPDLIM with small air gap, e.g., the air gap width is 9 mm, the resultant force at low slip frequency is the braking force in the motoring region and is the thrust force in the generating region. When the slip frequency is higher than 40 Hz, the resultant force increases the output thrust of the motor based on the normal traveling wave thrust. For the large air gap LPDLIM, the resultant force gradually increases to the maximum and then decreases with the increase of slip frequency under both the motoring and generating conditions. With the increase of the air gap width, the slope of resultant force curve decreases in the low slip frequency range. The new transverse edge effect coefficients reduce the resultant force in the motoring and generating regions.

Although the maximum resultant forces of various effects are similar in different air gaps, it should be noted that the normal traveling wave thrust without various effects increases sharply with the decrease of air gap. Therefore, for the large air gap LPDLIM, the resultant forces of various effects play a very important role in the total electromagnetic thrust.

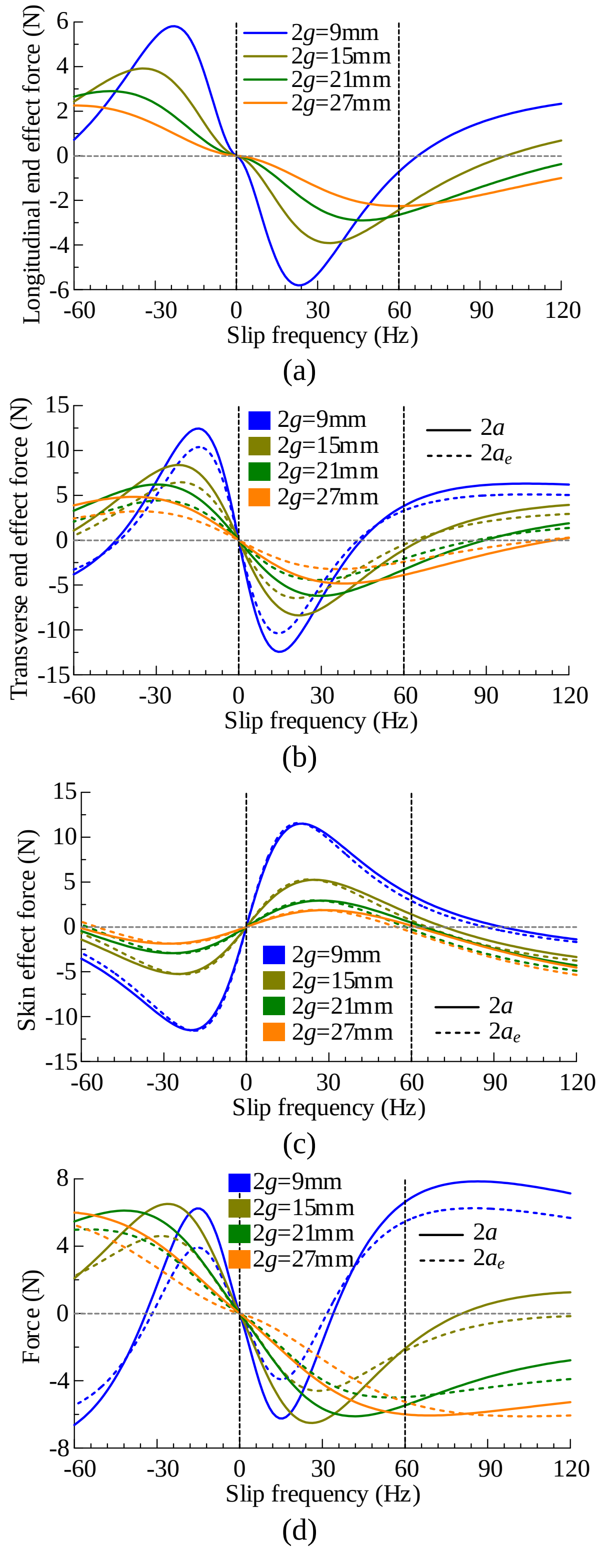

Fig. 9. Forces versus slip frequency with different mechanical air gap width $2g$. (a) Longitudinal end effect force. (b) Transverse edge effect force. (c) Skin effect force. (d) Resultant of force produced by various effects.

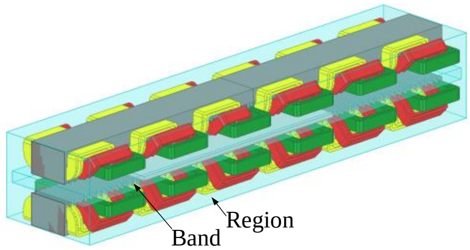

Fig. 10. 3D FEM of the LPDLIM.

C. Thrust characteristics

The electromagnetic thrust calculated by FEM 3D model (Figure 10) is used to verify the improved equivalent circuit model, and the simulation results are also used to compare with that of the traditional equivalent circuit with longitudinal end effect and transverse edge effect.

The 3D FEM model of the LPDLIM is performed using ANSYS 18.0, and the motor parameters used in the simulation model are listed in Table 1. The frequency of the power supply is 60 Hz, the current is 6.85 A, and the mechanical air gap widths are 9, 15, and 27 mm, respectively.

The thrust characteristic curves calculated by various equivalent circuit models are shown in Figure 11, and the 3D FEM simulation results are also shown in the figure. In the operation region of both motoring and generating regions, the force calculated by improved equivalent circuits are in good agreement with the 3D simulation results, while the calculation results of traditional equivalent circuit are obviously different from the simulation ones. Although there are slight differences between the characteristic curves calculated by the equivalent circuit model EC-LTeS (with new transverse edge effect coefficients C_{er} and C_{ex}) and EC-LTS (with transverse edge effect coefficients of C_r and C_x), the results of 3D simulation are closer to those of the equivalent circuit model EC-LTeS.

In the negative braking region, there is little difference between the results of the two equivalent circuits. The results of 3-D calculation seem to be closer to those of the equivalent circuit model EC-LT.

The thrust calculation errors are presented in Figure 12. In the negative braking region, the calculation errors of the equivalent circuit model EC-LTS are smaller than that of EC-LTeS, but they are almost the same as the traditional equivalent circuit models.

In the motoring and generating operation regions, the traditional equivalent circuit models (EC-LT and EC-LTe) have large errors, even more than 15%. Although the new transverse end effect coefficient circuit model EC-LTe can reduce the error to a certain extent, the calculation errors are still more than 10%. When the mechanical air gap of the LPDLIM is small, e.g., $2g = 9$ mm, the calculation error of the equivalent circuit model EC-LTS and EC-LTeS are almost the same, but for the large air gap motor, the errors of the EC-LTeS model are significantly reduced. This is because the electromagnetic air gap becomes larger, and the air gap magnetic field extends further in the lateral direction.

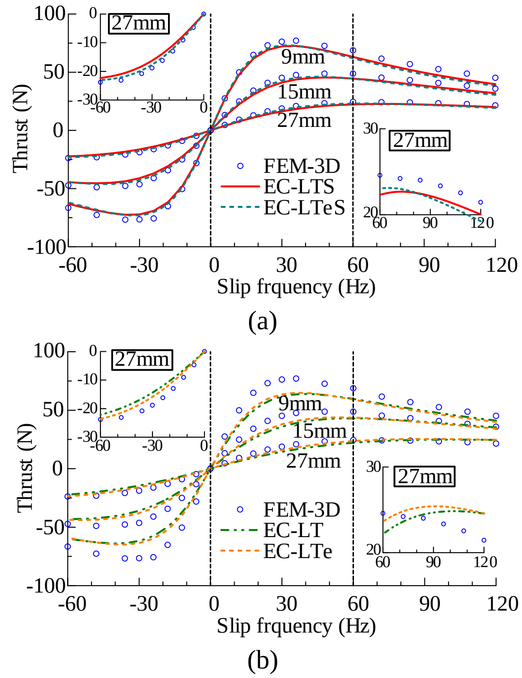

Fig. 11. Thrust characteristics of different mechanical air gap widths $2g$ solved by equivalent circuit model of (a) EC-LTS and EC-LTeS and (b) EC-LT and EC-LTe.

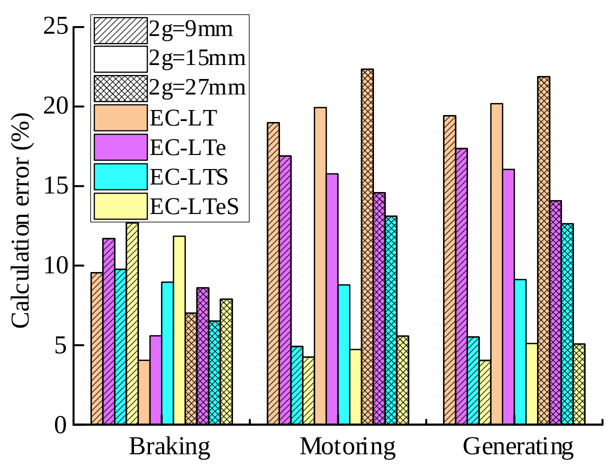

Fig. 12. Calculation error with various equivalent circuit models and operating regions.

V. CONCLUSION

The quasi-2D field model of the motor is established, and the secondary leakage reactance is solved, an improved equivalent circuit model for LPDLIM with the inhomogeneous distribution of air gap flux density vertically considered based on conventional equivalent circuits is proposed. By comparing the calculation results of the FEM 3D with those of the traditional and the improved equivalent circuits, conclusions include the following.

1. When skin effect is considered to the equivalent circuit of LPDLIM, the secondary resistance and excitation reactance can be corrected by two skin effect factors, respectively, and the factors are independent of the slip frequency.
2. The results show that the skin effect forces increase with the decrease of mechanical air gap. They are mainly thrust in the motoring region and braking force in the power generating region. While the slip characteristics of skin effect force and end/edge effect force are basically opposite, the resultant force of various effects of large air gap motor are mainly opposite to the thrust force of normal traveling wave.
3. The thrust characteristic curves calculated showed the improved equivalent circuit has better consistency with the simulation results and has smaller calculation error, in both the motoring and generating regions, compared with that of the traditional equivalent circuit. While in the negative braking region, the thrust calculated by the two equivalent circuits have almost the same errors.

ACKNOWLEDGMENT

This work was supported by the Fundamental Research Funds for the Central Universities under Grant 2021YJS159.

REFERENCES

[1] I. Boldea and S. A. Nasar, *Linear Electric Actuators and Generators.* Cambridge University Press, New York, USA, pp. 33-43, Sep. 2009.

[2] L. Bertola, T. Cox, P. Wheeler, S. Garvey, and H. Morvan, "Thermal design of linear induction and synchronous motors for electromagnetic launch of civil aircraft," *IEEE Trans. Plasma Sci.*, vol. 45, no. 7, pp. 1146-1153, Jul. 2017.

[3] G. Lv, T. Zhou, D. Zeng, and Z. Liu, "Influence of secondary constructions on transverse forces of linear induction motors in curve rails for urban rail transit," *IEEE Trans. Ind. Electron.*, vol. 66, no. 6, pp. 4231-4239, Jun. 2019

[4] S. E. Abdollahi, M. Mirzayee, and M. Mirsalim, "Design and analysis of a double-sided linear induction motor for transportation," *IEEE Trans. Magn.*, vol. 51, no. 7, pp. 1-7, Jul. 2015.

[5] M. Mihalachi, R. Leidhold, and P. Mutschler, "Long primary linear drive for material handling," *in 2009 International Conference on Electrical Machines and Systems*, Tokyo, Japan, pp. 1-6, Nov. 2009.

[6] R. A. H. de Oliveira, D. Berger, L. Schultz, R. M. Stephan, and A. C. Ferreira, "Finite element analysis of the forces developed on linear induction motors," *in 2015 IEEE 13th Brazilian Power Electronics Conference and 1st Southern Power Electronics Conference (COBEP/SPEC)*, Fortaleza, pp. 1-6, Nov. 2015.

[7] G. Lv, D. Zeng, and T. Zhou, "A novel MMF distribution model for 3-D analysis of linear induction motor with asymmetric cap-secondary for metro," *IEEE Trans. Magn.*, vol. 53, no. 9, pp. 1-7, Sep. 2017.

[8] P. Naderi and A. Shiri, "Modeling of ladder-secondary-linear induction machine using magnetic equivalent circuit," *IEEE Trans. Veh. Technol.*, vol. 67, no. 12, pp. 11411-11419, Dec. 2018.

[9] D. Zeng, G. Lv, and T. Zhou, "Equivalent circuits for single-sided linear induction motors with asymmetric cap secondary for linear transit," *IEEE Trans. Energy Convers.*, vol. 33, no. 4, pp. 1729-1738, Dec. 2018.

[10] A. H. Isfahani, B. M. Ebrahimi, and H. Lesani, "Design optimization of a low-speed single-sided linear induction motor for improved efficiency and power factor," *IEEE Trans. Magn.*, vol. 44, no. 2, pp. 266-272, Feb. 2008.

[11] B.-J. Lee, D.-H. Koo, and Y.-H. Cho, "Investigation of linear induction motor according to secondary conductor structure," *IEEE Trans. Magn.*, vol. 45, no. 6, pp. 2839-2842, Jun. 2009.

[12] H. Bolton, "Forces in induction motors with laterally asymmetric sheet secondaries," *Proc. Inst. Electr. Eng. UK*, vol. 117, no. 12, pp. 2241-2248, Dec. 1970.

[13] G. Lv, T. Zhou, D. Zeng, and Z. Liu, "Design of ladder-slit secondaries and performance improvement of linear induction motors for urban rail transit," *IEEE Trans. Ind. Electron.*, vol. 65, no. 2, pp. 1187-1195, Feb. 2018.

[14] J. Lu and W. Ma, "Research on end effect of linear induction machine for high-speed industrial transportation," *IEEE Trans. Plasma Sci.*, vol. 39, no. 1, pp. 116-120, Jan. 2011.

[15] K. Yoshida and I. Kawamura, "A method of two-dimensional analysis for short primary linear induction motors," *Elect. Eng. Jpn.*, vol. 100, no. 3, pp. 51-59, May 1980.

[16] S. Yamamura and H. Ito, "Three-dimensional analysis of linear induction motors," *Elect. Eng. Jpn.*, vol. 96, no. 2, pp. 55-61, Mar. 1976.

[17] S. Nonaka and N. Fujii, "Simplified two-dimensional analysis of linear induction motors," *IEEE Trans. Magn.*, vol. 23, no. 5, pp. 2832-2834, Sep. 1987.

[18] Konrad Woronowicz and Alireza Safaee, "A novel linear induction motor equivalent-circuit with optimized end effect model," *Can. J. Electr. Comput. Eng.*, vol. 37, no. 1, pp. 34-41, May 2014.

[19] H. Bolton, "Transverse edge effect in sheet-rotor induction motors," *Proc. Inst. Electr. Eng. UK*, vol. 116, no. 5, pp. 725-731, May 1969.

[20] T. Hirasa, S. Ishikawa, and T. Yamamuro, "Equivalent circuit of linear induction motors with end effect taken into account," *Elect. Eng. Jpn.*, vol. 100, no. 2, pp. 65-71, Apr. 1980.

[21] X. Long, *Theory and Magnetic Design Method of Linear Induction Motor*, China Science Press, Beijing, China, pp. 71-103, Apr. 2006.

[22] Q. Zhang, H. Liu, J. Ma, and Y. Li, "Calculation of electromagnetic performance for long primary double sided linear induction motors considering backward traveling wave," *Transactions of China Electrotechnical Society*, vol. 35, no. 7, pp. 1398-1409, Apr. 2020.

[23] I. Boldea and S. A. Nasar, *The Induction Machine Handbook (1st ed.)*, CRC Press LLC, Boca Raton, USA, pp. 671-679, Nov. 2001.

[24] W. Xu, J. G. Zhu, Y. Zhang, Y. Li, Y. Wang, and Y. Guo, "An improved equivalent circuit model of a single-sided linear induction motor," *IEEE Trans. Veh. Technol.*, vol. 59, no. 5, pp. 2277-2289, Jun. 2010.

Qian Zhang was born in China. He is currently working toward the Ph.D. degree in electrical engineering with Beijing Jiaotong University, Beijing, China. His research interests include the optimal design and analysis of novel permanent-magnet motors, linear induction machines, and hardware design of motor drive.

Hui-juan Liu was born in China. She received the Ph.D. degree in electrical engineering from Beijing Jiaotong University, Beijing, China, in 2009 and received the B.S. and M.S. degrees from Tianjin University, Tianjin, China, in 1989 and 1994, respectively. She worked as a Visiting Scholar with the Laboratory for Power Electronics & Electrical Machines, The Ohio State University, Columbus, OH, USA, in 2008. In 2011 and 2013, she worked as a Research Fellow with The Hong Kong Polytechnic University, Hong Kong. Since December 2015, she has been a Professor with Beijing Jiaotong University. Her current research interests mainly focus on numerical methods of electromagnetic field computation, optimal design and control of high-performance electrical machines and novel electrical motors, such as induction machine, doubly fed brushless machine, and permanent magnetic machine for wind power, and other new power source development.

Teng-fei Song received the M.S. degree from the School of Electrical Engineering, Beijing Jiaotong University, Beijing, China, in 2017. His research interest includes the analysis and optimal design of new structure electrical machines, such as Vernier-machine, and dflux-modulated motor for direct-drive applications.

Zhen-yang Zhang was born in Henan Province, China. He is currently working toward the Ph.D. degree with the School of Electrical Engineering, Beijing Jiaotong University, Beijing, China. His research interests include the analysis and optimal design of new structure electrical machines, the electromagnetic filed analysis and simulation of linear induction motor, and the performance prediction of annular linear induction pump.

Yu Wang was born in Henan Province, China. He is currently working toward the M.S. degree with the School of Electrical Engineering, Beijing Jiaotong University, Beijing, China. His research interests include the analysis and optimal design of linear induction motors.